Università Ca'Foscari Venezia

NADIR Plasma & Polymers

AREA SCIENCE PARK

Università degli Studi di Ferrara

Università degli Studi di Padova

Master's Degree

in Science and Technology of Bio and Nanomaterials

Final Thesis

Plasma assisted surface treatments for surface sterilization and for deposition of thin film with antibacterial and virucidal properties

Supervisor

Ch. Prof. Pietro Riello

Assistant supervisor
Ch. Prof. Barbara Zavan
Ch. Prof. Alessandro Patelli
Ch. Subject expert Paolo Scopece

Graduand
Peter Kimani
Matriculation number
881743

Academic Year
2020/2021

Abstract

The presence of harmful microorganisms in human health has become of great concern, due to the variety of infections and diseases. Rapid antibiotic resistance further worsens the situation. Antimicrobial thin films have the potential to provide a long-lasting antimicrobial protection. NTP can be used to polymerize certain monomers on the material surface creating a stable film. The functions and properties of the thin film are related to the kind of monomers used. In the first section of this thesis, NTP was used to polymerize three organic precursor monomers with antimicrobial properties (2-ethyl-2-oxazoline, Terpinene-4-ol and (Dimethyl amino) ethyl methacrylate) and one organic-inorganic monomer with antimicrobial properties (Bis (dimethyl amino) dimethyl silane). The substrates used in the polymerization process were conductive substrates (stainless steel and silicon wafer) and non-conductive substrates (HDPE and TPU). The effect of changing the NTP operating parameters on the chemical composition of the plasma deposited thin films was also investigated by FTIR. The results showed that increasing the argon carrier gas flow rate or the argon working gas flow rate beyond the optimum value generally resulted in decrease in the intensity of the functional groups. Pulsing the NTP during the treatment process was observed to guarantee congruent transfer of the target functional groups to the substrates and therefore generally higher peaks intensity compared to the continuous mode. The results also showed that generally higher peaks intensity was observed when compressed nitrogen was used as the type of cooling gas as compared to when compressed air was used as the type of cooling gas. The results showed that increasing the distance between the substrate and the plasma jet nozzle up to but not exceeding the optimum distance was observed to generally increase the peaks intensity. Finally, the results showed that increasing the plasma power beyond the optimum power value was observed to generally reduce the peaks intensity due to monomer fragmentation. The WCA of 2-ethyl-2-oxazoline thin film, Terpinene-4-ol thin film, and (Dimethyl ethyl) dimethyl silane thin film indicated that they were all hydrophilic while the WCA of Bis(dimethyl amino) dimethyl silane thin film indicated that it was hydrophobic. The antibacterial activity of the thin films was investigated against two Gram-positive bacteria (Streptococcus pyogenes and Staphylococcus aureus cells) and two Gram-negative bacteria (Escherichia coli and Pseudomonas aeruginosa cells). The antiviral activity of the thin films was investigated against enveloped Sars Covid 2 like virus. The antibacterial tests showed that all the thin films exhibited high antibacterial activity

(greater than 90 % bacterial reduction) compared to the control. The antibacterial tests also showed that the thin films can be classified as contact-active surfaces. The antiviral activity of the thin films was not fully determined potentially due very weak forces of interactions. The excellent antibacterial properties of the thin films allow their potential application in microbiological protection materials and related fields. The utilization of NTP to sterilize surfaces containing pathogenic microorganisms has gained appreciable attention in the past decades due to their widely documented superior advantages over other sterilization methods. In the second section of this thesis, NTP was used to sterilize *E. Coli* cells. The cell adhesion of *E. Coli* cells, and the cellular membrane integrity of the plasma-treated *E. Coli* cells was then imaged by SEM. *E. Coli* cells adhesion presents no problems on HDPE and TPU polymer surfaces, while being more dispersed on stainless steel and absent on silicon wafer substrate. Cumulative damages by the NTP treatment overrode the stress tolerance of *E. Coli* cells, eventually completing their death. Therefore, NTP has great potential for current and future practical use in decontamination and sterilization fields.

Dedication

I dedicate this thesis to my Great and visionary father, Dr. Stephen Kimani Muiruri who crystallized our family's vision, my vision specifically, and introduced me to my dream and became the pivotal and central support system to me. I shall honor him with great dedication, precision, and top-level creativity, every single day of my life, as the lord commands in Ephesians 6: 2-3. I shall also extend this honor to his lovely wife and life-partner (my mother) in equal measure and magnitude. He was, to say the least, the greatest gift to the earth from God after Jesus Christ.

He was a physicist with similar if not greater comprehension of physics laws and concepts with the likes of Albert Einstein, Isaac Newton, Michael Faraday, Marie Curie, Robert Hooke not forgetting Archimedes. I will be privileged and honored to be able to bring to the entire world, an insight into the greatest and the wisest mind to have ever lived by sharing his thoughts, principles, convictions, and perspectives through books.

Taking into consideration that I have his DNA; I have no aorta of doubt that as soon as they hit the shelves, they will rise to become best-selling books and that they will remain at the very top of the game for many years to come. They shall know no boundaries, no seasons, and no specific generation, but rather applicable and relevant to everyone and anyone, irrespective of their locality, disability, age or sexual orientation, religion, or belief, racial or ethnic origin.

Acknowledgements

I sincerely appreciate the almighty God for His graces, strength, sustenance and above all, His faithfulness and love from the beginning of my academic life up to this master's level. His benevolence has made me excel and successful in all my academic pursuits.

I acknowledge the generous financial support from the Italian Agency for Development Cooperation in partnership with Ca' Foscari University of Venice.

I express my sincere gratitude to all my supervisors for their valuable suggestions, ever encouraging and motivating guidance. Their unassuming approach to research and science was a source of inspiration.

I would like to appreciate the first line of my defense being all my prayer warriors who were based in my home country, Kenya. They were continuously on their knees, praying for me. This was our secret powerful weapon that made all the difference for me and my message to them is that may the almighty God bless them abundantly with his love, his grace, and his peace, Amen.

I would also like to greatly appreciate and recognize in a very special way, the second and the final line of my defense, being my family, starting with my father (Dr. Stephen Kimani Muiruri) and my mother (Dr. Mary Mweru Nyakiambi) followed by my siblings Dr. Joseph Muiruri Kimani (elder brother) and Dr. Brian Kariuki Kimani (our last born) for their abundant love and unconditional support. They were a source of inspiration as I hurdled through the path of this master's degree. My accomplishments and success are because they believed in me.

I would like to further single out my father and offer him a special thank you for his endless support and always standing behind me, and this was no exception. He fielded a ridiculous number of phone calls, to check out on me and always reminded me of the end goal.

Mother, thank you for always being there for me, calming me down, and for being my number one prayer partner. I will grant you, mother, a 24-hour exclusive access to me either physically or virtually, together with access to all the monetary and all the other forms of resources availed to me by God in the form of his blessings.

Table of contents

List of Figures

List of Tables

List of Abbreviations

Abbreviation	Meaning	Page
RS	Reactive species	1
ROS	Reactive oxygen species	1
RNS	Reactive nitrogen species	1
UV	Ultraviolet	1
NTP	Non-thermal plasma	2
CAP	Cold atmospheric plasma	2
DBD	Dielectric barrier discharge	4
APPJ	Atmospheric pressure plasma jet	4
AMR	Antimicrobial resistance	9
RONS	Reactive oxygen and/or nitrogen species	26
HDPE	High-density polyethylene	29
TPU	Thermoplastic polyethylene	29
CA	Contact angle	52
SD	Standard deviation	53
LB	Luria-bertani	56
PBS	Phosphate-buffered saline	115
CFUs	Colony forming units	
LS	Lipopolysaccharide	

1. Introduction

1.1 Plasma

Plasma is considered the fourth state of matter after solid, liquid and gas **(Figure 1).** Plasma is a Greek word meaning “that which is diffused” that is semi-transparent or unclear [1]. Scientists have defined it as “ionized matter”. It is simply a cocktail of highly reactive species (RS), for example, reactive oxygen species (ROS), reactive nitrogen species (RNS), among the others [2]. Some of the other active species produced includes positive and negative ions, electrons, free radicals, photons and neutral species containing high energy [3]. Therefore, plasma is a very complex and dynamic medium which acts in a collective and synergistic manner [4]. In man-made systems, it is triggered by the application of an electromagnetic or electric field to a gas. The applied field energy causes the free electrons to accelerate and ionizes the gas atoms and molecules, which gives rise to more free electrons that ultimately provoke additional ionizations. Additionally, the excited electrons form molecular dissociations, with the creation of fresh atoms and free radicals, also capable of exciting atoms and molecules to the upper energy levels.

Excited atoms and molecules, when retreating to the more stable state, releases the surplus energy in the form of broad-spectrum electromagnetic radiation, counting ultraviolet (UV) radiation [5]. Often, plasma is accompanied by the production of heat due to the collision of electrons, and the subsequent excitation, ionization, and dissociation process of the gas particles [6]. Depending on the temperature of the gas, plasmas are classified into two large groups: thermal plasmas and cold plasmas [7]. Thermal plasmas have a characteristic high temperature that can reach up to several thousand Celsius degrees and are significant especially where high temperatures are required, for example, in the chemical synthesis procedures such as in generating acetylene from natural gas or in casting procedures in the metallurgical industry. The effects of such thermal plasmas on tissues are non-selective and laborious to control due to the reason that they occur fundamentally through transfer of intense heat [8]. Cold plasmas, with temperatures close to room temperature, are on the contrary befitting for the treatment of heat delicate materials [5].

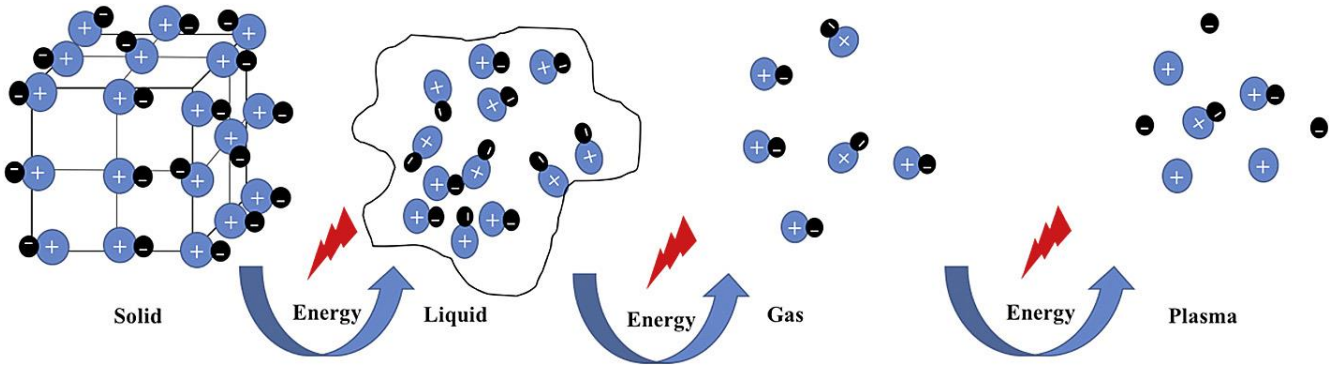

Figure 1| The four states of matter (adapted from [2])

1.2 Non-thermal atmospheric plasma

Non-thermal plasma (NTP), also referred to as cold atmospheric plasma (CAP), is acquired at lower power and at lower pressures with a low macroscopic temperature. Under these conditions, a significant amount of the coupled energy is transferred and transmitted into the electrons with a higher temperature, and the ions and neutral particles support only insignificant and inappreciable energy and are usually cold [9]. NTP plays an important part in introducing different functional groups depending on the type of gas (single gas or a mixture of gases) used in the plasma treatment. Several different gases can be used to set-up the NTP such as Argon, Nitrogen, Helium, Heliox (a mix of helium and oxygen) and air [10]. It has been reported that argon plasma could introduce free radicals while an oxygen plasma or plasma operated under atmospheric pressure conditions, could introduce a mixture of mainly hydroxyl and carboxyl functional groups [11, 12]. Plasmas produced in atmospheric pressure conditions, for example, are important sources of reactive nitrogen and oxygen species. Additionally, gas processing in atmospheric pressure conditions ensures that the electron and molecular density is formidably high in comparison to low pressure conditions [13].

The temperature and the gas constituents, as well as the strength and duration of the pulse of the electric field plays a substantial role in determining the exact composition of the plasma [14]. Therefore, as a matter of fact, it is possible to manipulate and vary the plasma density and chemical composition, producing distinct active chemical species within the plasma plume itself relatively and quite easily. Some of the charged and neutral reactive oxygen species (ROS)

includes O_2^-, O_3, $^{\bullet}OH$, H_2O_2, HO_2, O and OH [15] **(Figure 2).** Some of the charged and neutral reactive nitrogen species (RNS) includes NO, NO_2, $ONOO^-$, NO_2^+, and N_2O_3, NO^+ [16] (**Figure 2).**

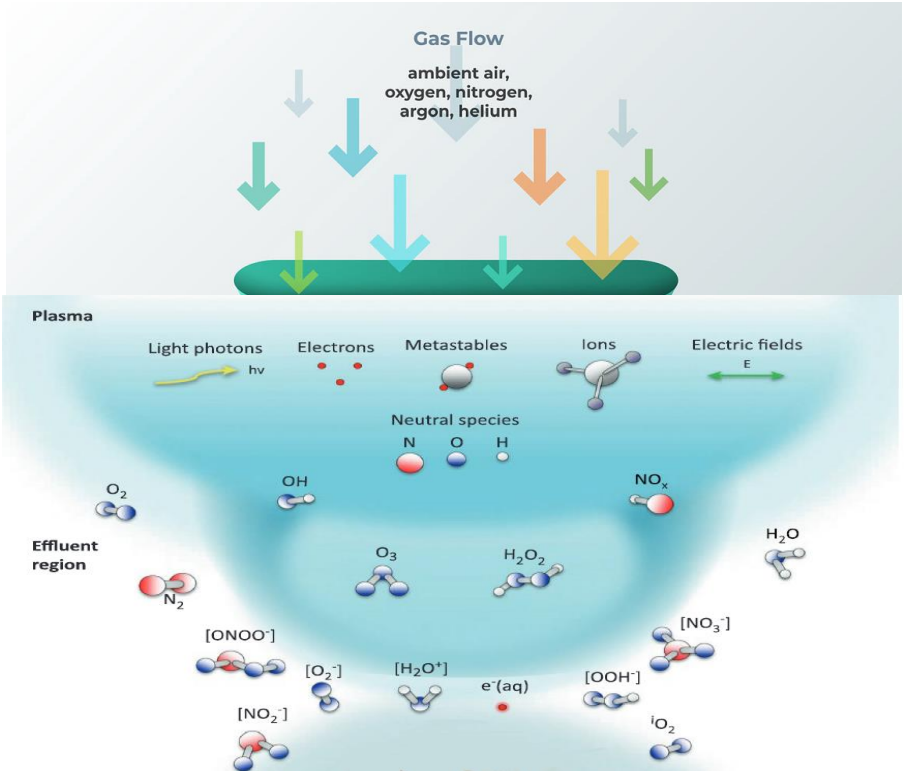

Figure 2| Complex cocktail of the plasma species (Adapted from [17, 18])

1.3 Plasma sources

There are several ways of producing NTP from several gases such as **a)** corona discharge, **b)** gliding arc discharge, **c)** dielectric barrier discharge, **d)** plasma jet, etc. **(Figure 3)**. Frequently

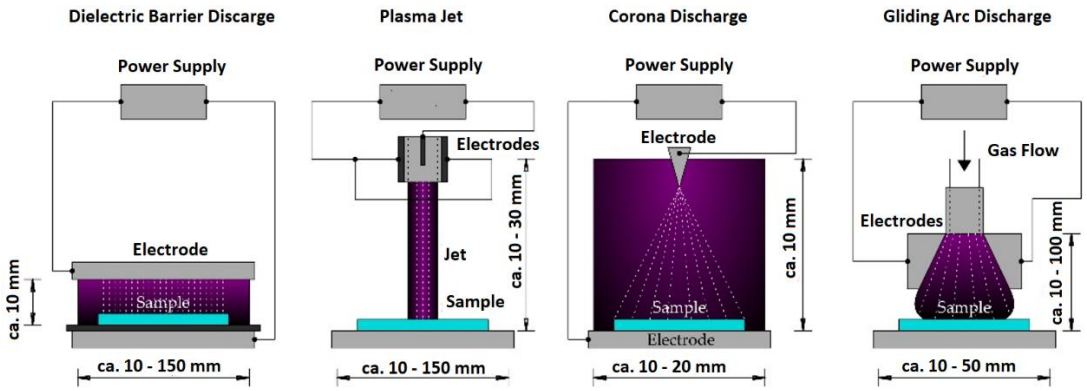

Figure 3|Schematic drawing of divergent atmospheric NTP sources (Adapted from [19])

used working gas includes helium, nitrogen, oxygen, air, argon and their combinations [20]. Dielectric barrier discharge (DBD) is produced by applying a high voltage (~kV) electric DC or AC current at high frequency (~kHz) across a movable gap (varying from tens of microns to several cm) in between two electrodes set apart by an insulating dielectric barrier. The arrangement of DBDs mostly consists of two parallel plates in cylindrical or planar arrangements. DBDs make use of a dielectric material such as ceramics, enamel, silicon, glass, quartz, mica, teflon and plastic to cover at least one of the electrodes. The nonconducting nature of the coating removes the passage of the discharge to an elecrical arc [21].

The atmospheric pressure plasma jet (APPJ) is a class of cold plasma discharge that releases a high velocity stream of extremely reactive chemical species having weak discharged light. APPJs normally comprises two concentric cylindrical electrodes. Short distance between the electrodes, in its typical geometry, makes it possible to operate in low applied electric field environment, and gas flow (mainly noble gases such as Ar or He) and this guarantees the low temperature character of plasma. APPJs can be provided by direct, pulsed direct, or high frequency alternating currents (radio frequency and microwave **(Figure 4)**) resulting in the ionization of the working gas. The gas exits through a nozzle giving it a “jet-like” appearance [22]. Based on the layout and used materials, APPJs can be split into dielectric-free electrode jets, DBD jets, DBD-like jets, and single electrode jets. Miniature plasma jets are known as plasma torches, plasma pens or plasma needles [23]. The major consituent of plasma needles is an electrode with a sharpened tip located at the interior section of the tube. The feed gas

(most routinely used being helium) is flowing across the tube and is mixed with air at the needle tip where a micro discharge is formed.

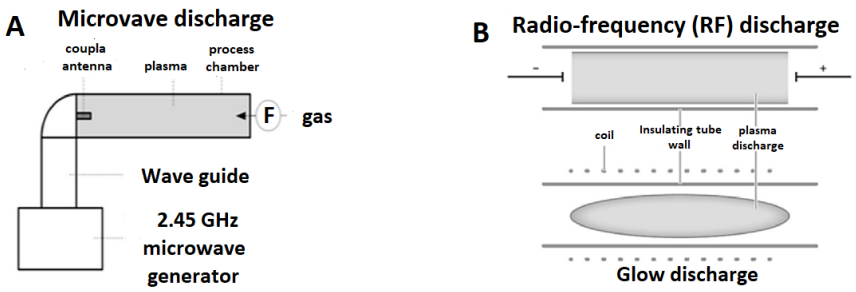

Figure 4| Schematic drawing of plasma production sources using Radiofrequency and Microwave sources. **(A)** Microwave discharge set-up. **(B)** Radiofrequency discharge set-up (Adapted from [24])

Corona discharge is produced by the utilization of high voltage in between two or more sharp electrodes. The colonizing electrode is normally realized as a needle or a thin wire. The process of ionization forms a crown around this active electrode. Coronas have a characteristic weak discharge, having diminished low electron and ion densities [25]. Gliding arc discharge plasma reactors are known as hot plasma sources, although, under specified conditions they may produce cold plasma as well. The gliding arc plasma has the potential to merge the advantages of both thermal and nonthermal plasmas (nonthermal plasma conditions are attained at higher power). The discharge is created by an increased voltage value at the region where the distance between the diverging electrodes is shortest (~ in the range of millimeters). Electrodes are positioned in a fast gas flow causing the discharge to increase in its volume and length in the direction of flow [26].

1.4 Thin film deposition mechanism of NTP

In comparison with previously used materials modification techniques, NTP surface modification technique is fast and appropriate. In comparison with previously used material modification techniques is fast and appropriate. Additionally, NTP only modifies the

characteristics of nanometer depth of the material surface, while it preserves most of the properties of the material. The five primary ways of NTP modification **(Figure 5)** of material surface properties, includes etching, modification/functionalization, activation, cleaning, and thin film deposition.

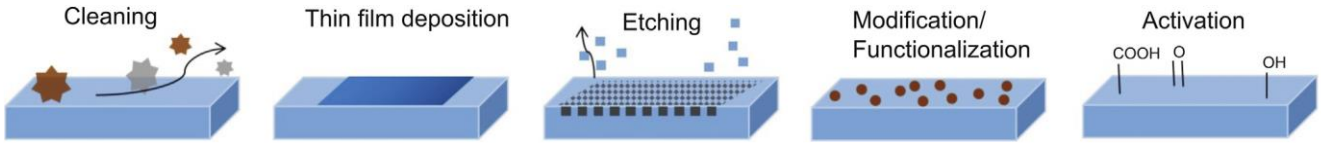

Figure 5| Five ways of using NTP to modify material surface properties (Adapted from [27])

Cleaning is beneficial for the direct contact between NTP and material surface, and can be the preliminary step of thin film deposition. Thin film deposition refers to NTP polymerizing certain monomers on the material surface create a stable thin film [28]. The functions and properties of the film are related to the kind of monomers used. The set-up of NTP jet used for the deposition of a thin film, for example, is shown in **Figure 6**. NTP jets gives, as a matter of fact, a unique prospect of positioning the substrate outside the source physical boundaries, since they can bring the plasma, and therefore the reactive plasma species such as metastables, ions and radicals in the external environment and even in open air.

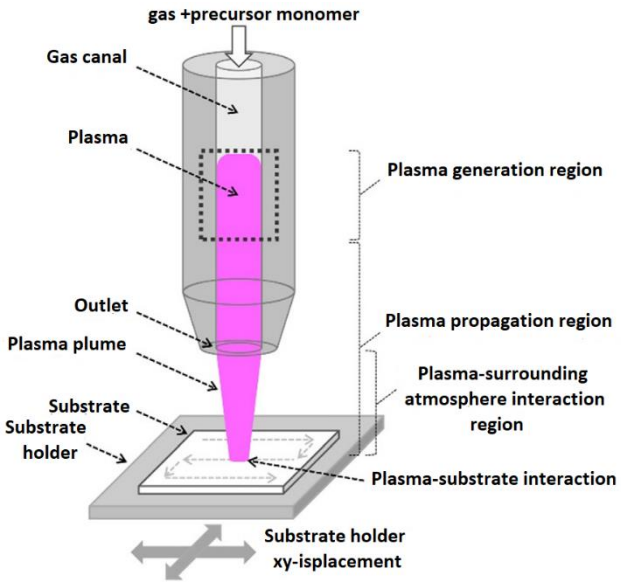

Figure 6| Schematic diagram of a general plasma jet device used in the deposition of thin films (Adapted from [29])

In plasma polymerization process, the electron impact segregation of the original monomer is behind the initial formation of several species including neutral radicals plus negative and positive ions. The plasma excitation and radicalization of the carrier gas and vapor phase monomer allows the excited species the opportunity to react forming a film through two basic steps: formation of a free radical $(\boldsymbol{R^{\blacksquare}})$ or reactive species, which initiates the process and propagation of the polymer chain via reaction (Equation 1 and Equation 2) with the monomers $\boldsymbol{(m)}$.

$$R^{\blacksquare} + m \rightarrow R_1{}^{\blacksquare} + m \rightarrow R_2{}^{\blacksquare} + m \rightarrow Uncross-linked\ polymer \qquad \textbf{Equation 1}$$

$$R_1{}^{\blacksquare} + m \rightarrow Crosslinked\ Product \qquad \textbf{Equation 2}$$

All these species, which are established in the plasma volume, contribute to the flux of species impinging on the substrate accomplishing the film growth in a synergistic way. The exact form of the species flux for a particlar precursor, and consequently, the features of the plasma produced thin films, normally relies on a considerable number of possible external parameters such as the electrode distance, power, pulse frequency, process pressure, gas mixture ratios (noble gas component/monomer) and duty cycle or ratio input flow rate/pumping speed (residence time) [30].

1.5 Functional principles of antimicrobial thin films

The strategies to achieve antimicrobial coatings can be classified according to the functional principle with which they operate. Antimicrobial coatings can be classified into three main groups: contact-killing surfaces, anti-adhesive surfaces and biocide releasing surfaces.

1.5.1 Contact-active surfaces

In contact-killing surfaces, antimicrobial species are anchored to the surface by the use of covalent bonds and consequently, do not leach any agents into the adjacent environment. Instead, these category of surfaces kill the bacteria upon contact. They can be developed by imparting antimicrobial nanosegments onto the material surface. Contact-killing surfaces do not result in microbial resistance, as do leaching surfaces. Considering the superiority of contact-killing surfaces, utilizing them is a good strategy for the fight against microbes [31].

1.5.2 Anti-adhesive surfaces

Anti-adhesive surfaces functions by reducing the adhesion force between bacteria and a solid surface. They therefore repell bacteria instead of killing them. Antiadhesive surface treatments typically use low surface energy **(Figure 7)** coatings including superhydrophobic films to reduce adhesion between the surface and bacteria [32]. They are inspired by nature such as the lotus leaf. Antiadhesive surfaces do not kill bacteria, however, so the existing bacteria still can be a threat to other targets, which is the biggest disadvantage of this type of surface.

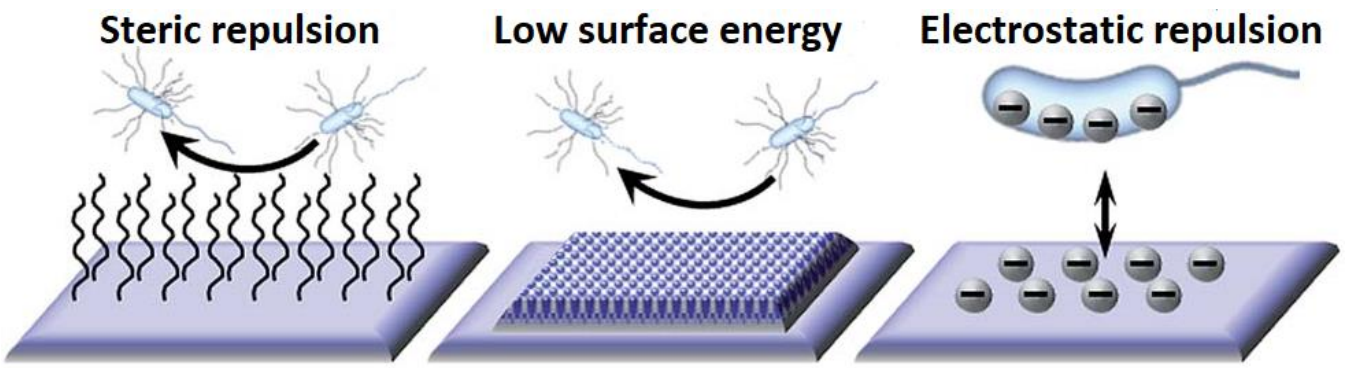

Figure 7| Divergent strategies employed by anti-adhesive surfaces (Adapted from [33])

1.5.3 Biocide releasing surfaces

Surfaces treated with leaching antibacterial agents use encapsulated agents released from the surface to kill the bacteria by damaging or destroying its cell walls. Triclosan, active chlorine,

metal, metal salts, quarternary ammonium salts, antibiotics and silver are commonly used antimicrobial agents [34]. The leaching mechanism is not an inherently long-term sustainable approach owing to reservoir limitations. Leaching agents are also one of the most important agents behind AMR [35]. Furthermore, leached agents accumulate in the environment, presenting a risk to the environment and mammalian cells [36].

1.6 Selected organic and organic-inorganic antimicrobial agents used in this study

Several types of inorganic particles have been used as an antibacterial agents including metal oxides, non-metal oxides, metals and others. These inorganic materials, particularly, silver (Ag), Copper (Cu), Zinc (Zn) and gold (Au), in the micro or nano forms, have been demostrated to be effective against bacteria [37]. The possible antibacterial mechanism of these inorganic agents is shown in **Figure 8a**. On the other side, organic materials, either natural sources or of synthetic origin are also used as antibacterial agents. Frequently used organic antibacterial agents includes triclosan, chlorhexidine (CHX) or polyethyleneimines (PEI) among others [38]. The possible antibacterial mechanism of these organic agents is shown in **Figure 8b**.

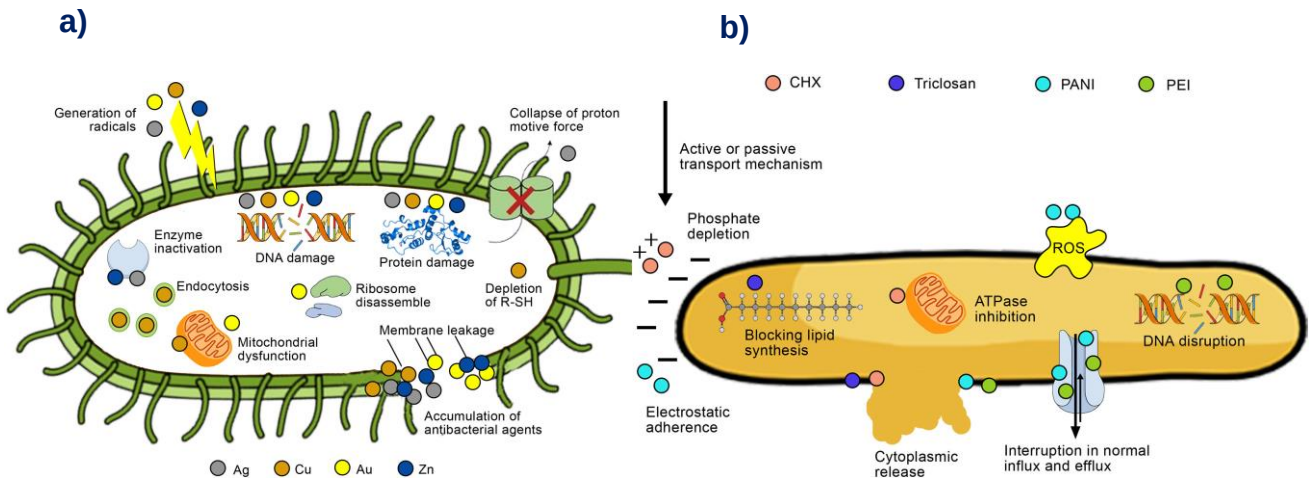

Figure 8| Possible antibacterial mechanisms of inorganic and organic agents. **a)** Possible antibacterial mechanisms of inorganic antibacterial agents such as Ag, Cu, Au and Zn **b)** Possible antibacterial mechanisms of organic antibacterial agents such as CHX, triclosan, PANI and PEI (Adapted from [39])

Additionally, the proposed antibacterial mechanism of secondary plant metabolites (PSMs) such as tea tree (*Melaleuca alternifolia*), Terpinen-4-ol, geranium, zataria and cinnamon oils is shown in **Figure 9**.

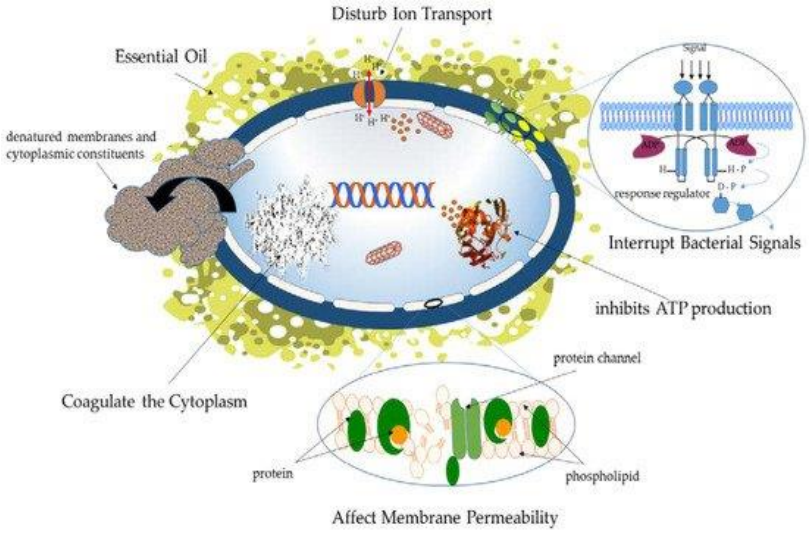

Figure 9| Scheme representing the proposed antibacterial mechanisms of secondary plant metabolites in their liquid form (Adapted from [39])

In this study, three organic precursor monomers that have antimicrobial properties (2-Ethyl-2-oxazoline, Terpinene-4-ol and 2-(Diethylamino) ethyl methacrylate) (**Figure 10a**, **Figure 10b** and **Figure 10c**, respectively) and one organic-inorganic monomer that has antimicrobial properties (Bis(dimethylamino) dimethyl silane)) (**Figure 10d**) were used to deposit thin films that have antimicrobial properties.

a) **b)** **c)** **d)**

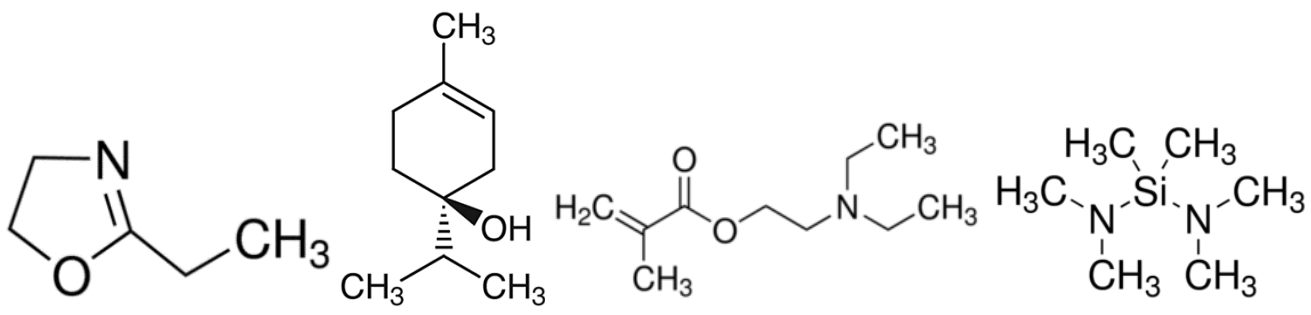

2-ethyl-2-oxazoline | Terpinene-4-ol | 2-(Diethyl amino) ethyl methacrylate | Bis(dimethyl amino) dimethyl silane

Figure 10| Molecular structures of precursor monomers with antimicrobial properties selected for this study **a)** Molecular structure of 2-ethyl-2-oxazoline precursor monomer **b)** Molecular strucure of terpinene-4-ol precursor monomer **c)** Molecular structure of 2-(Diethylamino) ethyl methacrylate precursor monomer **d)** Molecular structure of Bis(dimethylamino)dimethylsilane precursor monomer

Poly(2-oxazoline)s (POx) are emerging biomaterials showing comparable and even superior properties to well-established counterparts. Many 2-oxazoline monomers are currently commercially available. POx, in particular poly(2-ethyl-2-oxazoline) (PEtOx) and poly (2-methyl-2-oxazoline) (PMeOX), represent a class of water soluble, biocompatible, non-toxic and highly stable polymers displaying a number of new applications developed in recent years [40] Studies have shown POx can be used in pharmaceutical and medical applications. POx are non-ionic biocompatible materials with low cytotoxicity and without immunisuppressive effects. They show antibacterial properties similar to poly(ethylene glycol) (PEG), with higher stability (PEG is known to undergo oxidative degradation) and without any adverse effects in animal models [40]. POx coatings and thin films can be prepared using NTP from the corresponding organic precursor monomer via ring opening polymerization mechanism.

PSMs, for example terpinene-4-ol, have shown inherent bactericidal performance in their liquid and/or vapor form toward important pathogenic microbes. Terpinene-4-ol is major bioactive component of tea tree oil. In recent decade, it has enjoyed increased popularity as alternative medicine on account of its anti-microbial and anti-inflammatory properties [40]. Terpinene-4-ol has received attention as a natural antibacterial agent against bacterial species *pseudomonas aeruginosa*, *Escherichia coli*, and drug resistant *Staphylococcus aureus.* Terpinene-4-ol penetrates through the cell wall and cytoplasmic membrane of bacteria compromising there structure and loss of intercellular material [41]. Lipophilicity of the essential oils help them to penetrate through cytoplasmic membrane causing irreversible damage to cells ultimately leading to its death [42]. Poly(Terpinene-4-ol) coatings and thin films can be prepared using NTP from the corresponding organic precursor monomer via ring opening polymerization mechanism.

Poly(diethylaminoethyl methacrylate) (PDEAEMA) possesses antibacterial activities owing to their tertiary amine-functional groups [42]. The tertiary amine-functional groups contributes to bacterial retardation by interacting and distorting the negatively charged bacterial cell membrane. Other cytoplasmic constituents and K^+ ions will then be discharged, resulting in immediate death of bacteria. PDEAEMA thin films and coatings can be prepared using NTP from the corresponding organic precursor monomer via ring opening polymerization mechanism.

Poly(Bis (dimethylamino) dimethylsilane) (PBDMADMS) can also contain quarternary amino groups [43]. The tertiary amine-functional groups contributes to bacterial retardation by interacting and distorting the negatively charged bacterial cell membrane. Other cytoplasmic constituents and K^+ ions will then be discharged, resulting in immediate death of bacteria [38]. PBDMADMS thin films and coatings can be prepared using NTP from the corresponding organic-inorganic precursor monomer via ring opening polymerization mechanism [38].

1.7 Application of antimicrobial thin films

There has been a constant drive for smart technology towards development of materials and

surfaces capable of repelling or killing pathogenic microorganism present on various exteriors in our daily life (such as hospital tools, food packages, kitchen and bathroom etc.). Most of these surfaces are not intrinsically bactericidal and modifications such as the incorporation of antimicrobial thin films are thus required for microorganism destruction and prevention of further bacterial infections [44]. One of the methods to tackle biofilms, for example, involves prevention of biofilm formation by actively killing the bacteria as soon as they arrive on the surface and therefore prevent antimicrobial resistance [45]. Additionally, antibacterial thin films can also be used to prevent Hospital acquired infections (HAIs) in hospital settings. Other potential uses of antibacterial materials include household, industrial, and public facility product such as paints, toys, appliances, and kitchen, as well as school equipment [46].

In today's global society, disease outbreaks can spread rapidly and easily cross borders and continents, having a catastrophic impact on health and the global economy. There is no single solution to prevent the spread of viral infections. Different modes of infection transmissions such as through aerosol, droplets or fomites (everyday use surfaces), add to the problem [46]. Therefore, multiple-barrier protection is often required and, next to high hygiene standards and vaccination programmes, a number of control measures including adequate personal protective equipment (PPE) and the application of antiviral surfaces made of antiviral thin films in public facilities, such as schools, health centres or airports are important to reduce transmission of viruses.

1.8 Brief description of bacterial cells and their relation to NTP sterilization

1.8.1 Bacterial cell membrane

The cell membrane possesses numerous essential and fundamental cell functions including conveying messages to and from the environment, carrying molecules and certain metabolic functions [47]. Additionally, the cell membrane cushions the cells from countless damaging factors, as well as creating a balanced internal environment. The principal components of membranes are proteins, carbohydrates and phospholipids. A binary layer of phospholipids creates the chief membrane skeleton. Carbohydrate molecules clutches onto phospholids or integral proteins. The present membrane model detailing the composition of membranes is the

“Fluid mosaic model” **(Figure 11a)**. Persuant to the model, membranes are principally made of proteins, lipids and carbohydrates. The focal skeleton of the membranes is composed of phospholipids, which are arranged into two layers. Each phospholipid molecule has one hydrophobic and one hydrophilic region [48].

The hydrophobic domain of each molecule is found facing the core of the membrane. Conversely, the hydrophilic domain is found facing out of the layer. The model has been reformed by several scholars after its prime identification. The reformed model accommodated extra information not incorporated in the native model, for example, cytoskeletal and matrix interactions, protein and lipid aggregations and segregation into domains, among other hallmarks (Some of these hallmarks are shown in **Figure 11b** of Nicolson [49])

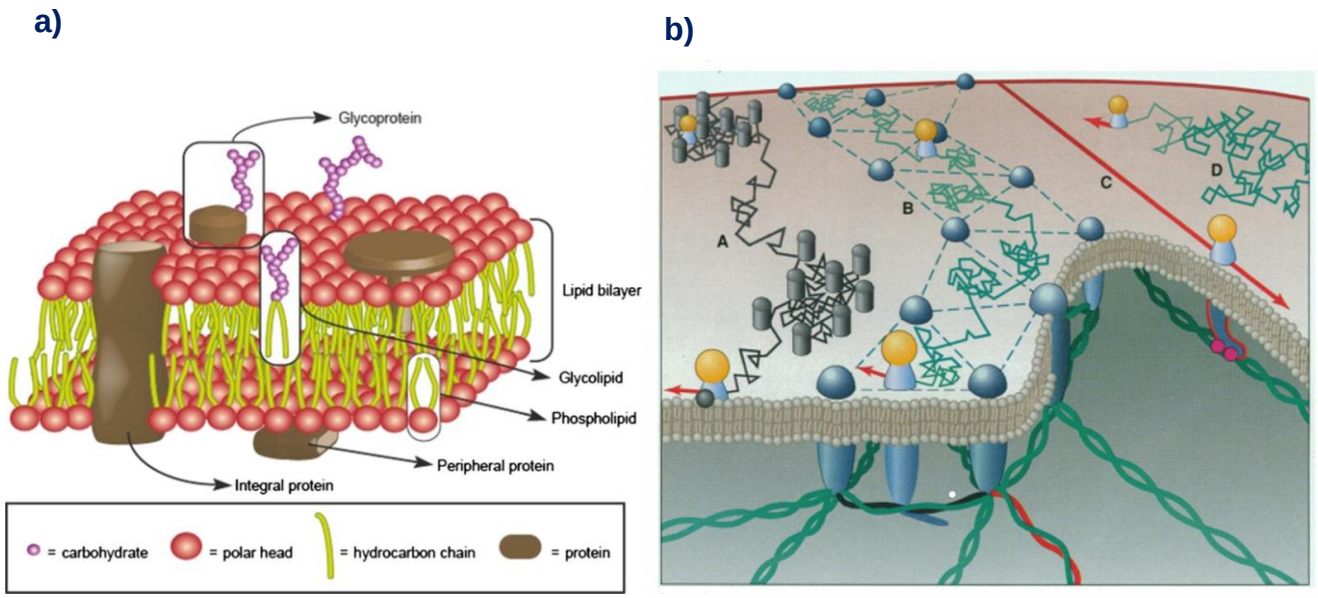

Figure 11| Proposed cell membrane models **a)** Fluid mosaic model portraying the current schematic view of biological membrane **b)** Divergent illustrations of integral membrane protein lateral mobility as envisaged by Jacobson and colleagues in 1995. Integral membrane protein lateral movements are reported as: transient confinement as a result of obstacle clusters **(A)**; transient confinement due to the obstacle clusters **(B)**; directed motion as a result of the attachment to the cytoskeleton **(C)**; and free, irregular diffusion in the membrane plane **(D)** (Adapted from Jacobson et al. [50]).

1.8.2 Bacterial cell wall

The bacteria cell wall is an intricate, web-like structure found in the bulk bacteria that is crucial for the conservation of the structural integrity and the cell shape. Beyong 100 years ago, Christian Gram (1884) advanced a staining protocol that permitted him to categorize nearly all bacteria into two large substantial groups, and this legendary stain is still used universally. One group of bacteria preserves Christian's stain, Gram-positive, and the other do not, Gram-negative [51]. The foundational principle underlying the Gram stain protocol, lies in the foundational structural differences in the cell envelope of these two groups of bacteria. The cell wall of Gram-negative bacteria comprises of a thin layer of peptidoglycan in the periplasmic space between the inner and outer lipid membranes. The outer membrane encompasses lipopolysaccharides on its exterior leaflet.

a) Gram negative bacteria

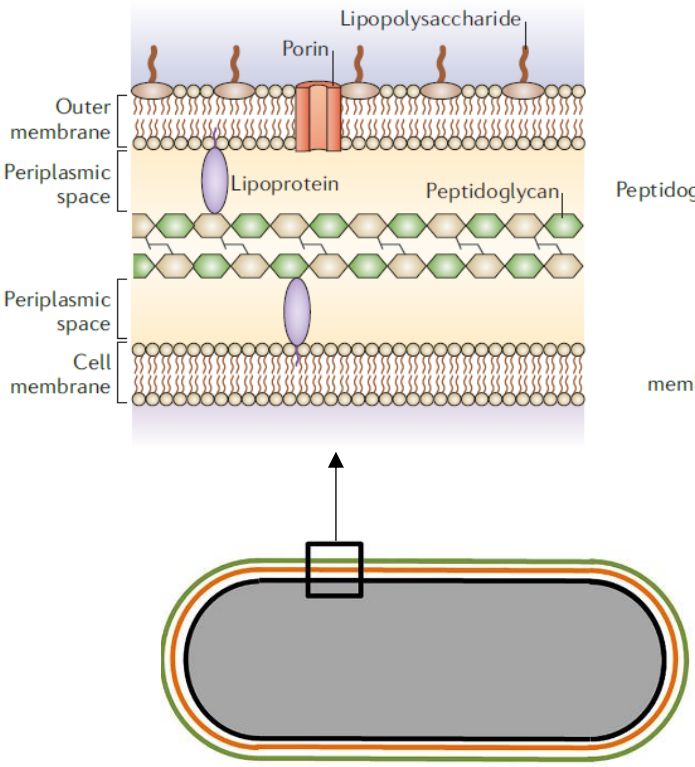

b) Gram positive bacteria

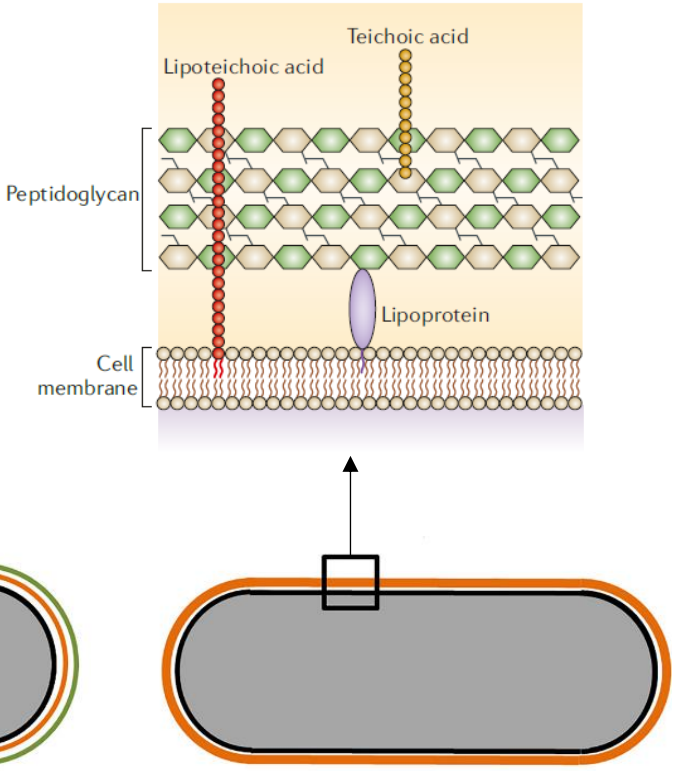

Figure 12| Cell wall structure of Gram-negative and Gram-positive bacteria **a)** Cell wall structure of Gram-negative bacteria **b)** Cell wall structure of Gram-positive bacteria (Adapted from [52])

The cell wall **(Figure 13)** comprises mostly of peptidoglycan (PG), a network of polysaccharide strands (constituted of a poly-[*N*-acetylglucosamine (GlcNAc)-*N*-acetylmuramic acid (MurNAc)] backbone) crosslinked through short peptide bridges connected to the MurNAc residues.

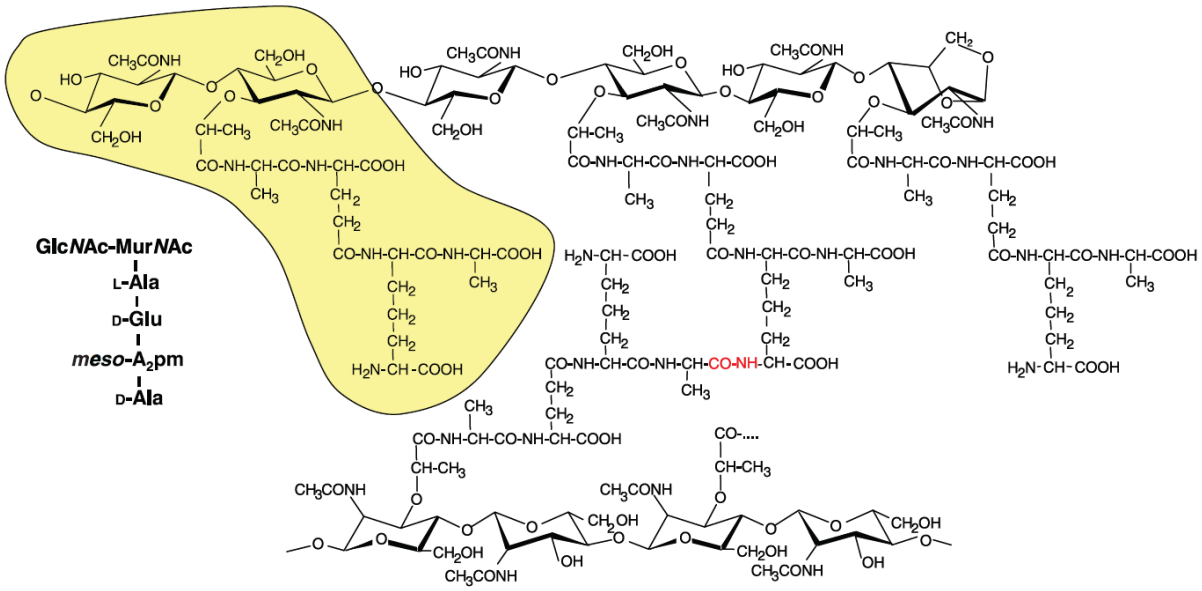

Figure 13| Structure of the peptidoglycan of Escherichia coli. The yellowish labelled part represents the basic disaccharide tetrapeptide subunit (monomer), which is also written with the conventional amino acid and hexosamine abbreviations on the left-hand side. The middle part shows a cross-linked peptide, with the amide group connecting both peptide stems drawn in red (Adapted from [53])

1.8.3 Bacterial cell morphology

The shape of a bacteria is elucidated by the physical margins of the cell [54]. The display of

bacterial cell shapes is time and again unvalued. Besides the familiar cocci and rods, more remote shapes, for example, mustaches, serpentines, branches and stars represent a vast, although unspecified, proportion [55]. The characteristic schematics in **Figure 15** provides a glance of this multiplicity, but barely do justice to the disparity of shape and size across the bacterial domain. Additionally, the bacterial cellular form can change shape during their life cycle.

1.8.4 Bacterial replication cycle and pathogenesis

The precise transfer of genetic information from one cell to its progeny is a crucial process for all organisms. The first step is to assemble a copy of the genome. Genome duplication is catalyzed by protein complexes that moderate various lead reactions that cover origin recognition and replication initiation, double-stranded (ds) DNA unwinding, replication of template single-stranded (ss) DNA, and termination upon completion of replication [56]. Bacterial pathogenicity happens through adhesion to host cells, usually using long appendages called pilli or fimbriae. Following attachment, the bacteria need to overturn host cell processes, frequently using secreted proteins. Exploiting and hijacking host cell signalling pathways terminate in the organized invasion of host cells, dodging of host immune responses and effective colonization, and eventually leads to disease [57].

1.8.5 Mechanism of bacterial attachment and stability on environmental surfaces

The bacterial cell envelope is particularly heterogeneous and accommodates several exposed lipids, proteins, and exopolysaccharides, besides fimbrial and non-fimbrial structures **(Figure 14)**. The configuration of these numerous biopolymers is dynamic and depends on the ionic strength and the environmental pH. Consequently, the bacterial cell envelope manifests divergent hydrophobicity and charges around the cell body dependent on growth conditions. Numerous bacteria cells possess several proteinaceous extracellular appendages that have a direct or indirect role in adhesion (Figure 9).

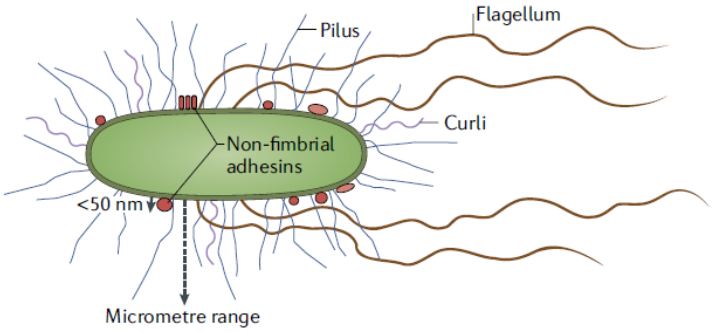

Figure 14| The heterogeneous nature of the bacterial cell wall surface. Various types of structures and molecules are involved in the primary interaction between the bacterium and the solid surface, as well as long fimbriae adhesins (such as curli and pili, represented in purple and blue, respectively) and flagella (depicted in brown) and non-fimbrial adhesins (such as LapA and Ag43 proteins, represented in red. Though non-fimbrial adhesins are more firm and normally protrude tens of nanometers (<50 nm) from the cell envelope, prolonged fimbrial adhesins can extend at the micrometer scale (Adapted from [58])

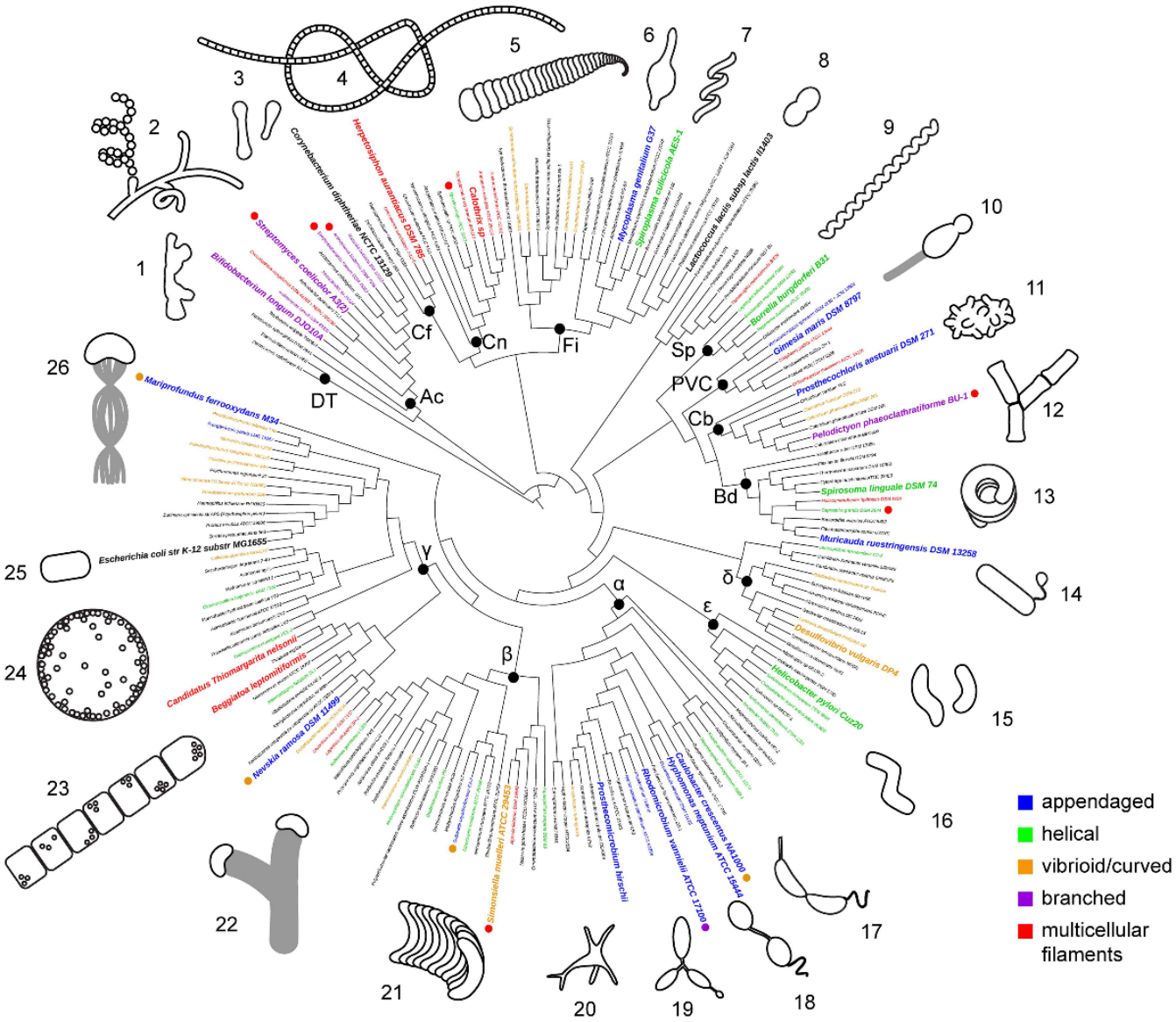
1
2
3
4
5
6
7
8
9
10
11
12
13
14
15
16
17
18
19
20
21
22
23
24
25
26
Cf
Cn
Fi
Sp
PVC
Cb
Bd
DT
Ac
α
β
γ
δ
ε
Corynebacterium diphtheriae NCTC 13129
Herpetosiphon aurantiacus DSM 785
Calothrix sp.
Mycoplasma genitalium G37
Spiroplasma culicicola AES-1
Lactococcus lactis subsp lactis IL1403
Streptomyces coelicolor A3(2)
Bifidobacterium longum DJO10A
Borrelia burgdorferi B31
Gimesia maris DSM 8797
Prosthecochloris aestuarii DSM 271
Pelodictyon phaeoclathratiforme BU-1
Spirosoma linguale DSM 74
Muricauda ruestringensis DSM 13258
Desulfovibrio vulgaris DP4
Helicobacter pylori Cuz20
Caulobacter crescentus NA1000
Hyphomonas neptunium ATCC 15444
Rhodomicrobium vannielii ATCC 17100
Prosthecomicrobium hirschii
Simonsiella muelleri ATCC 29453
Nevskia ramosa DSM 11499
Candidatus Thiomargarita nelsonii
Beggiatoa leptomitiformis
Escherichia coli str K-12 substr MG1655
Mariprofundus ferrooxydans M34
appendaged
helical
vibrioid/curved
branched
multicellular filaments

Figure 15| Multiple morphologies of the bacterial domain that have advanced over the years. **1**. *Bifidobacterium longum***. 2**. *Streptomyces coelicolor* (mycelial [multicellular] filament with spores and hyphae). **3**. *Corynebacterium diphtheriae* (dumbbell, two cells and club shapes). **4**. *Herpetosiphon aurantiacus* (filament of diverse cylindrical cells). **5.** *Calothrix* (filament of diverse diskshaped cells). **6.** *Mycoplasma genitalium*. **7.** *Spiroplasma culicicola*. **8.** *Lactococcus lactis* (ante-divisional cell). **9.** *Borrelia burgdorferi*. **10.** *Gimesia maris* (formerly Planctomyces maris, ante-divisional cell with proteinaceous stalk). **11.** *Prosthecochloris aestuarii*. **12.** *Pelodictyon phaeoclathratiforme* (filament of diverse trapezoidal cells). **13.** *Spirosoma linguale*. **14.** *Muricauda ruestringensis* (appendage encompasses nonreproductive bulb). **15.** *Desulfovibrio vulgaris* (two cells, helical and curved shapes). **16.** *Helicobacter pylori*. **17.** *Caulobacter crescentus* (ante-divisional cell). **18.** *Hyphomonas neptunium* (ante-divisional cell)**. 19.** *Rhodomicrobium vannielii* (filament of diverse ovoid cells, one is ante-divisional). **20.** *Prosthecomicrobium hirschii*. **21.** *Simonsiella muelleri* (filament of diverse curved cells). **22.** *Nevskia ramosa* (two cells with bifurcating slime stalk). **23.** *Beggiatoa leptomitiformis* (filament of diverse, huge cylindrical cells). **24**. *Thiomargarita nelsonii* (solitary, huge cell). **25.** *Escherichia coli.* **26.** *Mariprofundus ferrooxydans* (solitary cell with metal-encrusted stalk). Bacterial schematics are not to scale. Species names are colored in accord with the morphology as indicated in the key. Colored dots are appended to designate species with diverse morphologies. Names of species illustrated in schematics are highlighted in large, bold font (Adapted from [55])

1.9 Brief description of viral cells and their relation to NTP sterilization

1.9.1. Nature of viruses

Viruses are the most plentiful biological entities on earth with 10^{31} virions [59]. A distinguishing feature that many viruses have in common, is the potential to form hollow protein shells (capsids) safeguarding their genome from the external environment. Viruses can be split up into two groups depending on whether they have a lipid bilayer membrane on their exterior surface or not : enveloped viruses and non-enveloped viruses **(Figure 16)**. Enveloped viruses have a lipid bilayer that proceeds from the host cell while non-enveloped viruses lacks a membrane.

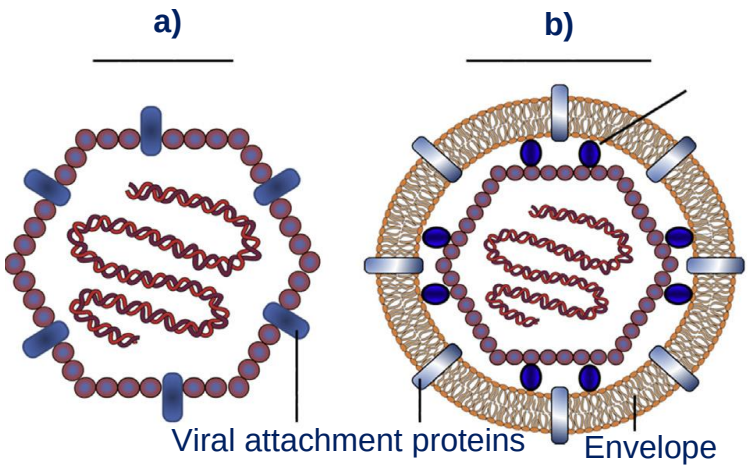

Figure 16| The two groups of viruses (non-enveloped virus and the enveloped virus). **a)** Non-enveloped virus and its lipid bilayer. **b)** Enveloped virus lacking a lipid bilayer (Adapted from [60])

1.9.2 Viral replication cycle and pathogenesis

The viral life cycle can be roughly estimated into seven stages which includes: attachment; penetration; uncoating; gene expression and replication; assembly; maturation; and release **(Figure 17)**. During gene expression, the viral proteins are manufactured and replication entails

the reproduction of the viral genome [61]. A virus is considered pathogenic for a specific host if it can infect the host and give rise to signs and symptoms of disease.

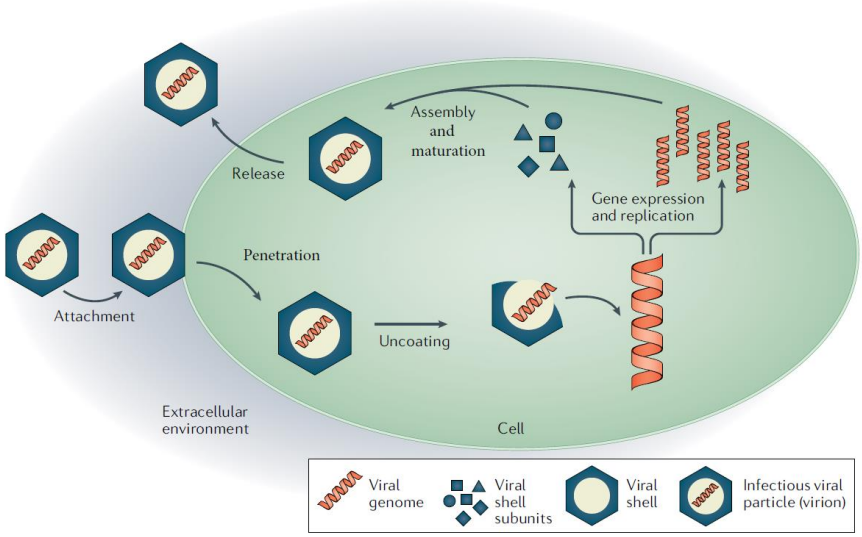

Figure 17| The life cycle of a virus (Adapted from [62])

1.9.3 Mechanism of viral attachment and stability on environmental surfaces

Viruses adsorb to surfaces via two leading mechanisms, van der waals (mostly mineral surfaces and, most importantly, electrostatic interactions (charged surfaces in the company of ions and/or neutral pH) [63]. Hydrogen bonding plays a leading role in the adsorption of viruses to the hydroxyl-containing surfaces and in the presence of an aqueous phase thin film layer. For example, considering the deadly severe acute respiratory syndrome coronavirus 2 (SARS-CoV 2), it remains viable on stainless steel and plastic for up to 72h [64]. The potential molecular interactions between the SARS-CoV-2 viral proteins and solid surfaces at divergent pH values and fluid chemistries is shown in **Figure 18**. There are four leading properties, which can influence the persistence of viruses on surfaces which comprises physical properties (including temperature, light exposure and humidity), chemical properties (such as antiviral coatings or pH) and biological properties (relying on the virus vulnerabilities such as an envelope) as well as topography or porosity [65].

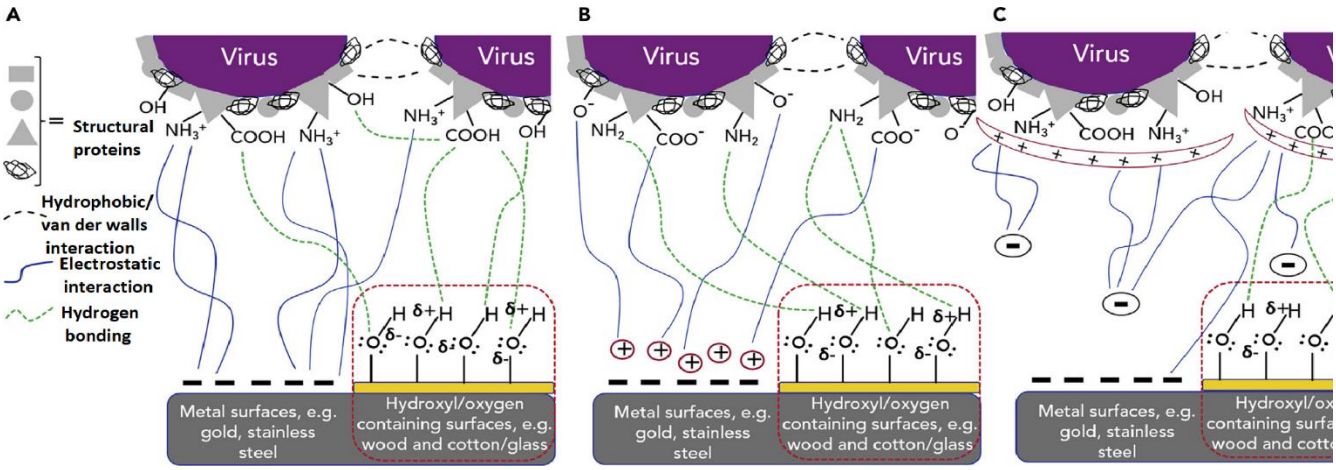

Figure 18| Molecular Interactions at SARS-CoV-2 viral interfaces in divergent environmental conditions. Model of the probable molecular interactions amid viruses and between virus and divergent solid surfaces possessing negative surface charge and/or hydroxyl functional groups at (**A**) nearly low pH environment, below the isoelectric point; (**B**) approximately high pH condition, exceeding the isoelectric point in presence of external ions such as salts; and (**C**) way below the isoelectric point in the occupancy of probable chemistries (for removal from surface purposes) with negative surface charge (Adapted from [66]).

1.9.4 Sterilization of bacteria and viruses using NTP

The utilization of physical means, such as NTP, to sterilize surfaces and environments containing pathogenic microorganisms has gained appreciable attention in the past decades. Sterilization is defined as the complete inactivation of all forms of living microorganisms as well as their spores. All traditional methods, for example, radiation, heat and chemical or physical means of sterilization, have numerous disadvantages that restrictions their utilization in treatment of heat sensitive and exposed objects such as liquids, foams, organic materials and living biological tissues [67]. Autoclaving functions at two conditions: steam heat of 121 °C with a pressure of 15 PSI foe 10 to 15 minutes and dry heat of 160 °C for two hours. Evidently, autoclaving is damaging to heat sensitive materials and those that are exposed to high pressure; furthermore, it is time consuming. Ultraviolet (UV) light in the wavelength range of 240 to 280 nm, is used to cleanse the laboratory instruments.

However, its use is bounded by its penetration and for safety reasons; furthermore, this method requires long time of radiation [68]. Other methods comprise the use of chemical substances such as ethylene oxide and hydrogen peroxide that creates toxic gases. Radiation such as γ-ray and x-ray has also some constraints mainly due to safety concerns. Considering viruses, alcohols, alkalis, acids, bleach, and chlorine are illustrations of chemical disinfectants, while on the contrary, pressure, filtration, temperature, and UV radiation are physical treatments [69]. The recurring drawbacks of these technologies are scalability problems, cost inefficiency and unsustainable power usage.

Consequently, there is a dire need for an environmentally friendly treatment that creates neither waste nor toxic byproducts, does not employ toxic chemicals, is simple and safe to work with, and is also effective and efficient in terms of virus inactivation. Consequently, in recent years, several non-thermal sterilization technologies have been put together for commercial purposes such as ultraviolet (UV), pulsed electric field (PEF), irradiation, electrolyzed water, high pressure processing (HPP) and Non-thermal plasma (NTP). NTP is a novel sterilization technology that has high efficiency and has huge potential in many applied research fields such as in sterilization of microorganisms *in vitro* and *in vivo* without any detrimental effects on living tissue and therefore provides a solution to all these features [70]. Inactivation of viruses using NTP, for example, is shown in **Figure 19**.

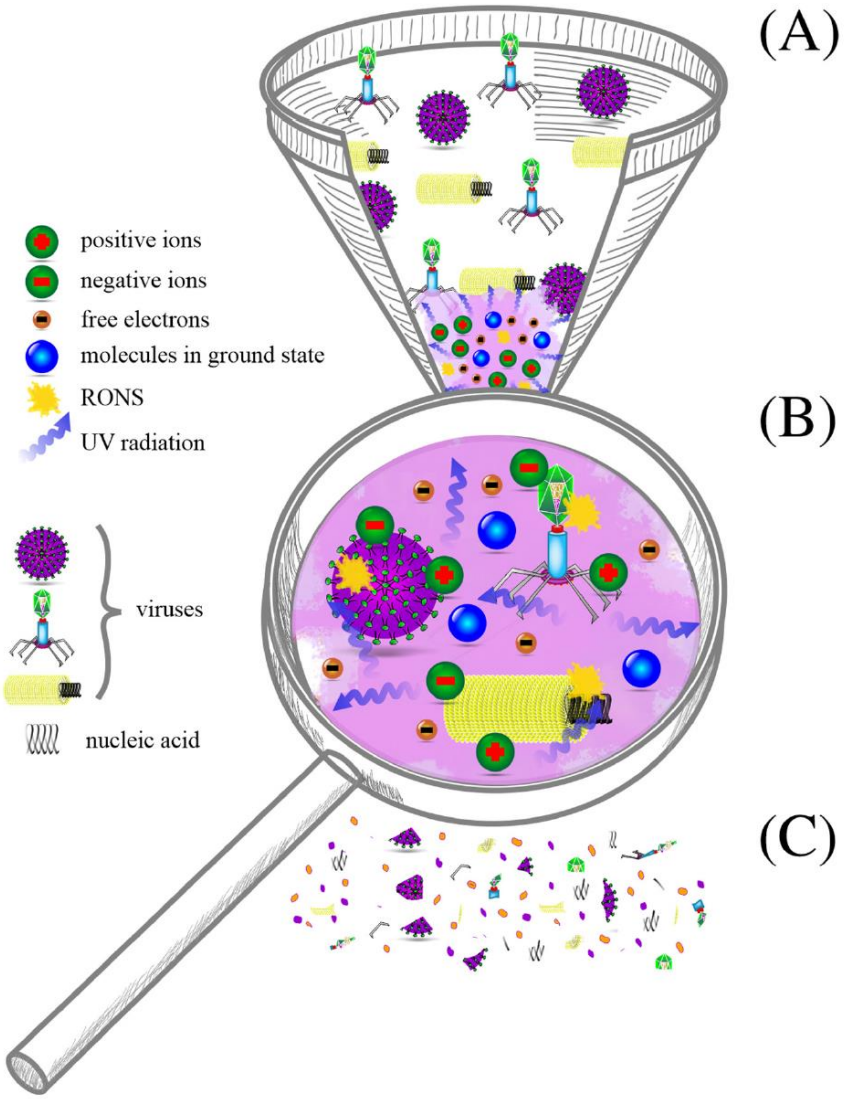

Figure 19| Inactivation of Viruses Using NTP. (**A**) Morphology divergent viruses treated with NTP. (**B**) Close-up of NTP properties responsible for virus inactivation. The most vital components in virus inactivation are reactive oxygen and/or nitrogen species (RONS), while UV radiation and charged particles such as electrons and ions can also play a role. Molecules that are in the ground state are neutral and therefore do not have any effects on virus inactivation. NTP can target both nucleic acids and viral proteins (or even the virus envelope when present). **(C)** Following NTP treatment, the nucleic acids and viral particles are partly or completely broken down to noninfective particles that cannot occasion harm to their hosts (Adapted from [71])

1.9.5 Factors determining the antimicrobial effectiveness of NTP

Sterilization by NTP is affected by various factors such as the plasma treatment time and the distance between the plasma source and the sample, frequency, and electrical input power (voltage), gas or the gas mixture with its flow rate, gas moisture content, whether the treatments are carried out directly or indirectly and microbial-related factors. Different plasma treatment times are described in the literature ranging from a few seconds up to several minutes. It is well-known that microbial inactivation increases with processing time, although not in all cases exponentially. Thus, a wide variety of inactivation kinetics are observed in the published data, where it is frequent to find both linear, concave-upward (tailing) and concave-downward (shoulders) kinetics [72, 73].

1.9.6 Potential mechanisms of microbial inactivation by NTP

Among the complex constituents of plasma, the discharge of reactive oxygen and/or nitrogen species (RONS) and UV radiation have the most predominant antimicrobial properties [74]. NTP can be used in direct treatment of microbes, when the treated microbes are in direct contact with plasma or indirect treatment, when the microbes do not come into direct contact with plasma but only with active particles previously generated in plasma. Although some insights are available on the possible impact of plasma species on microbes, a clear understanding of the process is lacking partially because different combinations of plasma sources and microbial models have been used and different explanations have been provided on the mode of virus inactivation. Therefore, the effects of NTP on microbial cells could occasion more than a single scenario [75]. Several key insights regarding the potential mechanism of NTP put forward are given below.

1.9.6.1 Biological mechanisms

1.9.6.1.1 DNA damage by UV radiation

In the earliest analysis done, DNA damage directly prompted by UV radiation created from plasma was suggested as the mechanism of microbial inactivation [76]. It has been established that UV light, mostly at around 260 nm, can lead to a reaction of cytosine and thymine in the same DNA strand into a dimer and damage the replicative ability of bacteria critically [77].

1.9.6.1.2 Lipid peroxidation

The oxidative destruction of cell membranes or intracellular components such as carbohydrates, proteins and nucleic acids was believed to be the practicable mechanism of killing bacteria and viruses by NTP. Of these elements, membrane lipid, particularly polyunsaturated fatty acids (PUFA), is believed to be the most unprotected one, due to their location close to the cell surface and their vulnerability to reactive oxygen species (ROS) [78].

1.9.6.1.3 Protein modulation

Besides membrane lipid, modulation of protein structure and role by NTP was disclosed as a mechanism responsible for microbial inactivation [79]. The chemical modification and degradation of membrane proteins has been revealed to occur after NTP treatment [80].

1.9.6.2 Physical mechanisms

1.9.6.2.1 Electrostatic disruption

The most considered physical mechanism of NTP is electrostatic disruption [81]. The electrostatic forces generated by buildup of charged particles produced NTP are proposed to cause disruption of the cell membrane, followed with cell death [82].

1.9.6.2.2 Electroporation

The electric field created by NTP particularly in direct mode, has a mechanism of action like that of PEF. Direct mode provides adequately strong electric field strength on the microbes,

which submerge within the plasma production region. Electroporation is an ably accepted mechanism of PEF which results in the formation of pores in cell membranes causing content leakage and finally cell death [83]. When the cell walls become the second electrode, the electric field increases significantly (E ≥ 30 KV/cm, which is sufficient to disrupt cell membranes [84].

.

2. Aim of the thesis

NTP can be used to polymerize certain monomers on the material surface creating a stable film. The functions and properties of the thin film are related to the kind of monomers used. In the first section of this thesis, NTP was also used to deposit three organic precursor monomers that have antimicrobial properties (2-Ethyl-2-oxazoline, Terpinene-4-ol and 2-(Diethylamino) ethyl methacrylate) and one organic-inorganic monomer that has antimicrobial properties (Bis(dimethylamino) dimethyl silane). The substrates used in the deposition process were stainless steel, silicon wafer, High-density polyethylene (HDPE) and Thermoplastic polyurethane (TPU). The effect of changing the NTP operating parameters on the chemical composition of the plasma deposited thin films was also investigated. These includes varying the argon carrier gas flow rate, varying the argon working gas flow rate, varying the NTP power source from continuous RF power to pulsed RF power, varying the distance between the substrate and the plasma jet nozzle and the effect of varying the plasma power. Their antimicrobial effect was investigated against *Escherichia Coli* cells, *Streptococcus pyogenes* cells, *Staphylococcus aureus* cells, Pseudomonas aeruginosa cells and SARS-CoV-2 like virus. The reduction in percentage of the bacterial count was calculated by comparing the bacterial growth in the control substrates.

The utilization of physical means, such as NTP, to sterilize surfaces and environments containing pathogenic microorganisms has gained appreciable attention in the past decades. Sterilization is defined as the complete inactivation of all forms of living microorganisms as well as their spores. All traditional methods, for example, radiation, heat and chemical or physical means of sterilization, have numerous disadvantages that restricts their utilization in treatment of heat sensitive and exposed objects such as liquids, foams, organic materials and living biological tissues. NTP is a novel sterilization technology that has high efficiency and has huge potential in many applied research fields such as in sterilization of microorganisms *in vitro* and *in vivo* without any detrimental effects on living tissue and therefore provides a solution to all these features. In the second section of this thesis, the bacterial sterilization and inactivation potential of the NTP jet was investigated. The microorganism selected for the sterilization and inactivation studies was *E. Coli*. The cell adhesion on the four substrates (stainless steel, silicon wafer, HDPE and TPU) and the cellular membrane integrity of the plasma-treated *E.Coli* was

then imaged by SEM.

3. Materials and methods

3.1 Physical and chemical characterization of the NTP deposited thin films

The first section of this thesis was done at the Scientific Campus Laboratories, Ca' Foscari University.

3.1.1 Materials

The antimicrobial precursor monomers used in the formation of antimicrobial thin films on selected substrates were 2-ethyl-2-oxazoline (C_5H_9NO, M.W. = 99.13 g/mol, purity > 99.99%, Merck), 4-Carvomenthenol (4-Terpinenol) ($C_{10}H_{18}O$, M.W. = 154.24 g/mol, purity > 99.99% purity, Merck), 2-(Diethylamino) ethyl methacrylate ($C_{10}H_{19}NO_2$, M.W. = 185.26 g/mol, purity > 99.99%, Merck) and Bis(dimethylamino)dimethylsilane) ($Cl(CH_2)_3Si(OCH_3)_3$, M.W. = 198.72 g/mol, purity > 99.99%, Merck). Single-crystal Si wafer with (100) orientation, 0.625 mm thick, cut into 2 cm x 2 cm (x x y) sizes and freshy prepared KBr substrates (approximately 1000 mg of KBr pressed into KBr pellets using a hydraulic press and applying 6-ton ram pressure to the KBr die for 1 minute) were used as model substrates towards optimizing the plasma jet operating parameters. White HDPE poly pellets and TPU poly pellets were polymerized using the injection-moulding process into HDPE polymer substrate and TPU polymer substrate which were then used in the preparation of the final samples. Stainless steel and other Single-crystal Si wafer substrates were also used in the preparation of the final samples. Distilled water (H_20, M.W. = 18 g/mol, purity > 99.99%) and diiodomethane (CH_2I_2, M.W. = 267.84 g/mol, 99.99% purity) were used for wettability studies. All the chemicals were used without further purification.

3.1.2 Preparation of HDPE and TPU polymer substrates

HDPE polymer substrates and TPU polymer substrates were prepared from white HDPE poly pellets and TPU pellets, respectively, by an injection-moulding process using an injection-moulding process using a Haake Minijet II **(Figure 20)** (Thermoscientific) with a barrel temperature of 230 °C, mould temperature of 30 °C, injection pressure at 950 bar and pressure

time of 10s, post-pressure at 450 bar and pressure time of 10s.

Figure 20| Haake Minijet II used to prepare the polymer substrates

3.1.3 The novel atmospheric plasma Jet

The patented atmospheric pressure device used in this study [85] is a DBD plasma jet designed such that no electrodes are in direct contact with plasma **(Figure 21)**. The advantage of that configuration with electrodes alienated from the plasma guarantees clean processes with no unwanted deposition since they remain intact and cannot be eroded. The electrodes position is external and coaxial to an alumina tube where argon gas is fluxed, and the plasma ignited. Two other ducts are present: an inner duct for the inlet of the precursor monomer in the aerosol phase or in the vapor phase and an outer duct for the control of the atmosphere located at the exit point of the torch, where nitrogen or air are generally used as the cooling gas. The main feature associated with the device is that it uses a double couple of electrodes: a first upstream

couple that is powered with a high voltage (HV) supply in the kilohertz regime (~17 KHz) and a downstream couple that is powered in the radio frequency (RF) range at about 27 MHz.

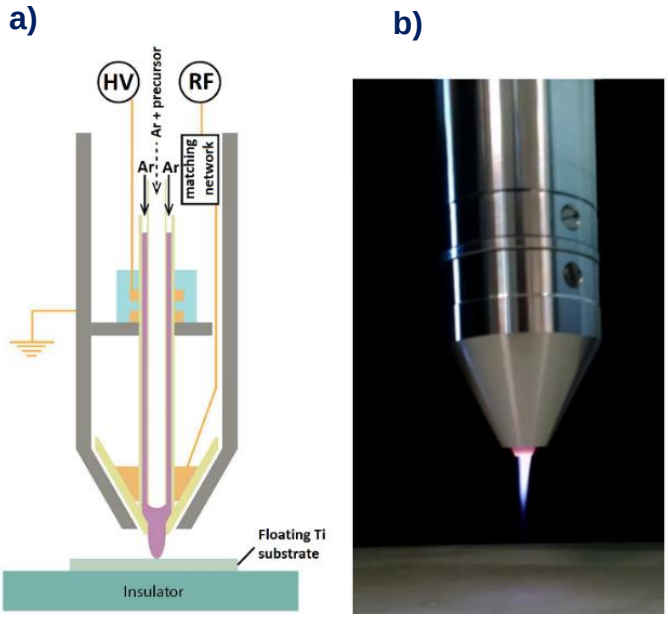

Figure 21| Internal and external schematic view of the NTP jet **a)** Scheme of the novel atmospheric plasma jet characterized by its three coaxial gas ducts and the double couple of electrodes RF and HV (on the left) **b)** Photograph (time averaged) of the device (adapted from [85])

The selection of argon noble gas as the gas of choice, which prevents the thermalization of energy by dissociation/recombination reactions and by roto-vibrational motion, allows to keep the temperatures of the plasma as low as possible. The use of helium is not considered because of the cost implications. Furthermore, the RF regime with its uniqueness of having fast oscillations prevents the creation of high current carrying streamers and it also favors and advances the generation of plasma in the volume and not on the surfaces and this leads to a more glow regime. Additionally, the choice of RF is further cemented by the fact that it reduces the thermal load on the surface being treated without losing in plasma density. The design is also the most used plasma jet design of the different plasma jets that are usually used for human body applications [86].

The general disadvantage of the design, however, is its ignition and stability in atmospheres when additional reactive species are added to the plasma. This condition is made better, at least, by the upstream couple of electrodes which solves this condition by assuring ignition and stability also when high voltages are needed, without the necessity to increase the RF power. The basic concept is that the configuration makes it possible to decouple plasma needs: the HV regulates ignition and stability with low power, while the RF regulates the plasma density. The coupling as a matter of fact is not just the overlapping of the two different plasmas but also their interaction with each other. The outstanding effect is that the streamers formed by the HV electrodes are blown up by the RF field that exponentially changes the polarity. As a result, if hundreds of mA streamers can be measured on a conductive substrate if HV is turned on when both power supplies are active, only a small number of current bumps of few tens of mA can be measured **(Figure 22b)**.

Streamers that are current carrying channels are warmer because of their high charged species densities and fields gradients. The new design allows to avoid their propagation on treated surfaces reducing local heating [85]. Streamers that carry the current are warmer due to their high charged species densities and field gradients. The new design makes it possible to prevent their propagation on the surfaces being treated and this reduces the local heating. The low temperature of the novel jet design can be seen in **Figure 22a** presenting a thermographic camera image obtained after 5 minutes of plasma treatment on a plastic substrate at 15W of RF power with argon noble gas as the process gas. The image, in more clear terms, shows that the plasma has no emissions in the infra-red spectral region since it is not thermal. The mirrored image of the jet can be observed on the substrate.

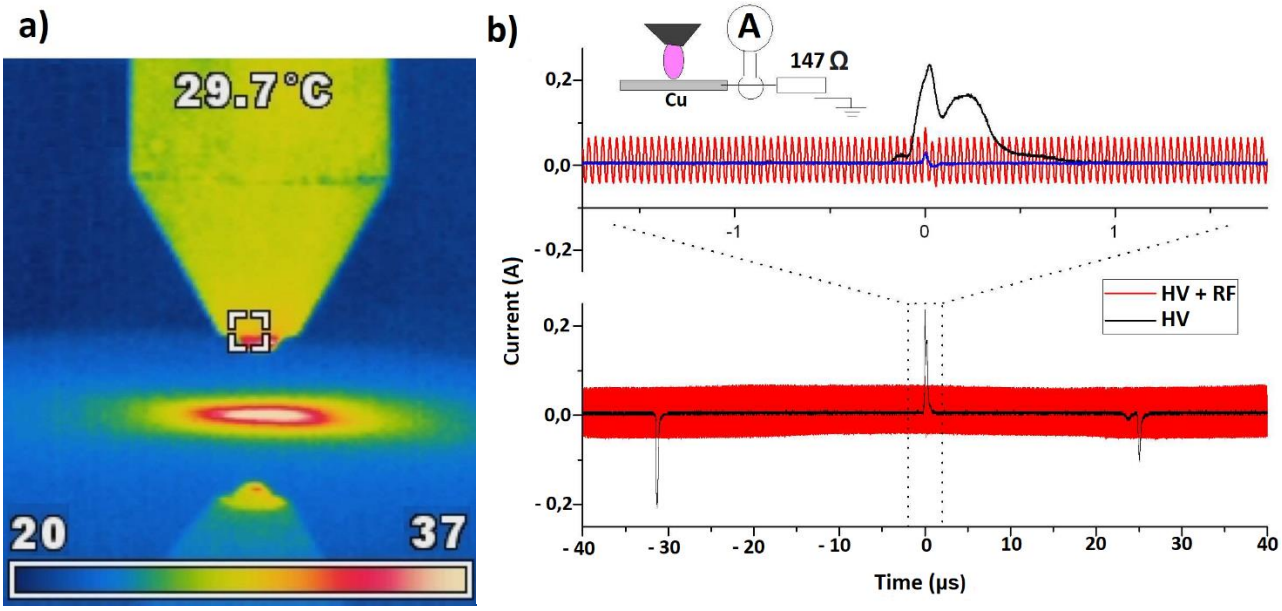

Figure 22| Schematic showing the advantages of the novel atmospheric plasma jet **a)** Image obtained with a thermographic camera of the plasma device on a plastic substrate in stationary conditions (after 5 minutes) **b)** Electrical characterization on a substrate of the coupling of the HV and RF plasmas (Adapted from [85])

3.1.4 Plasma-assisted thin film deposition

Plasma polymerization of the different selected precursor monomers were performed using the novel atmospheric plasma jet. The depositions of the selected antimicrobial precursor monomers to form antimicrobial thin films was done, first, on Silicon wafer and KBr pellets substrates for optimization if the NTP plasma operating parameters. Due to the presence of free charge carriers, plasma is electrically conductive [87] and may exhibit different behavior on conductive or non-conductive substrates. On Silicon wafer substrate, the current induced by plasma flows through the sample inducing zero charge accumulation on the top of the surface. In contrast, on insulating substrates (KBr), the charge can accumulate on the top of the surface.

The final depositions with the selected plasma operating parameters were done on silicon wafer, stainless-steel, HDPE polymer and TPU polymer substrates. The plasma device was

equipped with photodiodes to measure the plasma emission. The sample holder, located below the jet outlet, is provided with a computer-controlled xy translational stage, which enables the sample xy-displacements during the plasma process and, therefore, the enlargement of the sample area interested by the deposition. All silicon wafer substrates were coated with a thin film coating fabricated using a direct plasma conversion of the precursor monomers (99.99% purity) under RF plasma conditions under low pressure and ambient temperature conditions.

A gas flow controller was employed to regulate the flow rate of the plasma processing gases. Thin films were deposited with Argon (99.99% purity) as the working gas and at a flux of 8 L/min and with a gain of 40% HV power that translated to a voltage value of approximately 10 KV_{pp}, frequency of approximately 21 KHz and a power value of 17W. Working distance was 3 mm, while in the outer duct, there is either fluxed compressed air or fluxed nitrogen gas. The discharge was sustained in continuous mode (CM) and pulsed mode (PM) by using an RF power supply and pulse generator.

In pulsed mode plasmas the power fed to the reactor is modulated in time. Square wave modulation is most frequently applied as shown in **Figure 23**. The duration of the power ON fraction of the cycle (active glow) is $\tau_{ON,}$ while that of power OFF fraction of the cycle (afterglow) is $\tau_{OFF.}$ The pulse plasma is $\tau_P = \tau_{ON} + \tau_{OFF}$, and the duty ratio (or duty cycle) is defined as $D = \tau_{ON}/\tau_P$, i.e., the fraction of the cycle with power ON.

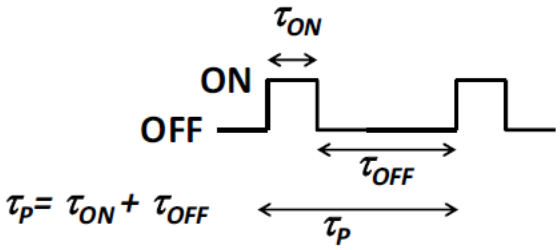

Figure 23| The square modulated nature of pulsed plasmas (Adapted from [88])

Pulsed RF power source used had a duty cycle of 50% (ON time of 500 µs, OFF time of 500 µs and a measured pulse time of 250 µs). Pulsed HV power source used had a duty cycle of 50% (ON time of 5ms and OFF time of 5ms).

The silicon wafer substrates were subjected to an isopropanol solution to remove any residual contamination. The substrates were then dried using compressed air and each one of them placed in the deposition chamber for the deposition process. In addition to the silicon substrates, KBr was employed as the model substrate. The clean silicon substrates were subjected to an isopropanol solution to remove any residual contamination. The substrates were then dried using compressed air. Each of the Si wafer substrates was placed in the deposition chamber, one at a time. The working gas (argon), cooling/shield gas and the HV power supply was then turned on in that order. At this point, the RF generator was turned on to form the flow discharge, and the substrates were exposed to an argon plasma for 30 seconds to remove any potential contaminants from the surface and prepare them for deposition.

The deposition chamber was then closed for the deposition process. The precursor monomer vapor, which was generated by monomer reservoir (bubbler), was allowed into the inner plasma duct by means of a carrier gas (argon, 99.99% purity). The precursor monomer vapor was delivered to the plasma chamber through a bubbling vessel under atmospheric pressure, and plasma discharge was produced by dual-frequency excitation. The precursor gas flow Φ_{pre} is a function of the argon gas flow Φ_{Ar}, the vapor pressure p_{pre} of the precursor and the atmospheric pressure p_o and can be calculated by **Equation 3** under the assumptions that the precursor is used at room temperature and the argon gas is saturated with the precursor vapors.

$$\Phi_{pre} = \Phi_{Ar} . \frac{p_{pre}}{p_o} \qquad \textbf{(Equation 3)}$$

The calculated value of the precursor monomer gas flow rates of the selected precursor monomers are shown in **Table 1**. The bubbling system can adjust the precursor monomer gas flow rate. Argon was therefore used to generate the plasma and carry the monomer vapors to the discharge area. All the experiments were carried out at room temperature. On the one hand, the main argon is used for maintaining discharge, and on the other hand, precursor monomer vapor is introduced into the tube nozzle by a small amount of inputting argon. Plasma polymerization was then carried out with various combinations of cooling/shield gas type and flow rate, RF power and carrier gas flow rate together with operating the plasma jet in both the RF mode and in pulse mode to obtain the optimal parameter combination.

The entire plasma system is therefore composed of a plasma jet, a bubbler system, a gas delivery system, and an x-y two-axis moving system. The plasma jet was operated using program number 33 in dictating the plasma jet movements (speed of 10 mm/s of the moving platform, track length of 3 mm by 5 mm and 3 scans). The novel atmospheric plasma jet used to deposit the antimicrobial thin films on selected substrates is shown in **Figure 24**. The preliminary NTP operating parameters and optimized NTP operating parameters used in the deposition of the antimicrobial thin films (2-ethyl-2-oxazoline thin film, Terpinene-4-ol thin film, (Diethyl amino) ethyl methacrylate thin film and Bis(dimethyl amino) dimethyl silane thin film) are shown from **Table 1** up to **Table 17**.

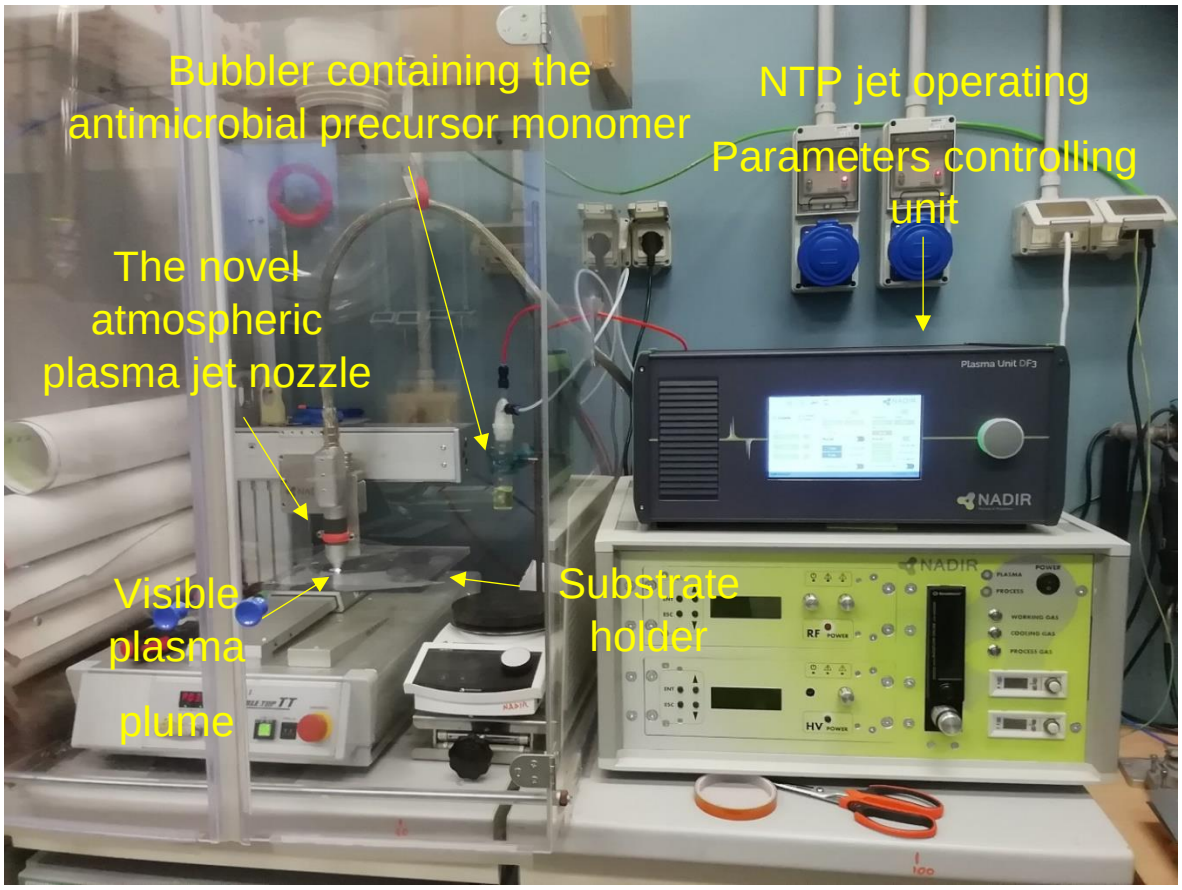

Figure 24| NTP jet set-up used in the deposition of antimicrobial thin films on selected substrates

Monomer	Molar mass (g/mol)	Density (g/ml)	Argon flow rate (l/min)	Argon flow rate (l/h)	Partial pressure of the precursor (hpa) at 20 °C	Partial pressure of the precursor (hpa) at 20 °C	Standard atmospheric pressure (pa)	Precursor flow rate (l/min)	Quantity / mole flow rate (mol/h)	Mass flow rate (g/h)	Volume flow rate (ml/h)
2-ethyl-2-oxazoline	99.13	0.982	1	60	13.1	1310	101325	0.7757	0.035	3.433	3.498
Terpinene-4-ol	154.25	0.933	1	60	0.056	5.6	101325	0.5243	0.012	2.576	2.582
(Diethyl amino) ethyl methacrylate	157.21	0.922	1	60	0.14	14	101325	0.6745	0.024	2.874	2.889
Bis(dimethyl amino) dimethy silane	198.72	1.09	1	60	6.667	66.67	101325	0.8786	0.079	3.876	3.888

Table 1| Calculated value of precursor monomer gas flow rate

Monomer	Sample number	HV % power (W)	RF power (W)	Ar Working gas flow rate (L/min)	Ar Carrier gas flow rate (L/min)	Distance from the substrate to the plasma jet nozzle (mm)	Cooling gas type	Cooling gas flow rate (L/min)	Scan number
2-ethyl-2-oxazoline	1	40	25	8	0.5	3	Compressed air	12	3
	2	40	25	8	1	3	Compressed air	12	3
	3	40	25	8	1.5	3	Compressed air	12	3

Table 2| SET A of selected NTP operating parameters applied to the deposition of 2-ethyl-2-oxazoline thin film on silicon wafer substrate and on KBr substrate (varying the argon carrier gas flow rate)

Monomer	Sample number	HV % power (W)	RF power (W)	Ar Working gas flow rate (L/min)	Ar carrier gas flow rate (L/min)	Distance from the substrate to the plasma jet nozzle (mm)	Cooling gas type	Cooling gas flow rate (L/min)	Scan number
2-ethyl-2-oxazoline	5	40	25	8	1	3	Compressed air	12	3
	7	40	25 + 50% RF duty cycle pulse, ON time of 500 µs, OFF time of 500 µs and measured pulse of 250 µs	8	1	3	Compressed air	12	3

Table 3| SET B of selected NTP operating parameters applied to the deposition of 2-ethyl-2-oxazoline thin film on silicon wafer substrate and on KBr substrate (varying the plasma power type from continuous RF power to pulsed RF power and using compressed air as the type of cooling gas used)

Monomer	Sample number	HV % power (W)	RF power (W)	Ar Working gas flow rate (L/min)	Ar carrier gas flow rate (L/min)	Distance from the substrate to the plasma jet nozzle (mm)	Cooling gas type	Cooling gas flow rate (L/min)	Scan number
2-ethyl-2-oxazoline	5	40	25	8	1	3	Compressed air	12	3
	9	40	25	8	1	3	Compressed nitrogen	12	3

Table 4| SET D of selected NTP operating parameters applied to the deposition of 2-ethyl-2-oxazoline thin film on silicon wafer substrate and on KBr substrate (varying the type of cooling gas used (compressed air or compressed nitrogen))

Monomer	Sample number	HV % power (W)	RF power (W)	Ar working gas flow rate (L/min)	Ar carrier gas flow rate (L/min)	Distance from the substrate to the plasma jet nozzle (mm)	Cooling gas type	Cooling gas flow rate (L/min)	Scan number
2-ethyl-2-oxazoline	4	40	40	15	8	3	Compressed air	12	3
	5	40	40	25	8	3	Compressed air	12	3
	6	40	40	35	8	3	Compressed air	12	3

Table 5| SET C of selected NTP operating parameters applied to the deposition of 2-ethyl-2-oxazoline thin film on silicon wafer substrate and on KBr substrate (varying the argon working gas flow rate)

Monomer	Sample number	HV % power (W)	RF power (W)	Ar working gas flow rate (L/min)	Ar carrier gas flow rate (L/min)	Distance from the substrate to the plasma jet nozzle (mm)	Cooling gas type	Cooling gas flow rate (L/min)	Scan number
2-ethyl-2-oxazoline	8	40	25 + 50% RF duty cycle pulse, ON time of 500 µs, OFF time of 500 µs and measured pulse of 250 µs	8	1	3	Compressed nitrogen	12	3
	9	40	25	8	1	3	Compressed nitrogen	12	3

Table 6| SET E of selected NTP operating parameters applied to the deposition of 2-ethyl-2-oxazoline thin film on silicon wafer substrate and KBr substrate (varying the plasma power type from continuous RF power and pulsed RF power while using compressed nitrogen as the type of cooling gas used)

Monomer	Sample number	HV % power (W)	RF power (W)	Ar working gas flow rate (L/min)	Ar carrier gas flow rate (L/min)	Distance from the substrate to the plasma jet nozzle (mm)	Cooling gas type	Cooling gas flow rate (L/min)	Scan number
2-ethyl-2-oxazoline	1B	40	25	8	1	3	Compressed air	12	9

Table 7| SET F of optimized NTP operating parameters applied to the deposition of 2-ethyl-2-oxazoline thin film on silicon wafer substrate and on KBr substrate

Monomer	Sample number	HV % power (W)	RF power (W)	Ar working gas flow rate (L/min)	Ar carrier gas flow rate (L/min)	Distance from the substrate to the plasma jet nozzle (mm)	Cooling gas type	Cooling gas flow rate (L/min)	Scan number
2-ethyl-2-oxazoline	2B	40	25 + 50% RF duty cycle pulse, ON time of 500 µs, OFF time of 500 µs and measured pulse of 250 µs	8	1	3	Compressed air	12	9

Table 8| SET G of optimized NTP operating parameters applied to the deposition of 2-ethyl-2-oxazoline thin film on silicon wafer substrate and on KBr substrate

Monomer	Sample number	HV % power (W)	RF power (W)	Ar working gas flow rate (L/min)	Ar carrier gas flow rate (L/min)	Distance from the substrate to the plasma jet nozzle (mm)	Cooling gas type	Cooling gas flow rate (L/min)	Scan number
2-ethyl-2-oxazoline	3B	40	25	8	1	3	Compressed nitrogen	12	9

Table 9| SET H of optimized NTP operating parameters applied to the deposition of 2-ethyl-2-oxazoline thin film on silicon wafer substrate and on KBr substrate

Monomer	Sample Number	HV % power (W)	RF power (W)	Ar working gas flow rate (L/min)	Ar carrier gas flow rate (L/min)	Distance from the substrate to the plasma jet nozzle (mm)	Cooling gas type	Cooling gas flow rate (L/min)	Scan number
Terpinene -4-ol	1	40 + 50% HV duty cycle pulse, ON time of 5 ms, OFF time of 5 ms	15	9	2	3	Compressed air	12	9
	2	40 + 50% HV duty cycle pulse, ON time of 5 ms, OFF time of 5 ms	15	6	2	3	Compressed air	12	9
	3	40 + 50% HV duty cycle pulse, ON time of 5 ms, OFF time of 5 ms	15	12	2	3	Compressed air	12	9

Table 10| SET I of selected NTP operating parameters applied to the deposition of Terpinene-4-ol thin film on silicon wafer substrate and on KBr substrate (varying the Argon working gas flow rate)

Monomer	Sample number	HV % power (W)	RF power (W)	Ar working gas flow rate (L/min)	Ar carrier gas flow rate (L/min)	Distance from the substrate to the plasma jet nozzle (mm)	Cooling gas type	Cooling gas flow rate (L/min)	Scan number
Terpinene-4-ol	1	40 + 50% HV duty cycle pulse, ON time of 5 ms, OFF time of 5 ms	15	9	2	3	Compressed air	12	9
	4	40 + 50% HV duty	15	9	2	5	Compressed	12	9

		cycle pulse, ON time of 5 ms, OFF time of 5 ms					air		

Table 11| SET J of selected NTP operating parameters applied to the deposition of Terpinene-4-ol thin film on silicon wafer substrate and on KBr substrate (varying the distance from the substrate to the plasma jet nozzle)

Monomer	Sample number	HV % power (W)	RF power (W)	Ar working gas flow rate (L/min)	Ar carrier gas flow rate (L/min)	Distance from the substrate to the plasma jet nozzle (mm)	Cooling gas type	Cooling gas flow rate (L/min)	Scan number
Terpinene-4-ol	1	40 + 50% HV duty cycle pulse, ON time of 5 ms, OFF time of 5 ms	15	9	2	3	Compressed air	12	9
	5	40 + 50% HV duty cycle pulse, ON time of 5 ms, OFF time of 5 ms	15	9	2	3	Compressed nitrogen	12	9

Table 12| SET K of selected NTP operating parameters applied to the deposition of Terpinene-4-ol thin film on silicon wafer substrate and KBr substrate (varying the type of cooling gas used (compressed air or compressed nitrogen))

Monomer	Sample number	HV % power (W)	RF power (W)	Ar working gas flow rate (L/min)	Ar carrier gas flow rate (L/min)	Distance from the substrate to the plasma jet nozzle (mm)	Cooling gas type	Cooling gas flow rate (L/min)	Scan number
Terpinene-4-ol	1	40 + 50% HV duty cycle pulse, ON time of 5 ms, OFF time of 5 ms	15	9	2	3	Compressed air	12	9
	6	40	15	9	2	3	Compressed air	12	9

Table 13| SET L of selected NTP operating parameters applied to the deposition of Terpinene-4-ol thin film on silicon wafer substrate and KBr substrate (varying the plasma power type from continuous HV power supply to pulsed HV power supply)

Monomer	Sample number	HV % power (W)	RF power (W)	Ar working gas flow rate (L/min)	Ar carrier gas flow rate (L/min)	Distance from the substrate to the plasma jet nozzle (mm)	Cooling gas type	Cooling gas flow rate (L/min)	Scan number
Terpinene-4-ol	1	40 + 50% HV duty cycle pulse, ON time of 5 ms, OFF time of 5 ms	15	9	2	3	Compressed air	12	9
	7	40 + 50% HV duty cycle pulse, ON time of 5 ms, OFF time of 5 ms	30	9	2	3	Compressed air	12	9

Table 14| SET M of selected NTP operating parameters applied to the deposition of Terpinene-4-ol thin film on silicon wafer substrate and on KBr substrate (varying the plasma power)

Monomer	Sample number	HV % power (W)	RF power (W)	Ar working gas flow rate (L/min)	Ar carrier gas flow rate (L/min)	Distance from the substrate to the plasma jet nozzle (mm)	Cooling gas type	Cooling gas flow rate (L/min)	Scan number
(Diethyl amino) ethyl methacrylate	1	35	20	9	2	3	Compressed air	12	9
	2	35 + 50% HV duty cycle pulsed, ON time of 5 ms, OFF time of 5 ms	20	9	2	3	Compressed air	12	9

Table 15| SET N of selected NTP operating parameters applied to the deposition of (Diethyl amino)ethyl methacrylate thin film on silicon wafer substrate and on KBr substrate (varying the plasma power type from continuous HV power supply to pulsed HV power supply)

Monomer	Sample number	HV % power (W)	RF power (W)	Ar working gas flow rate (L/min)	Ar carrier gas flow rate (L/min)	Distance from the substrate to the plasma jet nozzle (mm)	Cooling gas type	Cooling gas flow rate (L/min)	Scan number

Bis(dimethyl amino)dimethyl silane	Lone sample	35	30	7.5	1.5	3	Compressed air	10	6

Table 16| SET O of selected NTP operating parameters applied to the deposition of Bis(dimethyl amino) dimethyl silane thin film on silicon wafer substrate and on KBr substrate

Sample number	Monomer	HV % power (W)	RF power (W)	Ar working gas flow rate (L/min)	Ar carrier gas flow rate (L/min)	Distance from the substrate to the plasma jet nozzle (mm)	Cooling gas type	Cooling gas flow rate (L/min)	Scan number
Sample Number 2B	2-ethyl-2-oxazoline	40	25 + 50% RF duty Cycle pulse, ON Time of 500 µs, OFF time of 500 µs and measured pulse of 250 µs	8	1	3	Compressed air	12	9
Sample Number 7	Terpinene-4-ol	40 + 50% HV duty cycle pulse, ON time of 5 ms, OFF time of 5 ms	15	9	2	3	Compressed air	12	6
Sample Number 1	(Diethyl amino) ethyl methacrylate	35 + 50% HV duty cycle pulsed, ON time of 5 ms, OFF time of 5 ms	20	9	2	3	Compressed air	10	6
Lone sample	Bis(dimethyl amino)dimethyl silane	35	30	7.5	1.5	3	Compressed air	10	6

Table 17| Optimized NTP operating parameters used for the deposition of the optimal antimicrobial thin films on the selected substrates (HDPE polymer, TPU polymer, stainless steel, and silicon wafer) for antimicrobial studies

The NTP deposited antimicrobial thin films prepared using the optimized NTP operating parameters **(Table 17)** on HDPE polymer substrate, TPU polymer substrate, stainless steel substrate, and silicon wafer substrate, are shown in **Figure 25.**

a) **b)**

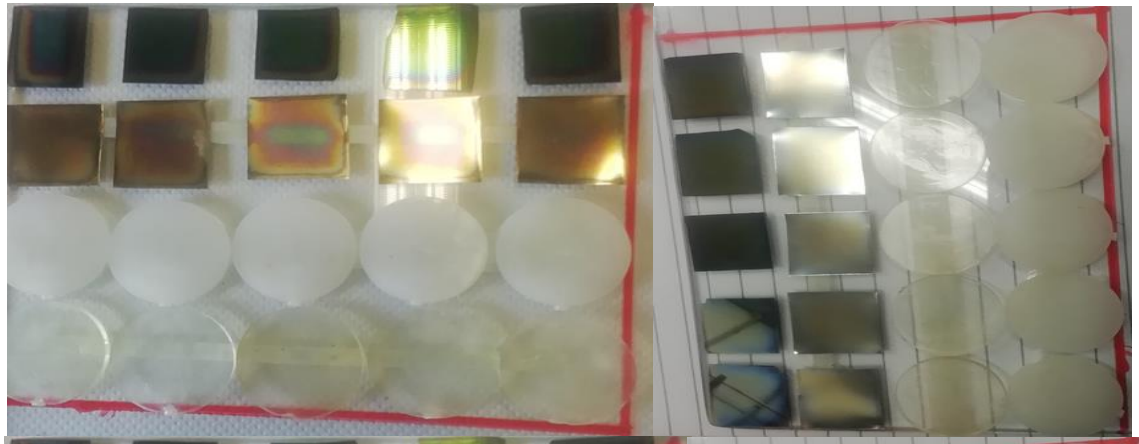

c) **d)**

Figure 25| Antimicrobial thin films ([a]2-ethyl-2-oxazoline thin film, [b]Terpinene-4-ol, [c](Diethyl amino) ethyl methacrylate thin film, [d]Bis(dimethyl amino) dimethyl silane thin film) prepared using optimized NTP operating parameters on the selected substrates (HDPE polymer, TPU polymer, stainless steel, and silicon wafer)

3.1.4 Surface characterization

3.1.4.1 Chemical composition

The chemical compositions (functional groups) of the plasma deposited thin films and the corresponding precursor monomer were characterized by the Fourier transform infrared spectroscopy (FTIR). The FTIR spectra were performed ex-situ, using a Bruker Vertex 70 Fourier-Transform Infrared Spectrometer operating in single beam mode with a 4 cm^{-1} resolution and 64 scans per analysis. The light source of absorbance was in the middle range infrared 4000-500 cm^{-1}. To interpret the results easily, the precursor monomers were analysed as a reference. For analysis of the precursor monomers, freshly cleaned, polished KBr were covered with a thin layer of liquid, whereas films were deposited in Si wafers and KBr pellets for FTIR analysis.

Approximately 100 mg of KBr (FTIR purity, spectroscopically dry, Sigma Aldrich) were weighted and transferred to an agate mortar, grinded together and KBr pellets were prepared using a hydraulic press.The samples were scanned against blank Si wafer and blank KBr pellet respectively. For all spectra, the baseline was corrected and smoothing done using the ORIGINPRO software (version 8.5.0).

3.1.4.2 Wetting properties and surface energy evaluation

The wettability of plasma polymerized thin films were assessed using the sessile liquid drops system [89]. The static contact angle (CA) was measured at room temperature using a Krüss DSA30S contact angle goniometer (Matthews, NC, USA). Wettability of all surfaces was measured for two different liquids, namely deionized water as polar probe liquid, and di-iodomethane as non-polar probe liquid (Merck Schuchardt OHG, Germany). Here, an approximately 2 µL drop of the liquid was placed on the samples (plasma deposited thin film on silicon wafer substrates) via a micro syringe, and the measurements were carried out three times at random positions (independently) on the substrates recording the related average

values, and the static CA was measured using high-speed video recording for 10 s at 64 frames per second.

For each sample and for each probe liquid (water and diiodomethane) the contact angle measurement was repeated three times recording the related average value and their corresponding standard deviations (±SD) (mean ± standard deviation). The contact angle diagrams were also recorded. WCA_S > 90° were considered hydrophobic. The contact angle was analyzed using the data analysis provided together with the instrumentation by fitting the sessile drop profile using the Young–Laplace curve fitting and had an inaccuracy of ±0.1 degrees [90].

This software draws a tangent to the drop at the three-phase-contact line and calculates numerically the angle between the plane of the surface and the tangent and then averages the left and right angles. For each sample, the contact angle measurements were performed one day (24h) after the sample preparation to reduce the influence of the plasma activation effect. Contact angle measurements on a clean Si wafer substrate were used as a reference. The values of the two liquids were then used for calculating the surface energy value of the treated samples with its related dispersive and polar components, by applying the Owens Wendt method [91].

3.1.5 Biological characterization of NTP deposited thin films and the NTP sterilization potential

The second section of this thesis was done at the Department of Translational Medicine and for Romagna, Ferrara, Italy, by Professor Barbara Zavan's research group.

3.1.5.1 Bacterial and viral strains

Escherichia coli, Streptococcus pyogenes, Staphylcoccocus aureus and *Pseudomonas aeruginosa* cells were inoculated in Luria-Bertani (LB) Broth (5 mL) (Department of Translational Medicine and for Romagna Laboratories) and incubated at 37 °C. After overnight cultivation, the cells (50 µL) were transferred into fresh LB media (5 mL) and cultured until the optical density at a wavelength of 600 nm reached 0.6. The cells were diluted in sodium phosphate buffer (10 mM, pH 7.4) to a concentration of 10^5 cells/mL CFU/mL in LB Broth. The culture was incubated further at 37 °C until it reached the logarithmic growth phase prior to exposing the bacterial culture to the plasma deposited antimicrobial thin films. SARS-CoV-2 like virus stock solution was also prepared using standard protocols at the Department of Translational Medicine and for Romagna Laboratories.

3.1.5.2 Antibacterial and antiviral tests

The antibacterial activity of the plasma deposited antimicrobial thin films on silicon wafer, stainless steel, HDPE and TPU substrates were investigated against gram-positive *Streptococcus pyogenes*, gram-positive *Staphylococcus aureus*, gram-negative *Escherichia coli* and gram-negative *Pseudomonas aeruginosa*. Under favorable conditions, a growing bacterial population doubles at regular intervals [46]. Growth is by geometric progression: 1, 2, 4, 8, etc. or 2^0, 2^1, 2^2, 2^3.....2^n, where n is the number of generations. Exponential growth is

only part of the bacterial life cycle, and not representative of the normal pattern of the bacteria growth in nature.

The rate of exponential growth of a bacterial culture is expressed as the generation time or the doubling time of bacterial population. The cells divide at a constant rate depending on the growth conditions. Antibacterial tests usually involve the incubation of coated and uncoated surfaces under consideration with bacteria to determine the bactericidal effect [92, 93]. Hence, in these experiments, uncoated surfaces are usually chosen as the control group. All the inoculums were diluted to 10^{-6}. The antibacterial tests were done using two methodologies.

In the first methodology, a 100 µL of the diluted bacterial inoculums were applied to the LB-agar medium and incubated for 30 min at 37 °C for diffusion of the diluted bacterial inoculums to the LB-agar medium. Then, the plasma deposited antimicrobial thin film substrates and the clean, unmodified substrates were placed on these medium and incubated at 37 °C for 24h. The substrates were removed from the LB-agar medium at the end of the incubation period and the colony forming units were determined [46].

In the second methodology, A 100 µL portion of these diluted inoculums were applied on both the clean, unmodified substrates and the plasma deposited thin films. These substrates were kept in the incubator at 37 °C for about 30 min for the diffusion of the inoculated bacteria from the surface to the LB-agar medium. After this process, coated and uncoated substrates were taken from the LB-agar medium, and this medium was incubated at 37°C for 24 h. Viable colony forming units of all samples, which belong to the coated and uncoated substrates were counted at the end of the 24-h incubation process [46].

The antiviral tests of the thin films were also determined using the two methodologies. The thin films were subjected against the Sars Covid 2 like virus to determine their antiviral effectiveness.

3.1.5.3 Evaluation of the bacterial colony forming units (CFUs)

After incubation, the substrates were gently washed twice with phosphate-buffered saline (PBS) to remove any nonadherent bacteria, and attached bacteria were then harvested with PBS to remove any nonadherent bacteria, and attached bacteria were then harvested in 1 mL BHI by sonication (Ultrasonic cleaner SH-2100; Sachan Ultrasonic) for 5 min. One hundred microliters of the harvested bacterial suspension were spread onto a solid agar plate and incubated for 24h at 5% CO_2 and 37 °C. The total number of colonies (colony forming units (CFUs)) was then counted to calculate the percentage reduction of the bacterial colonies caused by the thin films **(Equation 4)** [94, 95]**.** This was done by comparing the bacterial growth on the test thin films with bacterial growth in the control substrates.

$$\text{CFU reduction rate} = \frac{\text{Mean (control substrates)} - \text{Mean (substrates with the NTP deposited thin films) substrates)}}{\text{Mean (control substrates)}} \times 100$$

Equation 4

3.1.5.3 NTP operating parameters used in the sterilization process

Plasma application using the novel atmospheric plasma jet was performed against one selected microorganism (*Escherichia coli*) at pre-established times of 15s, 30s and 60s, except for time zero, for which no application was made. The distance between the nozzle and the substrate was standardized at 3 mm. Argon was used as the working gas at flow rate of 10 L/min while compressed air was used as the cooling gas at a flow rate of 12 L/min. The plasma was produced in continuous mode at 40% HV continuous power (approximately, 8.1 KV_{pp}) and at 25 W RF power.

3.1.5.4 Analysis of bacterial adhesion properties and its morphology before and after NTP treatment

To study the impact of the direct application of the novel atmospheric plasma jet on the inactivation of microorganism, gram-negative *Escherichia Coli* was used. The cell adhesion and the cellular membrane integrity of the plasma-treated *E.Coli* was imaged by SEM [96]. To prepare the substrates for SEM, 1 mL of the bacterial suspension (10^6 cells/mL) were added to the stainless-steel substrate, silicon wafer substrate, HDPE substrate and the TPU) polymer substrate and incubated for 24h. Time zero was considered as the control (without plasma application). The samples were then washed twice with 2.5 % glutaraldehyde solution overnight at 4 °C. The cells were then dehydrated with 50 %, 70 %, 80 %, 90 %, and 100 % ethanol for 20 min. The samples were then dried, coated with gold, and then examined with SEM (JSM 6310, Jeol Ltd., Akishima, Tokyo, Japan).

4. Results and Discussion

4.1 FTIR analysis

Different chemical reactions, such as random cross-linking, free radical polymerization, dissociation or etching occur during a NTP polymerization process. The specific reaction mechanisms affect the structure, growth rate and chemical composition of the deposited thin film [97]. The first precursor monomer that was plasma polymerized using NTP to form a thin film was 2-ethyl-2-oxazoline (POx thin film). The precursor monomer (2-ethyl-2-oxazoline) flow rate based on the selected value of the argon carrier gas flow rate and other selected NTP parameters is shown in **Table 1**. 2-ethyl-2-oxazoline precursor monomer was plasma polymerized using NTP jet into the corresponding POx thin film using a selected set of preliminary NTP operating parameters ((SET A (Sample Number 1, Sample Number 2 and Sample Number 3, **Table 2**)), (SET B (Sample Number 5 and Sample Number 7, **Table 3**)), (SET C (Sample Number 4, Sample Number 5 and Sample Number 6, **Table 5**)), (SET D (Sample Number 5 and Sample Number 9, **Table 4**)) and (SET E (Sample Number 8 and Sample Number 9, **Table 6**)).

The general FTIR spectra of NTP deposited POx thin film is shown in **Figure 26**. The thin film presents a broad –OH stretching band (3328–3250 cm^{-1}) originating from substrate hydration, and typical C–H stretching vibrations (2975–2832 cm^{-1}). More interestingly, several signals specific to the oxazoline ring are detected. Namely, the strong bands observed at 1660 cm^{-1} and 1108 cm^{-1} are associated with the stretching of the C=N and C–O bonds, respectively, constituting the oxazoline ring [98]. The presence of C=N and C–O bonds in the IR spectrum indicates the presence of oxazoline rings in the NTP deposited thin films.

The band around 3610–3315 cm^{-1} belongs to N–H stretching vibration while the band around 1539 cm^{-1} represents N–H bending vibrations [99]. The two peaks occurring at the frequency range of 1446–1369 cm^{-1} corresponds to $–CH_3$ and $–CH_2$ bending vibrations with the $–CH_3$ bending vibrations occurring at the highest frequency value. Finally, the sharp band present at

the region between 503-662 cm^{-1}, where *para* substituted aromatic ring skeletal vibration are typically found, could be indicative for the skeletal vibration of substituted oxazoline rings [100]. The summary of the general FTIR peak assignments of NTP deposited POx thin film is shown in **Table 18a**.

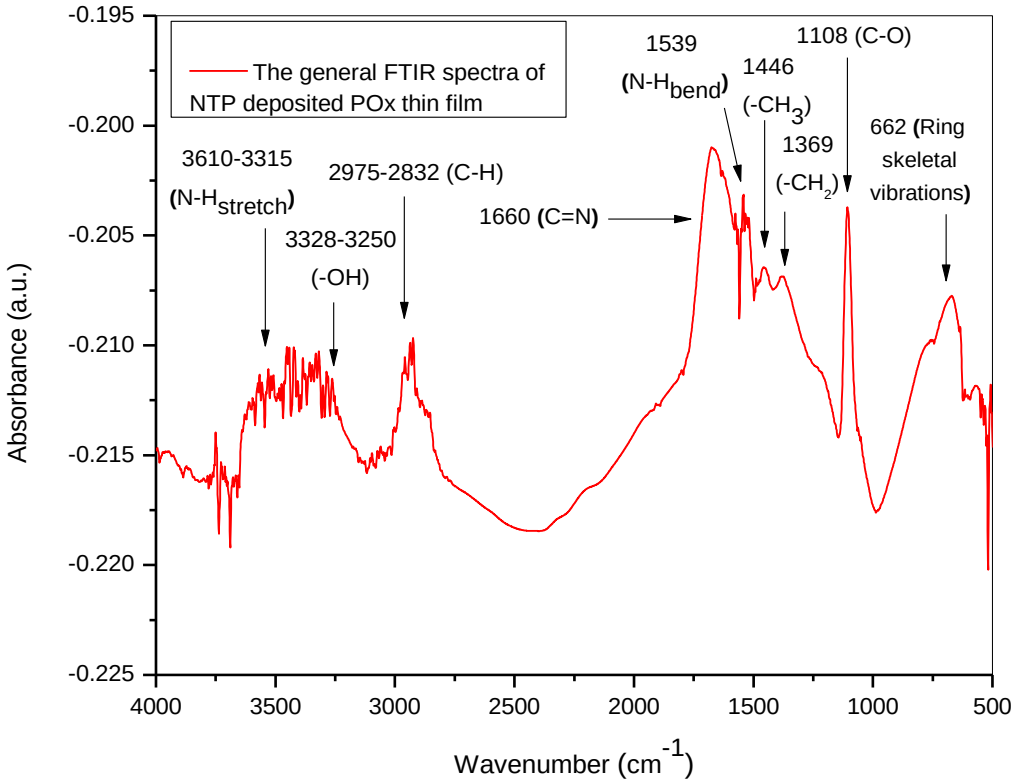

Figure 26| The general FTIR spectrum of NTP deposited POx thin film

To optimize the NTP operating parameters, the FTIR peak intensities of the targeted functional groups was used as the yardstick. The optimization process was achieved by investigating the effects of varying the NTP operating parameters on the chemical composition of the plasma deposited POx thin films. These includes varying the argon carrier gas, varying the argon working gas, varying the NTP power source from continuous RF power to pulsed RF power and varying the type of cooling gas used (compressed air or compressed nitrogen).

The effect of varying the argon carrier gas flow rate on the FTIR peak intensities of NTP deposited POx thin on Si wafer substrate was first investigated **(Figure 27)** and this formed the first set of preliminary NTP operating parameters to be optimized (SET A (Sample Number 1, Sample Number 2 and Sample Number 3, **Table 2)**.

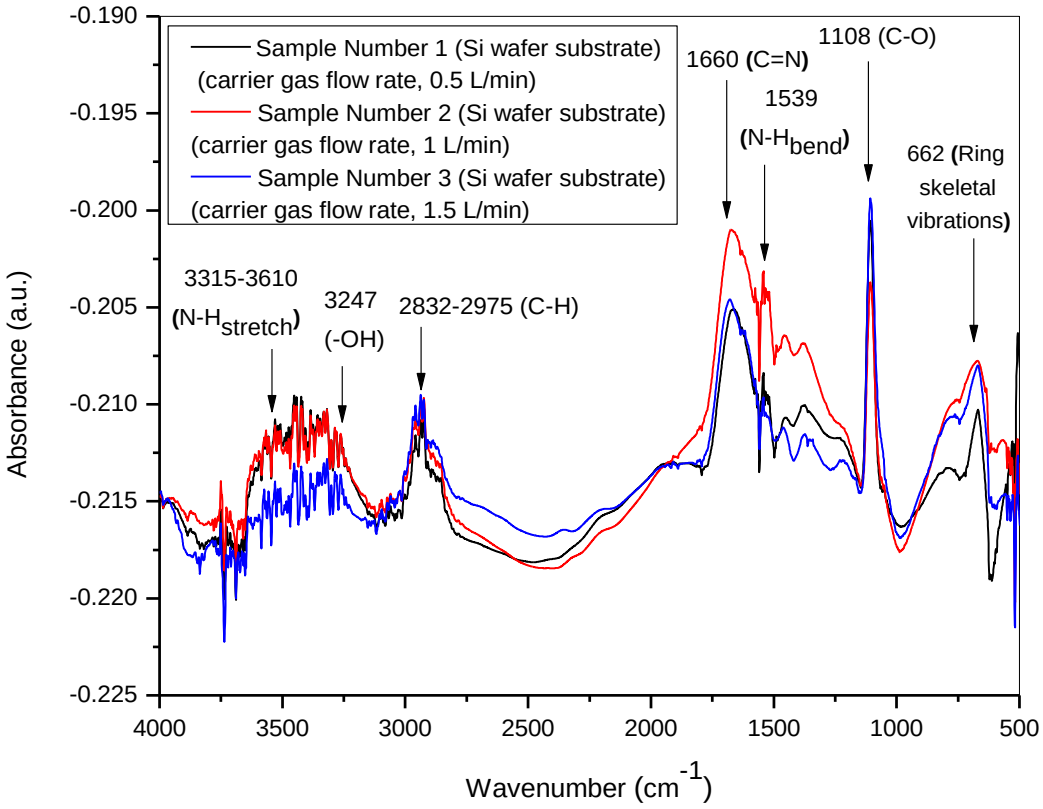

Figure 27| The effect of varying the argon carrier gas flow rate on the FTIR peak intensities of NTP deposited POx thin film on Si wafer substrate

Increasing the Ar carrier gas flow rates beyond the optimum value generally decreases the intensity of the observed peaks [101]. As seen in **Figure 27**, Increasing the Ar carrier gas flow rate from 0.5 L/min to 1.5 L/min decreases the FTIR peak intensities of the N-H stretching vibration, –OH stretching vibration, N–H bending vibrations, and the ring skeletal vibrations. Therefore, increased Ar carrier gas flow rate bares the penalty of a decreased local deposition rate which culminates in unwanted effects like etching and the formation of defects. Additionally,

the decrease in the intensity of the observed peaks with increasing monomer input demonstrated that a higher monomer concentration present at the same power level results in a decrease in available energy per monomer molecule. Moreover, for a higher carrier gas flow rate, the interaction time between the monomer molecules and the plasma reactive species becomes shorter, which in turn decreases the concentration of the targeted functional groups [101]. Similar observations were made in another study that investigated the role of varying the carrier gas flow rate in role-to-roll AP-PECVD synthesized silica moisture barrier films [102].

The effect of varying the argon working gas flow rate on the FTIR peak intensities of NTP deposited POx thin film on Si wafer substrate was then investigated **(Figure 28)** and this formed the second set of preliminary NTP operating parameters to be optimized (SET C (Sample Number 4, Sample Number 5, and Sample Number 6, **Table 5))**.

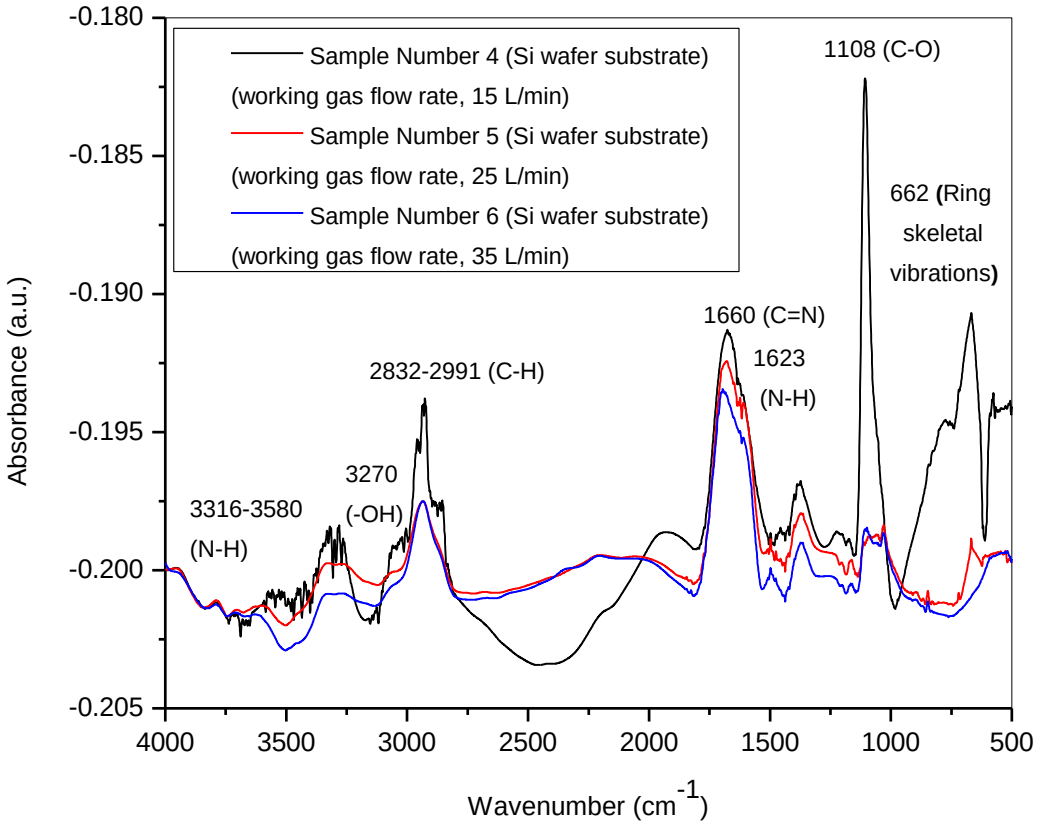

Figure 28| The effect of varying the argon working gas flow rate on the FTIR peak intensities of NTP deposited POx thin film on Si wafer substrate

Increasing the Ar working gas flow rates to higher values that are beyond the optimum value generally decreases the intensity of the observed peaks [103]. As seen in **Figure 28**, Increasing the Ar working gas flow rates from 15 L/min to 35 L/min decreases the peak intensity of the N–H stretching vibration, –OH stretching vibration, C–H stretching vibration, C=N stretching vibration, N–H bending vibration, C–O stretching vibration and the ring skeletal vibrations. Increased working gas flow rate is highly suspected to result in increased energy flux at the substrate surface, which can lead to a higher deposition rate. However, at a very high gas flow rate (more than an optimized one), the number of atomic collisions is more and results in higher rate of scattering of spattered atoms. Thus, too high a gas flow rate reduces the deposition rate and increases the penetration depth of an atom [104, 105]. Additionally, the residence times of the precursor monomer vapor, intermediates, and primary particles in the plasma reactor becomes shorter when the gas flow rate is increased. Because of the low residence time of the process gases, a high gas flow rate tends to remove potential particle generation from the sheath before they can form particles in the nucleation sites and provides less opportunities for the primary particles to grow [106]. Similar observations were made in another study that investigated the impact of Ar flow rates on micro-structural properties of WS_2 thin film by RF magnetron sputtering [107].

The effect of varying the NTP power source from continuous RF power to pulsed RF power while using compressed air as the type of cooling gas used on the FTIR peak intensities of NTP deposited POx thin film on Si wafer substrate was then investigated **(Figure 29)** and this formed the third set of preliminary NTP operating parameters to be optimized (SET B (Sample Number 5 and Sample Number 9, **Table 3)**.

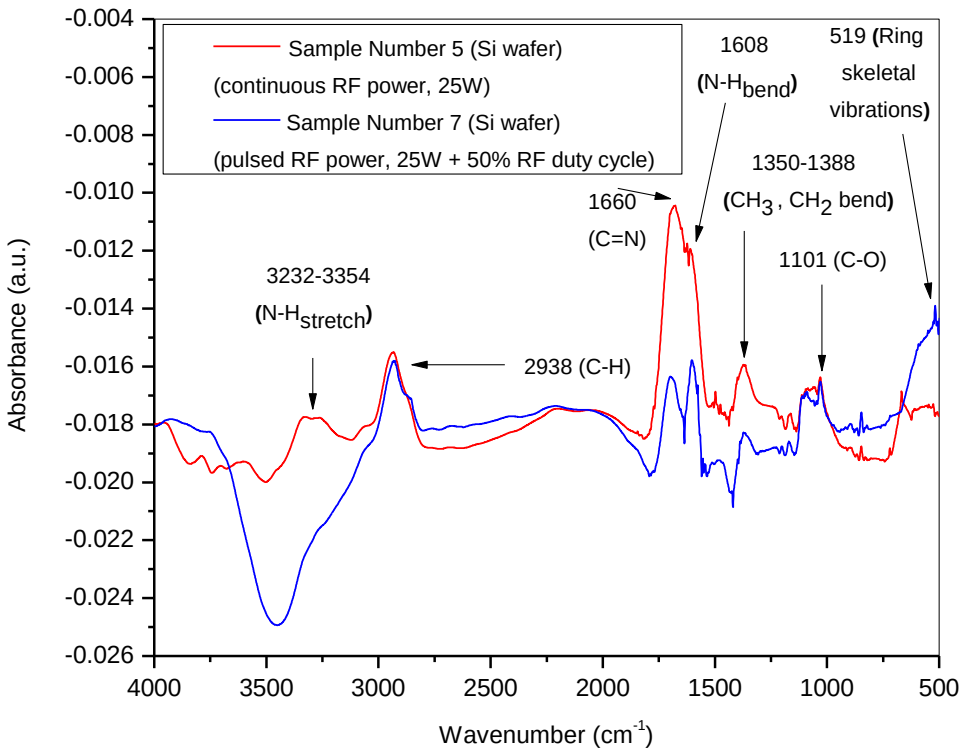

Figure 29| The effect of varying the NTP power source from continuous RF power to pulsed RF power while using compressed air as the type of cooling gas used on the FTIR peak intensities of NTP deposited POx thin film on Si wafer substrate

When NTP is operated in a continuous mode, the magnitude of the breakdown voltage and the dielectric temperature rapidly increases [88]. However, when the plasma is operated in pulsed mode, the discharge is constantly turned on and off such that the breakdown voltage is achieved at the beginning of each pulse and at the same time, the dielectric temperature is kept low, which is desirable for surface treatment [88]. Pulsing of the incoming electrical energy absorbed by the targeted vapor, ultimately minimizes bond scission and guarantees energetic molecular structure rearrangement to hold on to beneficial functional groups. Pulsing therefore ensures congruent transfer of the target material to the substrate [108]. Additionally, continuous wave plasma deposition, leads to higher monomer fragmentation and therefore the loss of some monomer functionalities [97]. Therefore, pulse plasma deposition partly overcomes these drawbacks of continuous wave plasma deposition.

As it can be seen in **Figure 29**, sharp and well resolved –C=N stretching peak and –N=H bending peak were observed in pulsed RF mode as opposed to similar peaks obtained in continuous RF mode. These and other advantages of using pulsed RF power has also been well documented in a review done on the use of pulsed plasma etching for semiconductor manufacturing as opposed to the use of continuous RF power [88].

The effect of varying the type of cooling gas used (compressed air or compressed nitrogen) on the FTIR peak intensities of NTP deposited POx thin film on Si wafer substrate was then investigated **(Figure 30)** and this formed the fourth set of preliminary NTP operating parameters to be optimized (SET D (Sample Number 8 and Sample Number 9, **Table 4))**.

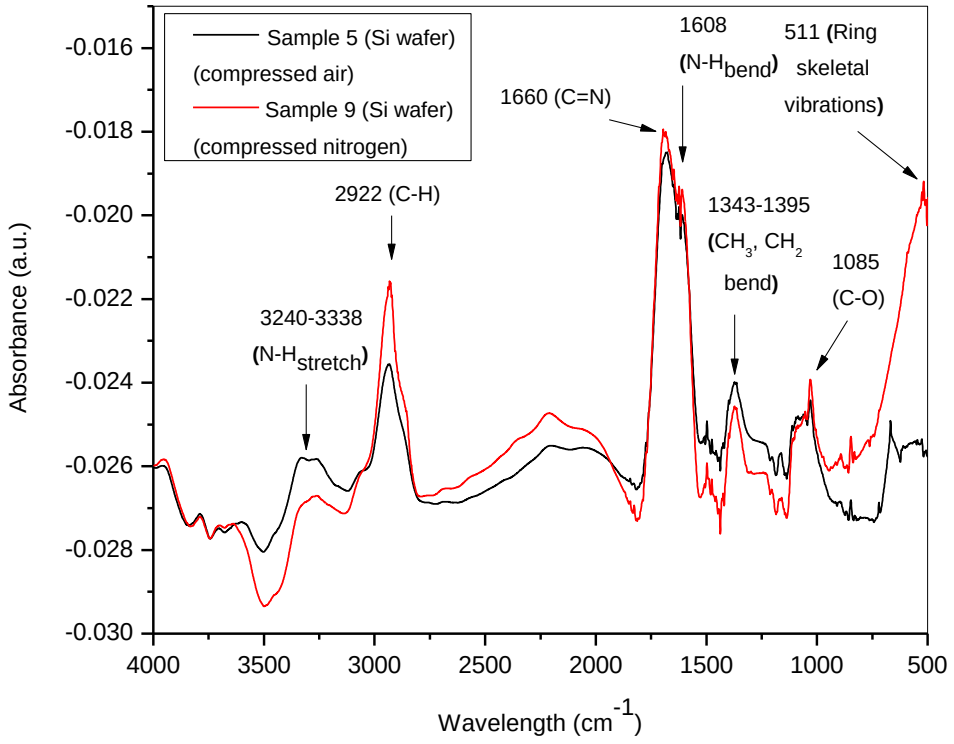

Figure 30| The effect of varying the type of cooling gas used (compressed air or compressed nitrogen) on the FTIR peak intensities of NTP deposited POx thin film on Si wafer substrate.

The POx thin film was deposited in both compressed nitrogen environment which usually reduces moisture intrusion, oxidation, degradation, and contamination and in compressed air which is an oxygenating environment. In compressed air cooling, oxygen molecules tend to neutralize free electrons from the plasma, making it less effective from a physicochemical point of view [87]. As it can be seen in **Figure 30**, the FTIR peaks of NTP deposited POx thin film in compressed nitrogen atmosphere were generally slightly higher in intensity than those deposited in compressed air atmosphere. These peaks, specifically, includes the C–H stretching vibration, C=N stretching vibration, N–H bending vibration, C–O stretching vibration and the ring skeletal vibrations. Similar observations were made when Silk Fibroin was deposited using NTP on different surfaces in both air and nitrogen environments [87].

The effect of varying the NTP source from continuous RF power to pulsed RF power while using compressed nitrogen as the type of cooling gas used on the FTIR peak intensities of NTP deposited POx thin film on Si wafer substrate was then investigated **(Figure 31)** and this formed the fifth set of preliminary NTP operating parameters to be optimized (SET E (Sample Number 8 and Sample Number 9, **Table 6))**.

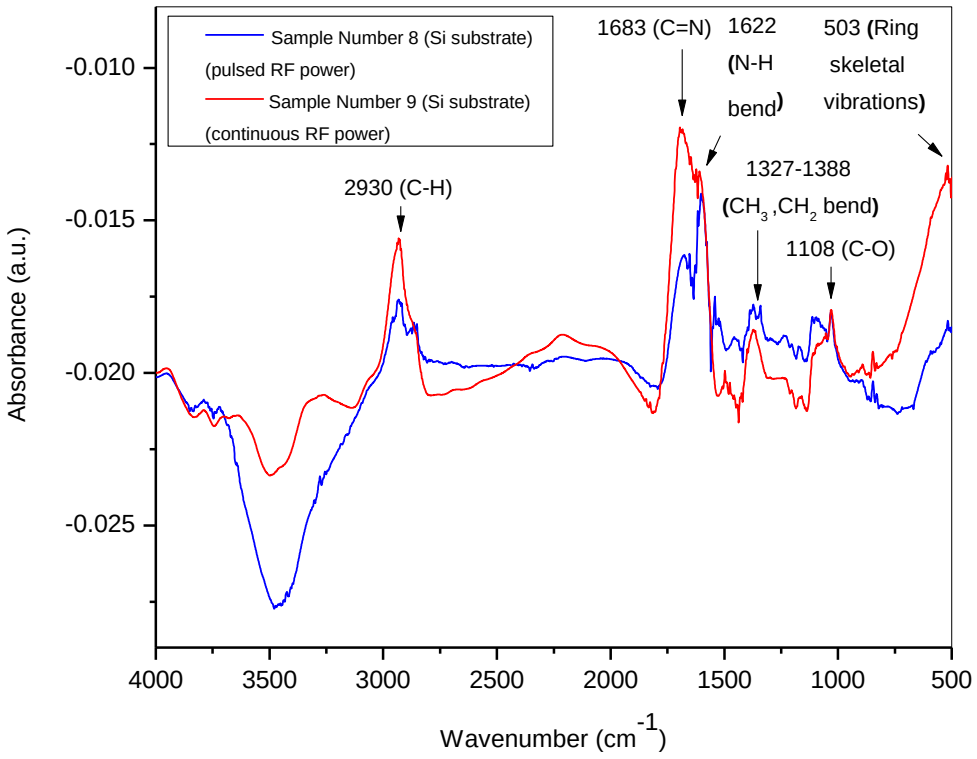

Figure 31| The effect of varying the NTP power source from continuous RF power to pulsed power while using compressed nitrogen as the type of cooling gas used on the FTIR peak intensities of NTP deposited POx thin film on Si wafer substrate.

As it can be seen in **Figure 31**, the benefits of using pulsed RF plasma mode as compared to using continuous RF plasma mode were also observed in nitrogen environment. Sharp and well resolved –C=N stretching peak and –N=H bending peak were observed while using pulsed RF mode in comparison with similar peaks observed while using continuous RF mode **(Figure 31)**. No new peaks were observed when the substrate was changed from the conductive Silicon wafer substrate to the non-conductive KBr substrate (Appendix A, Appendix B, Appendix C, Appendix D, Appendix E, Appendix I and Appendix J).

The FTIR spectra of NTP deposited POx thin film was also compared to the FTIR spectra of the corresponding precursor monomer (reference spectrum). This comparison is shown in

Figure 32a and **Figure 32b**. The IR band positions and attributions of 2-ethyl-2-oxazoline precursor monomer was used as a base for the interpretation of the NTP deposited POx thin films. Hence, it appeared that 2-ethyl-2-oxazoline precursor monomer structure seemed to be well-retained in the NTP deposited POx thin film as the -OH stretching band, C-H stretching band, C=N stretching band, N-H band, and the C-O band were detected. The decrease in the intensity of the C=N band from the 2-ethyl-2-oxazoline precursor monomer to the NTP deposited POx thin film shows the success of the plasma polymerization process. Finally, from the presence of additional peaks at 3323-3596 cm^{-1} and 662 cm^{-1} related to the N-H stretching vibration and the ring skeletal vibrations, it was assumed to a lesser extent, the plasma polymerization induced the formation of secondary chemical groups.

The optimized NTP operating parameters that gave the highest intensity of the targeted functional groups in the NTP deposited POx thin films are shown in **Table 17**.

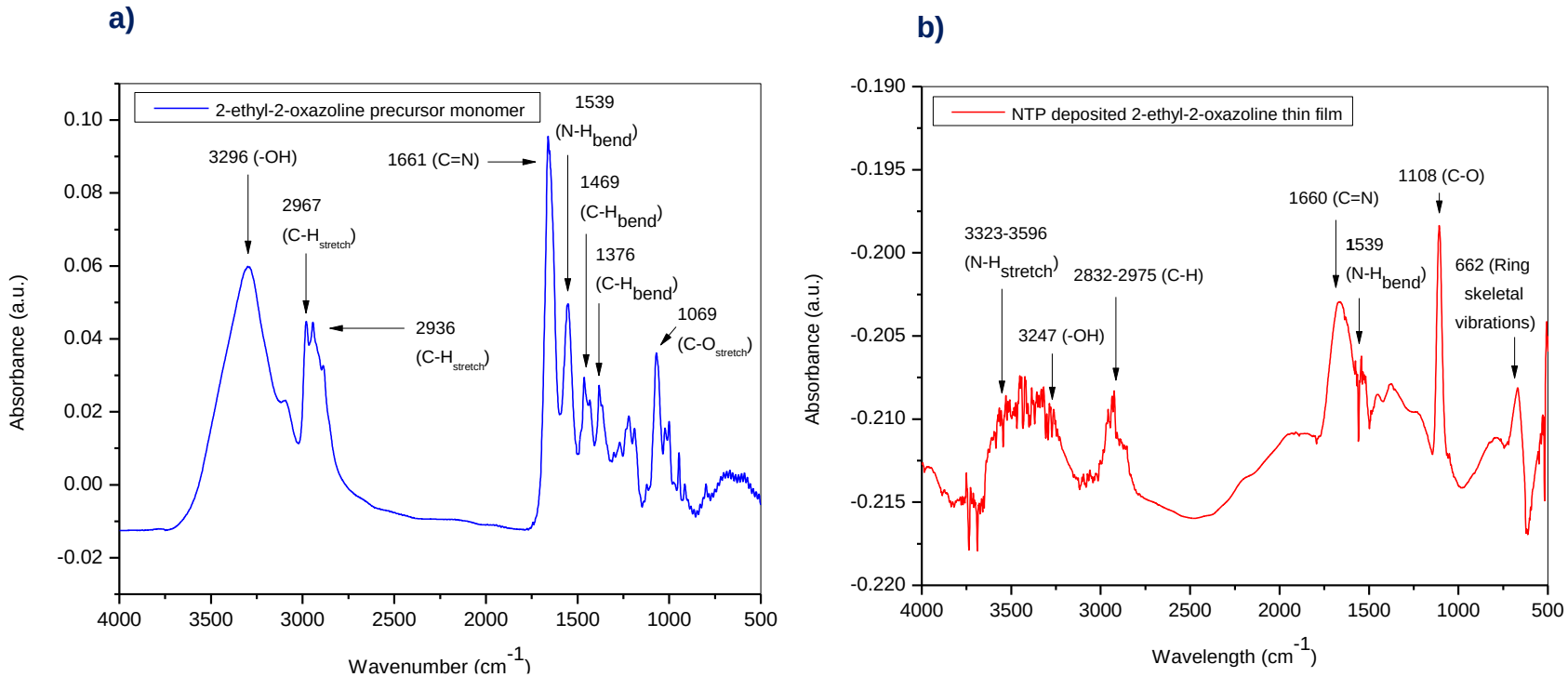

Figure 32| Comparison of the general FTIR sectra of plasma polymerized POx thin film to the corresponding precursor monomer **a)** FTIR spectra of 2-ethyl-2-oxazoline precursor monomer covering on a freshly prepared KBr pellet (reference spectrum) **b)** FTIR spectra of plasma deposited PO_x thin film on Si wafer substrate

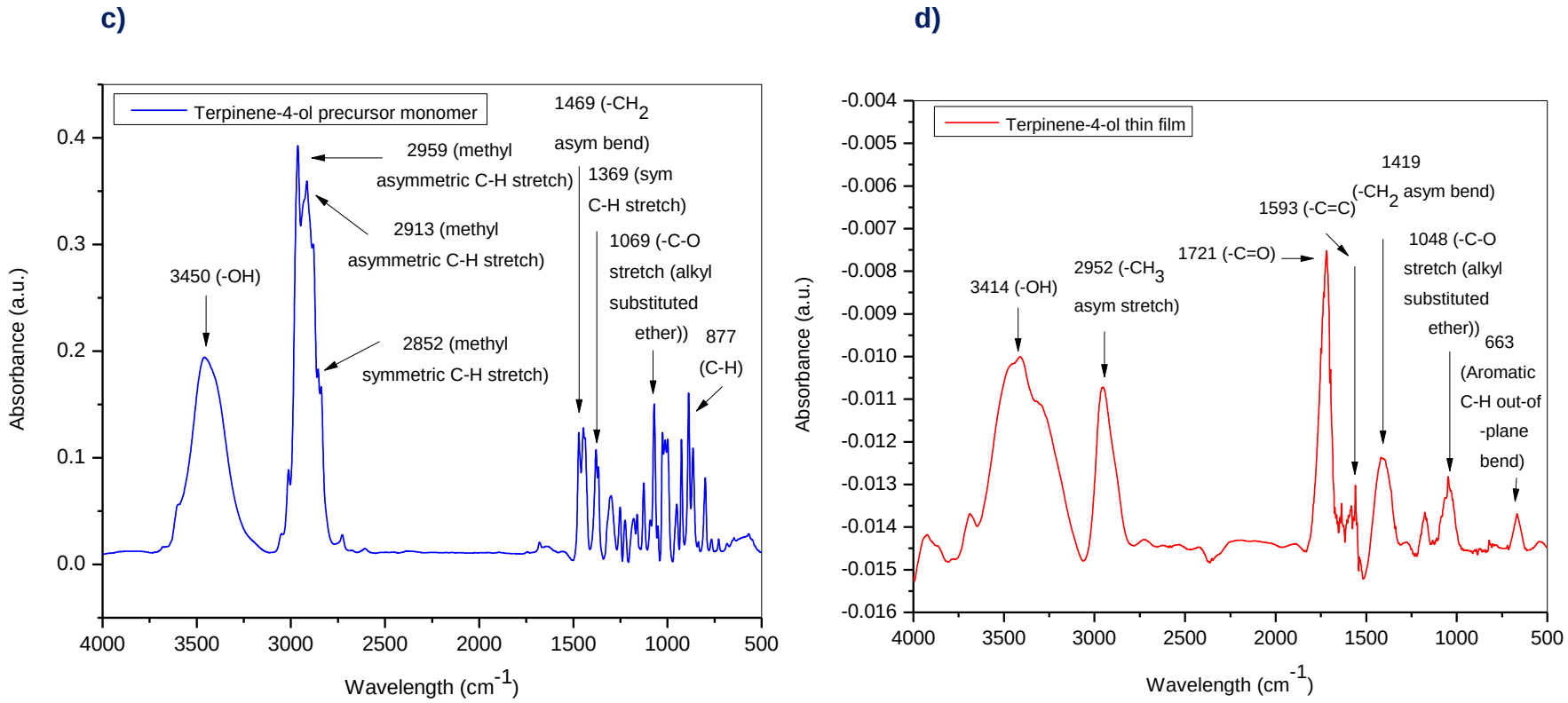

Figure 33| Comparison of the general FTIR spectra of plasma polymerized Terpinene-4-ol thin film to the corresponding precursor monomer **c)** FTIR spectra of Terpinene-4-ol precursor monomer covering on a freshly prepared KBr pellet (reference spectrum) **d)** FTIR spectra of plasma deposited Terpinene-4-ol thin film on KBr substrate

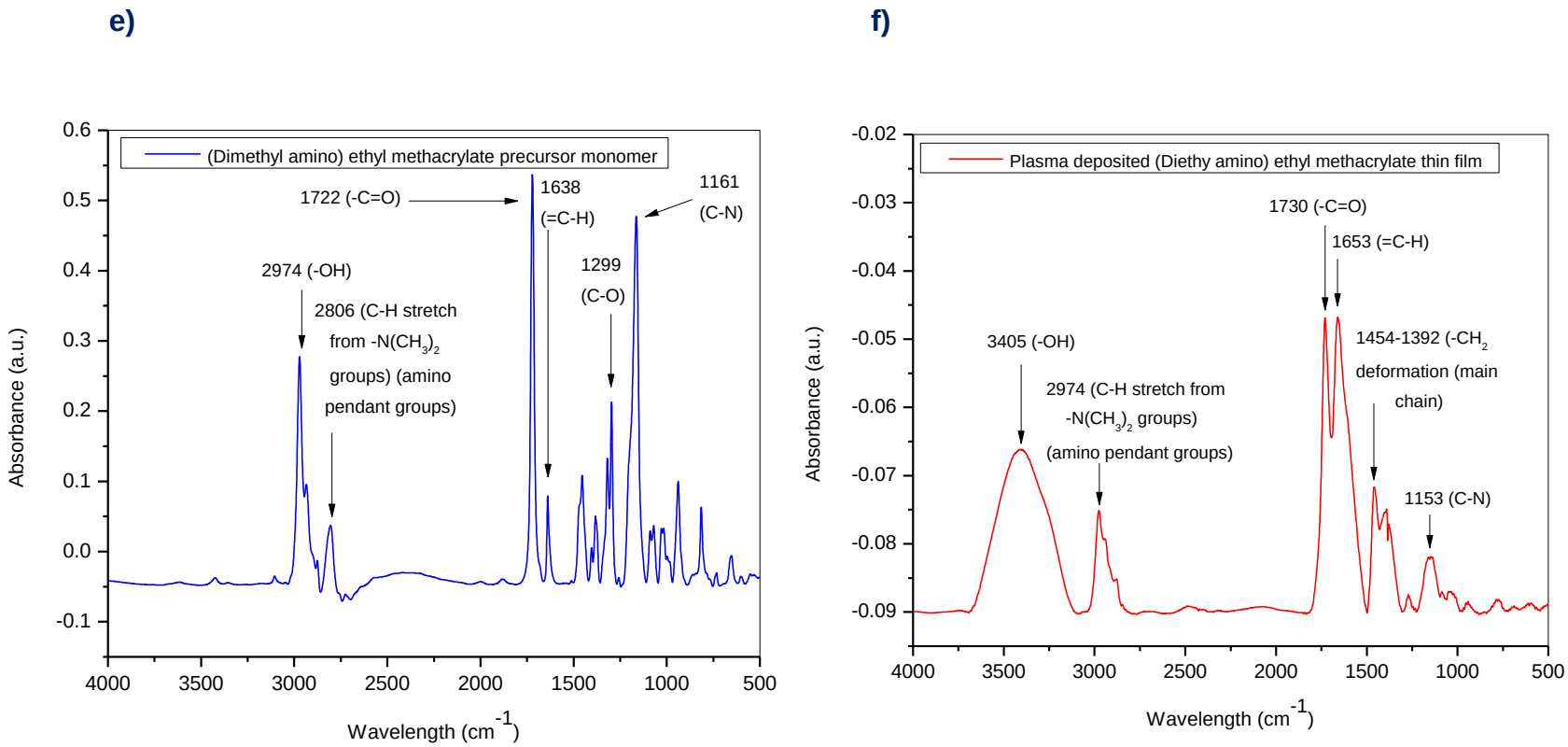

Figure 34| Comparison of the general FTIR spectra of plasma polymerized (Diethyl amino) thin film to the corresponding precursor monomer **e)** FTIR spectra of (Diethyl amino)ethyl methacrylate precursor monomer covering on a freshly prepared KBr pellet (reference spectrum) **f)** FTIR spectra of plasma deposited (Diethylamino)ethyl methacrylate thin film on KBr substrate

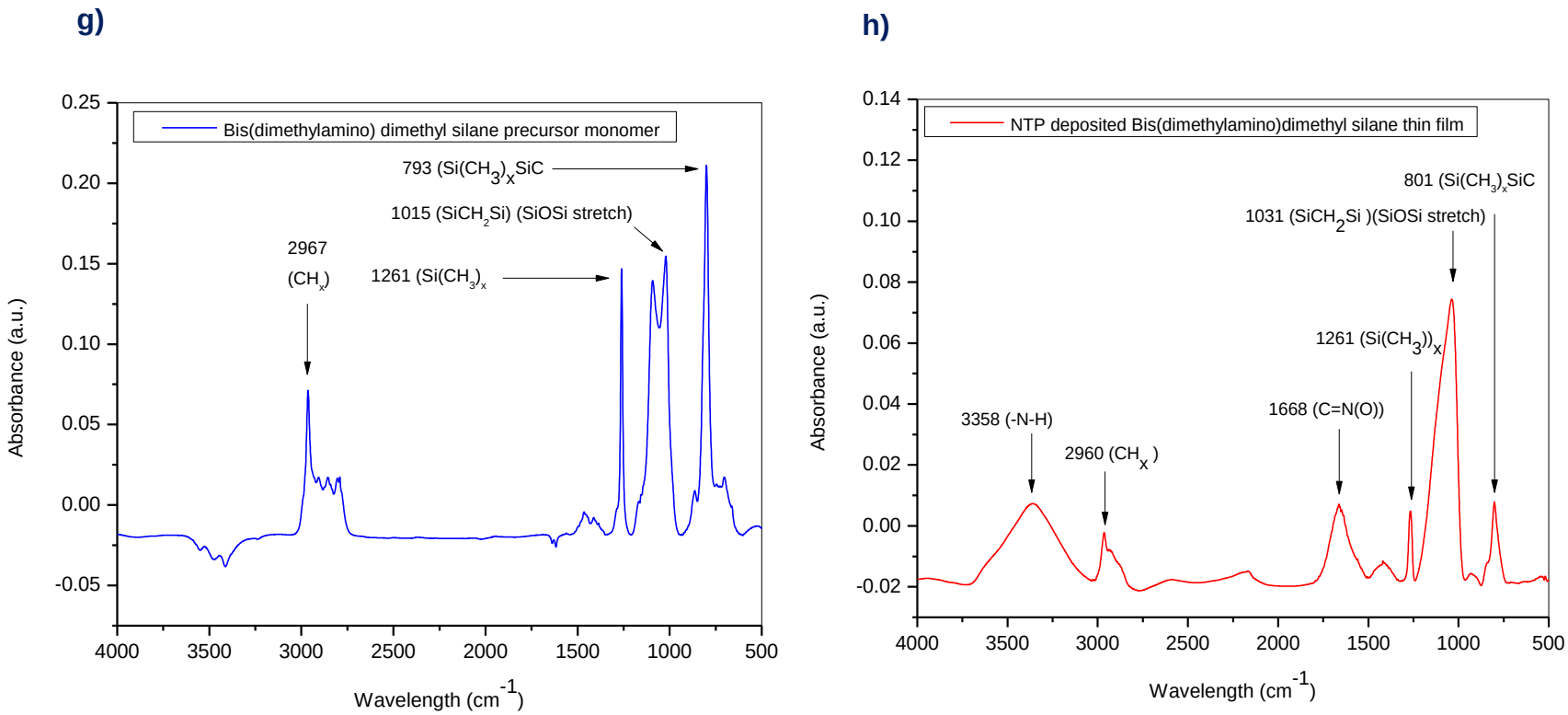

Figure 35| Comparison of the general FTIR spectra of plasma polymerized Bis(dimethyl amino) dimethyl silane thin film to the corresponding precursor monomer **g)** FTIR spectra of Bis(dimethyl amino) dimethyl silane precursor monomer covering on a freshly prepared KBr pellet (reference spectrum) **h)** FTIR spectra of plasma deposited Bis(dimethyl amino) dimethyl silane thin film on Si wafer substrate

a)

Peak positions (cm^{-1}) Silicon wafer substrate	Peak assignment
3610–3315	ν (–N–H) [100]
3247	ν (–OH) [100]
2975–2832	ν (–C–H) [100]
1660	ν (–C = N) [100]
1539	Θ (–N–H) [100]
1327–1388	Θ (CH_3, CH_2 bending) [100]
1108	ν (–C–O) [100]
662	Ring skeletal vibrations [100]

b)

Peak positions (cm^{-1}) Silicon wafer substrate	Peak assignment
3490-3429	ν (–OH) [97]
2968	ν_{as} (–CH_3) [97]
2930	ν_{as} (–CH_2) [97]
2885	ν_s (–CH_3) [97]
1706	ν (–C=O) [97]
1593	ν (–C=C-) [97]
1463	Θ (–CH_2) [97]
1403	Θ_s (–CH_3) [97]
1048	ν (–C–O) [97]
670	Θ_{as} (–C-H) [97]

Table 18| The summary of the general FTIR peak assignments of plasma deposited POx thin film and Terpinene-4-ol thin film **a)** The summary of the general FTIR peak assignments of the plasma deposited POx thin film **b)** The summary of the general FTIR peak assignments of plasma deposited Terpinene-4-ol thin film. Annotations: ν – stretching vibrations, Θ – bending vibrations, ν_{as} (Θ) – asymmetric bending vibrations, ν_{as} – asymmetric stretching vibrations, ν_s – symmetric stretching vibrations, Θ_s – symmetric bending vibrations, Θ_{as} – asymmetric bending vibrations

c)

Peak positions (cm^{-1}) Silicon wafer substrate	Peak assignment
3405	ν (–OH) [109]
2974	ν (C–H) from $–N(CH_3)_2$ groups [109]
1653	ν (=C-H) [109]
1730	ν (–C=O) [109]
1454–1392	Θ (–CH_2 deformation (main chain)) [109]
1153	ν (C–N) [109]

d)

Peak positions (cm^{-1}) Silicon wafer substrate	Peak assignment
3358	ν (–N–H) [110]
2960	ν (CH_x) [110]
1668	ν(C=N(O)) [110]
1384	Θ (–CH_3) [110]
1261	Θ (Si$(CH_3)_x$ [110]
1031	ν ($SiCH_2Si$) (Si–O–Si) [110]
801	ν (Si$(CH_3)_x$SiC) [110]

Table 19| The summary of the general FTIR peak assignments of plasma deposited (Diethyl amino) ethyl methacrylate thin film and Bis(dimethyl amino) dimethyl silane thin film **c)** The summary of the general FTIR peak assignment of plasma deposited (Diethyl amino) ethyl methacrylate thin film **d)** The summary of the general FTIR peak assignment of plasma deposited Bis(dimethyl amino) dimethyl silane thin film

The second precursor monomer that was plasma polymerized using NTP to form a thin film was Terpinene-4-ol (Terpinene-4-ol thin film). The precursor monomer (Terpinene-4-ol) flow rate based on the selected value of the argon carrier gas flow rate based on the selected value of the argon carrier gas flow rate and other selected NTP parameters is shown in **Table 1**. Terpinene-4-ol precursor monomer was plasma polymerized using NTP jet into the corresponding Terpinene-4-ol thin film using a set of preliminary NTP operating parameters ((SET I(Sample Number 1, Sample Number 2 and Sample Number 3, **Table 10**), (SET J (Sample Number 1 and Sample Number 4, **Table 11**), (SET K, Sample Number 1 and Sample Number 5, **Table 12**), (SET L, Sample Number 1 and Sample Number 6, **Table 13**) and (SET M, Sample Number 1 and Sample Number 7, **Table 14**)). The NTP deposition of Terpinene-4-ol was performed in pulsed HV mode following earlier observed advantages of using pulsing mode.

The general FTIR spectra of NTP deposited Terpinene-4-ol thin film is shown in **Figure 36**.

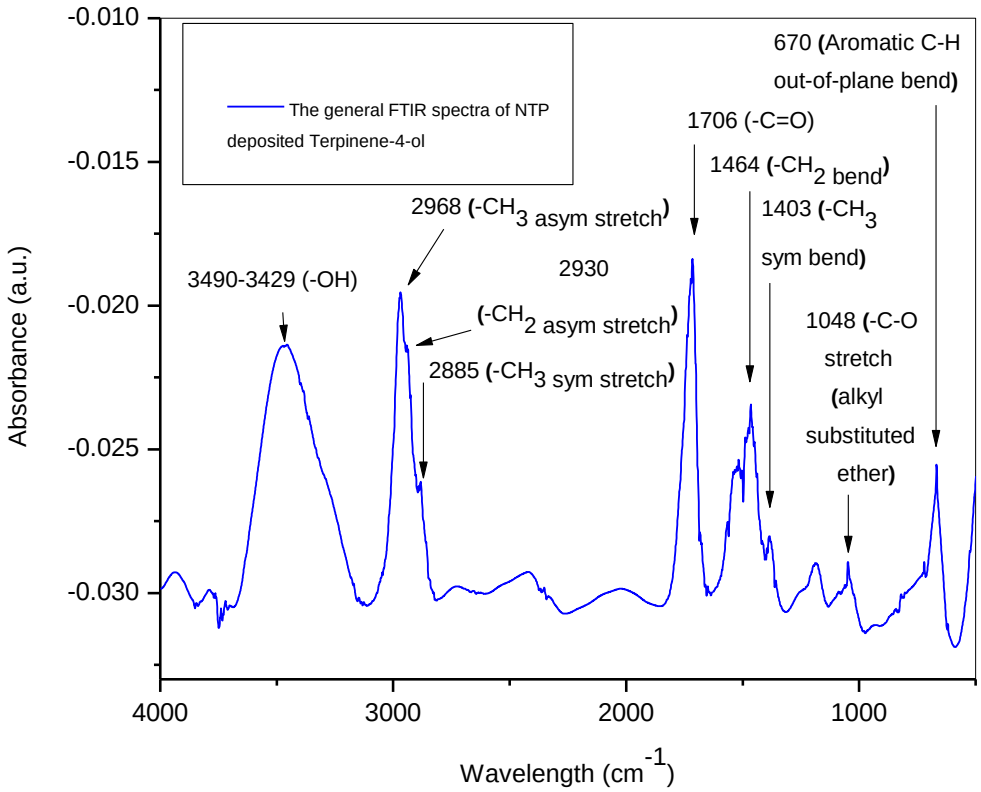

Figure 36| The general FTIR spectrum of NTP deposited Terpinene-4-ol thin film

The broad FTIR peak for the NTP deposited Terpinene-4-ol thin film centered around 3490-3429 cm^{-1} is indicative of the –OH stretch [97]. The peak at 2968 cm^{-1} corresponds to an asymmetric methyl stretch while the peak observed at 2930 cm^{-1} corresponds to an asymmetric methylene C–H stretch. The intensity of the peak at 1706 cm^{-1} represents –C=O [111] stretching in the carboxyl group. The peak intensity at 1463 cm^{-1} represents methylene C-H bending vibrations. The peak at 1403 cm^{-1} corresponds to a symmetric methyl bending vibrations. The peak at 1048 cm^{-1} represents the phenolic –C–O stretch. Finally, the intensity of the peak at 670 cm^{-1} represents an aromatic –C–H out-of-plane bend. The summary of the general FTIR peak assignments of NTP deposited POx thin film is shown in **Table 18b**.

To optimize the NTP operating parameters, the FTIR peak intensities of the targeted functional groups was used as the yardstick. The optimization process was achieved by investigating the effects of varying the NTP operating parameters on the chemical composition of the plasma deposited Terpinene-4-ol thin films. These includes varying the argon working gas, varying the distance between the substrate and the plasma jet nozzle, varying the type of cooling gas used (compressed air or compressed nitrogen), varying the NTP power source from continuous RF power to pulsed RF power and the effect of varying the plasma power.

The effect of varying the argon working gas flow rate on the FTIR peak intensities of NTP deposited Terpinene-4-ol thin film on Si wafer substrate was first investigated **(Figure 37)** and this formed the first set of preliminary NTP operating parameters to be optimized (**SET I** (Sample Number 1, Sample Number 2 and Sample Number 3**, Table 10)**. As seen earlier, increasing the working gas flow rate results in increased energy flux at the substrate surface leading to a higher deposition rate [104, 105]. This remains the case up to an optimum flow rate, and when this value is surpassed, the rate of deposition decreases and the penetration depth of the gas atoms increases [105].

As can be seen in **Figure 37**, increasing the Ar working gas flow rates from 9 L/min to 12 L/min increases the peak intensities of the –OH stretching vibration, $–CH_3$ asymmetric stretching vibration, $–CH_2$ asymmetric stretching vibration, –C=O stretching vibration, $–CH_2$ bending vibration, $–CH_3$ symmetric bending vibration and the aromatic C–H out-of-plane bending vibration. Therefore, the argon working gas flow rate of 12 L/min falls under the range of optimum argon flow rate values needed to ensure high intensity peaks as opposed to the argon flow rate value of 35 L/min seen previously which turned out to have undesired effects. The importance of using the optimum argon flow rate to deposit thin films that have high quality in terms of refractive index, smoothness, and uniformity was also validated in another study on the analysis of silica thin films deposited by PECVD using an oxygen-TEOS-Argon mixture [112].

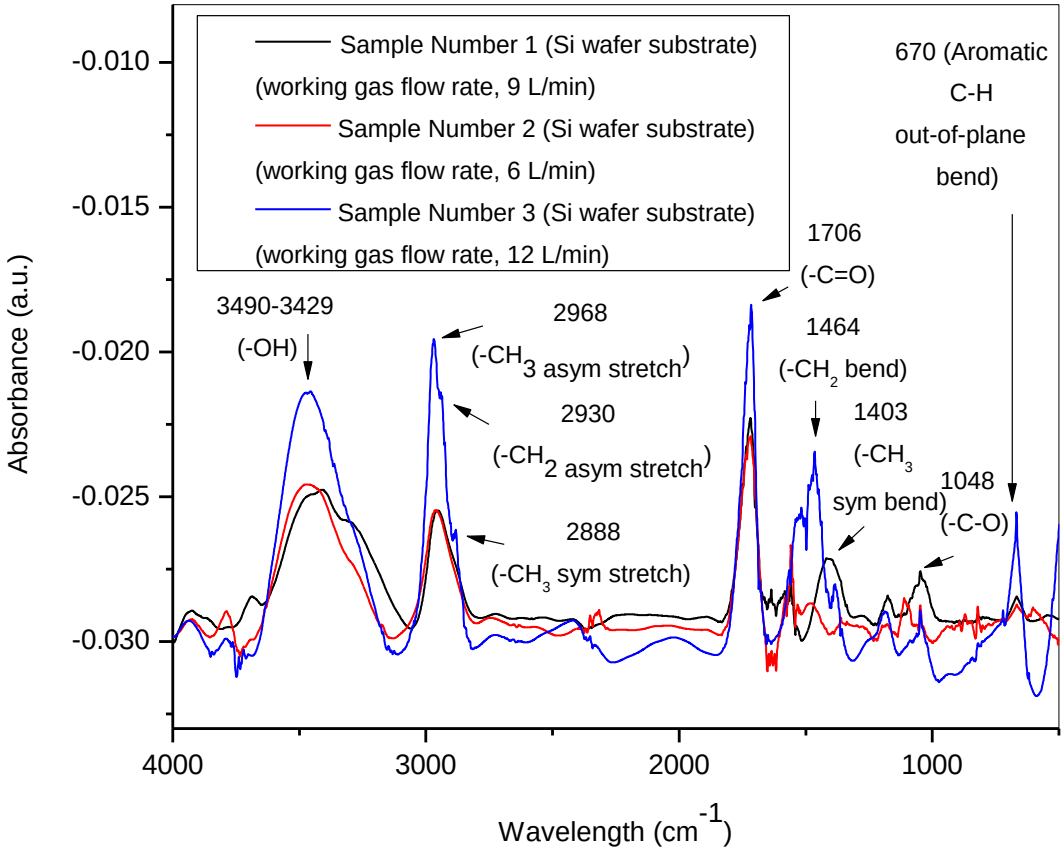

Figure 37| The effect of varying the argon working gas flow rate on the FTIR peak intensities of NTP deposited Terpinene-4-ol thin film on Silicon wafer substrate

The effect of varying the distance from the substrate to the plasma jet nozzle on the FTIR peak intensities of NTP deposited Terpinene-4-ol thin on Si wafer substrate was then investigated **(Figure 38)** and this formed the second set of preliminary NTP operating parameters to be optimized (**SET J**, Sample Number 1 and Sample Number 4, **Table 11**). The thin film deposition rate increases when the distance between the substrate and the plasma nozzle is increased up a certain distance which is the optimum distance beyond up which the gains are reversed [113]. As can be seen in **Figure 38**, increasing the distance between the substrate and the plasma jet nozzle up to but not exceeding the optimum value increases the intensity of the –OH stretching vibration, $–CH_3$ asymmetric stretching vibration, –C=O stretching vibration, $–CH_2$ bending vibration and the aromatic C–H out-of-plane bending vibration. Increasing the distance to an optimum value also ensures that the substrate is away from the hotter and the most reactive zone of the plasma. When the heat on the substrate is too high, crystallization of the growing thin film occurs [114].

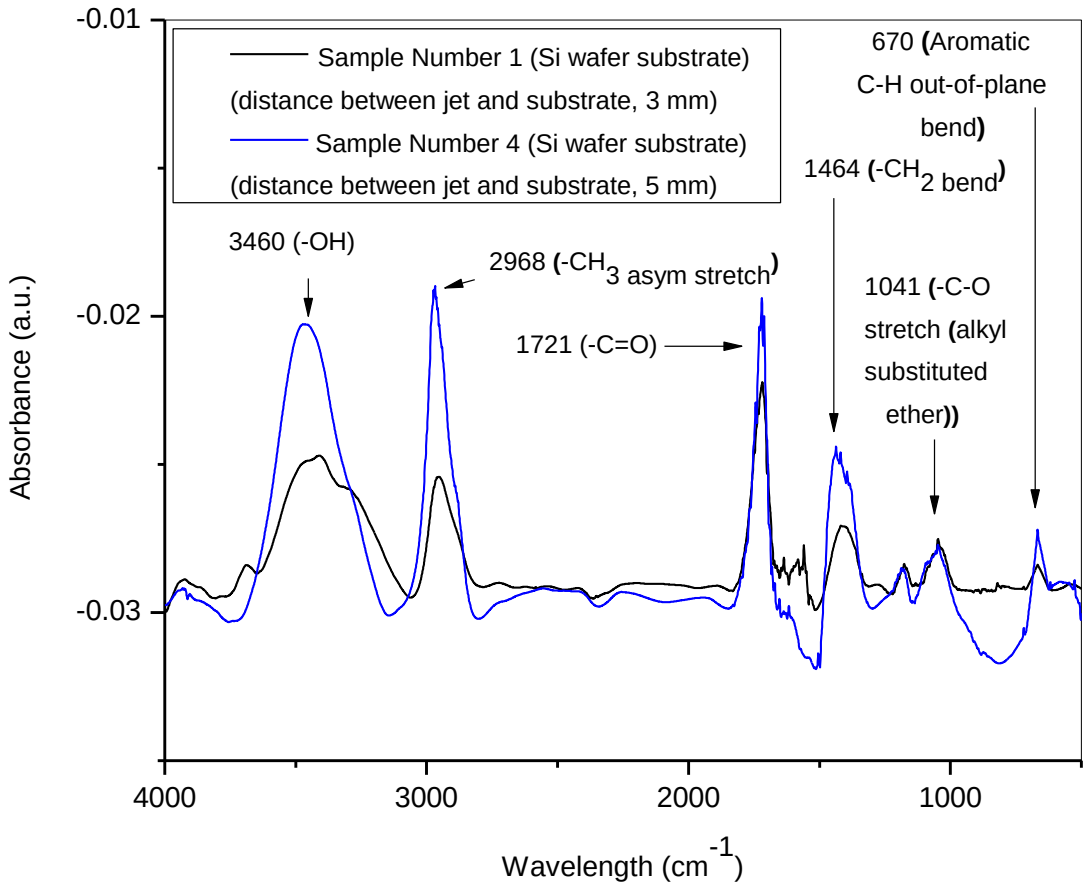

Figure 38| The effect of varying the distance between the substrate and the plasma jet nozzle on the FTIR peak intensities of NTP deposited Terpinene-4-ol thin film on Silicon wafer substrate

The effect of varying the type of cooling gas used (compressed air or compressed nitrogen) on the FTIR peak intensities of NTP deposited Terpinene-4-ol thin film on Si wafer substrate was then investigated **(Figure 39)** and this formed the third set of preliminary NTP operating parameters to be optimized **(SET K,** Sample Number 1 and Sample Number 5, **Table 12)**.

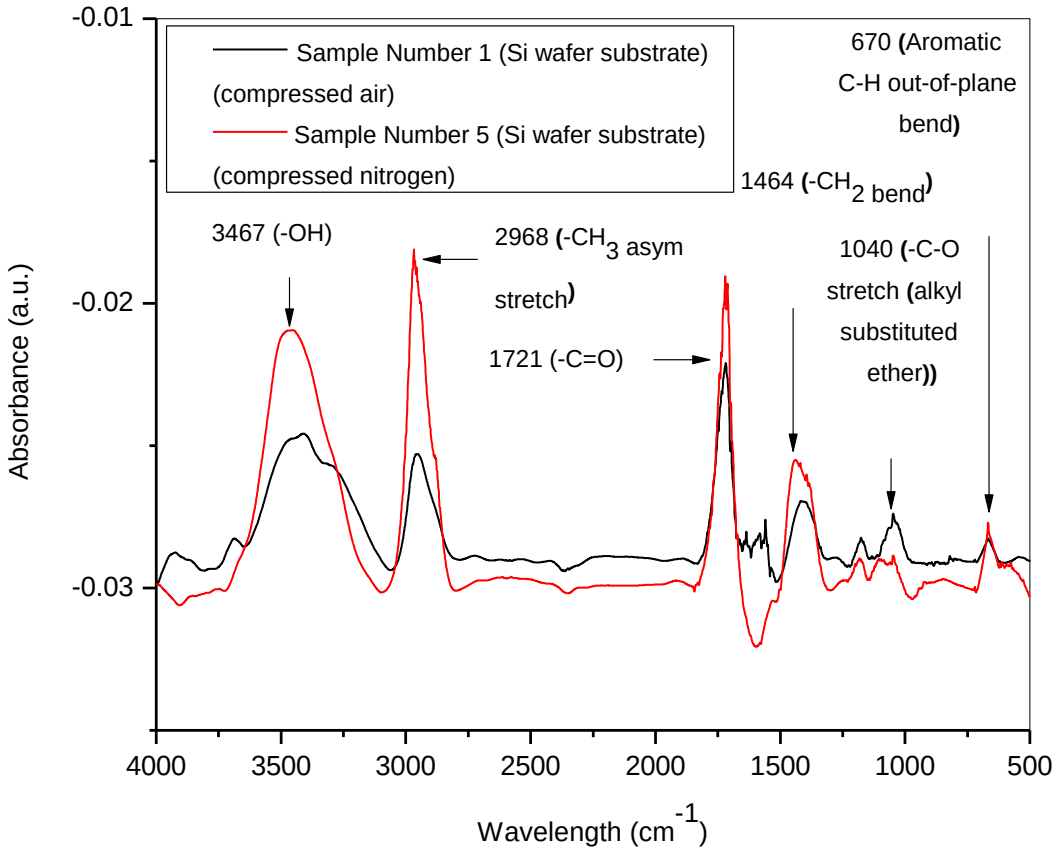

Figure 39| The effect of varying the type of cooling gas used (compressed air or compressed nitrogen) on the FTIR peak intensities of NTP deposited Terpinene-4-ol thin film on Si wafer substrate

As it can be seen in **Figure 39**, the FTIR peaks of NTP deposited Terpinene-4-ol thin film on Si wafer substrate and in compressed nitrogen atmosphere were generally higher in intensity than those deposited in compressed air atmosphere. These peaks, specifically, includes the –OH stretching vibration, $–CH_3$ asymmetric stretching vibration, –C=O stretching vibration, $–CH_2$ bending vibration and the aromatic C–H out-of-plane bending vibration. This was also observed to be the case under similar conditions in NTP deposited POx thin film.

The effect of varying the NTP source from continuous HV power to pulsed HV power while using compressed air as the type of cooling gas used on the FTIR peak intensities of NTP deposited Terpinene-4-ol thin film on Si wafer substrate was then investigated **(Figure 40)** and this formed the fourth set of preliminary NTP operating parameters to be optimized (**SET E,** Sample Number 1 and Sample Number 6, **Table 6)**.

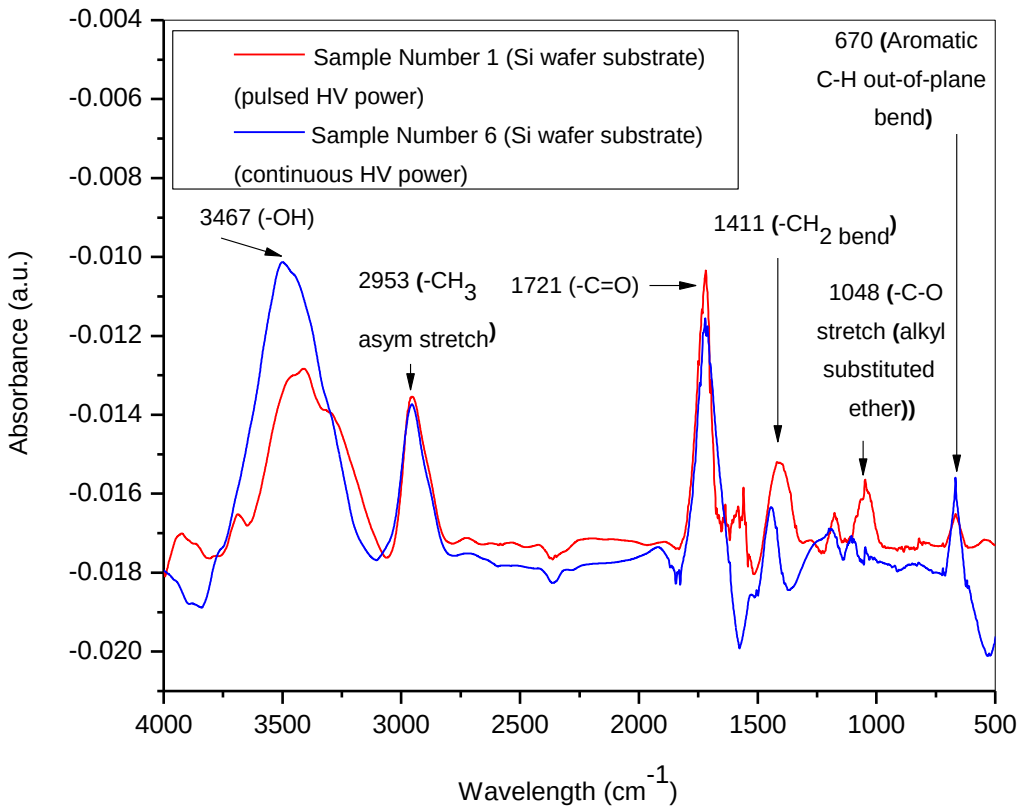

Figure 40| The effect of varying the NTP power source from continuous RF power to pulsed RF power while using compressed nitrogen as the type of cooling gas used on the FTIR peak intensities of NTP deposited Terpinene-4-ol thin film on Si wafer substrate.

As it can be seen in **Figure 40**, sharp and well resolved peaks including the $–CH_3$ asymmetric stretching vibration, –C=O stretching vibration, $–CH_2$ bending vibration and –C–O stretching vibration belonging to the alkyl substituted ether functional group were observed when the plasma was operated in pulsed mode. This was also observed to be the case under similar conditions in NTP deposited POx thin film.

The effect of increasing the plasma power on the FTIR peak intensities of NTP deposited Terpinene-4-ol thin film on Si wafer substrate was then investigated **(Figure 41)** and this formed the fifth set of preliminary NTP operating parameters to be optimized **(SET E,** Sample Number 1 and Sample Number 7, **Table 6).**

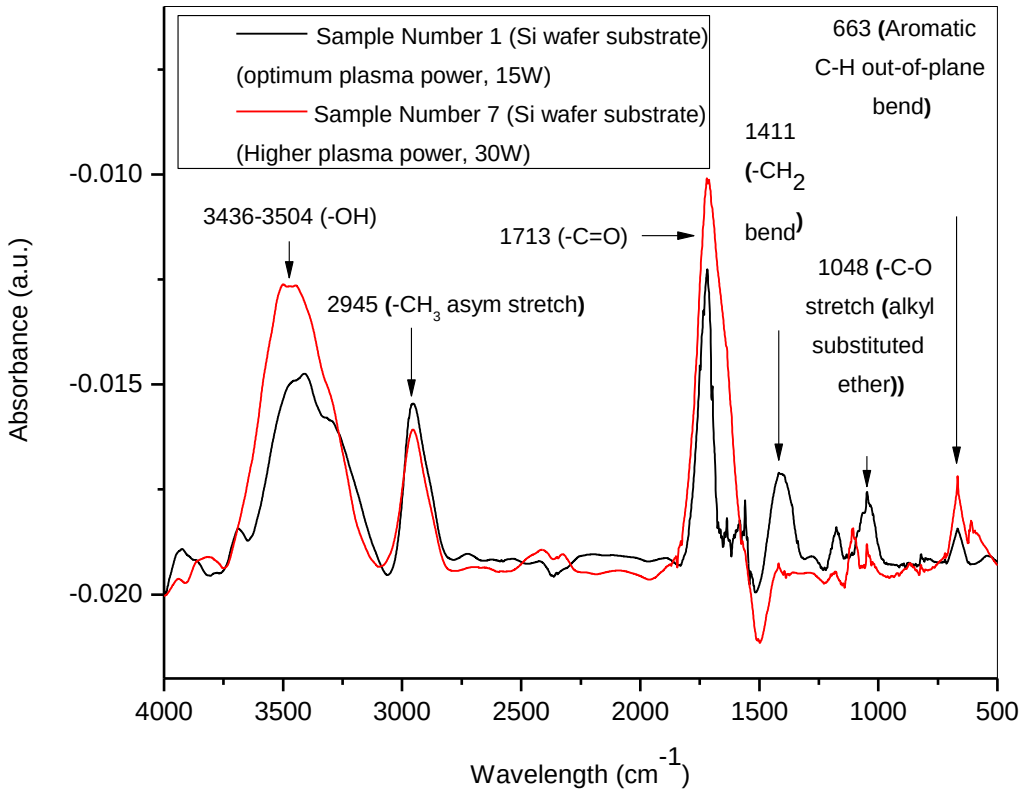

Figure 41| The effect of increasing the plasma power on the FTIR peak intensities of NTP deposited Terpinene-4-ol thin film on Silicon wafer substrate

Increasing the plasma power beyond the optimum power value, increases the electron density in the plasma leading to greater likelihood of monomer fragmentation due to the electron impacts [115]. The number of functional groups as a result reduces due to greater monomer fragmentation. On the contrally, deposition at lower powers reduces monomer fragmentation, which results in deposition of relatively intact monomer molecules on the substrates [116]. As it can be seen in **Figure 41**, using optimized plasma power preserves the $–CH_2$ functional group and the –C–O functional group. Increasing the plasma power reduces these functional groups. In a similar study on the exploitation of the reactor geometry to manipulate the properties of plasma polymerized acrylic acid thin films, increasing the plasma power leads to increased fragmentation of acrylic acid monomer molecules reducing the carboxyl group concentrations [117].

An extra, well resolved, functional group (–C=C–) was observed in the FTIR spectrum of plasma polymerized Terpinene-4-ol when the substrate was changed from the conductive Silicon wafer substrate to the non-conductive KBr substrate.

The effect of varying the argon working gas flow rate on the FTIR peak intensities of NTP deposited Terpinene-4-ol thin film on KBr substrate was also investigated (**Figure 42**) and this formed the first set of preliminary NTP operating parameters to be optimized (**SET I**, Sample Number 1, Sample Number 2 and Sample Number 3, **Table 10**).

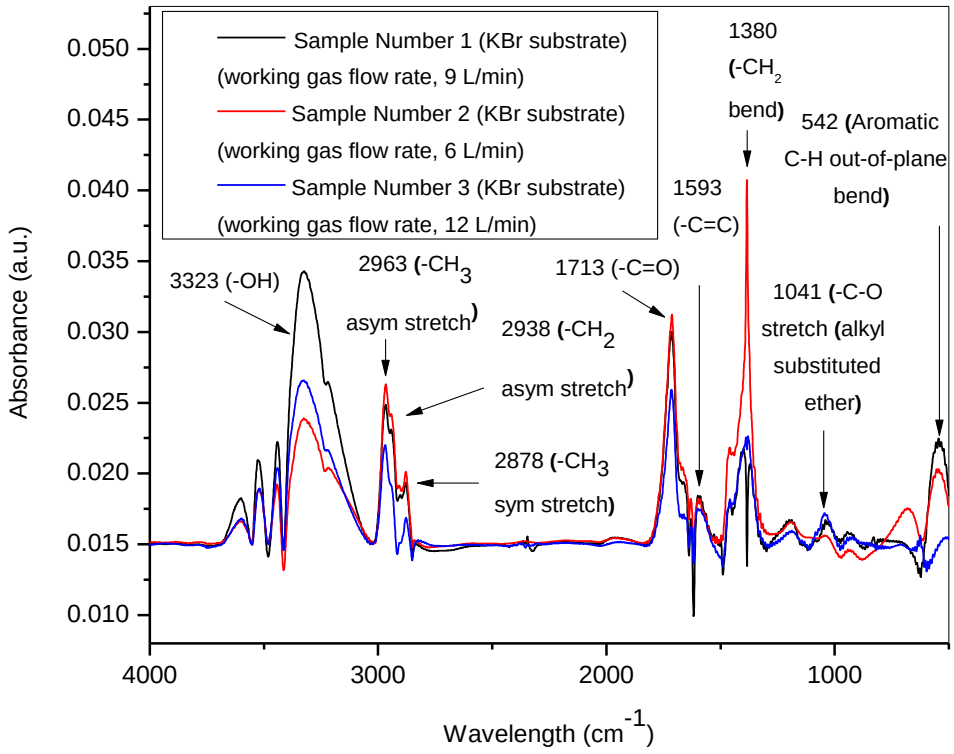

Figure 42| The effect of varying the argon working gas flow rate on the FTIR peak intensities of NTP deposited Terpinene-4-ol on KBr substrate

As was seen previously, increasing the Ar working gas flow rates generally decreases the intensity of the observed peaks. Increasing the Ar carrier gas flow rate from 6 L/min to 12 L/min **(Figure 42)** decreases the FTIR peak intensities of the –OH stretching vibration, $–CH_3$ asymmetric stretching vibration, $–CH_2$ asymmetric stretching vibration, $–CH_3$ symmetric stretching vibration, –C=O stretching vibration, –C=C– stretching vibration, $–CH_2$ bending vibration and –C–O stretching vibration. The well resolved –C=C– stretching vibration at 1593 cm^{-1} can also be seen **(Figure 42)**.

The effect of varying the distance between the substrate and the plasma jet nozzle on the FTIR peak intensities of NTP deposited Terpinene-4-ol thin film on KBr substrate was also investigated **(Figure 43)** and this formed the second set of preliminary NTP operating parameters to be optimized **(SET J,** Sample Number 1 and Sample Number 4, **Table 11)**.

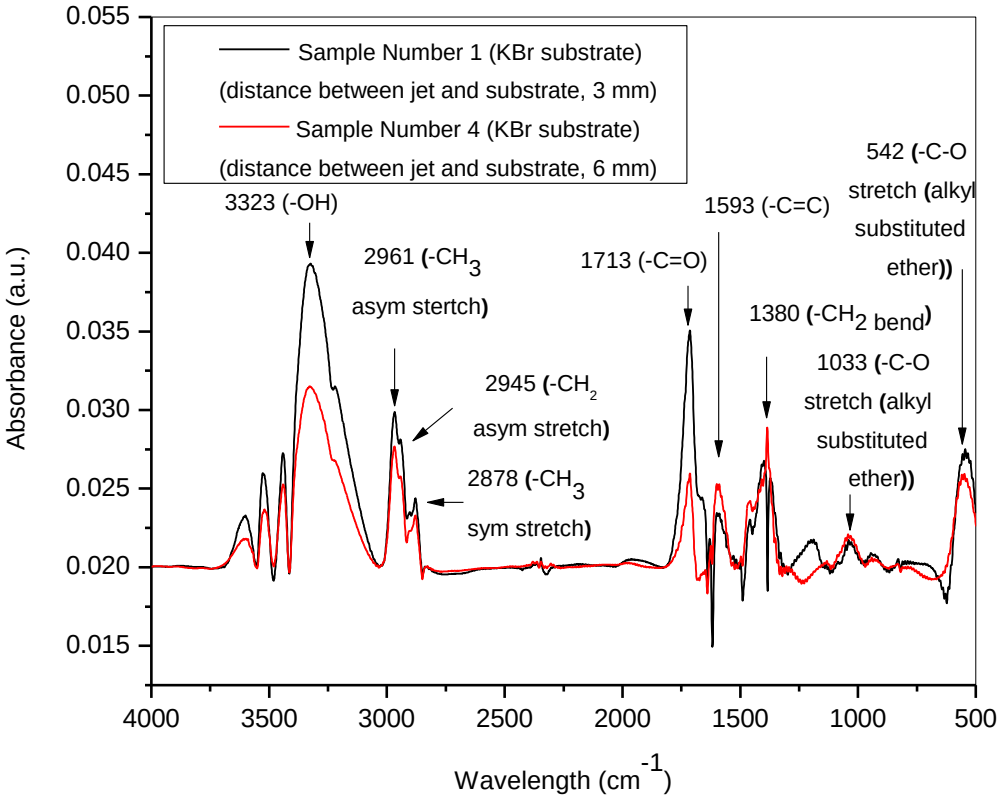

Figure 43| The effect of varying the distance between the substrate and the plasma jet nozzle on the FTIR peak intensities of NTP deposited Terpinene-4-ol on KBr substrate

As seen previously, increasing the distance between the substrate and the plasma jet nozzle up to but not exceeding the optimum distance generally increases the intensity of the observed peaks. Increasing the distance between the substrate and the plasma jet nozzle from 3 mm to 6 mm increases the intensity of the –C=C– stretching vibration, $–CH_2$ bending vibration and the –C–O stretching vibration. The well resolved –C=C– stretching vibration at 1593 cm^{-1} can also be seen **(Figure 43)**.

The effect of varying the type of cooling gas used (compressed air or compressed nitrogen) on the FTIR peak intensities of NTP deposited Terpinene-4-ol thin film on Si wafer substrate was also investigated **(Figure 44)** and this formed the third set of preliminary NTP operating parameters to be optimized **(SET K,** Sample Number 1 and Sample Number 5, **Table 13)**.

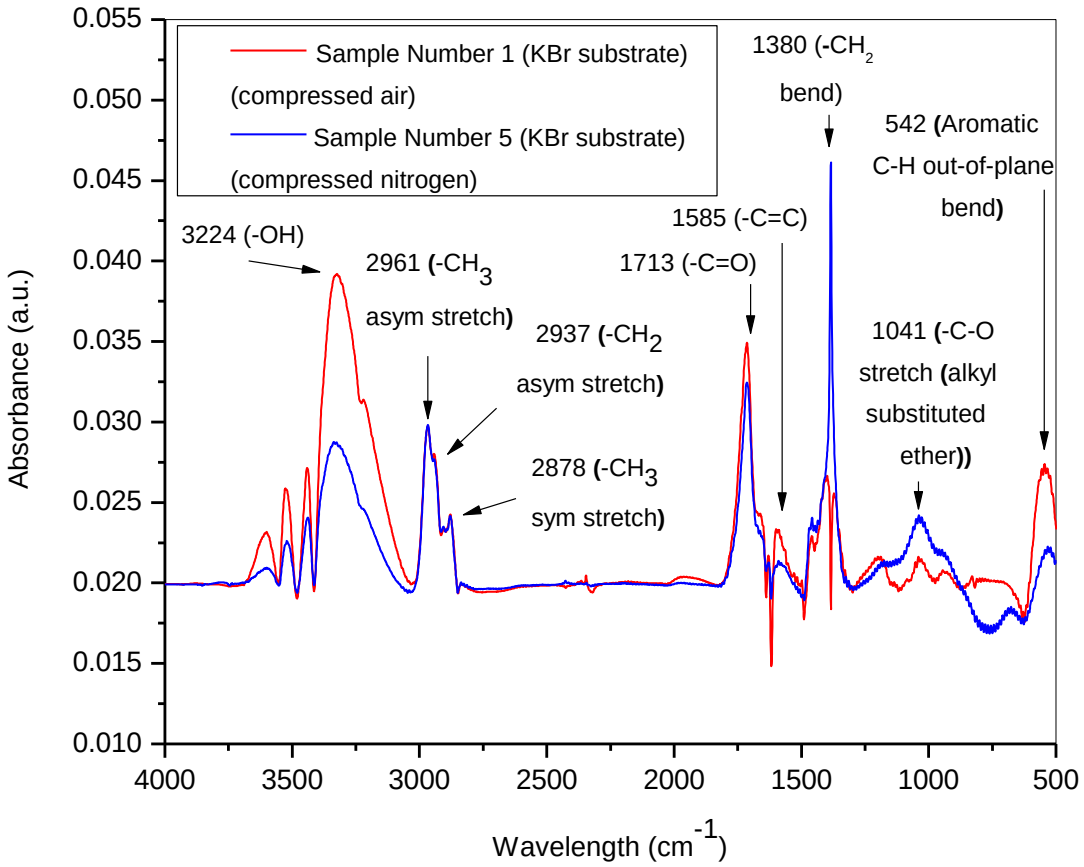

Figure 44| The effect of varying the type of cooling gas (compressed air or compressed nitrogen) used on the FTIR peak intensities of NTP deposited Terpinene-4-ol thin film on KBr substrate

As seen previously, FTIR peaks of the thin films obtained in compressed nitrogen environment were generally higher in intensity than those obtained in compressed air atmosphere. These specific peaks includes the $–CH_3$ asymmetric stretching vibration, $–CH_2$ asymmetric stretching vibration, $–CH_3$ asymmetric stretching vibration, $–CH_2$ bending vibration and the –C=O stretching vibration **(Figure 44)**. The well resolved –C=C– stretching vibration at 1585 cm^{-1} can also be seen **(Figure 44)**.

The effect of varying the NTP source from continuous HV power to pulsed HV power while using compressed air as the type of cooling gas used on the FTIR peak intensities of NTP deposited Terpinene-4-ol thin film on KBr substrate was also investigated **(Figure 45)** and this

formed the fourth set of preliminary NTP operating parameters to be optimized **(SET L,** Sample Number 1 and Sample Number 6, **Table 13)**.

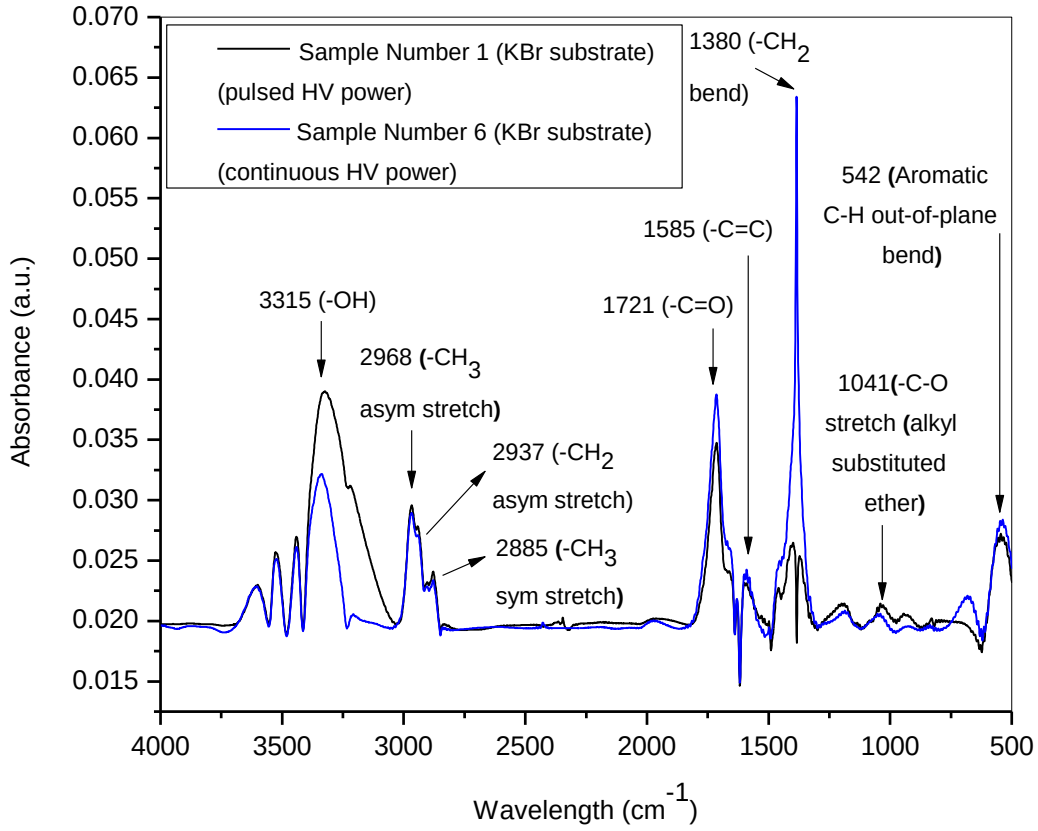

Figure 45| The effect of varying the NTP source from continuous HV power to pulsed HV power while using compressed air as the type of cooling gas used on the FTIR peak intensities of NTP deposited Terpinene-4-ol thin film on KBr substrate.

As seen previously, pulsing ensures congruent transfer of the target material to the substrate. As seen in **Figure 45**, pulsing preserves better the –C=O, –C=C-, $–CH_2$ and the C–H functional groups. The well resolved –C=C– stretching vibration at 1585 cm^{-1} can also be seen **(Figure 45)**.

The effect of increasing the plasma power on the NTP deposited Terpinene-4-ol thin film on

KBr substrate was also investigated **(Figure 46)** and this formed the fifth set of preliminary NTP operating parameters to be optimized **(SET M,** Sample Number 1 and Sample Number 7, **Table 14)**.

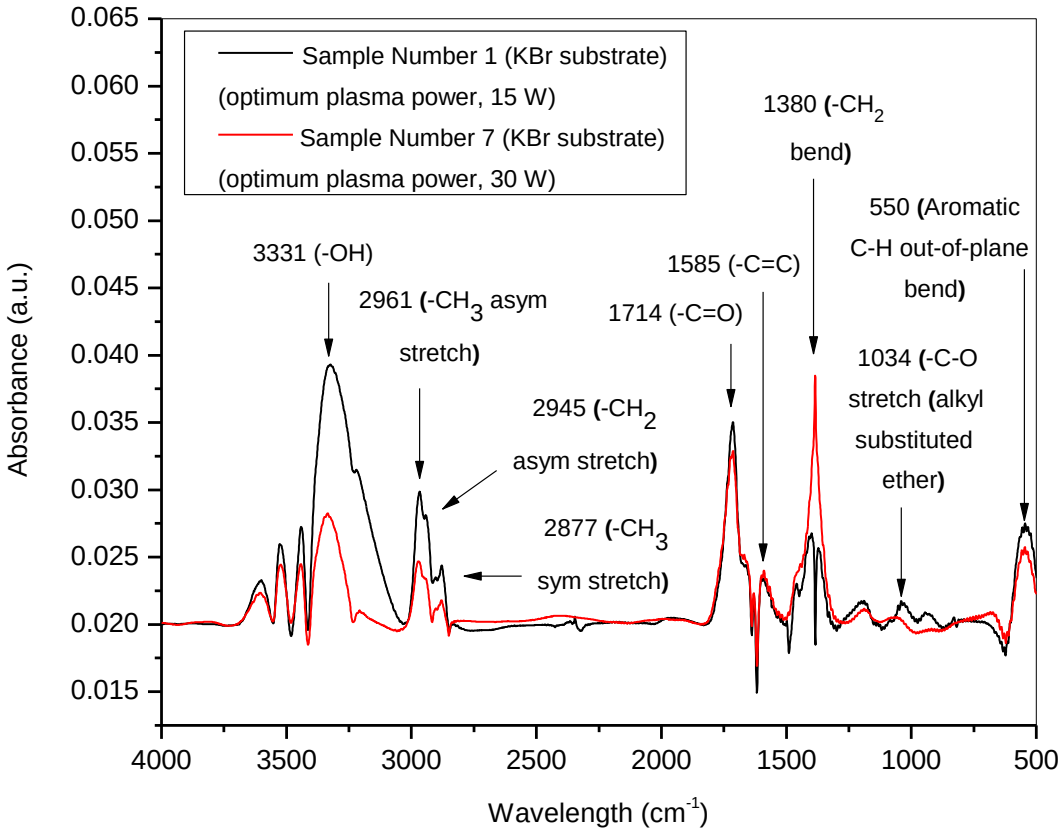

Figure 46| The effect of increasing the plasma power on the FTIR peak intensities of NTP deposited Terpinene-4-ol thin film on Silicon wafer substrate

As seen previously, increasing the plasma power beyond the optimum power value increases the electron density in the plasma leading to greater likelihood of monomer fragmentation due to the electron impacts. As seen in **Figure 46**, increasing the plasma power decreases the intensity of the –OH stretching vibration, $–CH_3$ asymmetric stretching vibration, $–CH_2$ asymmetric stretching vibration and the aromatic C–H out-of-plane bending vibration. The well resolved –C=C– stretching vibration at 1585 cm^{-1} can also be seen **(Figure 46)**.

The comparison between the FTIR spectra of NTP deposited Terpinene-4-ol thin film on Si wafer substrate and the FTIR spectra of NTP deposited Terpinene-4-ol thin film on KBr substrate is also demonstrated in Appendix section (**Appendix K** and **Appendix L**).

The FTIR spectra of NTP deposited Terpinene-4-ol thin film was also compared to the FTIR spectra of the corresponding precursor monomer (reference spectrum). This comparison is shown in **Figure 33c** and **Figure 33d**. The IR band positions and attributions of Terpinene-4-ol precursor monomer was used as a base for the interpretation of the NTP deposited Terpinene-4-ol thin films. Hence, it appeared that Terpinene-4-ol precursor monomer structure seemed to be well-retained in the NTP deposited Terpinene-4-ol thin film as the -OH stretching band, methyl stretching band, C-H stretching band and the C-H bending vibration were detected.

The optimized NTP operating parameters that gave the highest intensity of the targeted functional groups in the NTP deposited Terpinene-4-ol thin films are shown in **Table 17**.

The third precursor monomer that was plasma polymerized using NTP to form a thin film was (Diethyl amino) ethyl methacrylate ((Diethyl amino) ethyl methacrylate thin film). The precursor monomer ((Diethyl amino) ethyl methacrylate) flow rate based on the selected value of the argon carrier gas flow rate and other selected NTP parameters is shown in **Table 1**. (Diethyl amino) ethyl methacrylate was plasma polymerized using NTP jet into the corresponding (Diethyl amino) ethyl methacrylate thin film using a set of preliminary NTP operating parameters (**SET N**, Sample Number 1 and Sample Number 2, **Table 15**).

The general FTIR spectra of NTP deposited (Diethyl amino) ethyl methacrylate thin film is shown in **Figure 47**.

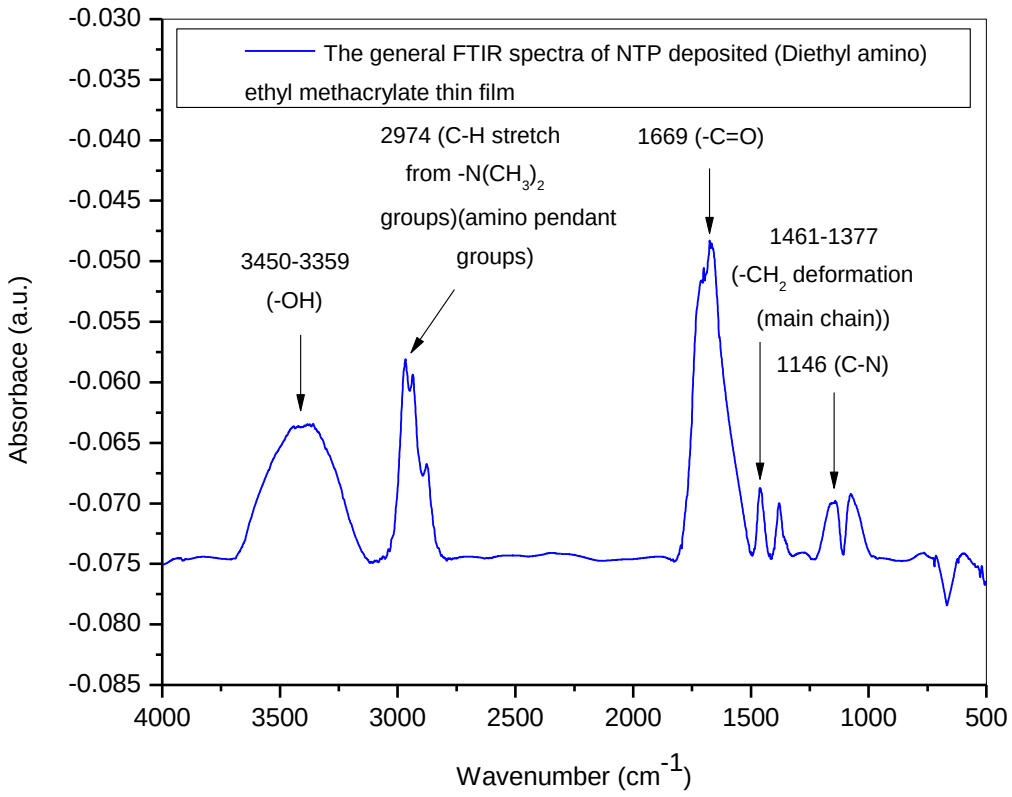

Figure 47| The general FTIR spectra of NTP deposited (Diethyl amino) ethyl methacrylate thin film

The band around 3450-3359 cm^{-1} can be associated to N–H vibrations. The next band around 2974 cm^{-1} can be referred to as amino pendant groups related to the C–H stretching vibration of the -$N(CH_3)_2$ functional group [31]. The peak around 1669 cm^{-1} can be attributed to the –C=O bonds. The band around 1461-1377 cm^{-1} can be attributed to –CH_2 deformations of the main chain. The band at 1146 cm^{-1} can be attributed to the C–N stretching vibration [31]. The summary of the general FTIR peak assignments of NTP deposited (Diethyl amino) ethyl methacrylate thin film are summarized in **Table 19C**.

To optimize the NTP operating parameters, the FTIR peak intensities of the targeted functional groups was used as the yardstick. The optimization process was achieved by investigating the effects of varying the NTP operating parameters on the chemical composition of the plasma deposited (Diethyl amino) ethyl methacrylate thin films. These included varying the NTP power

source from continuous RF power to pulsed RF power.

The effect of varying the NTP source from continuous HV power to pulsed HV power while using compressed air as the type of cooling gas used on the FTIR peak intensities of NTP deposited (Diethyl amino) ethyl methacrylate on Silicon wafer substrate was investigated **(Figure 48)** and this formed the first and the only set of preliminary NTP operating parameters to be optimized **(SET N,** Sample Number 1 and Sample Number 2, **Table 15)**. As seen previously, pulsing ensures congruent transfer of the target material to the substrate. As seen in **Figure 48**, pulsing produces sharp and well resolved C-H functional groups belonging to the amino pendant groups.

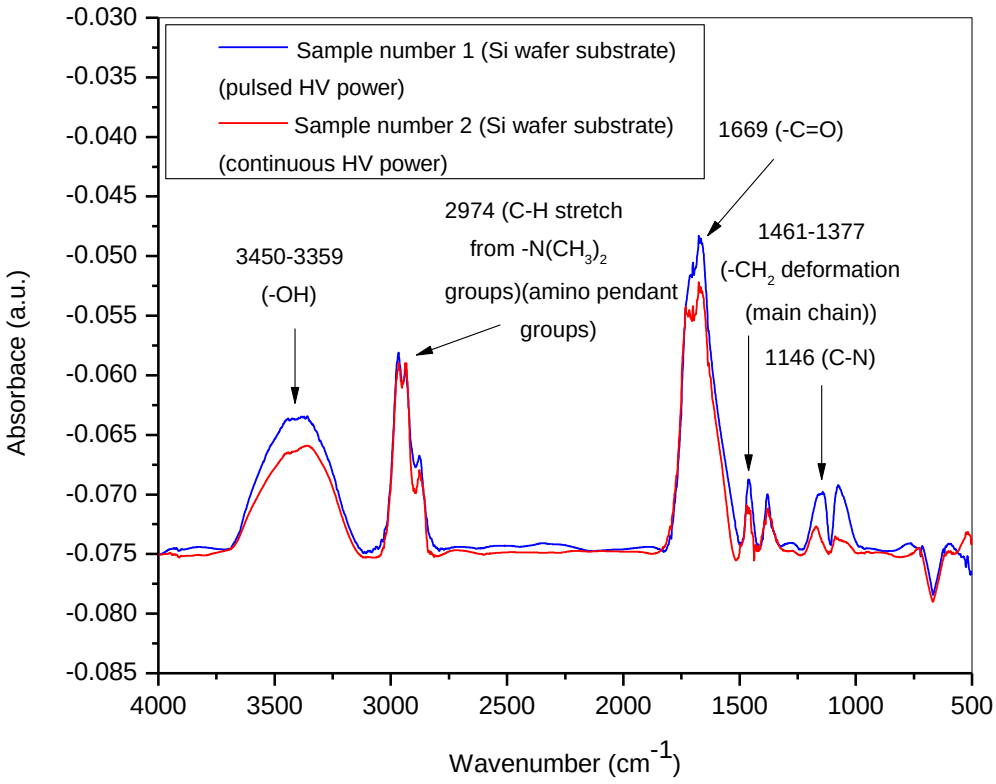

Figure 48| The effect of varying the NTP source from continuous HV power to pulsed HV power while using compressed air as the type of cooling gas used on the FTIR peak intensities of NTP deposited (Diethyl amino) ethyl methacrylate thin film on Silicon wafer substrate

An extra, well resolved, functional group (=C-H) was observed in the FTIR spectra of plasma polymerized (Diethyl amino) ethyl methacrylate when the substrate was changed from the conductive silicon wafer substrate to the non-conductive KBr substrate **(Figure 49)**. As seen previously, pulsing produces sharp and well resolved C-H functional groups belonging to the amino pendant groups. As seen in **Figure 49**, pulsing produces sharp and well-resolved -C=O stretching vibration and the =C-H stretching vibration.

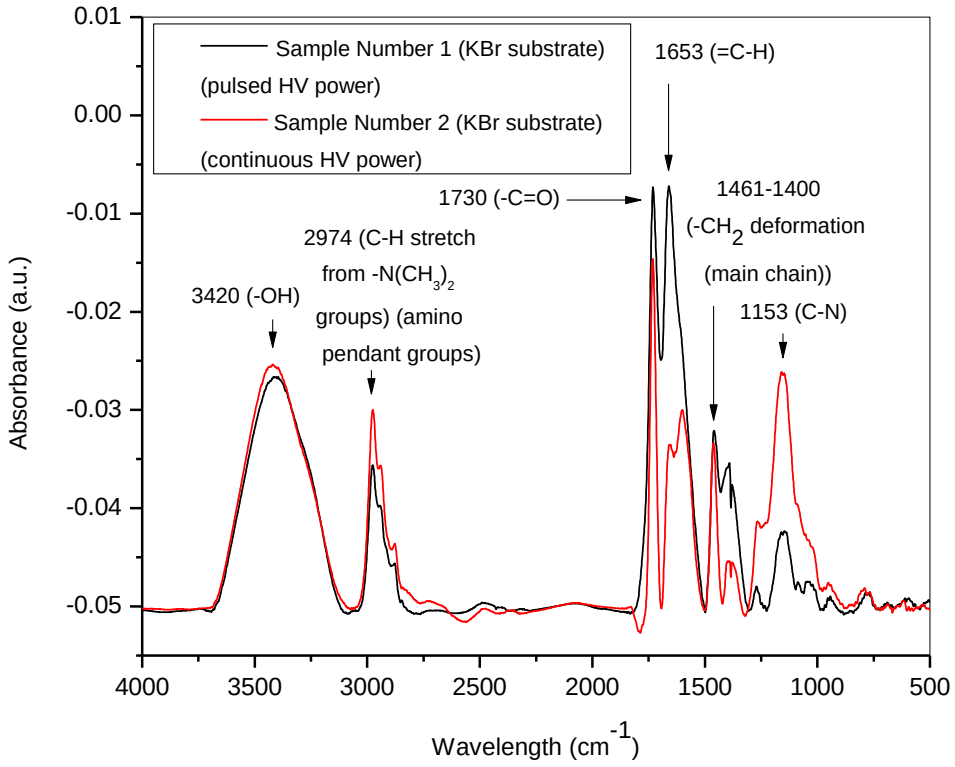

Figure 49| The effect of varying the NTP source from continuous HV power to pulsed HV power while using compressed air as the type of cooling gas used on the FTIR peak intensities of NTP deposited (Diethyl amino) ethyl methacrylate thin film on KBr substrate

The FTIR spectra of NTP deposited (Diethyl amino) ethyl methacrylate thin film was also compared to the FTIR spectra of the corresponding precursor monomer (reference spectrum). This comparison is shown in **Figure 34e** and **Figure 34f**. The IR band positions and attributions of (Diethyl amino) ethyl methacrylate precursor monomer was used as a base for the

interpretation of the NTP deposited (Diethyl amino) ethyl methacrylate thin films. Hence, it appeared that 2-ethyl-2-oxazoline precursor monomer structure seemed to be well retained in the NTP deposited (Diethyl amino) ethyl methacrylate thin film as the -OH stretching band, C-H stretching band from the amino pendant groups, =C-H stretching vibration and the C-N stretching vibration. Finally, from the increase in the intensity of the C-H stretching vibration from the $-N(CH_3)_2$ groups (amino pendant groups), it was assumed to a lesser extent that the plasma polymerisation induced the formation of secondary chemical groups.

The optimized NTP operating parameters that gave the highest intensity of the targeted functional groups in the NTP deposited (Diethyl amino) ethyl methacrylate thin films are shown in **Table 17**.

The fourth precursor monomer that was plasma polymerized using NTP to form a thin film was Bis(dimethyl amino) ethyl methacrylate (Bis(dimethyl amino) dimethyl silane thin film). The precursor monomer flow rate based on the carrier gas flow rate and other parameters is shown in **Table 1**. Bis(dimethyl amino) dimethyl silane was plasma polymerized using NTP jet into the corresponding Bis(dimethyl amino) dimethyl silane thin film using a single set of already optimized NTP operating parameters (**SET O**, Lone sample, **Table 16**).

The general FTIR spectra of NTP deposited Bis(dimethyl amino) dimethyl silane thin film is shown in **Figure 50**.

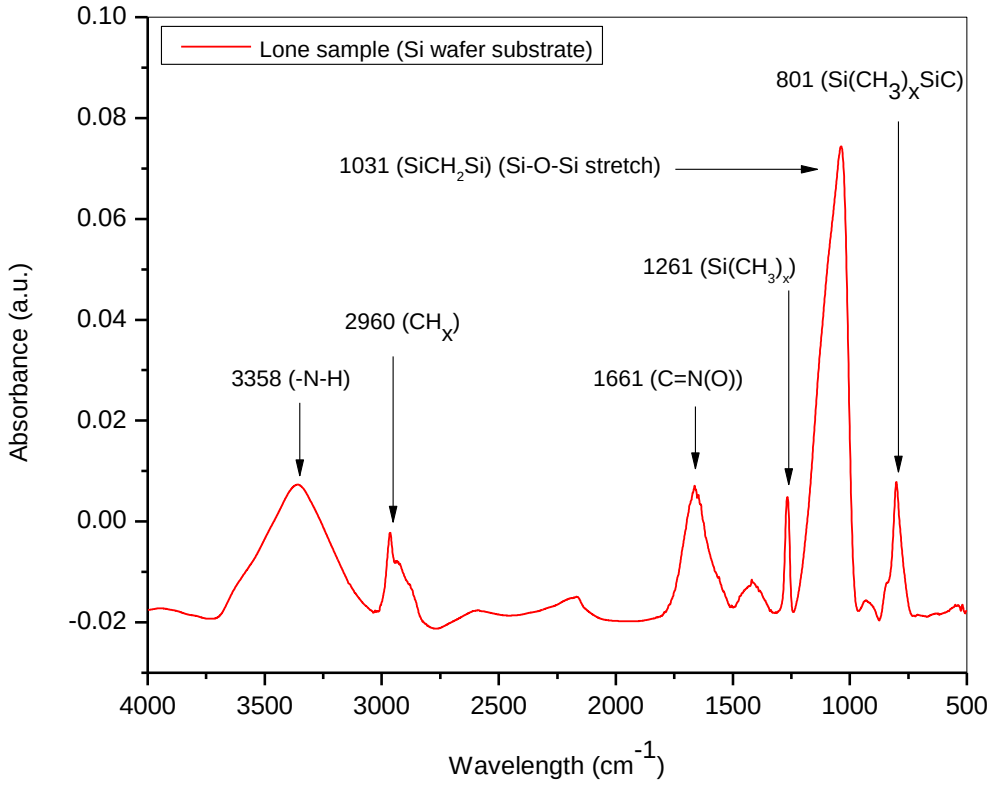

Figure 50| The general FTIR spectra of NTP deposited Bis(dimethyl amino) dimethyl silane thin film on Silicon wafer substrate

The band around 3358 cm^{-1} can be associated to the -N-H stretching vibration. The next band around 2960 cm^{-1} can be reffered to as the CH_x groups [110]. The band around 1661 cm^{-1} can be attributed to the C=N(O) stretching vibration. The band at 1261 cm^{-1} can be attributred to the $Si(CH_3)_x$ vibration. The peak around 1031 cm^{-1} can be associated to the $SiCH_2Si$ vibration. The peak around 801 cm^{-1} can be associated to the $Si(CH_3)_xSiC$ vibration [110].

An extra, well resolved, functional group ($-CH_3$ bending vibration) was observed in the FTIR spectra of plasma polymerized Bis(dimethyl amino) dimethyl silane thin film when the substrate was changed from the conductive silicon wafer substrate to the non-conductive KBr substrate **(Figure 51)**.

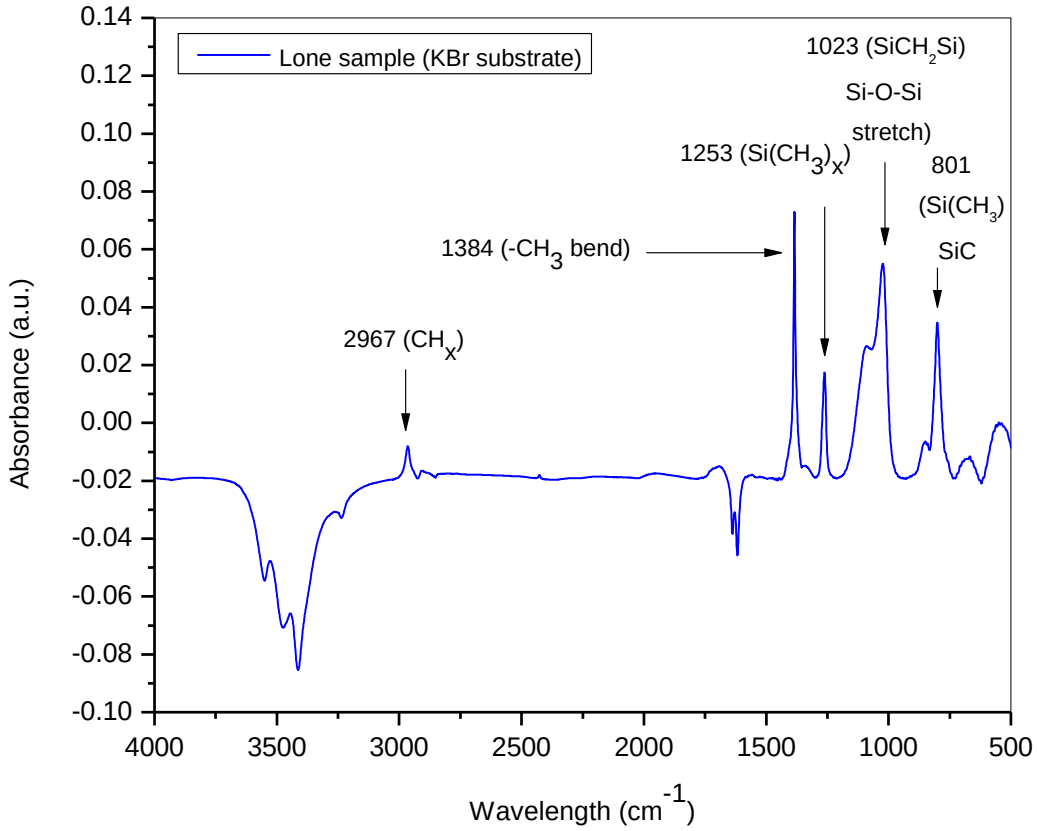

Figure 51| The general FTIR spectra of NTP deposited Bis(dimethyl amino) dimethyl silane thin film on Silicon wafer substrate

The FTIR spectra of Bis (dimethyl amino) dimethyl silane thin film was also compared to the FTIR spectra of the corresponding precursor monomer (reference spectrum). This comparison is shown in **Figure 35g** and **Figure 35h**. The IR band positions and attributions of 2-ethyl-2-oxazoline precursor monomer was used as a base for the interpretation of the NTP deposited Bis(dimethyl amino) dimethyl silane thin films. Hence, it appeared that Bis(dimethyl amino) dimethyl silane thin film as the N-H functional groupsm $SiCH_2Si$ functional groups and the $Si(CH_3)_xSiC$ functional groups were detected.

The already optimized NTP operating parameters used in the deposition of Bis(dimethyl amino) dimethyl silane thin films is shown in **Table 17**.

4.2 Surface wettability and energy analysis

Surface wettability can affect bacteria and cell adhesivity and conditions of cell proliferation [118]. The static water contact angle was measured as an indicator of the coating's wettability. A small water contact angle on the solid surface means that the surface is hydrophilic and possesses a large surface energy; conversely, a large contact angle indicates a hydrophobic surface with low surface energy [119].

The column graph with error bars of the water contact angle of the first NTP polymerized thin film (plasma polymerized POx thin film from the corresponding organic POx precursor monomer) using optimized NTP operating parameters (**SET G**, Sample Number 2B, **Table 8**) is shown in **Figure 52a**. The water contact angle of one of the three replicate measurements of the reference (clean, unmodified silicon wafer substrate) was 43 ± 2 ° (**Figure 52b**), showing its character as being relatively hydrophilic. The water contact angle of one of the three replicate measurements of the NTP deposited POx thin film on Silicon wafer substrate using the optimized NTP operating parameters was 24 ± 10 ° (**Figure 52c)**.

The decrease in contact angle of the reference from 43 ± 2 ° to 24 ± 10 °, when the POx thin films were deposited using NTP means that the POx thin films can be considered as being hydrophilic in character. The polar character of several functional groups contained in the POx thin films such as the hydroxyl groups and the amino groups contributes to their higher ionic solvation with water molecules. The observed WCA values for the reference and the determination that the NTP deposited POx thin films were hydrophilic in character corroborates previously published data [120].

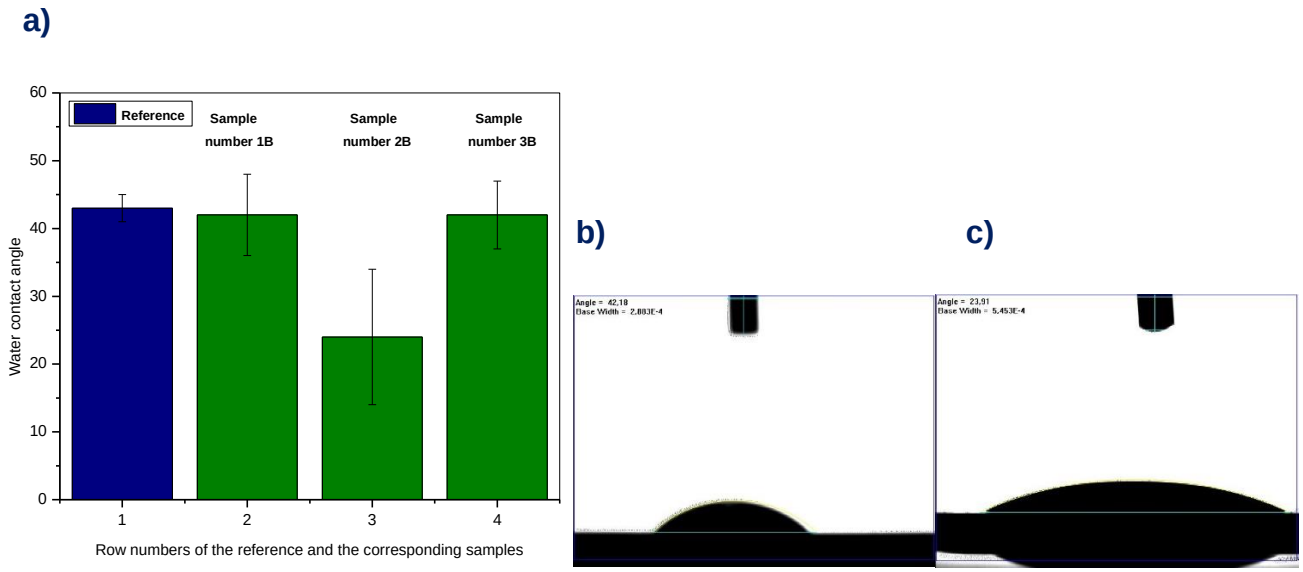

Figure 52| The column graph with error bars of the water contact angle of NTP deposited POx thin film and the corresponding water contact angle diagrams. **a)** The column graph with error bars of the water contact angle of the first NTP deposited thin film (plasma deposited POx thin film) using optimized NTP operating parameters. **b)** The water contact angle diagram of one of the three replicate measurements of the reference (clean, unmodified silicon wafer substrate). **c)** The water contact angle diagram of one of the three replicate measurements of the NTP deposited POx thin film on Silicon wafer substrate using the optimized NTP operating parameters. Error bars represent the standard deviation of the mean (n=3)

The column graph with error bars of the water contact angle of the second NTP polymerized thin film (plasma polymerized Terpinene-4-ol thin film from the corresponding organic Terpinene-4-ol precursor monomer) using optimized NTP operating parameters (**SET M**, Sample Number 7, **Table 14**) is shown in **Figure 53a**. The water contact angle of one of the three replicate measurements of the reference (clean, unmodified silicon wafer substrate) was 53 ± 4 ° (**Figure 53b**), showing its character as being relatively hydrophilic. The water contact angle of one of the three replicate measurements of the NTP deposited POx thin film on Silicon wafer substrate using the optimized NTP operating parameters was 16 ± 8 ° (**Figure 53c)**. The great decrease in the contact angle of the reference from 53 ± 4 ° to 16 ± 8°, when the Terpinene-4-ol thin films were deposited using NTP means that the Terpinene-4-ol thin films

can be considered as being hydrophilic in character.

The polar character of several functional groups contained in the Terpinene-4-ol thin films such as the hydroxyl groups and the carbonyl groups contributes to their higher ionic solvation with the water molecules. The observed WCA values for the reference and the determination that the NTP deposited Terpinene-4-ol thin films were hydrophilic in character corroborates previously data [97].

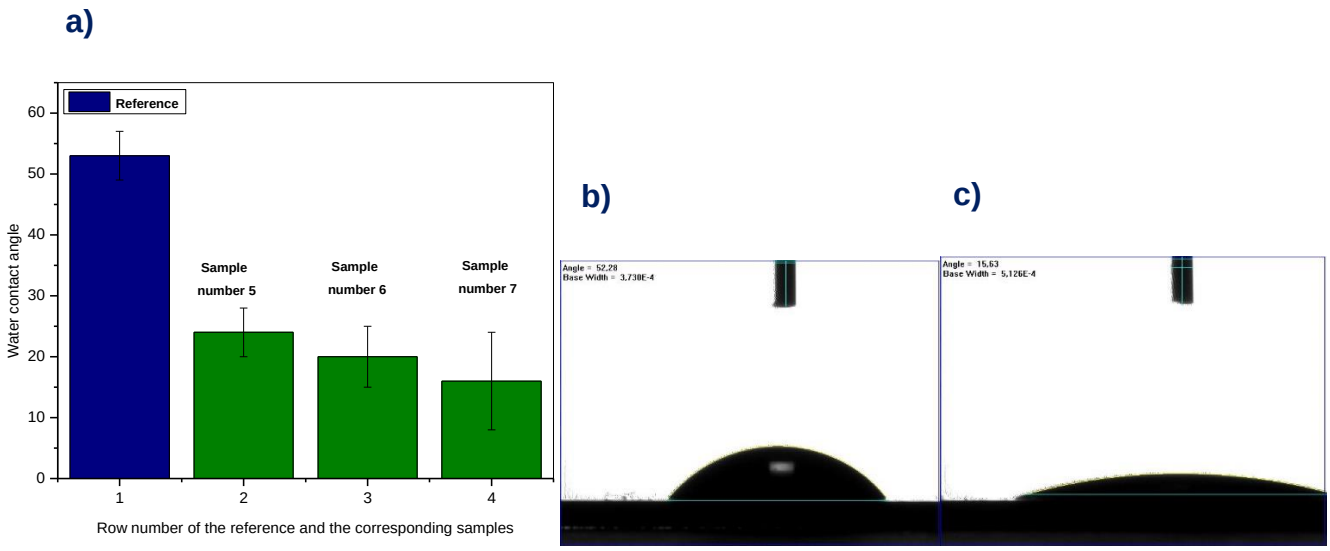

Figure 53| The column graph with error bars of the water contact angle of NTP deposited Terpinene-4-ol thin film and the corresponding water contact angle diagrams. **a)** The column graph with error bars of the water contact angle of the second NTP deposited thin film (plasma deposited Terpinene-4-ol thin film). **b)** The water contact angle diagram of one of the three replicate measurements of the reference (clean, unmodified silicon wafer substrate). **c)** The water contact angle diagram of one of the three replicate measurements of the NTP deposited Terpinene-4-ol thin film on silicon wafer substrate using the optimized NTP operating parameters. Error bars represent the standard deviation of the mean (n=3)

The column graph with error bars of the water contact angle of the third NTP polymerized thin

film (plasma polymerized (Diethyl amino) ethyl methacrylate thin film from the corresponding organic (Diethyl amino) ethyl methacrylate precursor monomer) using optimized NTP operating parameters (**SET N**, Sample Number 1, **Table 15**) is shown in **Figure 54a**. The water contact angle of one of the three replicate measurements of the reference (clean, unmodified silicon wafer substrate) was 49 ± 2 ° (**Figure 54b**), showing its character as being relatively hydrophilic.

The water contact angle of one of the three replicate measurements of the NTP deposited ((Diethyl amino) ethyl methacrylate thin film) on Silicon wafer substrate was 17 ± 3 ° (**Figure 54c)**. The decrease in the contact angle of the reference from 49 ± 2 ° to 17 ± 3 °, when the (Diethyl amino) ethyl methacrylate thin films were deposited using NTP means that the (Diethyl amino) ethyl methacrylate thin films can be considered as being hydrophilic in character. The polar character of several functional groups contained in the (Diethyl amino) ethyl methacrylate thin films such as the hydroxyl groups, amino groups and the carbonyl groups contributes to their higher ionic solvation with the water molecules [31].

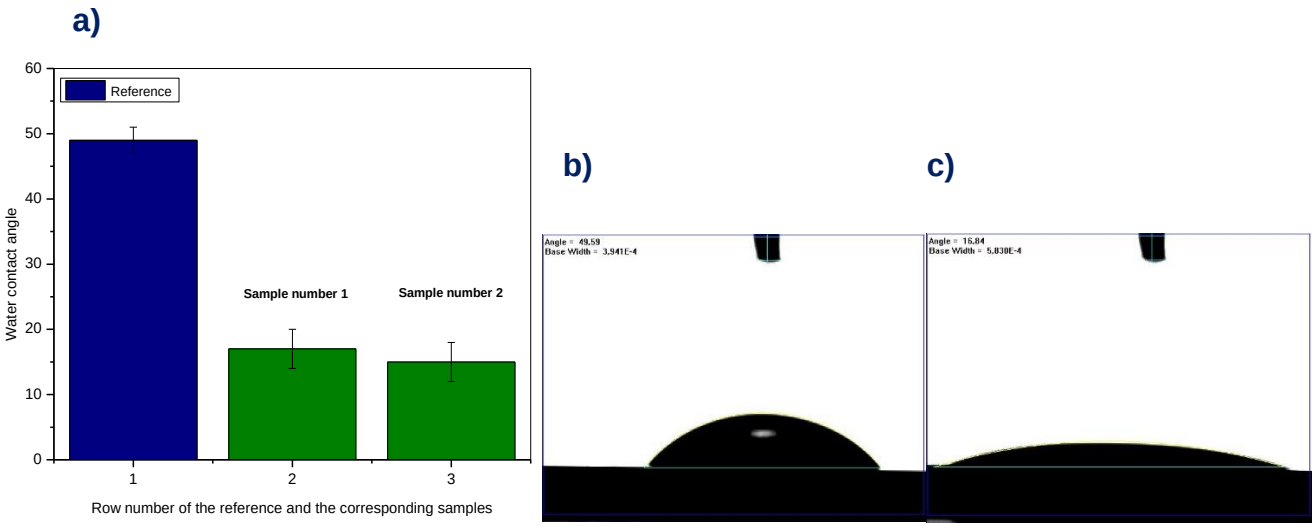

Figure 54| The column graph with error bars of the water contact angle of NTP deposited (Dimethyl amino) ethyl methacrylate thin film and the corresponding water contact angle diagrams **a)** The column graph with error bars of the water contact angle of the third NTP deposited thin film (plasma deposited (Dimethyl amino) ethyl methacrylate thin film) **b)** The water contact angle diagram of one of the three replicate measurements of the reference (clean, unmodified silicon wafer substrate) **c)** The water contact angle diagram of one of the three

replicate measurements of the NTP deposited ((Dimethyl amino) ethyl methacrylate thin film) on silicon wafer substrate using the optimized NTP operating parameters. Error bars represent the standard deviation of the mean (n=3)

The column graph with error bars of the water contact angle of the fourth NTP polymerized thin film (plasma polymerized Bis(dimethyl amino) dimethyl silane thin film from the corresponding organic-inorganic Bis(dimethyl amino dimethyl silane precursor monomer) using optimized NTP operating parameters (**SET O**, Lone sample, **Table 16**) is shown in **Figure 55a**. The water contact angle of one of the three replicate measurements of the reference (clean, unmodified silicon wafer substrate) was 64 ± 2 ° (**Figure 55b**), showing its character as being relatively hydrophilic. The water contact angle value of one of the three replicate measurements of the NTP deposited Bis(dimethyl amino) dimethyl silane thin film on Silicon wafer substrate was 85 ± 5 ° (**Figure 55c)**.

The increase in the contact angle of the reference from 64 ± 2 ° to 85 ± 5 °, when the organic-inorganic Bis(dimethyl amino) dimethyl silane thin films were deposited using NTP means that the (Diethyl amino) ethyl methacrylate thin films can be considered as being slightly hydrophobic in character. The polar character is contributed by the amino groups and the cyano groups while the non-polar character that usually overrides the effects of the polar character is contributed by the high number of methyl groups. The observed WCA values for the reference and the determination that the NTP deposited Bis(dimethyl amino) dimethyl silane thin films were hydrophobic corroborates previously published data [121].

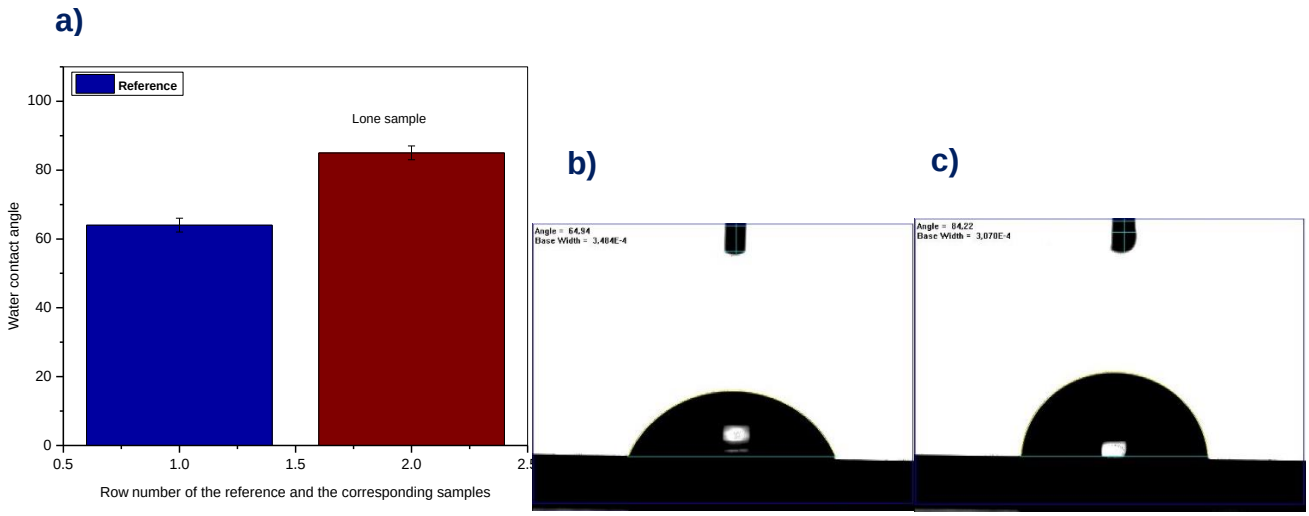

Figure 55| The column graph with error bars of the water contact angle of NTP deposited (Dimethyl amino) ethyl methacrylate thin film and the corresponding water contact angle diagrams. Bis(dimethyl amino) dimethyl silane thin film and the corresponding water contact angle diagrams. **a)** The column graph with error bars of the water contact angle of the third NTP deposited thin film (plasma deposited (Dimethyl amino) ethyl methacrylate thin film. **b)** The water contact angle diagram of one of the three replicate measurements of the reference (clean, unmodified silicon wafer substrate). **c)** The water contact angle diagram of one of the three replicate measurements of the NTP deposited ((Dimethyl amino) ethyl methacrylate thin film) on silicon wafer substrate using the optimized NTP operating parameters. Error bars represent the standard deviation of the mean (n=3)

The surface energy is the energy associated with the intermolecular forces at the interface between two media, which were between the NTP deposited thin films and liquid on the surface in this study [122]. The surface energy is typically measured by the contact angle of a liquid on a solid surface, and a low contact angle indicates a high surface energy, while a high contact angle indicates a low surface energy of the solid surface in relation to the liquid [122]. The results of the control and the reference groups were determined using contact angle measurements with two liquids, distilled water (DW), which is a polar liquid, and diiodomethane (DM), which is a nonpolar liquid.

The column graphs of the surface energy of the first NTP polymerized thin film (plasma polymerized POx thin film) using optimized NTP operating parameters (**SET G**, Sample Number 2B, **Table 8**) is shown in **Figure 56**. The total surface energy value of the reference (clean, unmodified silicon wafer substrate) was 62.36 mN/m with its components being the dispersive component having the surface energy value of 39.61 mN/m and its polar component having the surface energy value of 22.75 mN/m (**Figure 56**). The total surface energy of one of the three replicate measurements of the NTP deposited POx thin film was 71.61 mN/m with its components being the dispersive component having the surface energy value of 40.11 mN/m and the polar component having the surface energy value of 31.5 mN/m (**Figure 56)**.

Therefore, the surface energy of the NTP deposited POx thin films, which was calculated according to Owens-Wendt method, increased compared to that in the untreated reference samples. The surface energy calculations confirm the increased surface polarity for the NTP deposited POx thin films. The dispersive component (γ_{SD}) does not change significantly, while the polar component (γ_{SP}) increases by about 9 units, and thus, in total an increased surface energy revealing that the NTP deposited POx thin films were hydrophilic. The observed surface energy values for the reference and the the NTP deposited POx thin films corroborates previously published data [120].

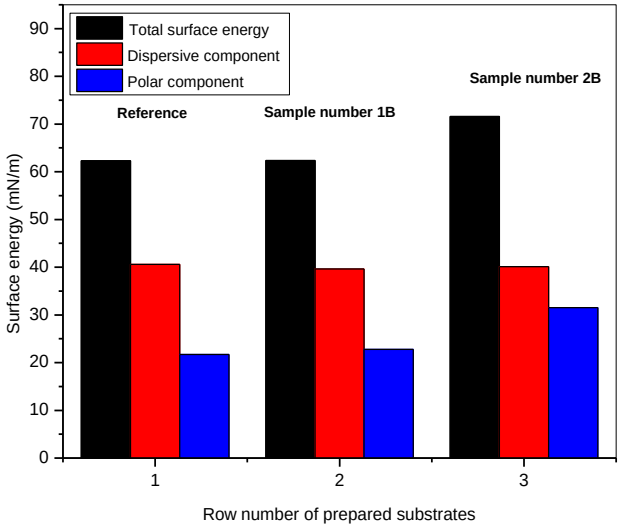

Figure 56| Column graphs of the surface energy measurements of the NTP deposited POx thin film under selected final plasma operating parameters

The column graphs of the surface energy of the second NTP polymerized thin film (plasma polymerized Terpinene-4-ol thin film) using optimized NTP operating parameters (**SET M**, Sample Number 7, **Table 14**) is shown in **Figure 57**. The total surface energy value of the reference (clean, unmodified silicon wafer substrate) was 56.3 mN/m with its components being the dispersive component having the surface energy value of 40.11 mN/m and its polar component having the surface energy value of 16.19 mN/m (**Figure 57**).

Therefore, the surface energy of the NTP deposited Terpinene-4-ol thin films, which was calculated according to Owens-Wendt method, increased compared to that in the untreated reference samples. The surface energy calculations confirm the increased surface polarity for the NTP deposited POx thin films. The dispersive component (γ_{SD}) remains constant, while the polar component (γ_{SP}) increases by about 18 units, and thus, in total an increased surface energy revealing that the NTP deposited Terpinene-4-ol thin films were hydrophilic. The observed surface energy values for the reference and the the NTP deposited Bis(dimethyl amino) dimethyl silane thin films corroborates previously published data [97].

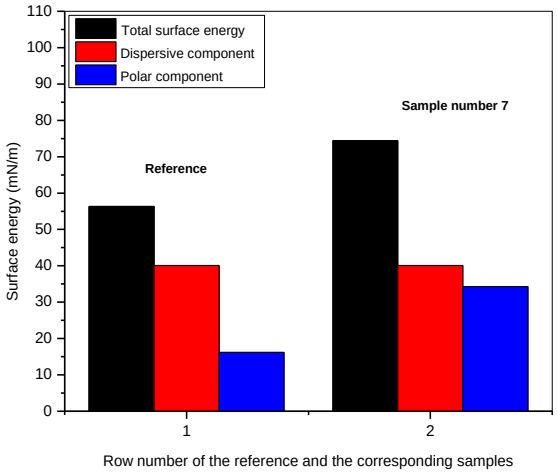

Figure 57| Column graphs of the surface energy measurements of the NTP deposited Terpinene-4-ol thin film under final selected plasma operating parameters

The column graphs of the surface energy of the third NTP polymerized thin film (plasma polymerized (Dimethyl amino) ethyl methacrylate thin film) using optimized NTP operating parameters (**SET N**, Sample Number 1, **Table 15**) is shown in **Figure 58**. The total surface energy value of the reference (clean, unmodified silicon wafer substrate) was 59.69 mN/m with its components being the dispersive component having the surface energy value of 42.03 mN/m and its polar component having the surface energy value of 17.66 mN/m (**Figure 58**). The total surface energy of one of the three replicate measurements of the NTP deposited POx thin film was 75.09 mN/m with its components being the dispersive component of surface energy value of 42.49 mN/m and the polar component of the surface energy value of 32.6 mN/m (**Figure 58)**.

Therefore, the surface energy of the NTP deposited (Dimethyl amino) dimethyl silane thin films thin films, which was calculated according to Owens-Wendt method, increased compared to that in the untreated reference samples. The dispersive component (γ_{SD}) remains almost constant, while the polar component (γ_{SD}) increases by about 15 units, and thus, in total an increased surface energy revealing that the NTP deposited (Dimethyl amino) ethyl methacrylate thin films were hydrophilic. The observed surface energy values for the reference and the NTP deposited Bis(dimethyl amino) dimethyl silane thin films corroborates previously published data [123].

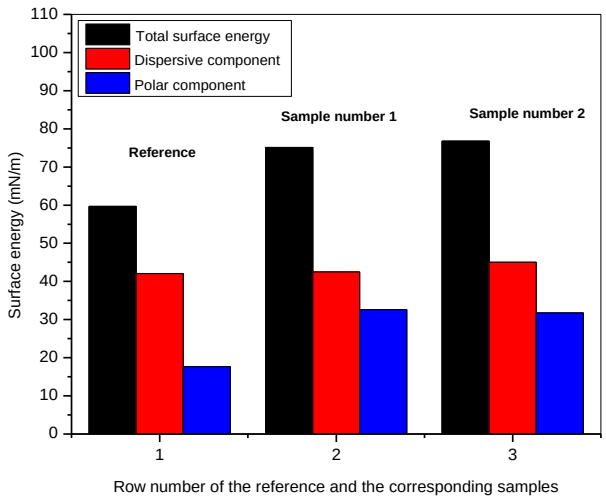

Figure 58| Column graphs of the surface energy measurements of the NTP deposited (Dimethyl amino) ethyl methacrylate thin film under final selected plasma operating parameters

The column graphs of the surface energy of the fourth NTP polymerized thin film (plasma polymerized Bis(dimethyl amino) dimethyl silane thin film) using optimized NTP operating parameters (**SET N**, Sample Number 1, **Table 15**) is shown in **Figure 59**. The total surface energy value of the reference (clean, unmodified silicon wafer substrate) was 50.62 mN/m with its components being the dispersive component having the surface energy value of 40.6 mN/m and its polar component having the surface energy value of 10.02 mN/m (**Figure 59**). The total surface energy of one of the three replicate measurements of the NTP deposited Bis(dimethyl amino) dimethyl silane thin film was 37.21 mN/m with its components being the dispersive component of surface energy value of 34.27 mN/m and the polar component of the surface energy value of 2.937 mN/m (**Figure 59)**.

Therefore, the surface energy of the NTP deposited Bis(dimethyl amino) dimethyl silane thin films, which was calculated according to Owens-Wendt method, increased compared to that in the untreated reference samples. The surface energy calculations confirm the increased non-polar character of the NTP deposited Bis(dimethyl amino) dimethyl silane thin films. The dispersive component (γ_{SD}) does not change significantly, while the polar component (γ_{SP}) decreases by about 8 units, and thus, in total a decrease in the surface energy revealing that the NTP deposited Bis(dimethyl amino) dimethyl silane thin films were hydrophobic. The observed surface energy values for the reference and the the NTP deposited Bis(dimethyl amino) dimethyl silane thin films corroborates previously published data [124].

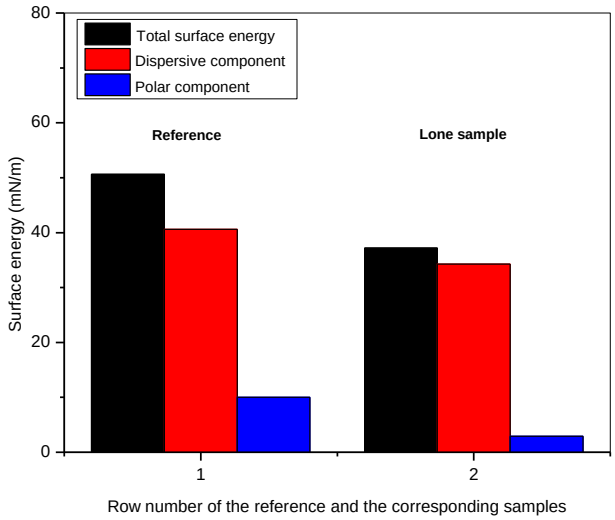

Figure 59| Column graphs of the surface energy measurements of the NTP deposited Bis(dimethyl amino) dimethyl silane thin film under final selected plasma operating parameters

4.3 Antimicrobial properties of the thin films

To evaluate the antimicrobial activities of the NTP deposited antimicrobial thin films (2-ethyl-2-oxazoline thin film, Terpinene-4-ol thin film, (Dimethyl amino) dimethyl silane thin film and Bis(dimethyl amino) dimethyl silane thin film), we challenged them with four typical pathogenic bacteria and one enveloped virus. The pathogenic bacteria used in the antibacterial tests were the Gram-positive *Streptococcus pyogenes*, Gram-positive *Staphylococcus aureus*, Gram-negative *Escherichia coli* and the Gram-negative *Pseudomonas aeruginosa*. The virus used in the antiviral tests was the enveloped Sars covid 2 like virus.

The biocidal efficiencies of the NTP deposited thin films deposited on the four selected substrates are summarized in **Table 20** (determined according to the AATCC test method 100-2004) [125]. The use of CFUs for enumeration is since, in many applications, the presence of CFUs is more relevant than the presence of dead bacteria that are non-culturable [126]. The substrates without the antimicrobial thin films or any other antimicrobial ingredients were used

as the control. The biocidal efficiencies were determined after 1440 minutes of incubation. In the antibacterial tests, both the Gram-positive and the Gram-negative bacteria in the control substrates, exhibited robust growth trend.

The initial populations of *S. pyogenes*, *S. aureus*, *E. coli* and *P. aeruginosa* cells on the HDPE polymer substrate were 5×10^5 CFU/cm^{-2}, 4×10^5 CFU/cm^{-2}, 4×10^5 CFU/cm^{-2} and 2×10^5 CFU/cm^{-2}, respectively. The initial populations of *S. pyogenes*, *S. aureus*, *E. coli* and *P. aeruginosa* cells on the TPU polymer substrate were 6×10^5 CFU/cm^{-2}, 5×10^5 CFU/cm^{-2}, 5×10^5 CFU/cm^{-2} and 1×10^5 CFU/cm^{-2}, respectively. The initial populations of *S. pyogenes*, *S. aureus*, *E. coli* and *P. aeruginosa* cells on the stainless-steel substrate were 3×10^5 CFU/cm^{-2}, 6×10^5 CFU/cm^{-2}, 6×10^5 CFU/cm^{-2} and 2×10^5 CFU/cm^{-2}, respectively. The initial populations of *S. pyogenes*, *S. aureus*, *E. coli* and *P. aeruginosa* cells on the silicon wafer substrate were 3×10^5 CFU/cm^{-2}, 6×10^5 CFU/cm^{-2}, 6×10^5 CFU/cm^{-2} and 2×10^5 CFU/cm^{-2}, respectively. In the antiviral tests, the Sars Covid 2 like virus, after being subjected to both the control substrates and the thin films, did not attach nor proliferate, and therefore, the initial population of the virus was taken to be zero.

2-ethyl-2-oxazoline thin film deposited on HDPE polymer substrate using the NTP jet promoted an ~ 97 %, ~ 93 %, ~ 92 % and ~ 92 % deactivation of *S. pyogenes*, *S. aureus*, *E. coli* and *P. aeruginosa* microbial populations, respectively, with respect to the control. On changing the substrate to TPU polymer, the thin film promoted an ~ 97 %, ~ 89 %, ~ 91 % and ~ 97 % deactivation of *S. pyogenes*, *S. aureus*, *E. coli* and *P. aeruginosa* microbial populations, respectively, with respect to the control. On changing the substrate to stainless steel, the antibacterial thin film promoted an ~ 97 %, ~ 89 %, ~ 91 % and ~ 97 % deactivation of *S. pyogenes*, *S. aureus*, *E. coli* and *P. aeruginosa* microbial populations, respectively, with respect to the control. On changing the substrate to silicon wafer, the antibacterial thin film promoted an ~ 91 %, ~ 86 %, ~ 93 % and ~ 90 % deactivation of *S. pyogenes*, *S. aureus*, *E. coli* and *P. aeruginosa* microbial populations, respectively, with respect to the control.

As observed, the NTP deposited 2-ethyl-2-oxazoline antibacterial thin film possessed high antibacterial activity towards the test bacteria. The thin film was also observed to have generally greater antibacterial activity against the Gram-negative bacteria as opposed to the Gram-positive bacteria. These findings match very well the results reported in Refs. [127]. These findings may be due to the differences in the structure of the bacterial cell wall and the cell membrane which controls the access of different molecules inside the cell and to their sites of action. This suggestion is like the one reported [128]. The type of substrates used ((conductive (stainless steel and silicon) or non-conductive (HDPE and TPU)) in the 2-ethyl-2-oxazoline thin film deposition process did not appear to cause a major difference in the antibacterial activity of the antibacterial thin film. These findings agree with those obtained from the FTIR studies which illustrated similar functional groups, even with change of substrates.

While the complete picture as to why plasma deposited POx thin films resist bacterial growth is yet to be understood, one may hypothesize that the POx thin films disrupt signaling pathways between bacteria, and in turn impede bacterial intercommunication necessary for bacterial growth. This hypothesis is similar to the one reported [100]. Another plausible hypothesis is that the thin films can hydrate in aqueous solvents which would lead to the softening of the thin film resulting in weaker bacterial adhesion. This hypothesis is similar to the one reported [100]. Additionally, the retention of the oxazoline ring as observed in the FTIR studies (C-O and C=N functional groups, **Figure 26**), is assumed to be highly beneficial for antibacterial applications. This hypothesis is similar to the one reported [99].

Terpinene-4-ol thin film deposited on HDPE polymer substrate using the NTP jet promoted an ~ 93 %, ~ 97 %, ~ 96 % and ~ 79 % deactivation of *S. pyogenes*, *S. aureus*, *E. coli* and *P. aeruginosa* microbial populations, respectively, with respect to the control. On changing the substrate to TPU polymer, the thin film promoted an ~ 96 %, ~ 86 %, ~ 91 % and ~ 98 % deactivation of *S. pyogenes*, *S. aureus*, *E. coli* and *P. aeruginosa* microbial populations, respectively, with respect to the control. On changing the substrate to stainless steel, the thin film promoted an ~ 92 %, ~ 90 %, ~ 82 % and ~ 99 % deactivation of *S. pyogenes*, *S. aureus*, *E. coli* and *P. aeruginosa* microbial populations, respectively, with respect to the control. On

changing the substrate to silicon wafer, the antimicrobial thin film promoted an ~ 98 %, ~ 98 %, ~ 99 % and ~ 91 % deactivation of *S. pyogenes*, *S. aureus*, *E. coli* and *P. aeruginosa* microbial populations, respectively, with respect to the control.

As observed, the NTP deposited Terpinene-4-ol thin film possessed high antibacterial activity towards the test bacteria. The thin film was also observed to have generally greater antibacterial activity against the Gram-negative bacteria as opposed to the Gram-positive bacteria. These findings match very well the results reported in Refs. [97]. These findings may be due to the differences in the structure of the bacterial cell wall and the cell membrane which controls the access of different molecules inside the cell and to their sites of action. This suggestion is like the one reported [128]. The type of substrates used ((conductive (stainless steel and silicon) or non-conductive (HDPE and TPU)) in the 2-ethyl-2-oxazoline thin film deposition process did not appear to cause a major difference in the antibacterial activity of the antibacterial thin film. These findings agree with those obtained from the FTIR studies which illustrated similar functional groups, even with change of substrates.

While the complete picture as to why plasma deposited Terpinene-4-ol thin films resist bacterial growth is yet to be understood, and one may hypothesize that the combined effect of the hydrophilic nature of the surface together with the retention of the monomer molecules as observed in the FTIR studies, is the possible reason for the enhanced antibacterial performance of the thin films. This hypothesis is similar to the one reported [129]. Another plausible hypothesis is that the thin film interacts with the plasma membranes and subsequently reorganizes the bacterial cell membrane lipids. This hypothesis is similar to the one reported [130].

(Dimethyl amino) dimethyl silane thin film deposited on HDPE polymer substrate using the NTP jet promoted an ~ 94 %, ~ 99 %, ~ 91 % and ~ 84 % deactivation of *S. pyogenes*, *S. aureus*, *E. coli* and *P. aeruginosa* microbial populations, respectively, with respect to the control. On changing the substrate to TPU polymer, the thin film promoted an ~ 97 %, ~ 98 %, ~ 87 % and

~ 92 % deactivation of *S. pyogenes*, *S. aureus*, *E. coli* and *P. aeruginosa* microbial populations, respectively, with respect to the control. On changing the substrate to stainless steel, the thin film promoted an ~ 94 %, ~ 91 %, ~ 96 % and ~ 98 % deactivation of *S. pyogenes*, *S. aureus*, *E. coli* and *P. aeruginosa* microbial populations, respectively, with respect to the control.

As observed, the NTP deposited (Dimethyl amino) dimethyl silane thin film possessed high antibacterial activity towards the test bacteria. The thin film was also generally observed to have greater antimicrobial activity against the Gram-negative bacteria as opposed to the Gram-positive bacteria. These findings match very well the results reported in Refs. [31]. These findings may be due to the differences in the structure of the bacterial cell wall and the cell membrane which controls the access of different molecules inside the cell and to their sites of action. This suggestion is like the one reported [131]. The type of substrates used ((conductive (stainless steel and silicon) or non-conductive (HDPE and TPU)) in the 2-ethyl-2-oxazoline thin film deposition process did not appear to cause a major difference in the antibacterial activity of the antibacterial thin film. These findings agree with those obtained from the FTIR studies which illustrated similar functional groups, even with change of substrates.

The formation of secondary chemical groups associated to the amino pendant groups, as observed in the FTIR studies, may be associated to the dry-quaternization of the amino groups using the oxygen NTP jet treatment and therefore the high antibacterial activity. This suggestion is similar to the one reported [130]. Additionally, the decrease in colony count can be attributed to the complexation of the quaternary amino groups (positively charged) with the bacterial cell membrane (negatively charged due to PO_4^- of phosphatic group). It has been reported that the bacterial cell membrane is negatively charged due to lipopolysaccharide network present on the outer membrane of cell [132]. The cell membrane provides the shape and required strength for cell to withstand the internal osmotic pressure. Thus, it has been reported that the complexation with the cells outer membrane results in interruption of osmotic balance which leads to the release of intracellular electrolytes [133]. The release of intracellular electrolytes results in lysis of the cell. This finding is like the one reported [134].

Bis(dimethyl amino) dimethyl silane thin film deposited on HDPE polymer substrate using the NTP jet promoted an ~ 96 %, ~ 86 %, ~ 95 % and ~ 91 % deactivation of *S. pyogenes*, *S. aureus*, *E. coli* and *P. aeruginosa* microbial populations, respectively, with respect to the control. On changing the substrate to TPU polymer, the thin film promoted an ~ 97 %, ~ 87 %, ~ 91 % and ~ 94 % deactivation of *S. pyogenes*, *S. aureus*, *E. coli* and *P. aeruginosa* microbial populations, respectively, with respect to the control. On changing the substrate to stainless steel, the thin film promoted an ~ 95 %, ~ 98 %, ~ 99 % and ~ 82 % deactivation of *S. pyogenes*, *S. aureus*, *E. coli* and *P. aeruginosa* microbial populations, respectively, with respect to the control.

As observed, the NTP deposited Bis(dimethyl amino) dimethyl silane thin film possessed high antibacterial activity towards the test bacteria. The thin film was also generally observed to have greater antimicrobial activity against the Gram-negative bacteria as opposed to the Gram-positive bacteria. These findings match very well the results reported in Refs. [135]. These findings may be due to the differences in the structure of the bacterial cell wall and the cell membrane which controls the access of different molecules inside the cell and to their sites of action. This suggestion is like the one reported [131]. The type of substrates used ((conductive (stainless steel and silicon) or non-conductive (HDPE and TPU)) in the 2-ethyl-2-oxazoline thin film deposition process did not appear to cause a major difference in the antibacterial activity of the antibacterial thin film. These findings agree with those obtained from the FTIR studies which illustrated similar functional groups, even with change of substrates.

The high antibacterial activity of the Bis(dimethyl amino) dimethyl silane thin film can be associated to the ability of the oxygen NTP jet to form a silane coating containing quaternary ammonium silane groups starting from the corresponding precursor monomer. As seen before, the quaternary ammonium compounds interact electrostatically with the negatively charged surfaces of bacteria followed by permeation of the alkyl chains into the bacterial membranes leading to bacterial death due to the dissolution of the bacterial cells. This suggestion is similar to the one reported [136]. Therefore, it has been reported that the antibacterial activity of quaternary ammonium silane groups is derived from the alkyl chain groups [137]. The lysis of

bacterial cells by binding to the cell wall is an antibacterial mechanism of quaternary ammonium groups widely considered to be “contact killing” [138] in the presence of the alkyl chain groups as mentioned previously.

The antiviral activity of the thin films against the enveloped Sars covid 2 like virus was not fully determined since the virus did not attach, neither proliferate in both the control substrates and the thin films, after the incubation period. The attachment of viruses on surfaces has been reported to rely on the strength of the van der Waals interactions, electrostatic interactions and the hydrogen bonding between the viral structural proteins and material surfaces [63]. The hypothesis advanced was therefore that the lack of attachment of the Sars covid 2 like virus on the material surfaces in this study was because of very weak van der Waals interactions, electrostatic interactions and hydrogen bonding interactions between the viral structural proteins and the material surfaces.

No coating	**Contact time (min)**	**Substrates**	***Streptococcus pyogenes* (CFU*/cm^{-2})**	***Staphylococcus aureus* (CFU*/cm^{-2})**	***Escherichia coli* (CFU*/cm^{-2})**	***Pseudomonas aeruginosa* (CFU*/cm^{-2})**	**Sars covid 2 like virus (CFU*/cm^{-2})**
Control	1440	HDPE	5×10^5	4×10^5	4×10^5	2×10^5	No presence
		TPU	6×10^5	5×10^5	5×10^5	1×10^5	No presence
		Stainless steel	3×10^5	6×10^5	6×10^5	2×10^5	No presence
		Silicon	2×10^5	2×10^5	2×10^5	2×10^5	No presence
	Reduction in relation to the control Bacterial reduction (%)						
NTP deposited antimicrobial thin film	**Contact time (min)**	**Substrates**	***Streptococcus pyogenes* (CFU*/cm^{-2})**	***Staphylococcus aureus* (CFU*/cm^{-2})**	***Escherichia coli* (CFU*/cm^{-2})**	***Pseudomonas aeruginosa* (CFU*/cm^{-2})**	**Sars covid 2 like virus (CFU*/cm^{-2})**
2-ethyl-2-oxazoline antimicrobial thin film	1440	HDPE	92	93	92	92	No presence
		TPU	97	89	91	97	No presence
		Stainless steel	91	95	96	89	No presence
		Silicon	91	86	93	90	No presence
Terpinene-4-ol thin film		HDPE	93	97	96	79	No presence
		TPU	96	86	91	98	No presence
		Stainless steel	92	90	82	99	No presence
		Silicon	98	98	99	91	No presence
(Dimethyl amino) dimethyl silane thin film		HDPE	94	99	91	84	No presence
		TPU	97	98	87	92	No presence
		Stainless steel	94	91	96	98	No presence
Bis (dimethyl amino)		HDPE	96	86	95	91	No presence
		TPU	97	87	91	94	No presence

dimethyl silane thin film		Stainless steel	95	98	99	82	No presence

***CFU**-colony forming units

Table 20| Biocidal activities (Test 1) of selected NTP deposited thin films against S. pyogenes, S. aureus, E. coli, P. aeruginosa and Sars covid 2 like virus after 24 hours of culture

In the second antibacterial tests, the four NTP deposited thin films did not have any effect on the bacterial populations (percentage increase or decrease in proliferation) with respect to the control substrates after incubation. These findings showed that the thin films did not release any biocides to the bacterial cells. **(Table 21)**. In the second antiviral tests, the four NTP deposited thin films did not have any effect on the viral cells (percentage increase or decrease) since, in the first place, the viral cells did not attach nor proliferate all together in both the control substrates and the thin films. The four NTP deposited thin film can therefore be classified as contact-active surfaces. These findings agree with the ones reported [100] for 2-ethyl-2-oxazoline thin film, [97] for Terpinene-4-ol thin film, [31] for (Dimethyl amino) dimethyl silane thin film and [135] for Bis(dimethyl amino) dimethyl silane thin film.

	Reduction in relation to the control Bacterial reduction (%)						
NTP deposited antimicrobial thin films	**Contact time (min)**	**Substrates**	**Streptococcus pyogenes (CFU*/cm^{-2})**	**Staphylococcus aureus (CFU*/cm^{-2})**	**Escherichia coli (CFU*/cm^{-2})**	**Pseudomonas aeruginosa (CFU*/cm^{-2})**	**Sars covid 2 like virus (CFU*/cm^{-2})**
2-ethyl-2-oxazoline antimicrobial thin film	1440	HDPE	No effect	No effect	No effect	No effect	No effect
		TPU	No effect	No effect	No effect	No effect	No effect
		Stainless steel	No effect	No effect	No effect	No effect	No effect
		Silicon	No effect	No effect	No effect	No effect	No effect
Terpinene-4-ol thin film		HDPE	No effect	No effect	No effect	No effect	No effect
		TPU	No effect	No effect	No effect	No effect	No effect
		Stainless steel	No effect	No effect	No effect	No effect	No effect
		Silicon	No effect	No effect	No effect	No effect	No effect
(Dimethyl amino) dimethyl silane thin film		HDPE	No effect	No effect	No effect	No effect	No effect
		TPU	No effect	No effect	No effect	No effect	No effect
		Stainless steel	No effect	No effect	No effect	No effect	No effect
Bis (dimethyl amino) dimethyl silane thin film		HDPE	No effect	No effect	No effect	No effect	No effect
		TPU	No effect	No effect	No effect	No effect	No effect
		Stainless steel	No effect	No effect	No effect	No effect	No effect

***CFU**-colony forming units

Table 21| Biocidal activities (Test 2) of selected NTP deposited thin films against S. pyogenes, S. aureus, E. coli, P. aeruginosa and Sars covid 2 like virus after 24 hours of culture

4.4 Bacterial adhesion on the substrates

SEM observations showed that *E. Coli* readily adhered to the TPU and HDPE substrates while being more scarcely on stainless steel substrate and absent on the silica substrate (**Figure 60** and **Figure 61**). Similar findings were observed on another study on *E. Coli* adhesion on polymeric substrates. They observed considerable adhesion of the *E. Coli* on the polymeric substrates [139]. They observed considerable *E. Coli* adhesion on the polymeric substrates. Both TPU polymer and HDPE polymer have been observed to be hydrophobic in nature [140, 141]. The hydrophobic lipopolysaccharide (LS) surface of Gram-negative bacteria accounts for the favored binding of E. Coli to a hydrophobic surface over hydrophilic surface. These findings are similar to the ones reported [142].

4.5 Effect of NTP on bacterial cell morphology

The SEM analysis was carried out to observe the morphological changes in plasma-untreated *E. Coli* cells found on the four substrates (TPU polymer, HDPE polymer, stainless steel, and silicon) in comparison to the cells treated with the plasma for 60 sec, 30 sec, and 15 sec (**Figure 60**, **Figure 61**, **Figure 62**, and **Figure 63**). However, the morphological changes were mainly based on NTP treatment of *E. Coli* cells found on the polymer substrates (TPU polymer and HDPE polymer) after incubation due to *E. Coli* better adhesion properties on the polymer substrates.

Rod-shaped, and live bacteria with a smooth surface were observed in the untreated control *E. Coli* cells before NTP treatment (blue rings, **Figure 60**, and **Figure 61**). Treatment for 15 sec caused the E. Coli surfaces to noticeable wrinkles and a small fraction of cells had major damages on cell surfaces (yellow rings, **Figure 60**, and **Figure 61**). However, not all cells suffered serious external damage that would lead to their death. The rod-shaped, and live bacteria with a smooth surface observed could be explained by considering that the NTP sterilization was achieved by moving the NTP jet nozzle physically by means of hand and it was therefore very difficult to completely cover the entire sample surface (around 5 sq cm).

Cell walls of bacteria have been reported to confer shape and rigidity of the cell, in addition to protecting against osmotic lysis [143]. Hence, damage to the cell wall will induce morphological changes. A longer exposure time (30 sec) led to serious damage to the *E. Coli* cells, as evidenced by their ruptured morphology (green rings, **Figure 60**, and **Figure 61**). The treatment was therefore sufficient for bacterial destruction. A much longer exposure time (60 sec) led to much more serious damage to *E. Coli* cells, as evidenced by the considerable differences in the cell morphology whose physiological condition indicates they are all flattened, ruptured and dead (red rings, **Figure 60**, and **Figure 61**).

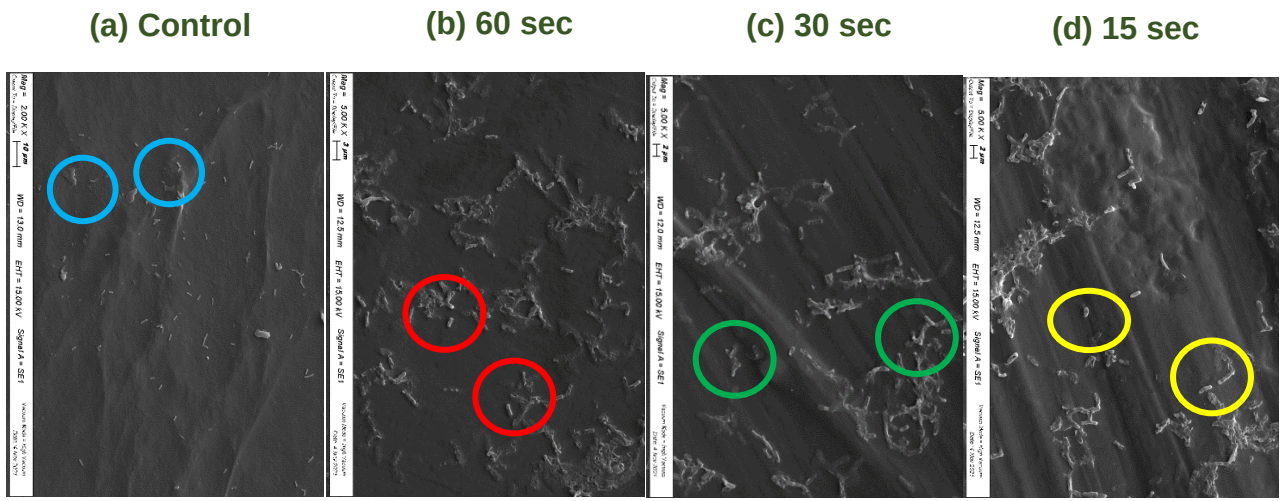

Figure 60| Scanning electron micrographs of *E.coli* bacteria on TPU polymer substrate **a)** Untreated control; **(b)** 60 sec NTP treatment; **(c)** 30 sec NTP treatment; **(d)** 15 sec NTP treatment. The blue rings indicate the well-rounded and live bacteria before NTP treatment. Red rings indicate visibly deformed structures after 1 min NTP treatment. Green rings indicate visibly deformed structures after 30 sec NTP treatment. Yellow rings indicate visibly deformed structures after 15 sec NTP treatment

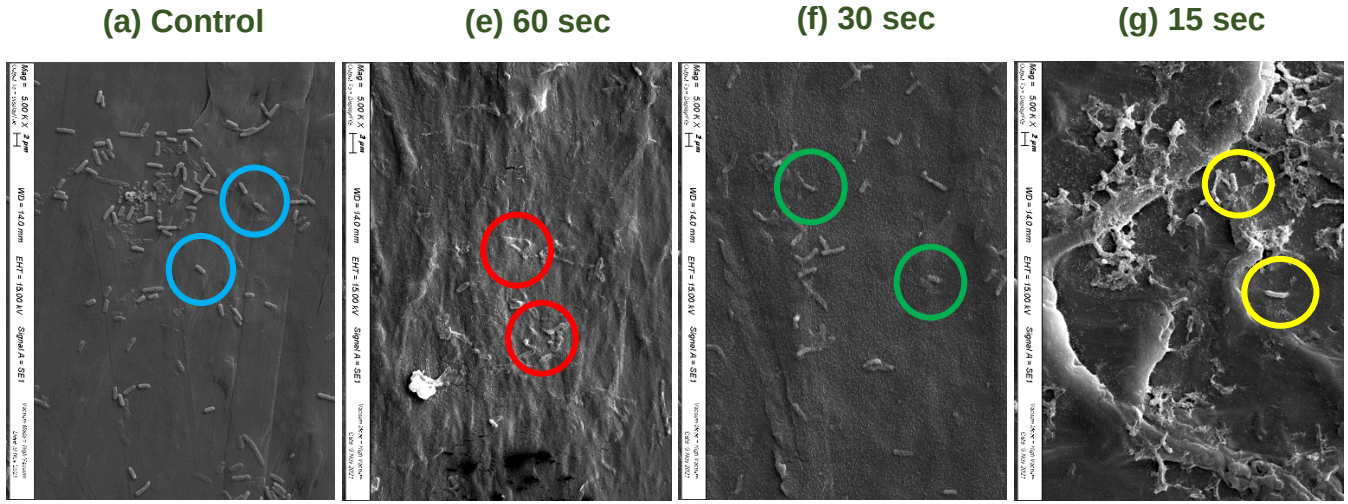

Figure 61| Scanning electron micrographs of *E.coli* bacteria on HDPE polymer substrate **a)** Untreated control; **(e)** 1 min NTP treatment; **(f)** 30 sec NTP treatment; **(g)** 15 sec NTP treatment. The blue rings indicate the well-rounded and live bacteria before NTP treatment. Red rings indicate visibly deformed structures after 1 min NTP treatment. Green rings indicate visibly deformed structures after 30 sec NTP treatment. Yellow rings indicate visibly deformed structures after 15 sec NTP treatment

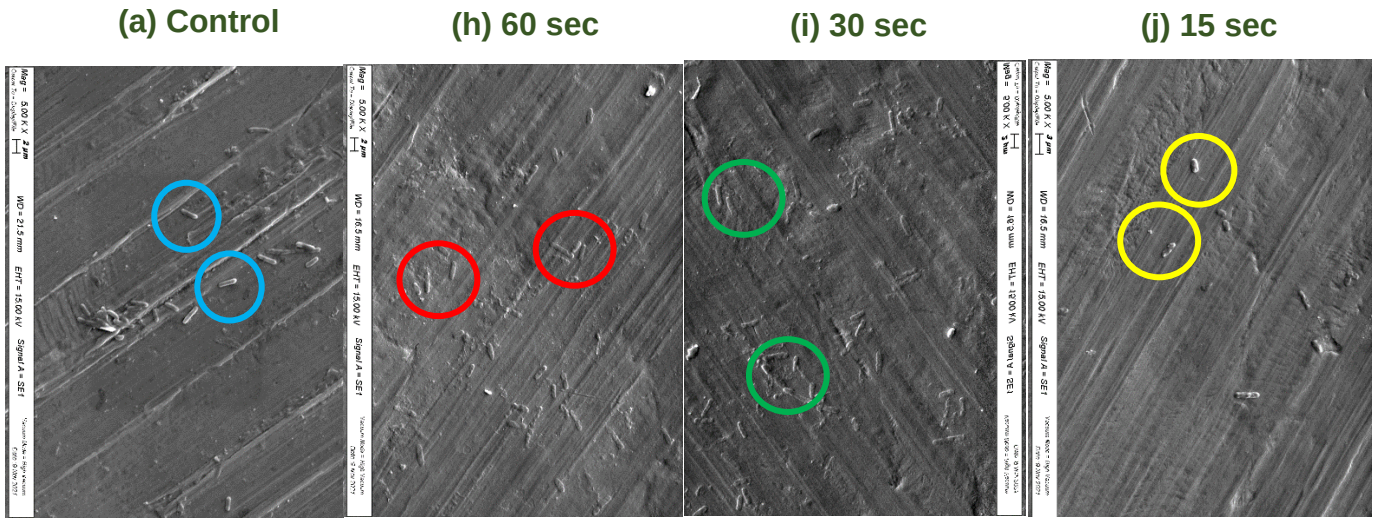

Figure 62| Scanning electron micrographs of *E.coli* bacteria on stainless steel substrate **a)** Untreated control; **(h)** 1 min NTP treatment; **(i)** 30 sec NTP treatment; **(j)** 15 sec NTP treatment. The blue rings indicate the well-rounded and live bacteria before NTP treatment. Red rings indicate visibly deformed structures after 1 min NTP treatment. Green rings indicate visibly deformed structures after 30 sec NTP treatment. Yellow rings indicate visibly deformed structures after 15 sec NTP treatment

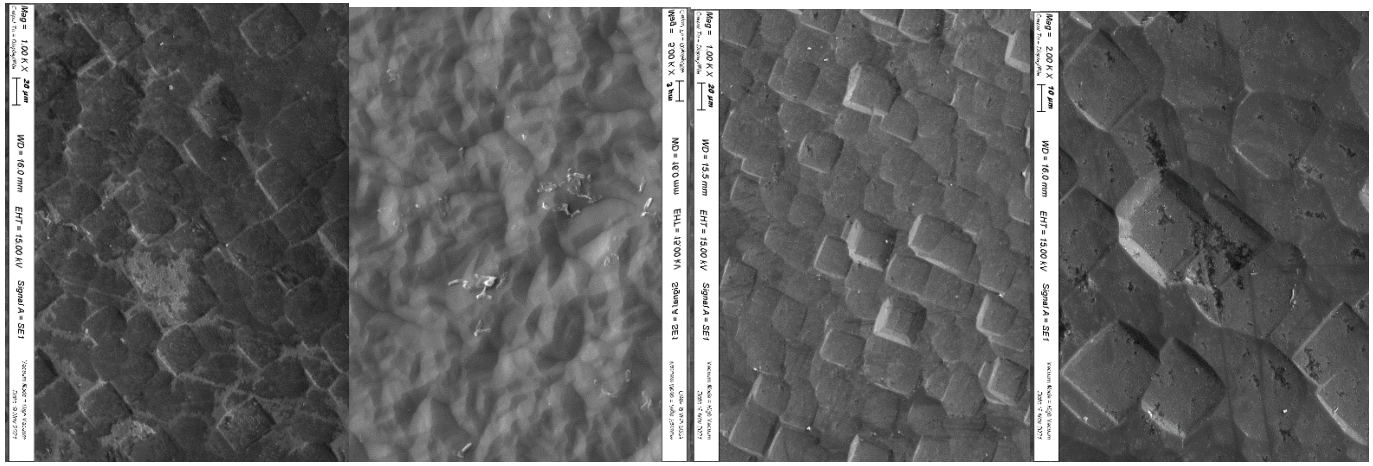

Figure 63| Scanning electron micrographs of *E.coli* bacteria on silicon wafer substrate **a)** Untreated control; **(k)** 1 min NTP treatment; **(l)** 30 sec NTP treatment; **(m)** 15 sec NTP treatment.

As reported, the physical effects of NTP have been well recognized as one of the major modes of bacterial inactivation [144, 145]. Although NTP treatment can kill bacteria, the mechanisms underlying its effects are unclear. The RONS can penetrate cells and are known to cause oxidative and nitrosative damage to lipids and protein in bacteria. This damage induces lipid peroxidation, inhibition of enzyme functions and alteration of DNA, which ultimately accounts for bacterial cell death. These proposed bacterial inactivation mechanisms are like the ones reported [144]. The chemical reaction between reactive species and acidification of the milieu, combined are responsible for the lethality to the microorganism. These findings are like the ones reported [145].

5. Conclusion

In the first part of this work, antimicrobial 2-ethyl-2-oxazoline thin films, Terpinene-4-ol thin films, (Dimethyl amino) dimethyl silane thin films and Bis(dimethyl amino) dimethyl silane thin films were deposited on conductive substrates (Stainless steel and Silicon) and on non-conductive substrates (HDPE and TPU) using the novel atmospheric plasma jet. Argon was used as the working gas for the discharge, 2-ethyl-2-oxazoline, Terpinene-4-ol, (Dimethyl amino) dimethyl silane thin film and Bis(dimethyl amino) dimethyl silane vapors were admixed to the argon flow and used as the precursor monomers. This gas composition made it possible to obtain a homogeneous discharge, which led to the deposition of homogeneous thin films. The chemistry of the thin films was analyzed by FTIR and water contact angles. The antibacterial tests on the thin films were conducted by subjecting them to both the Gram-positive bacteria (Streptococcus pyogenes and Staphylococcus aureus) and Gram-negative bacteria (Escherichia coli and Pseudomonas aeruginosa) while the antiviral tests of the thin films were conducted by subjecting them to Enveloped Sars covid 2 like virus followed by a 24-hour incubation period.

2-ethyl-2-oxazoline thin film caused a decrease in the population of *Streptococcus pyogenes* cells, *Staphylococcus aureus* cells, *Escherichia coli* cells and *Pseudomonas aeruginosa* cells by approximately 93%, 94%, 93% and 90%, respectively, with respect to the control. Terpinene-4-ol thin film caused a decrease in the population of *Streptococcus pyogenes* cells, *Staphylococcus aureus* cells, *Escherichia coli* cells and *Pseudomonas aeruginosa* cells by approximately 95%, 93%, 92% and 92%, respectively, with respect to the control. (Dimethyl amino) dimethyl silane thin film caused a decrease in the population of *Streptococcus pyogenes* cells, *Staphylococcus aureus* cells, *Escherichia coli* cells and *Pseudomonas aeruginosa* cells by approximately 95%, 96%, 91% and 91%, respectively, with respect to the control. Bis(dimethyl amino) dimethyl silane thin film caused a decrease in the population of *Streptococcus pyogenes* cells, *Staphylococcus aureus* cells, *Escherichia coli* cells and *Pseudomonas aeruginosa* cells by approximately 96%, 90%, 95% and 89%, respectively, with respect to the control.

The high antibacterial activity of 2-ethy-2-oxazoline thin films was associated to the retention of the oxazoline ring as observed in the FTIR spectra. The retention of the oxazoline ring is assumed to be highly beneficial for antimicrobial applications. The high antibacterial activity of Terpinene-4-ol thin films was associated to the combined effect of the hydrophilic nature of the surface together with the retention of the monomer molecules as observed in the FTIR studies. The high antibacterial activity of (Dimethyl amino) dimethyl silane thin films was associated to the ability of the oxygen NTP jet treatment to dry-quartanize the amino groups (positively charged) as observed in the FTIR studies accelerating the interference of the bacterial cell membrane (negatively charged due to PO_4^- of the phosphatic group). The high antibacterial activity of the Bis(dimethyl amino) dimethyl silane thin films was associated to the ability of the oxygen NTP jet to form a silane coating containing quaternary ammonium silane groups (positively charged) starting from the corresponding monomer accelerating the interference of the cell membrane (negatively charged due to PO_4^- of the phosphatic group).

The antibacterial tests also showed that the thin films can be classified as contact-active surfaces, since they did not cause any change to the microbial populations after 24-hour incubation period meaning that they did not release any biocides, and they can therefore be used without causing microbial resistance.

The antiviral activity of the thin films against the enveloped Sars covid 2 like virus was not fully determined since the virus did not attach, neither proliferate in both the control substrates and the thin films, after the incubation period. The hypothesis advanced was that the forces of interactions (van der Waals, electrostatic and hydrogen bonding) between the viral structural proteins and the material surfaces used in this study were very weak to support any attachment. WCA of the NTP deposited POx thin films decreased with respect to the control resulting in an increase in the wettability due to the hydrophilic nature of the thin films. WCA of the NTP deposited Terpinene-4-ol thin films also decreased with respect to the control resulting in an increase in the wettability due to the hydrophilic nature of the thin films. WCA of the NTP deposited (Diethyl amino) ethyl methacrylate thin films also decreased with respect to the control resulting in an increase in the wettability due to the hydrophilic nature of the thin films.

WCA of the NTP deposited Bis(dimethyl amino) dimethyl silane thin films increased with respect to the control resulting in a decrease in the wettability due to the hydrophobic nature of thin films.

The effect of changing the NTP operating parameters on the chemical composition of the plasma deposited thin films was also investigated. These includes varying the argon carrier gas flow rate, varying the argon working gas, varying the NTP power source from continuous RF power source to pulsed RF power, varying the distance between the substrate and the plasma jet nozzle and the effect of varying the plasma power. Increasing the argon carrier gas flow rate beyond the optimum flow rate was observed to decrease the FTIR peak intensities of the functional groups associated with the NTP deposited thin films. Increasing the argon working gas flow rate beyond the optimum flow rate was also observed to decrease the FTIR peak intensities of the functional groups associated with the NTP deposited thin films. Operating the NTP in pulsed mode ensured congruent transfer of the functional groups from the precursor monomers to the corresponding NTP deposited thin films. Operating the NTP in continuous mode promoted monomer fragmentation to a certain extent and therefore the former, pulsed mode, was the preferred mode of operation.

Increasing the distance between the substrate and the plasma jet nozzle up to but not exceeding the optimum value was observed to increase the FTIR peak intensities of the NTP deposited thin films. Finally, increasing the plasma power value beyond the optimum power value, increased the likelihood of monomer fragmentation due to the electron impacts resulting in the decrease in the FTIR peak intensities. Having exhibited excellent antibacterial properties against all bacterial strains used, the deposited thin films could be used as coatings with antibacterial properties in the medical, biomedical, industrial, and commercial sectors of the economy. Further studies on the stability and durability of these antimicrobial thin films are encouraged and advocated for.

In the second part of this work, the bacterial sterilization and inactivation potential of the NTP jet was investigated. The microorganism selected for the sterilization and inactivation studies was *E. Coli*. The cell adhesion on the four substrates (stainless steel, silicon wafer, HDPE and TPU) and the cellular membrane integrity of the plasma-treated *E. Coli* was then imaged by SEM. SEM observations showed that E. Coli readily adhered to the TPU and HDPE substrates while being more scarcely on stainless steel and absent on the silica substrate. The hydrophobic lipopolysaccharide (LS) surface of E. Coli favored the hydrophobic polymer substrates (TPU and HDPE) and hence, the higher adhesion potential compared to the other two substrates (stainless steel and silicon).

SEM images indicated that the surface morphology of the NTP-treated E. Coli changed substantially with respect to the control and that the change was directly proportional to the treatment time. Three treatment time (15 sec, 30 sec and 60 sec). This could be mainly attributed to different mechanisms that occur during the plasma treatment involving neutral, ionized, and reactive species as well as UV photons, causing oxidative stress within the cells and consequently accelerating death of the bacterial cells. These results demonstrated that plasma treatment results in a rapid inactivation and sterilization and therefore, NTP has promising applications prospects in current and future disinfection technologies for future real-world applications.

Appendix

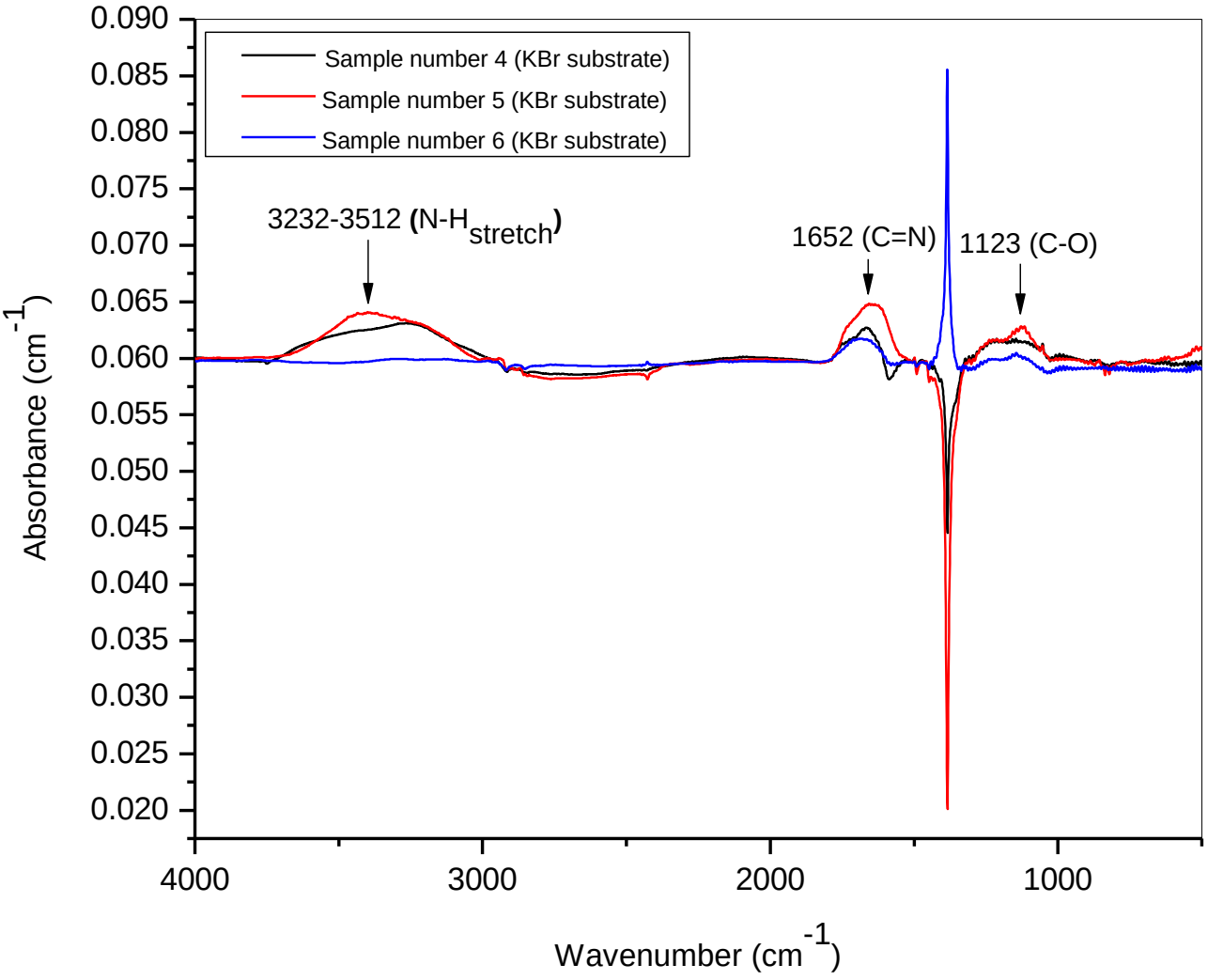

Appendix A| FTIR spectra of plasma deposited PO_x thin film on KBr substrate under specific NTP operating parameters (SET B) (first category of samples)

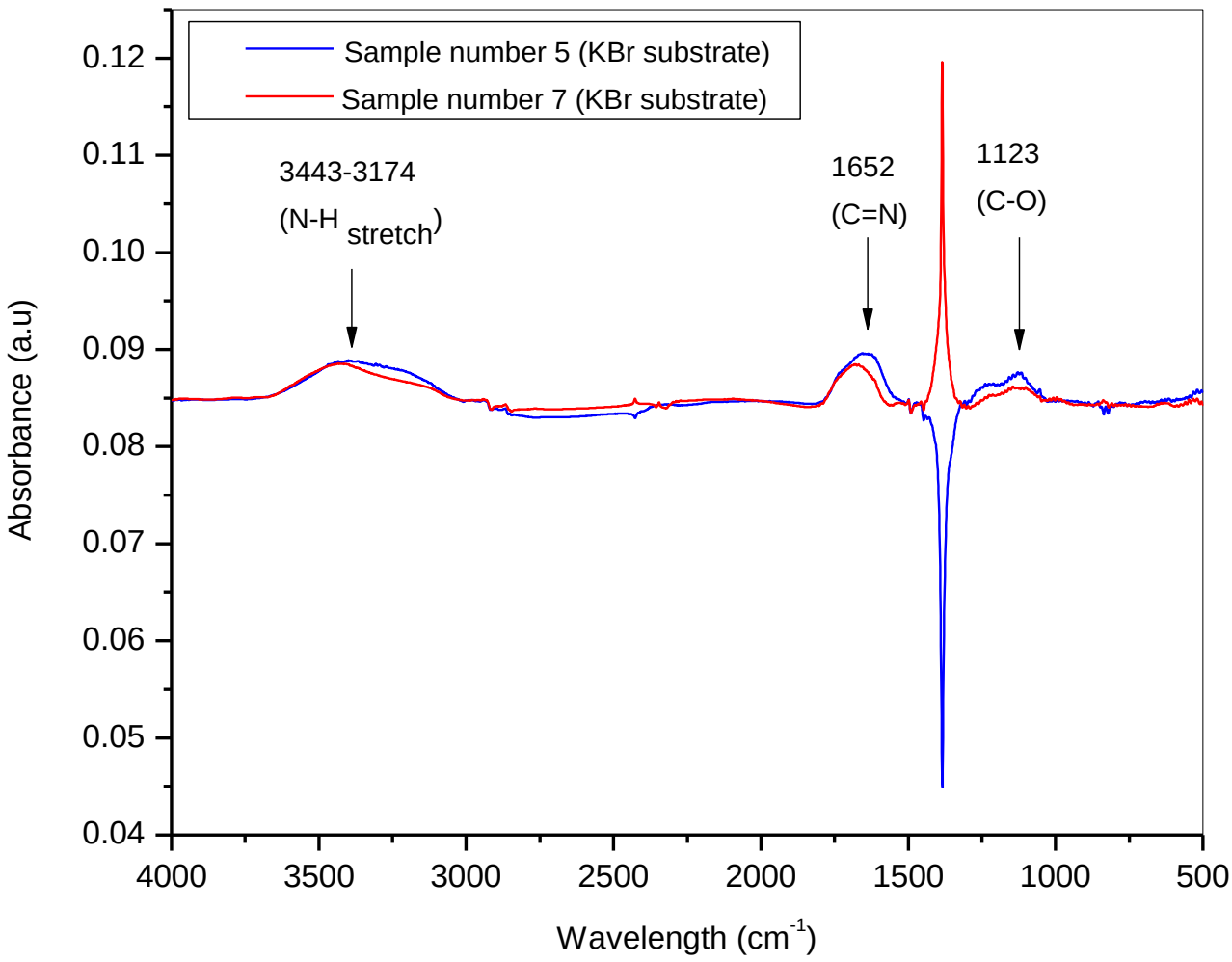

Appendix B| FTIR spectra of plasma deposited PO_x thin film on KBr substrate under specific NTP operating parameters (SET C) (first category of samples)

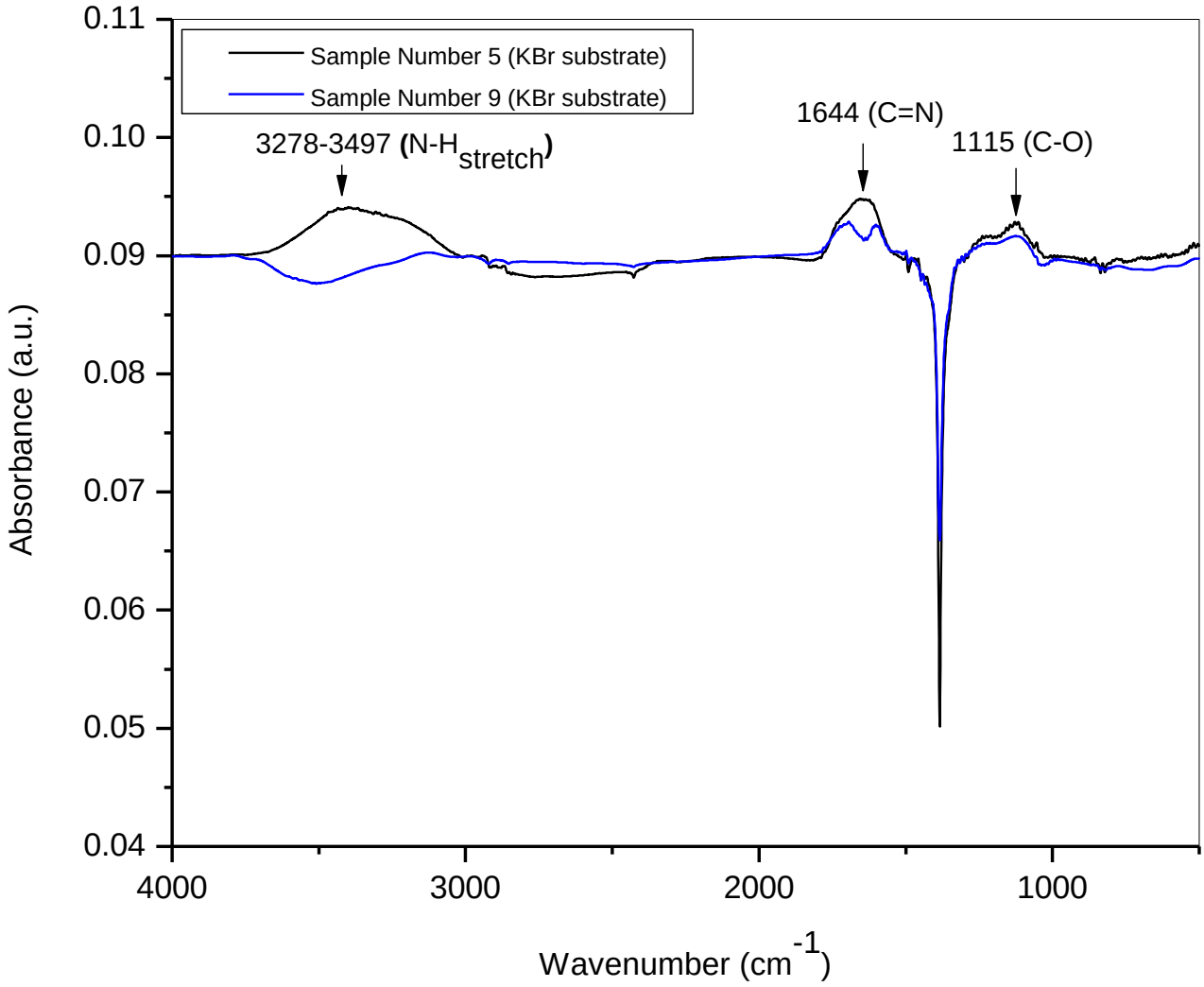

Appendix C| FTIR spectra of plasma deposition PO_x thin film on KBr substrate under specific NTP operating parameters (SET D) (first category of samples)

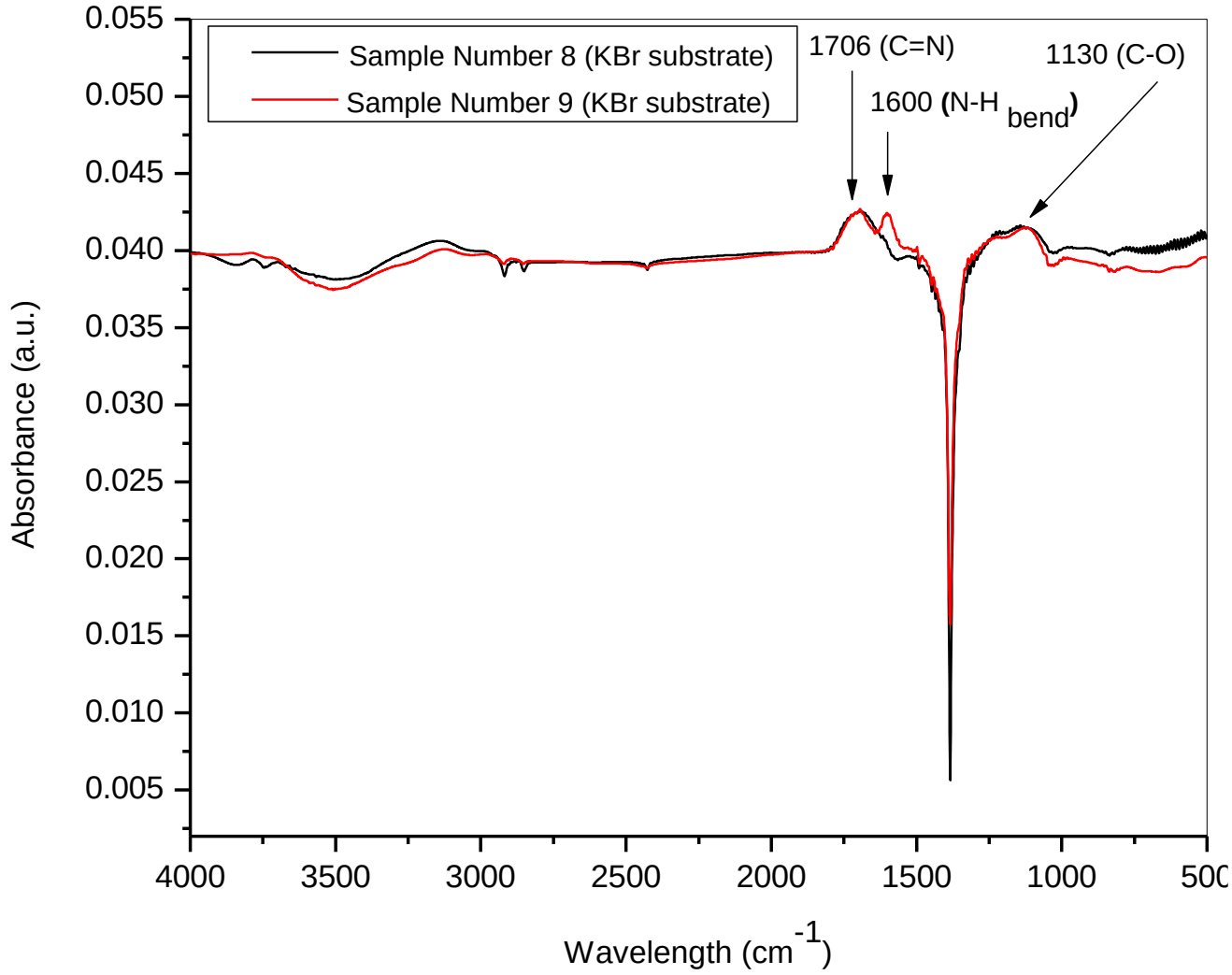

Appendix D| FTIR spectra of plasma deposited PO_x thin film on KBr substrate under specific NTP operating parameters (SET E) (first category of samples)

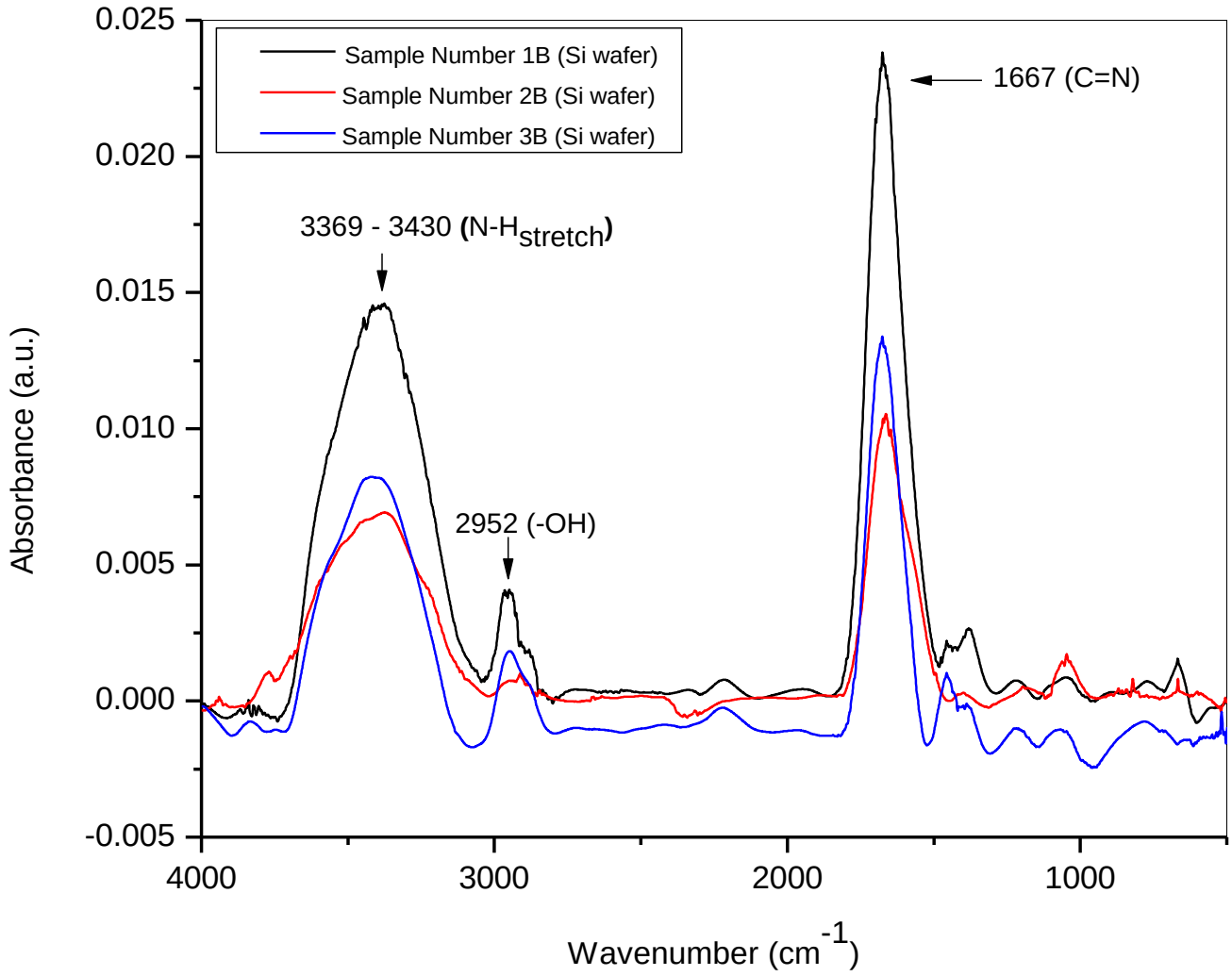

Appendix E| FTIR spectra of plasma deposited PO_x thin film on Si wafer substrate under specific NTP operating parameters (SET A, SET B and SET E) (first category of samples)

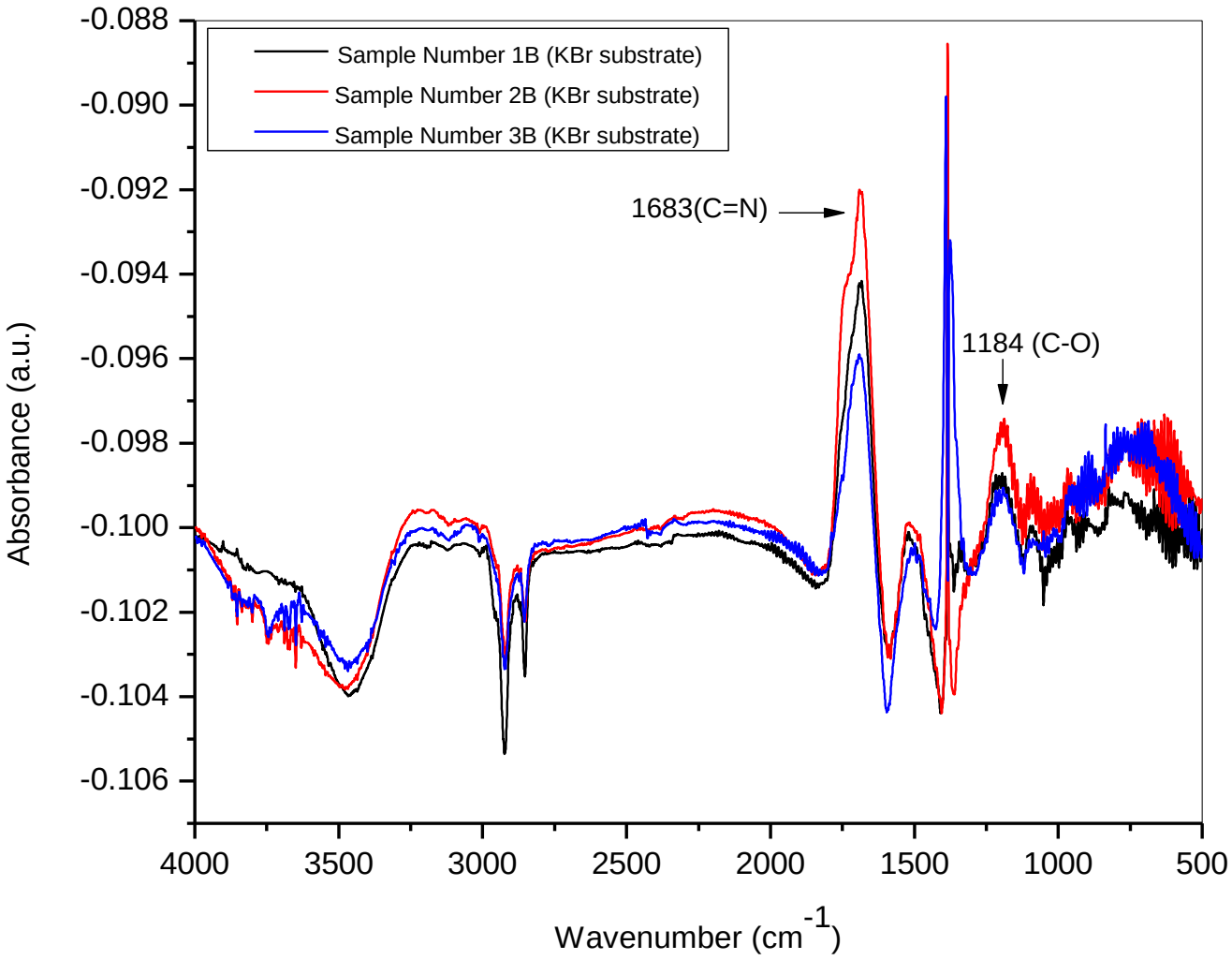

Appendix F| FTIR spectra of plasma deposited PO_x thin film on KBr substrate under specific NTP operating parameters (SET A, SET B and SET E) (first category of samples)

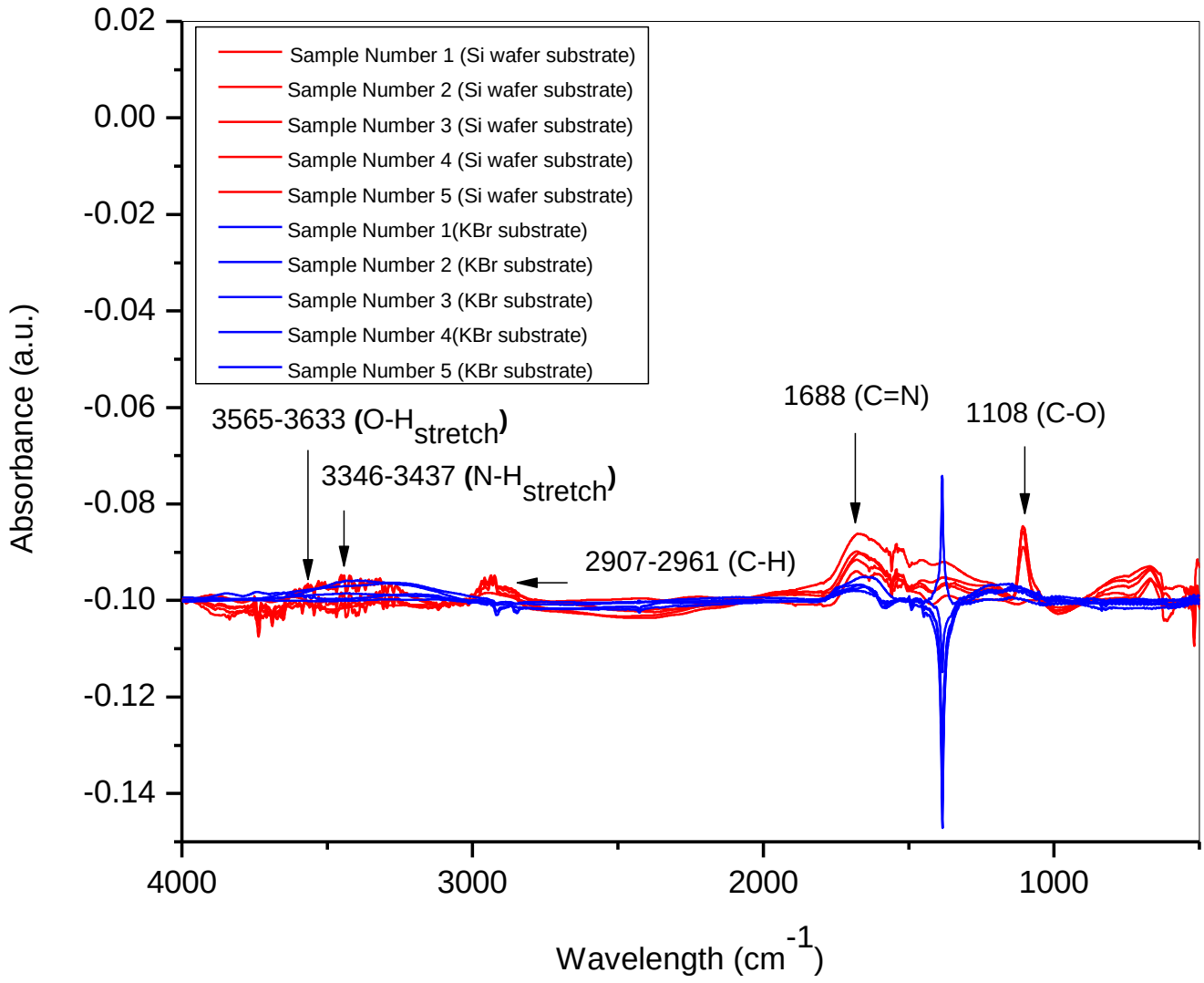

Appendix G| Comparison of the FTIR spectra of NTP deposited PO_x thin film on Si wafer substrate and on KBr substrate (first category of samples) (Part A)

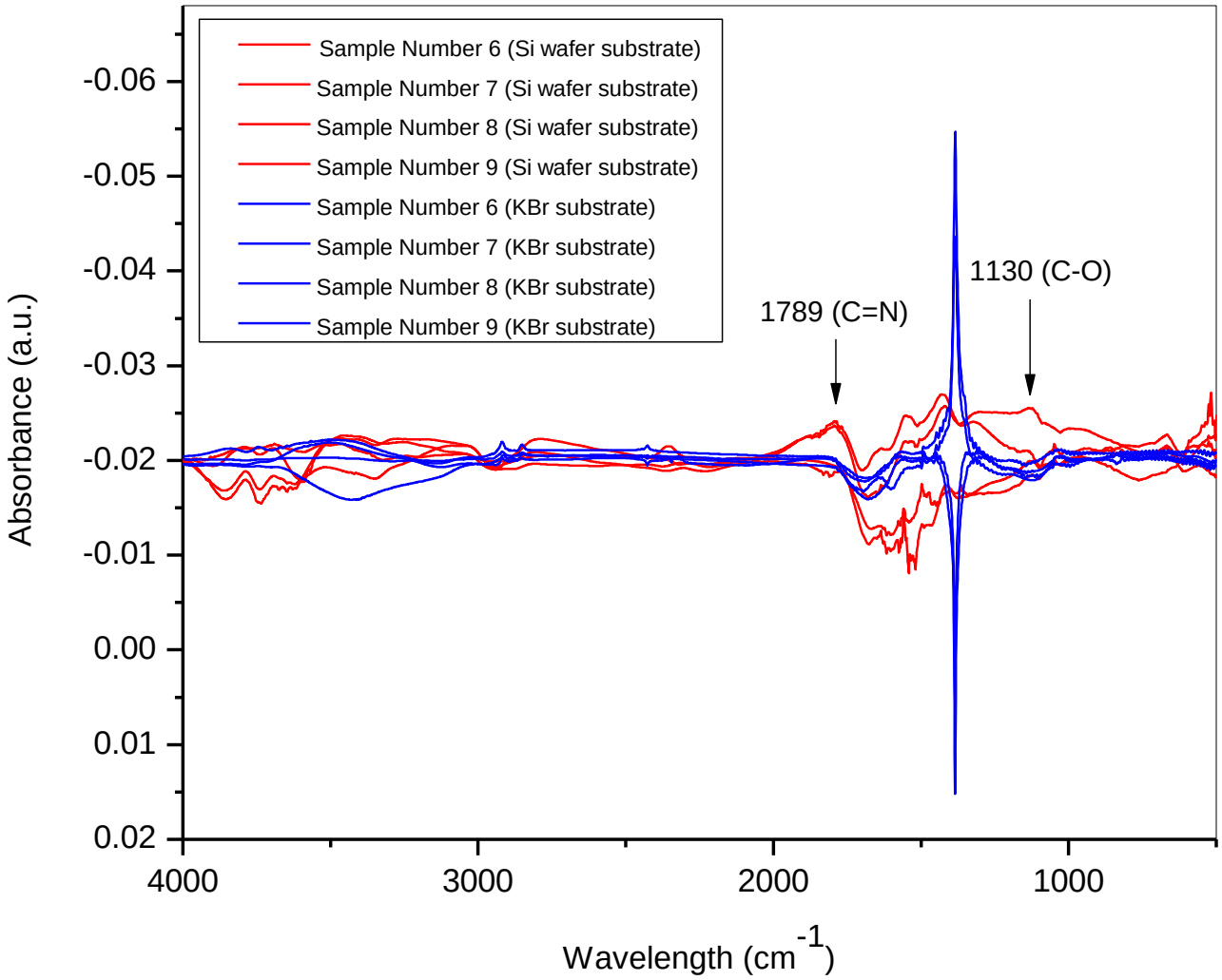

Appendix H| Comparison of the FTIR spectra of NTP deposited PO_x thin film on Si wafer substrate and on KBr substrate (first category of samples) (Part B)

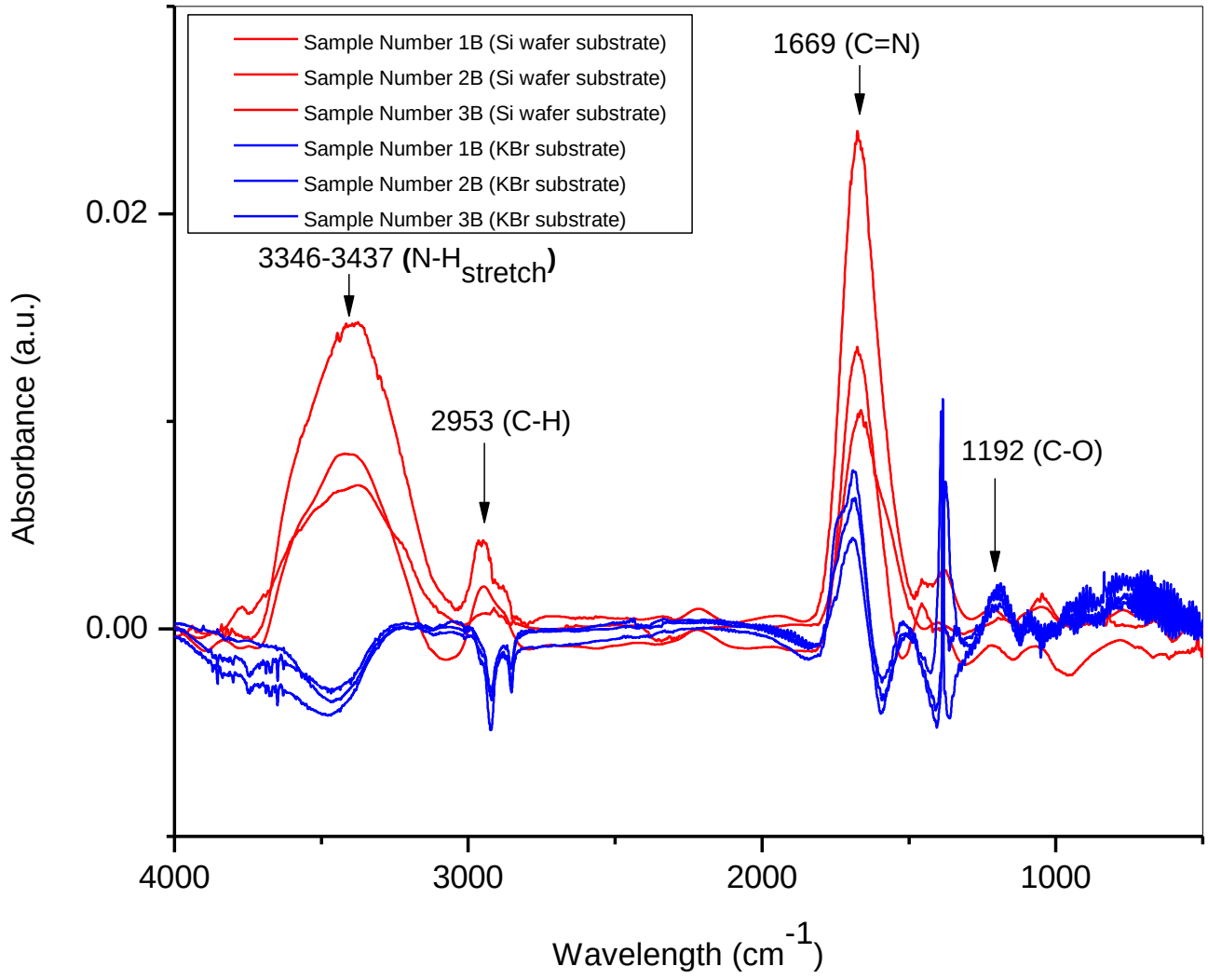

Appendix I| Comparison of the FTIR spectra of NTP deposited PO_x thin film on Si wafer substrate and on KBr substrate (second category of samples)

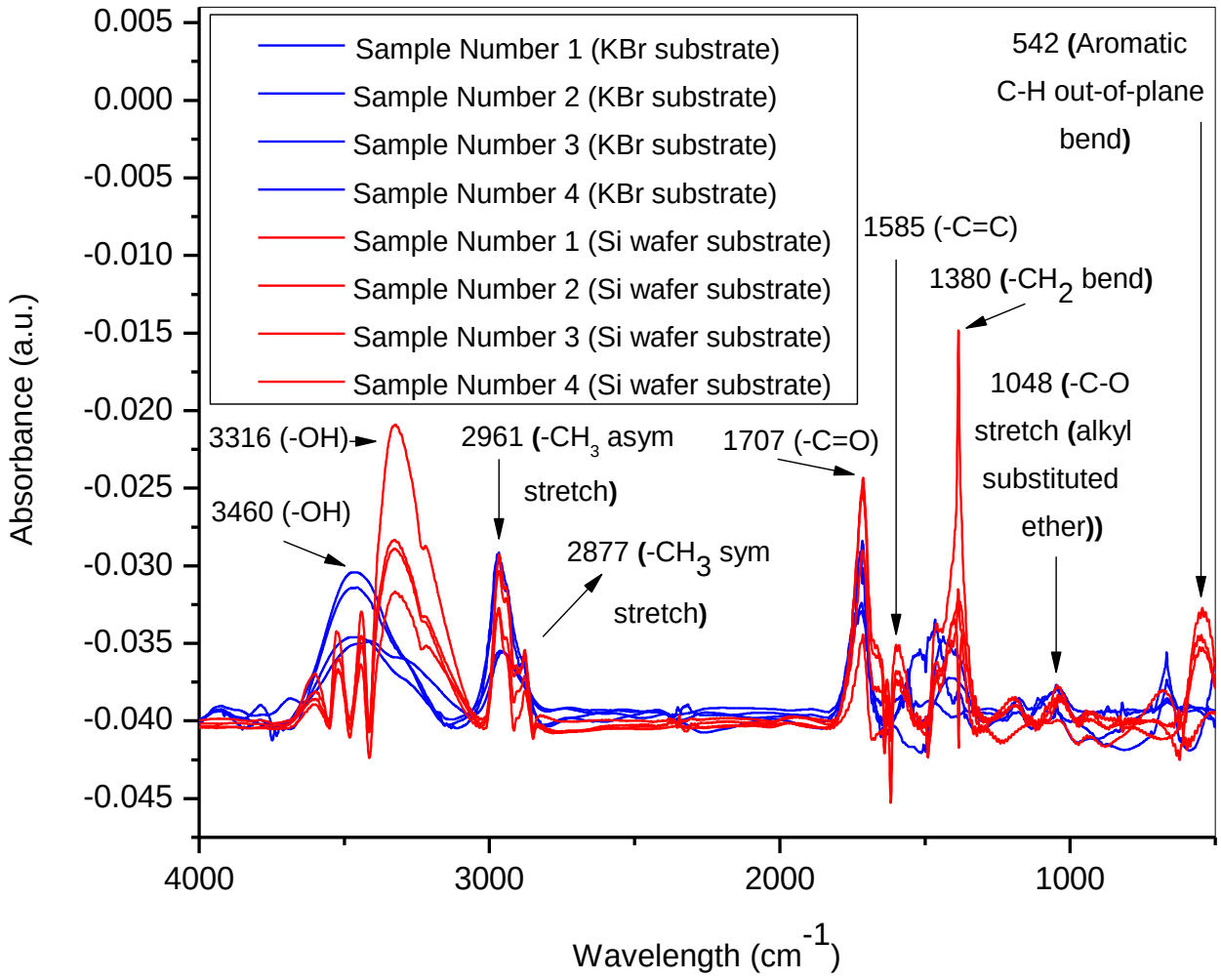

Appendix J| Comparison of the FTIR spectra of NTP deposited Terpinene-4-ol thin film on KBr substrate and on Si wafer substrate (lone category of samples) (Part A)

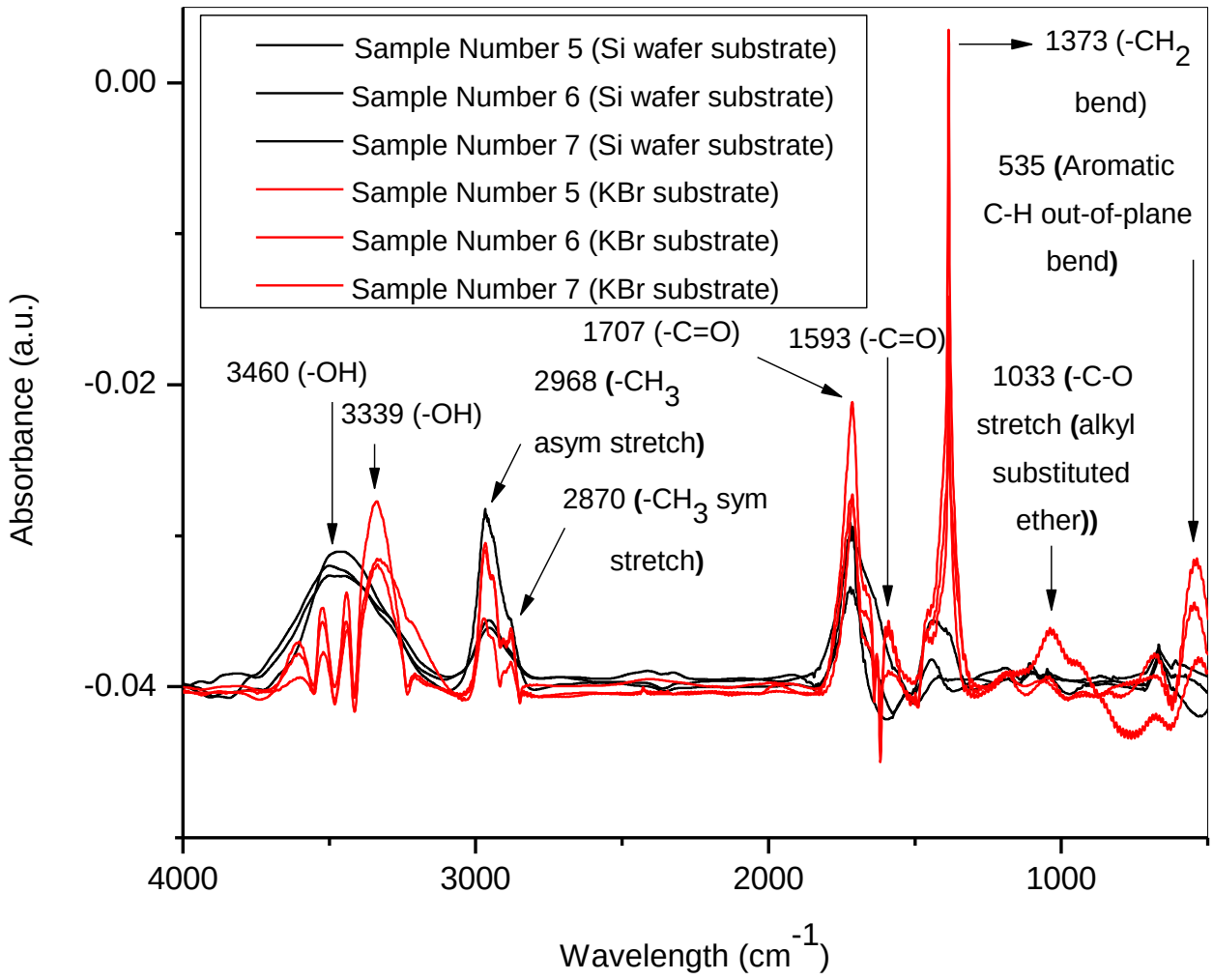

Appendix K| Comparison of the FTIR spectra of NTP deposited Terpinene-4-ol thin film on KBr substrate and on Si wafer substrate (lone category of samples) (Part B)

Monomer	Samples	Samples	Contact angle[a]		Surface energy (mN/m)[a]		
			θ (H_20)	θ (CH_2I_2)	γ_s	γ_{SD}	γ_{SP}
2-ethyl-2-oxazoline	Reference	Reference	43 ± 2	38 ± 2	62.3	40.6	21.7
	First category of samples	Sample number 1	44 ± 2	21 ± 1	65.6	47.5	18.1
		Sample number 2	40 ± 4	22 ± 3	67.5	47.2	20.4
		Sample number 3	43 ± 5	22 ± 4	66.0	47.2	18.8
		Sample number 4	45 ± 2	21 ± 4	65.1	47.5	17.6
		Sample number 5	48 ± 5	21 ± 3	63.5	47.5	16.0
		Sample number 6	48 ± 1	21 ± 4	63.5	47.5	16.0
		Sample number 7	48 ± 2	20 ± 2	63.7	47.8	15.9
		Sample number 8	52 ± 6	21 ± 4	61.4	47.5	13.9
		Sample number 9	48 ± 2	18 ± 1	64.0	48.4	15.7
	Reference	Reference	42 ± 6	40 ± 6	62.36	39.61	22.75
	Second category of samples	Sample number 1B	42 ± 6	40 ± 6	62.36	39.61	22.75
		Sample number 2B	24 ± 10	39 ± 10	71.61	40.11	31.5
		Sample number 3B	42 ± 5	40 ± 5	62.36	39.61	22.75
Terpinene-4-ol	Reference	Reference	53 ± 4	39 ± 3	56.3	40.11	16.19
	Lone category of samples	Sample number 1	20 ± 4	37 ± 3	73.53	41.09	32.44
		Sample number 2	28 ± 2	30 ± 5	71.78	44.22	27.56
		Sample number 3	28 ± 3	37 ± 5	70.32	41.09	29.23
		Sample number 4	25 ± 5	33 ± 3	72.45	42.93	29.51
		Sample number 5	24 ± 4	37 ± 2	72.03	41.09	30.94

		Sample number 6	20 ± 5	39 ± 1	73.13	40.11	33.02
		Sample number 7	16 ± 8	39 ± 2	74.4	40.11	34.29
(Dimethyl amino) ethyl methacrylate	Reference	Reference	49 ± 2	35 ± 5	59.69	42.03	17.66
	Lone category of samples	Sample number 1	17 ± 3	34 ± 2	75.09	42.49	32.6
		Sample number 2	15 ± 3	28 ± 2	76.76	45.03	31.73
Bis(dimethyl amino) dimethyl silane	Reference	Reference	64 ± 2	38 ± 3	50.62	40.6	10.02
	Sole sample	Lone sample	85 ± 5	50 ± 5	37.21	34.27	2.937

[a] Measured 24h after NTP thin film deposition

Appendix L| Wettability and surface energy. Contact angle values of water and diiodomethane are reported in the first two columns, as an average value obtained from 3 replicate measurements, and the surface energy values computed using the Owens Wendt method.

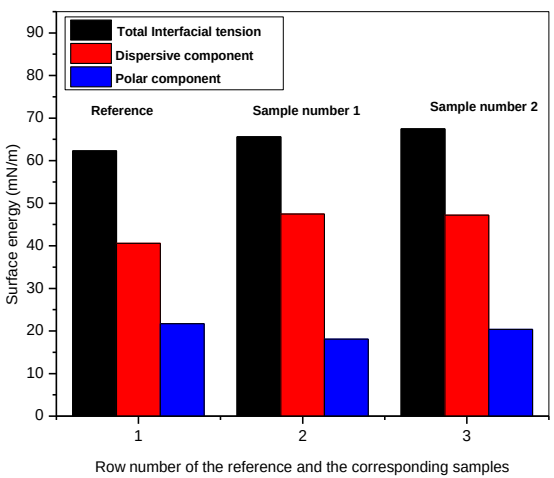
Total Interfacial tension
Dispersive component
Polar component
Reference
Sample number 1
Sample number 2
Surface energy (mN/m)
Row number of the reference and the corresponding samples

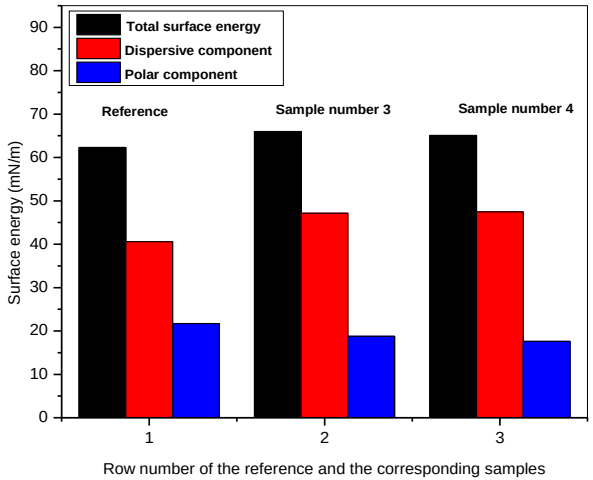
Total surface energy
Dispersive component
Polar component
Reference
Sample number 3
Sample number 4
Surface energy (mN/m)
Row number of the reference and the corresponding samples

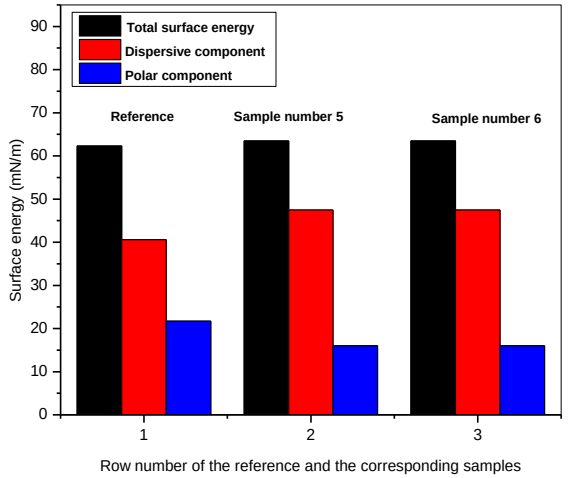
Total surface energy
Dispersive component
Polar component
Reference
Sample number 5
Sample number 6
Surface energy (mN/m)
Row number of the reference and the corresponding samples

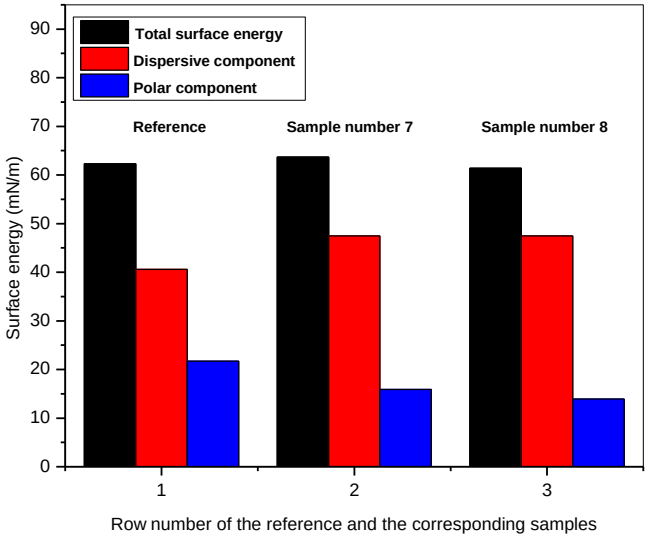
Total surface energy
Dispersive component
Polar component
Reference
Sample number 7
Sample number 8
Surface energy (mN/m)
Row number of the reference and the corresponding samples

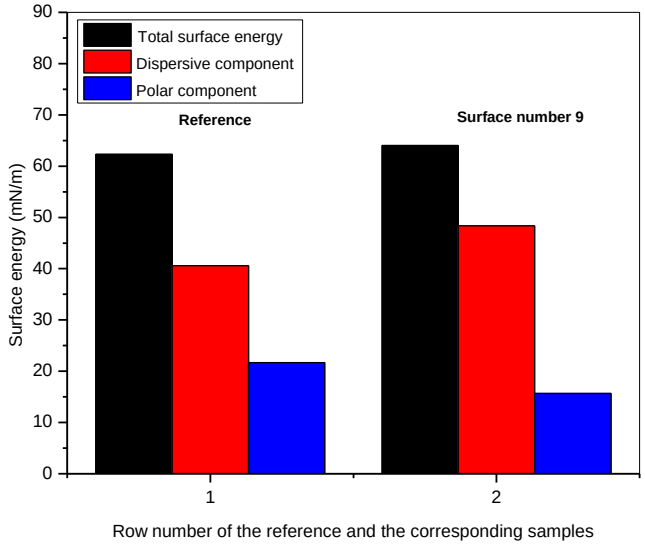
Total surface energy
Dispersive component
Polar component
Reference
Surface number 9
Surface energy (mN/m)
Row number of the reference and the corresponding samples

Appendix M| Column graphs of the surface energy measurements of the first category of samples (NTP deposited PO_x thin film)

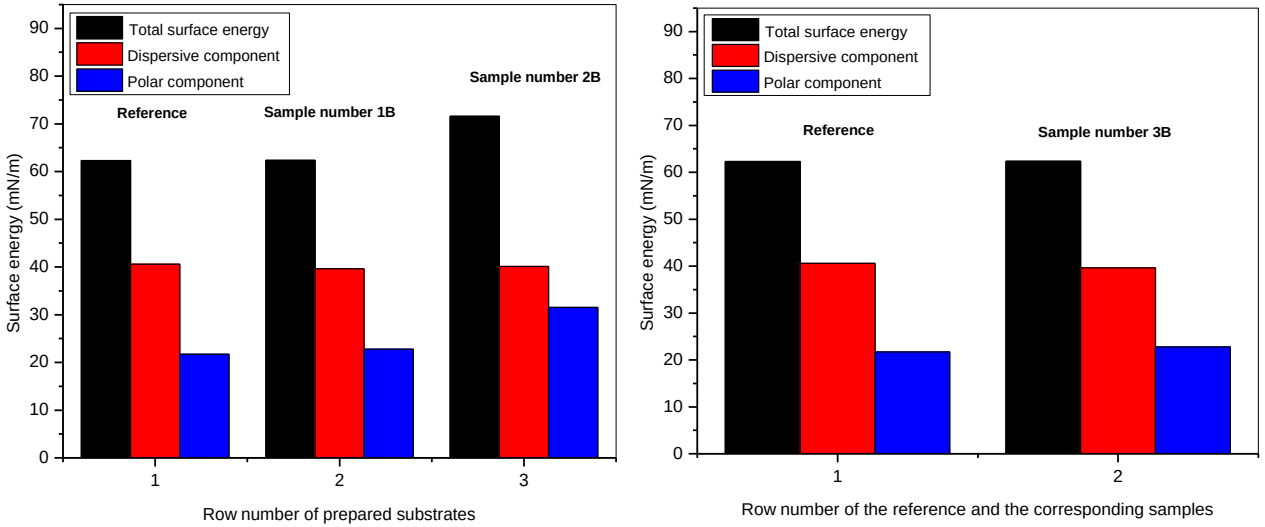

Appendix N| Column graphs of the surface energy measurements of the second category of samples (NTP deposited PO_x thin film)

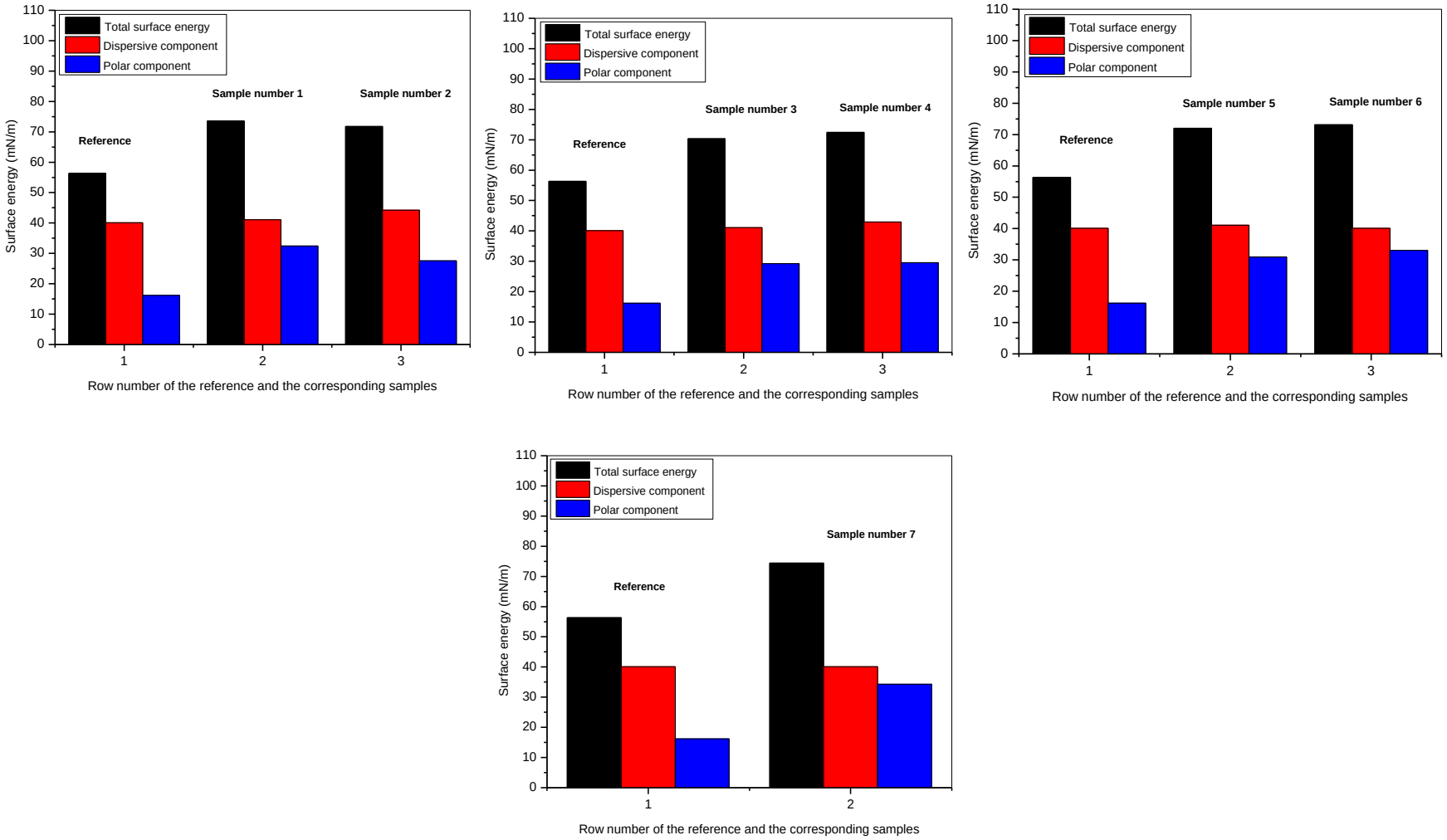

Appendix O| Column graphs of the surface energy measurement values of the lone category of samples (NTP deposited Terpinene-4-ol thin film)

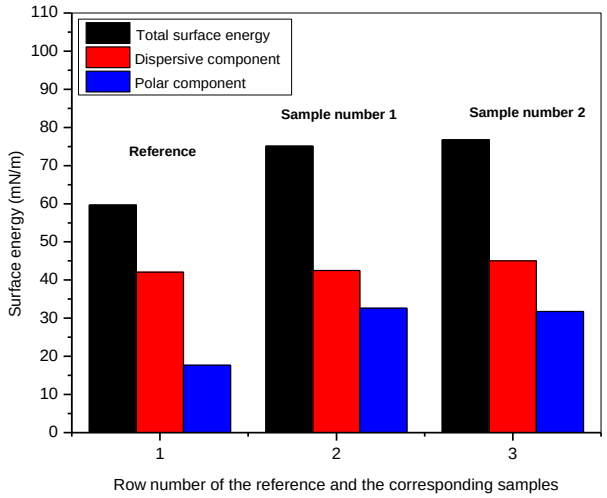

Appendix P| Column graph of the surface energy measurement values of the lone category of samples (NTP deposited (Dimethyl amino) ethyl methacrylate thin film)

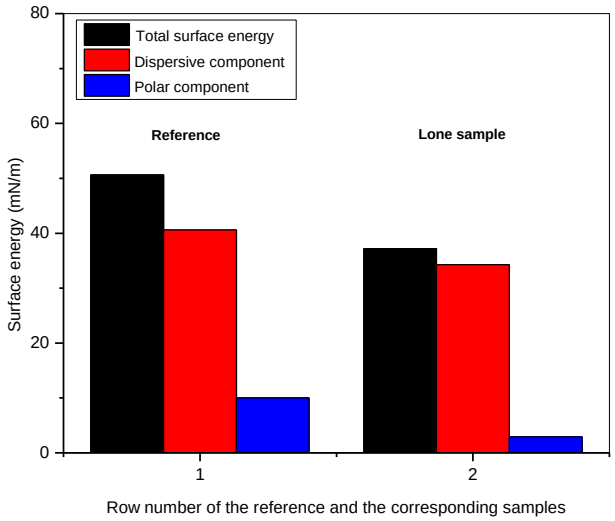

Appendix Q| Column graph of the surface energy measurement values of the lone sample (NTP deposited Bis(dimethyl amino) dimethyl silane thin film))

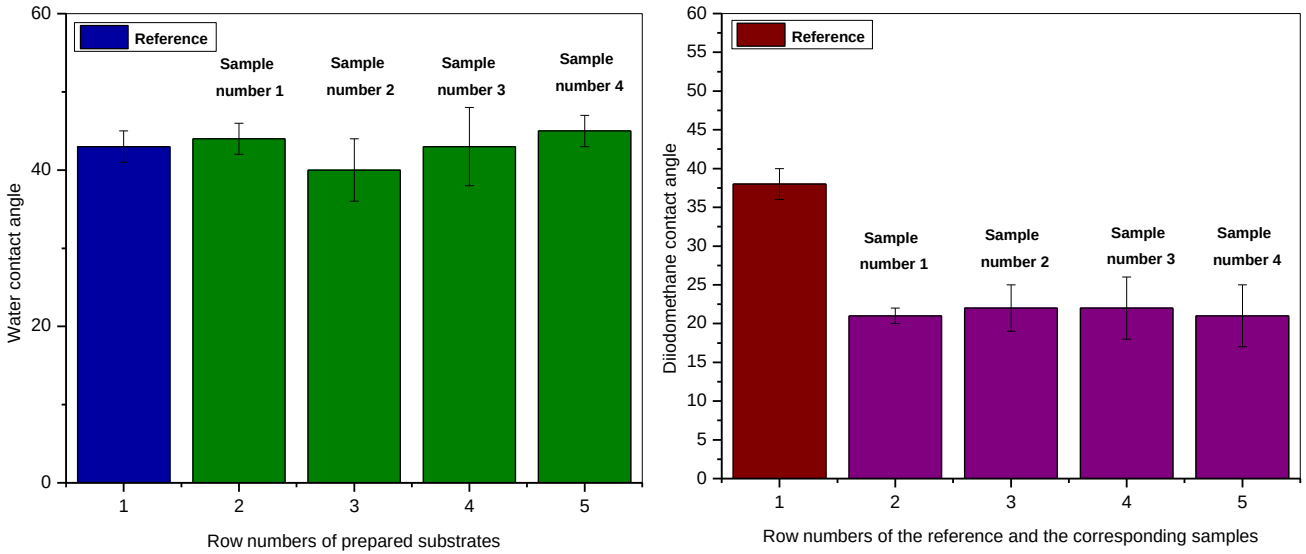

Appendix R| Column graphs with error bars of the contact angle measurement values of the first category of samples (NTP deposited PO_x thin film) (part A)

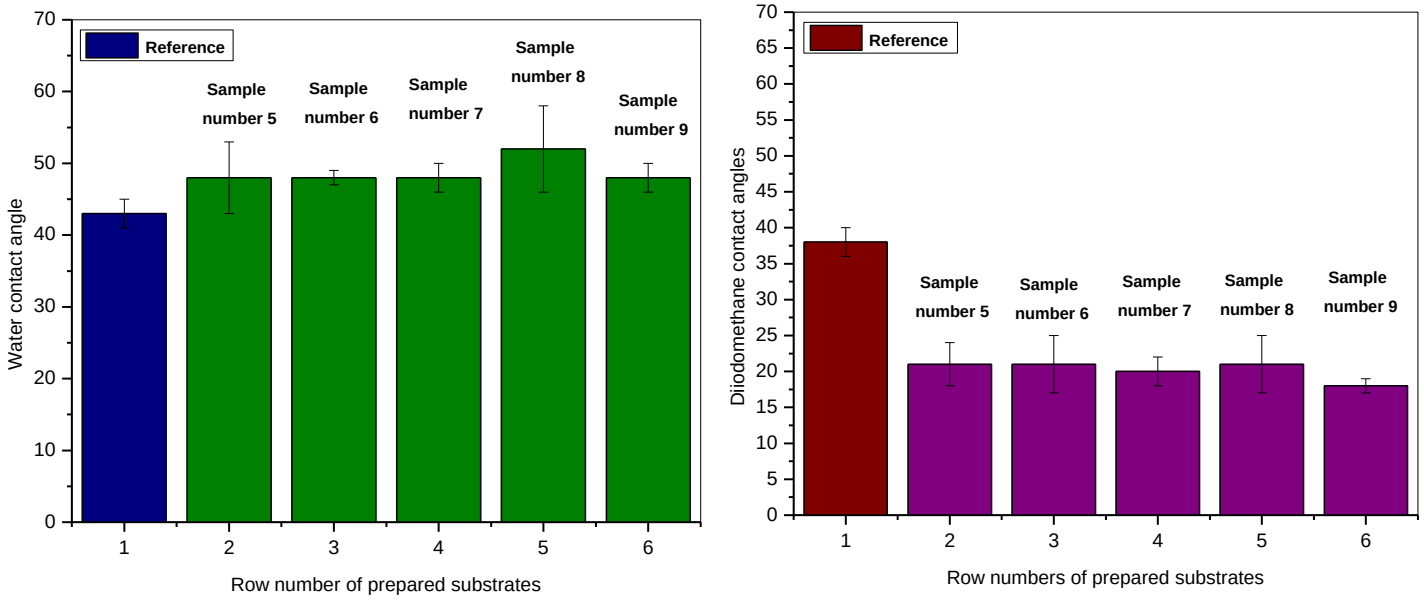

Appendix S| Column graphs with error bars of the contact angle measurement values of the first category of samples (NTP deposited PO_x thin film) (part B)

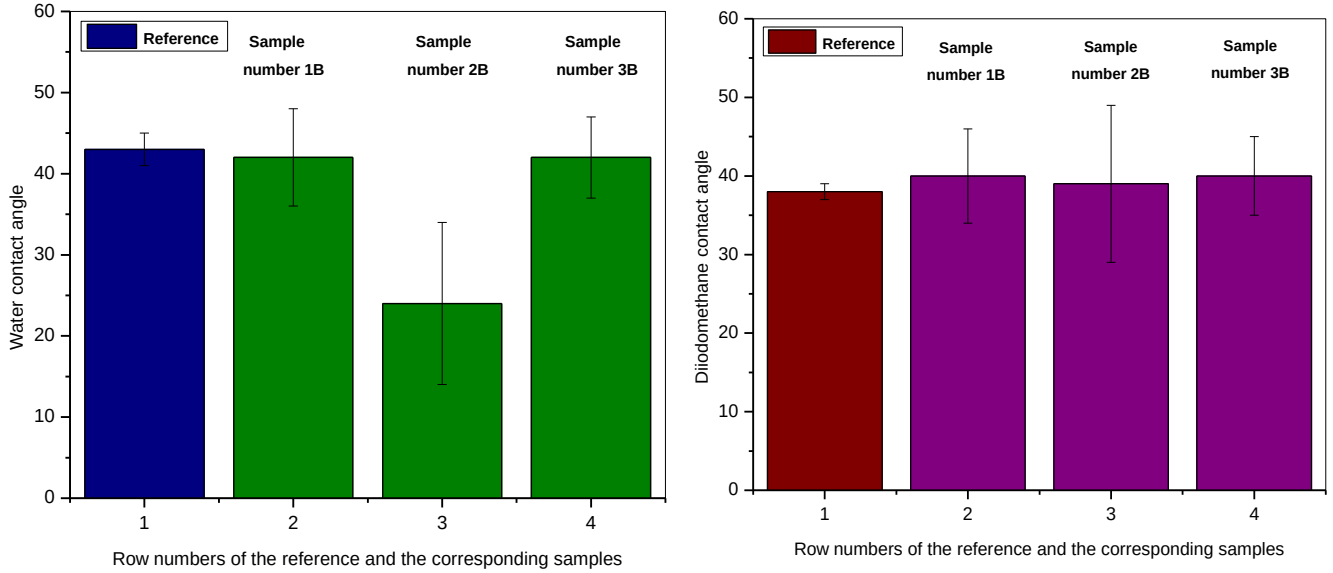

Appendix T| Column graphs with error bars of the contact angle measurement values of the second category of samples (NTP deposited PO_x thin film)

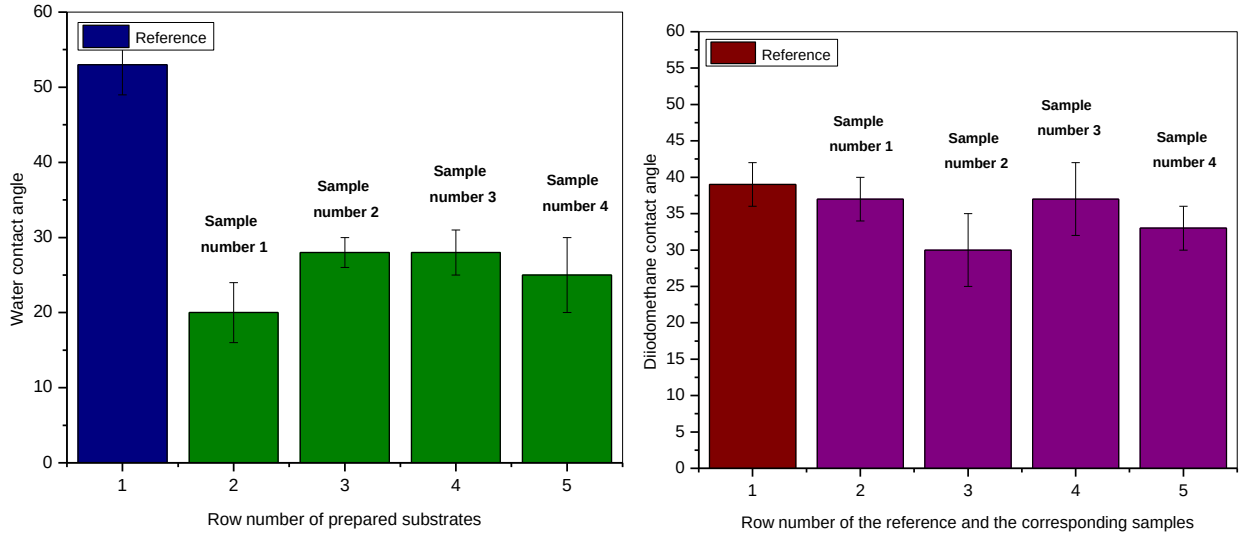

Appendix U| Column graphs with error bars of the contact angle measurement values of the lone category samples (NTP deposited Terpinene-4-ol thin film) **(Part A)**

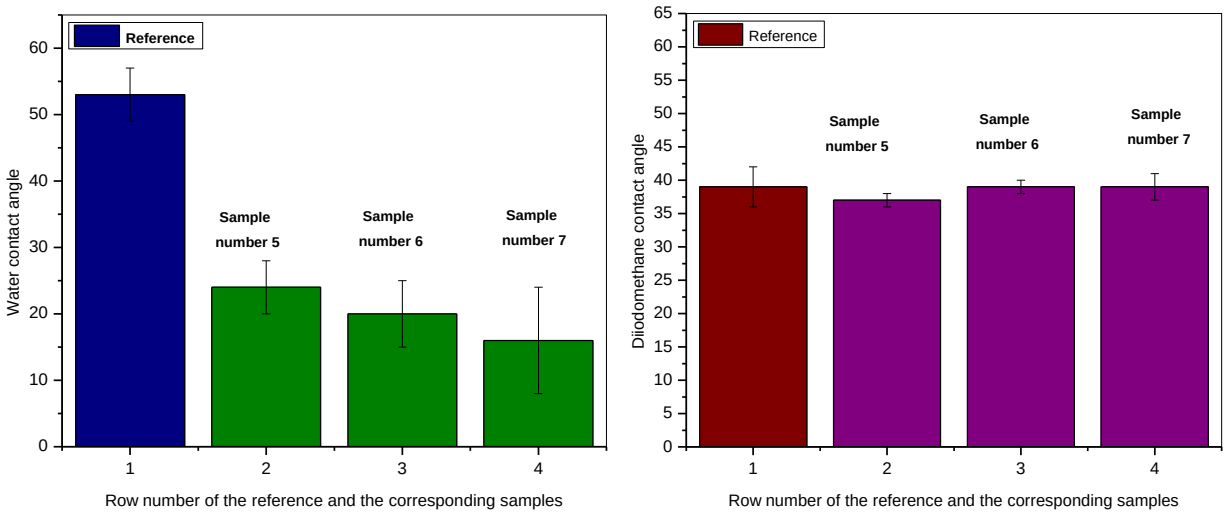

Appendix V| Column graphs with error bars of the contact angle measurement values of the lone category of samples (plasma deposited Terpinene-4-ol thin film) **(Part B)**

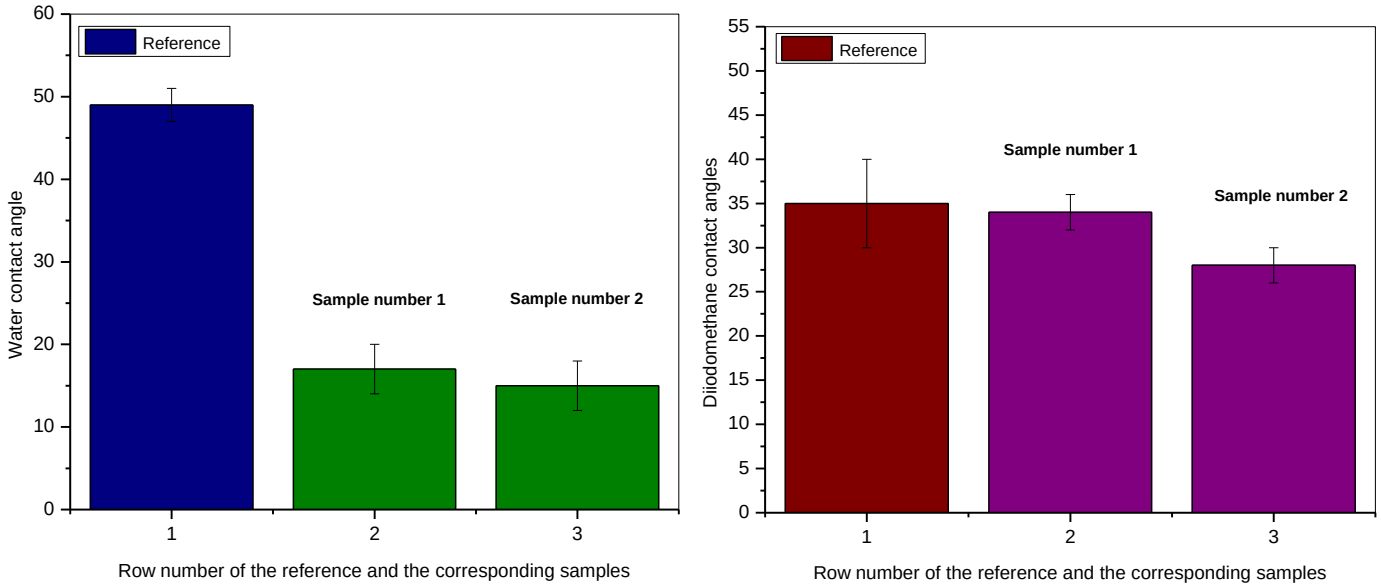

Appendix W| Column graphs with error bars of the contact angle measurement values of the lone category of samples (NTP deposited (Dimethyl amino)ethyl methacrylate thin film)

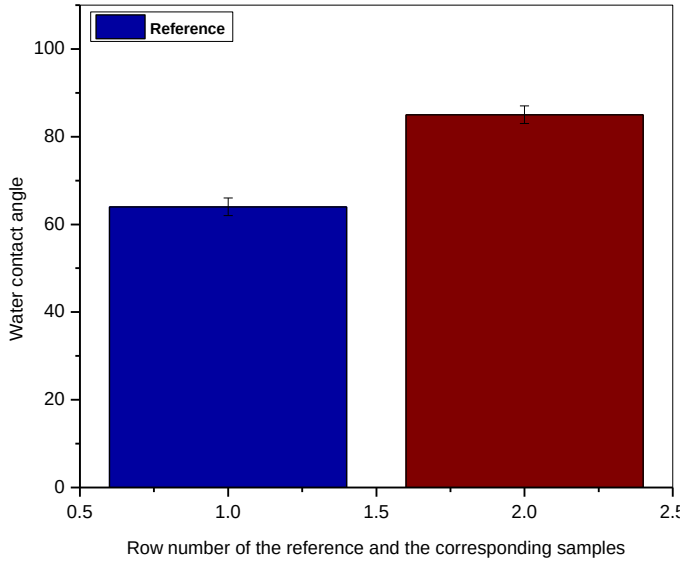

Appendix X| Column graph of the surface energy measurement values of the lone sample (NTP deposited Bis(dimethyl amino) dimethyl silane thin film)

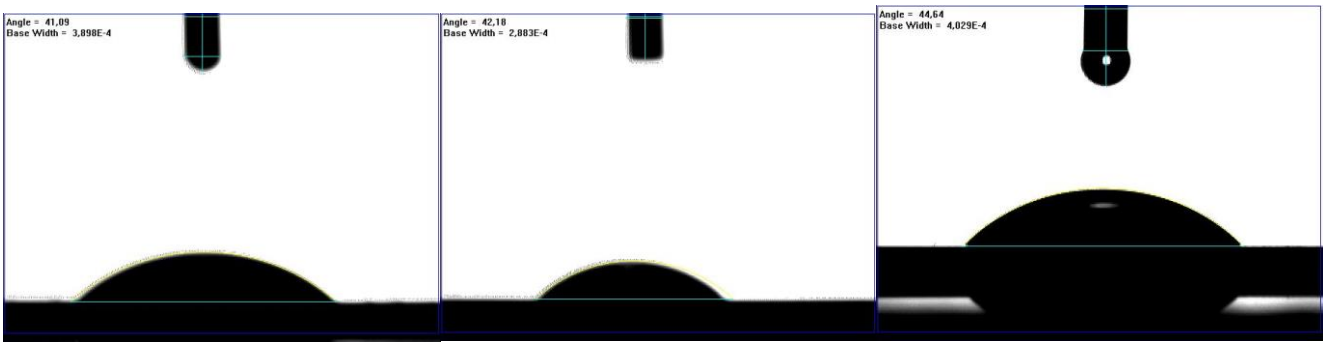

Water contact angle diagrams of silicon wafer as the reference

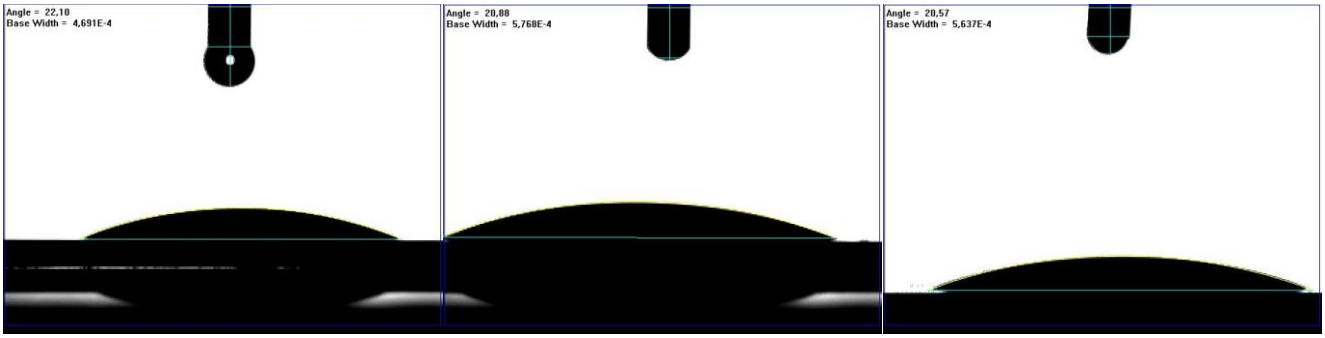

Water contact angle diagrams of Sample 1 (first category of samples)

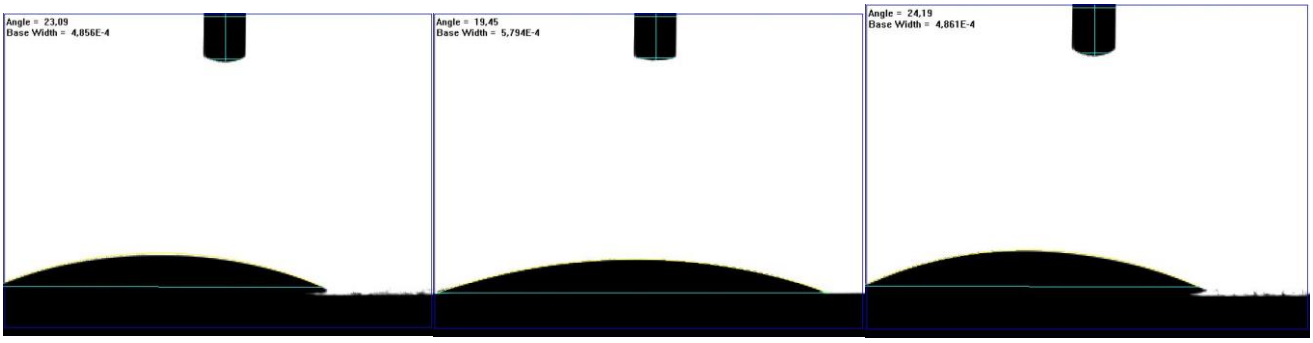

Water contact angle diagrams of Sample 2 (first category of samples)

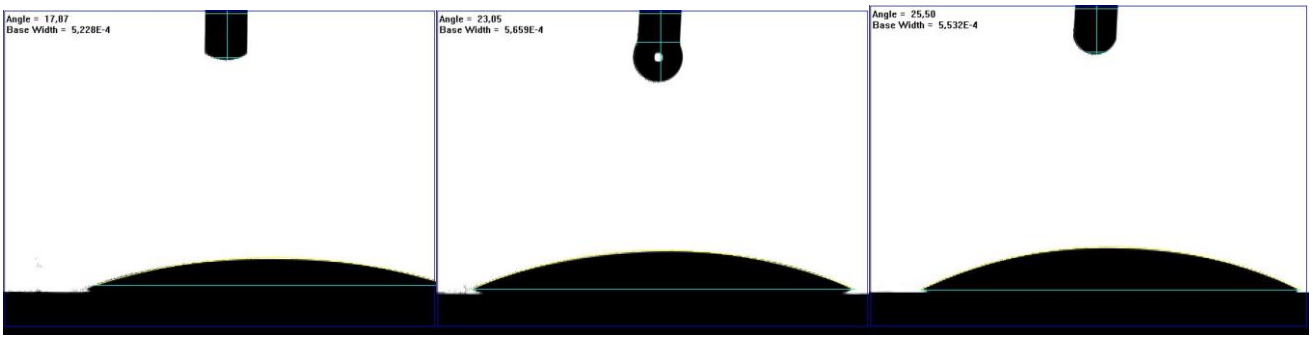

Water contact angle diagrams of Sample 3 (first category of samples)

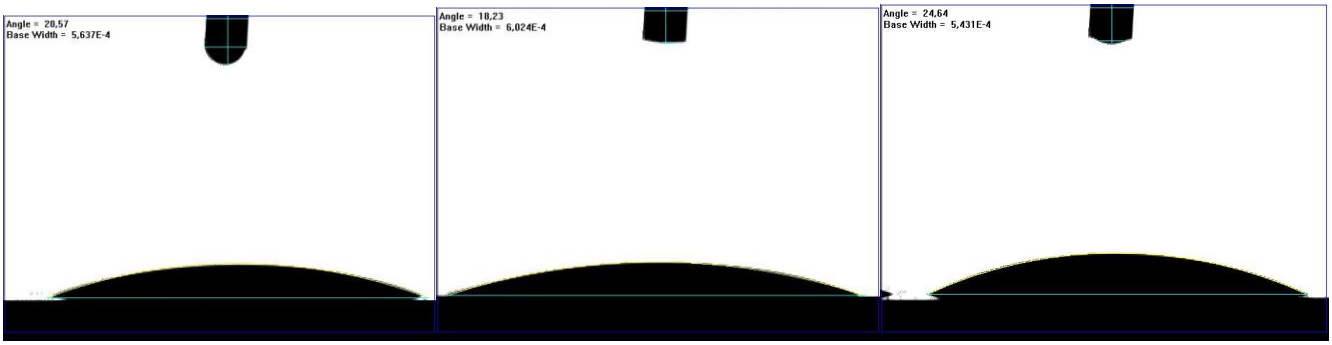

Water contact angle diagrams of Sample 4 (first category of samples)

Water contact angle diagrams of Sample 5 (first category of samples)

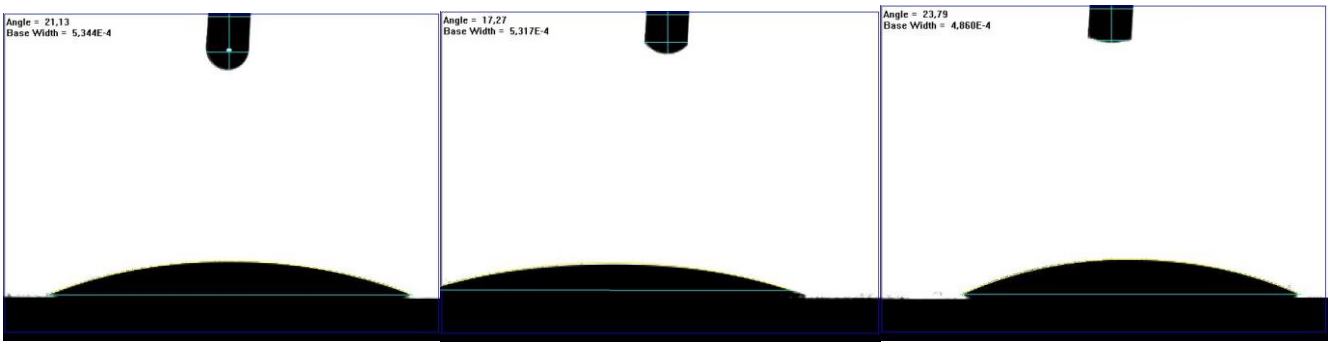

Water contact angle diagrams of Sample 6 (first category of samples)

Water contact angle diagrams of Sample 7 (first category of samples)

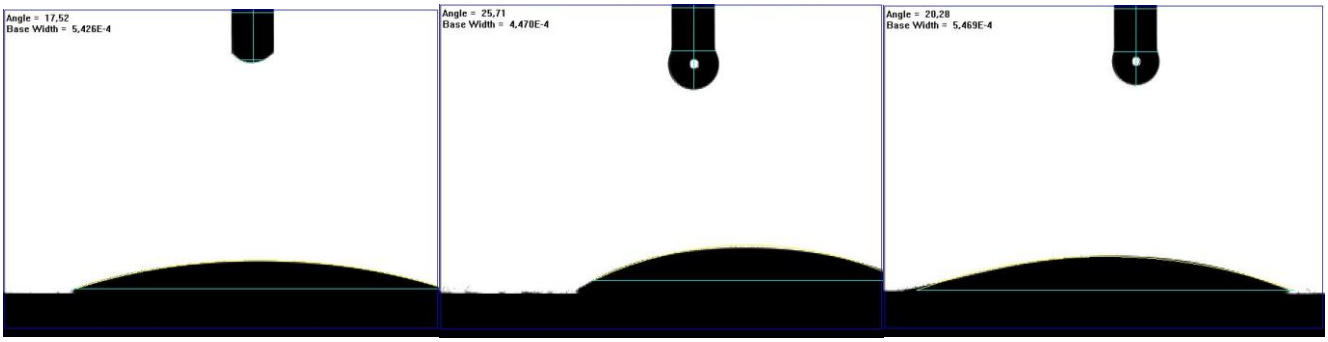

Water contact angle diagrams of Sample 8 (first category of samples)

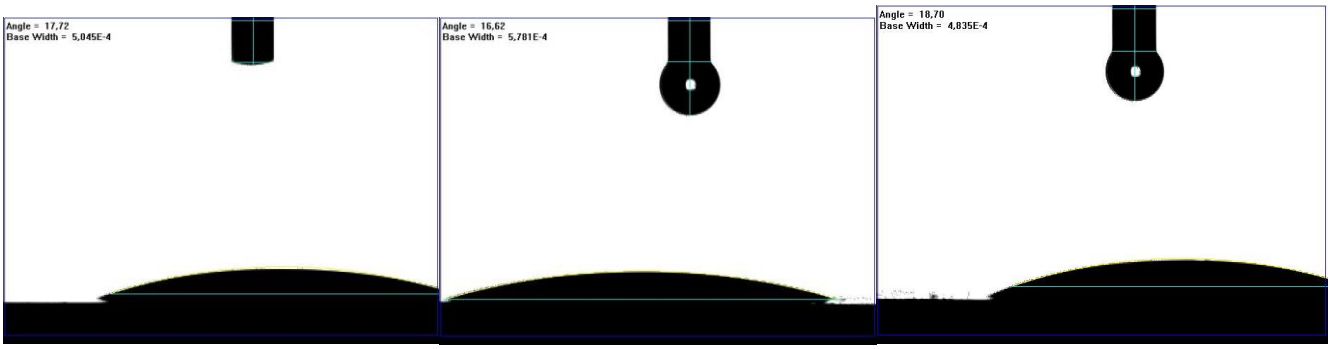

Water contact angle diagrams of Sample 9 (first category of samples)

Appendix Y| Water contact angle diagrams of the first category of samples (NTP deposited PO_x thin film)

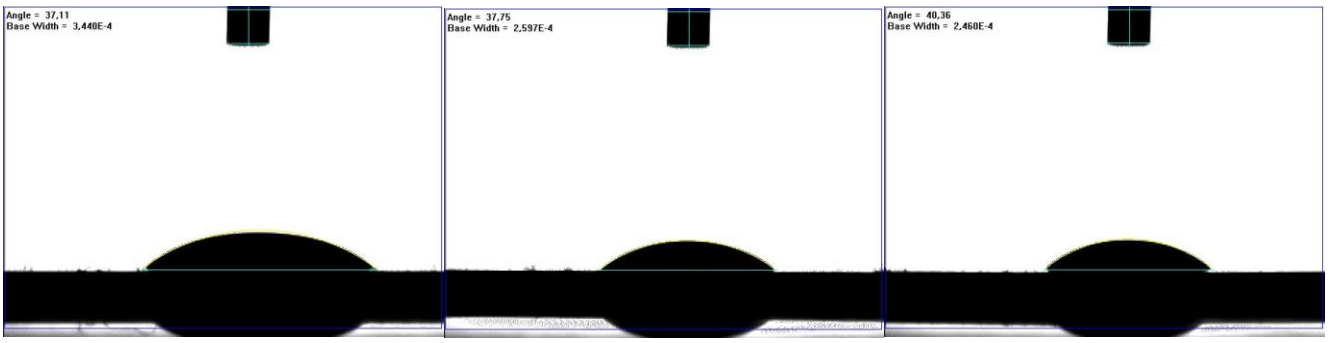

Diiodomethane contact angle diagrams of Silicon wafer as the reference

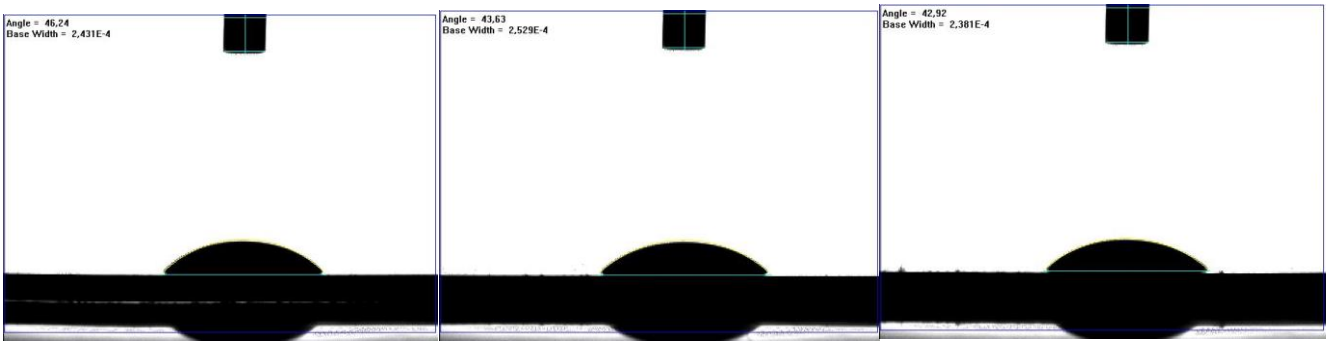

Diiodomethane contact angle diagrams of Sample 1 (first category of samples)

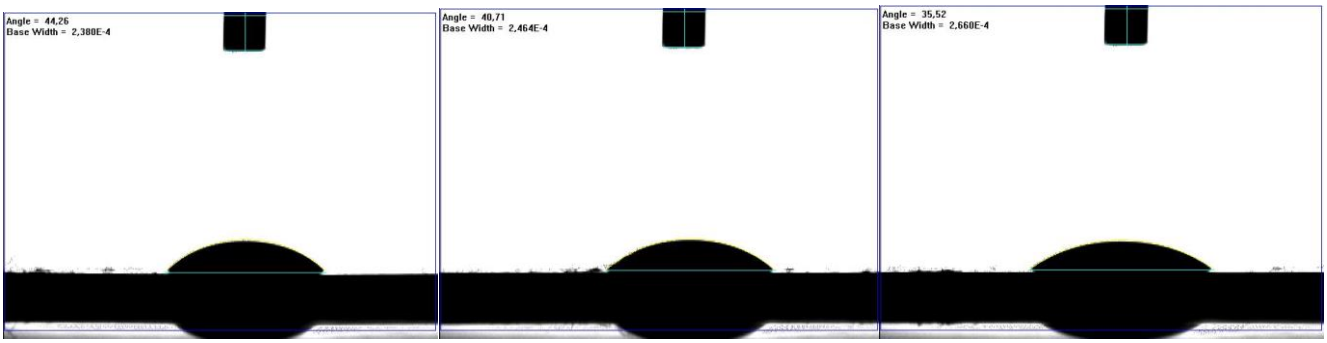

Diiodomethane contact angle diagrams of Sample 2 (first category of samples)

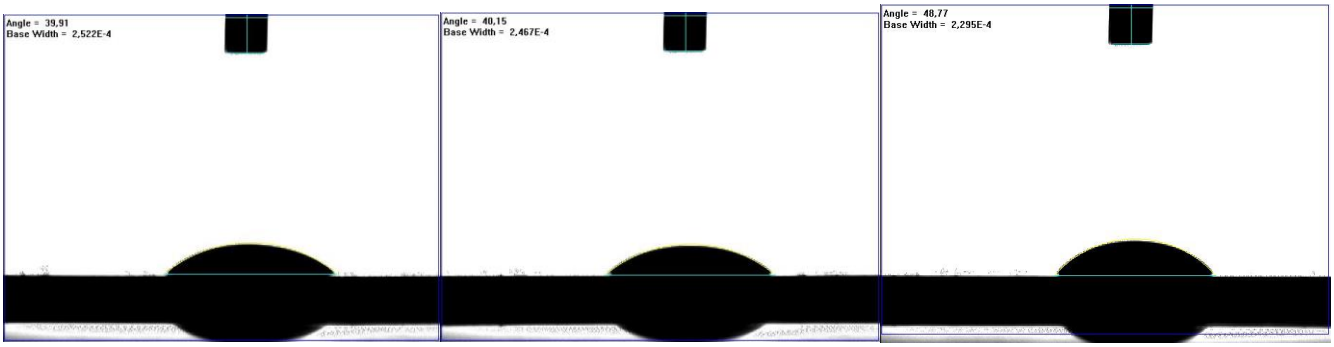

Diiodomethane contact angle diagrams of Sample 3 (first category of samples)

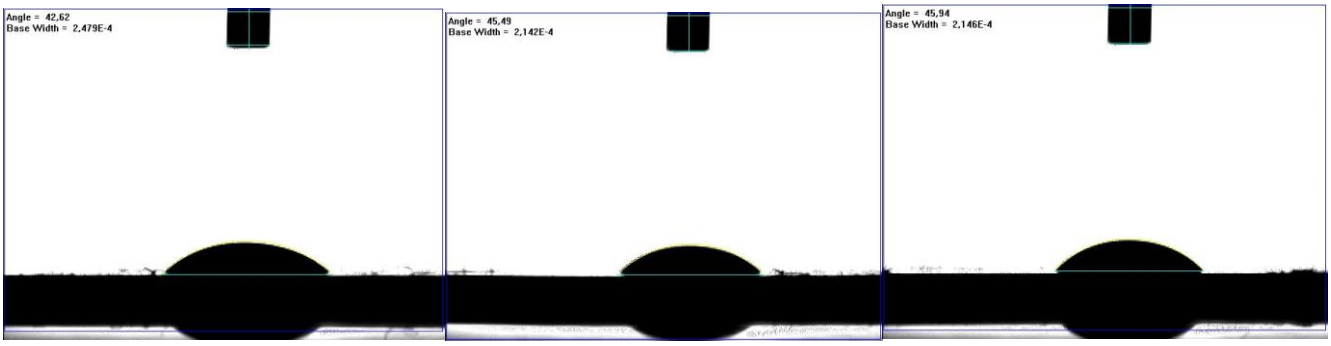

Diiodomethane contact angle diagrams of Sample 4 (first category of samples)

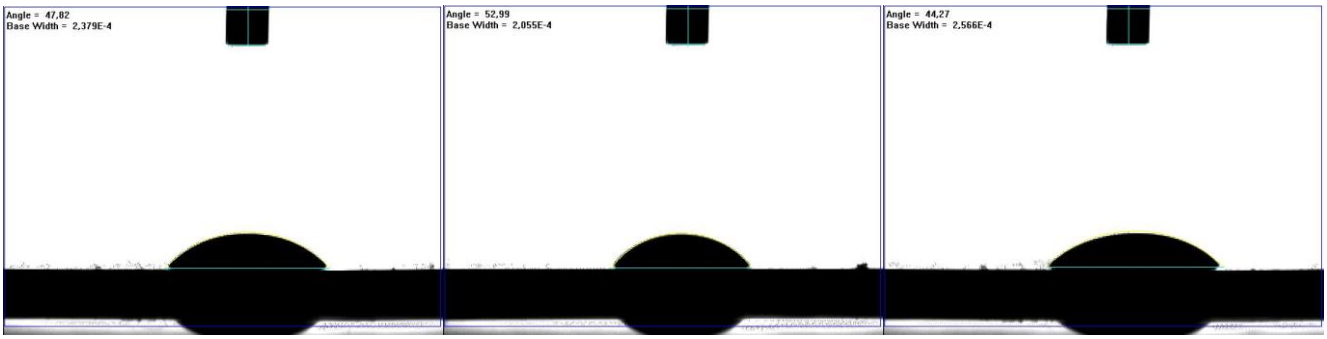

Diiodomethane contact angle diagrams of Sample 5 (first category of samples)

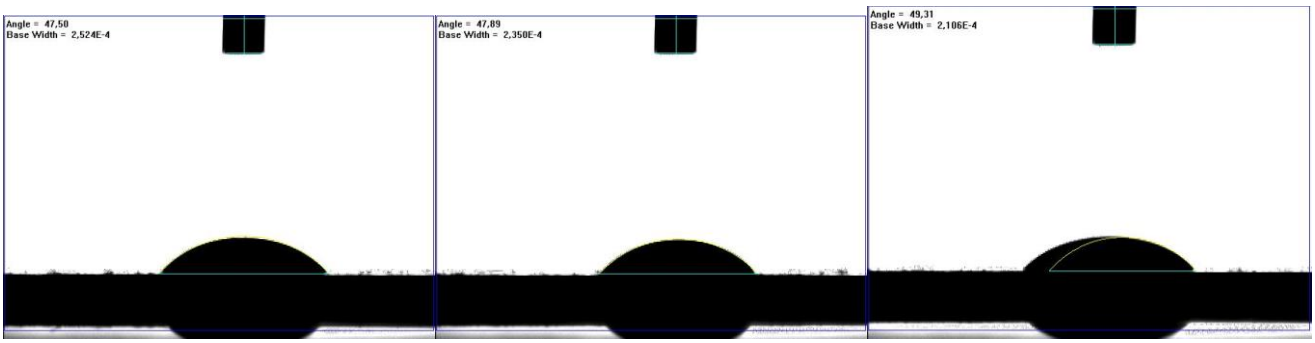

Diiodomethane contact angle diagrams of Sample 6 (first category of samples)

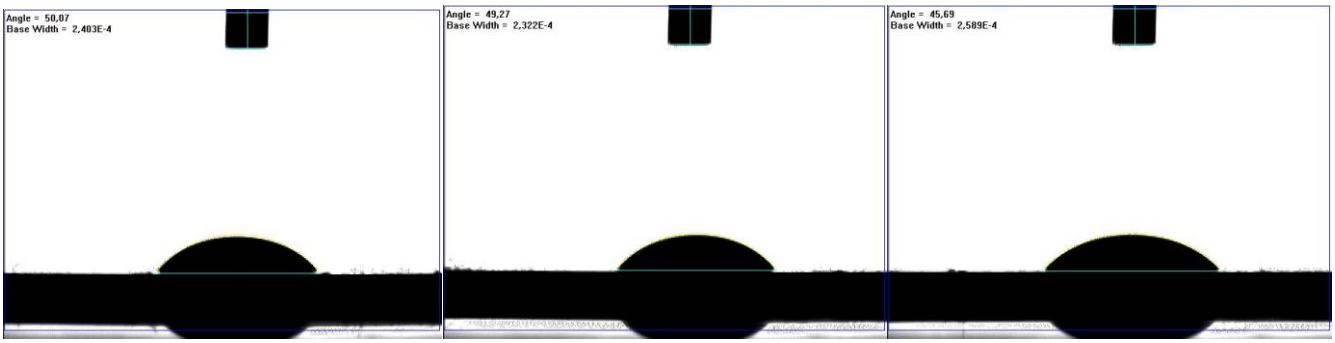

Diiodomethane contact angle diagrams of Sample 7 (first category of samples)

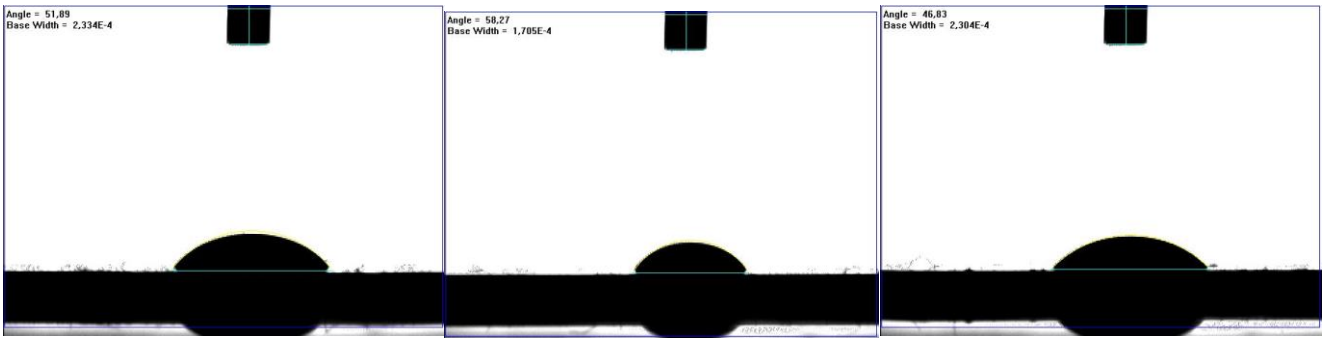

Diiodomethane contact angle diagrams of Sample 8 (first category of samples)

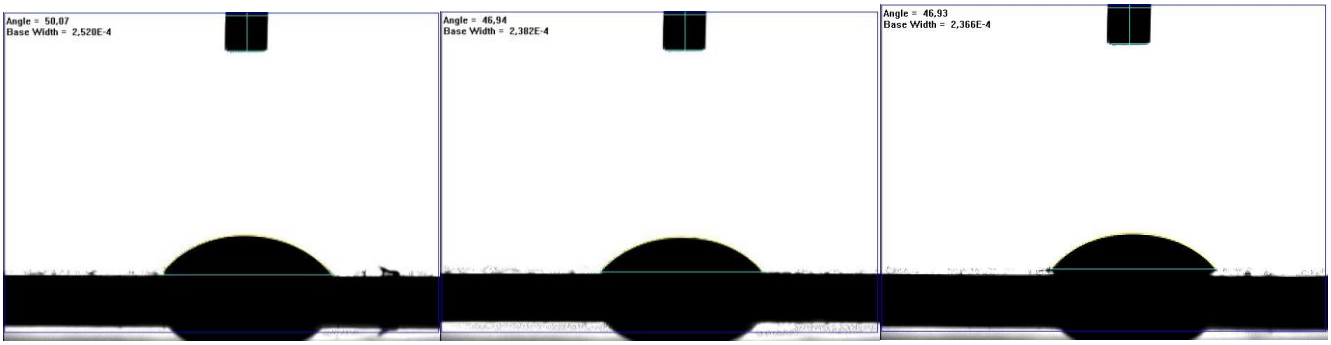

Diiodomethane contact angle diagrams of Sample 9 (first category of samples)

Appendix Z| Diiodomethane contact angle diagrams of the first category of samples (NTP deposited PO_x thin films)

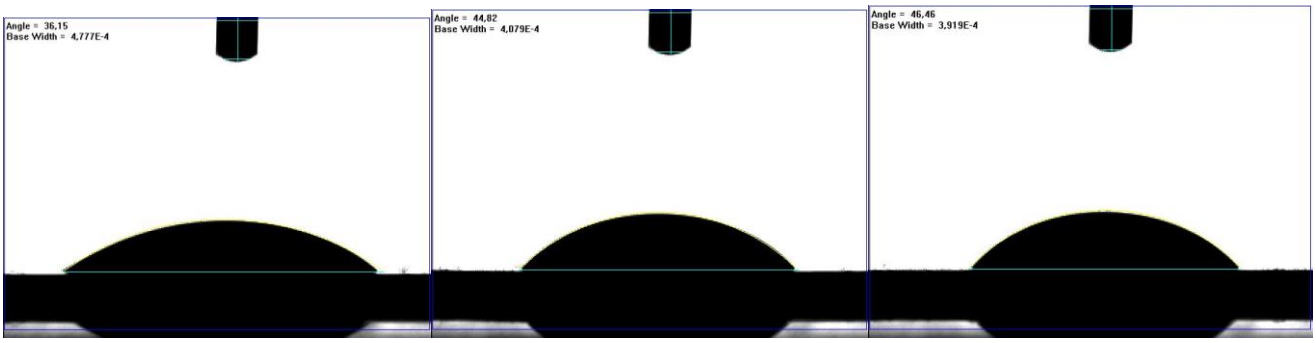

Water contact angle diagrams of Sample 1B (second category of samples)

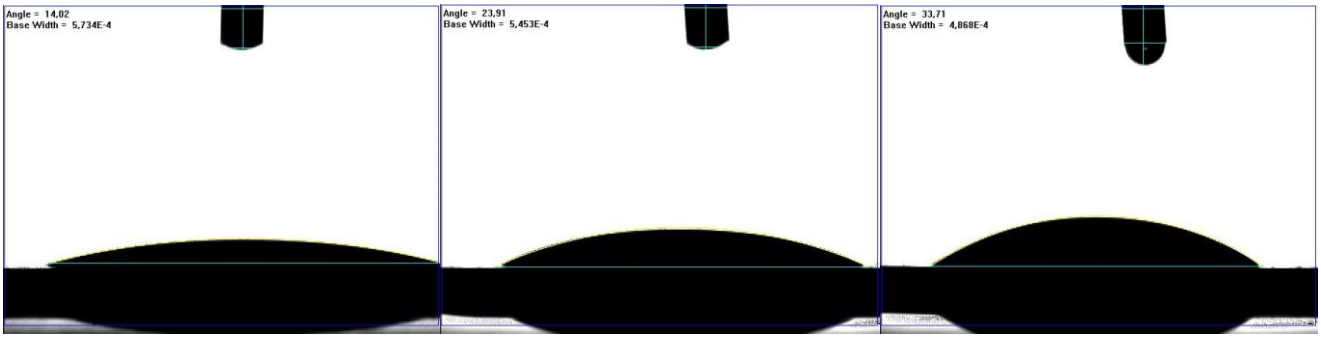

Water contact angle diagrams of Sample 2B (second category of samples)

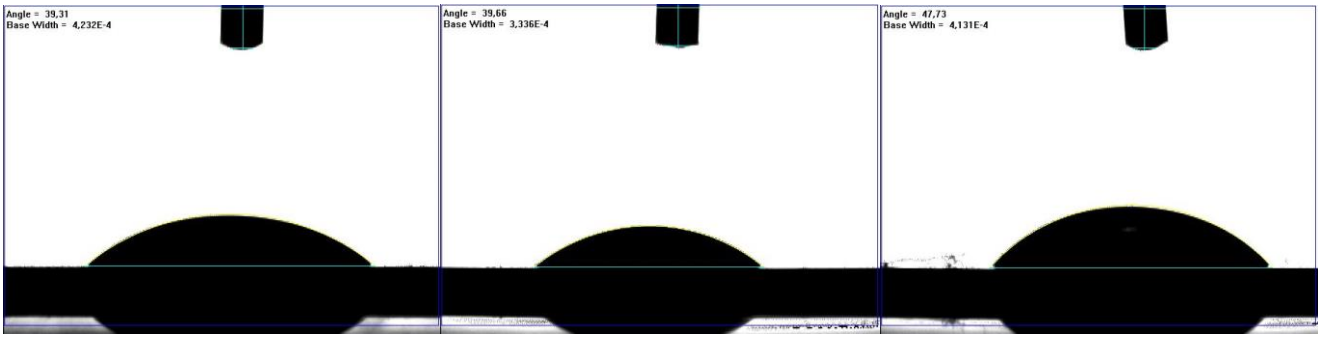

Water contact diagrams of Sample 3B (second category of samples)

Appendix AA| Water contact angle diagrams of the second category of samples (NTP deposited PO_x thin film)

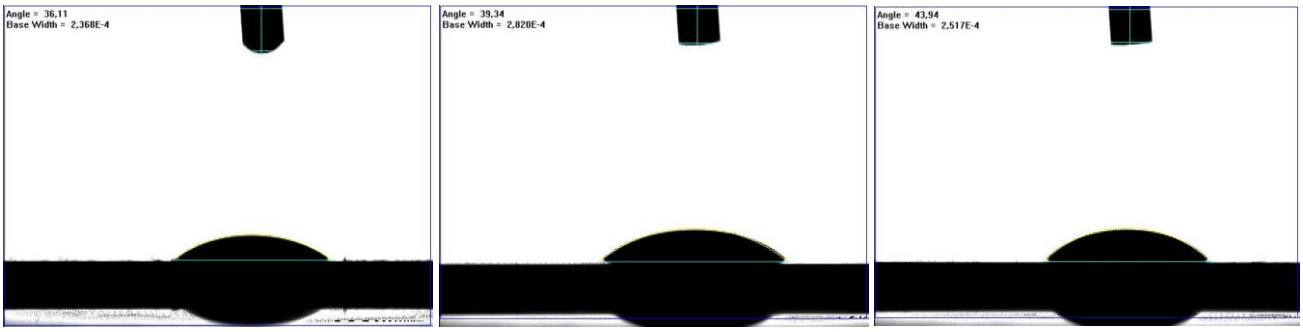

Diiodomethane contact angle diagrams of Sample 1B (second category of samples)

Diiodomethane contact angle diagrams of Sample 2B (second category of samples)

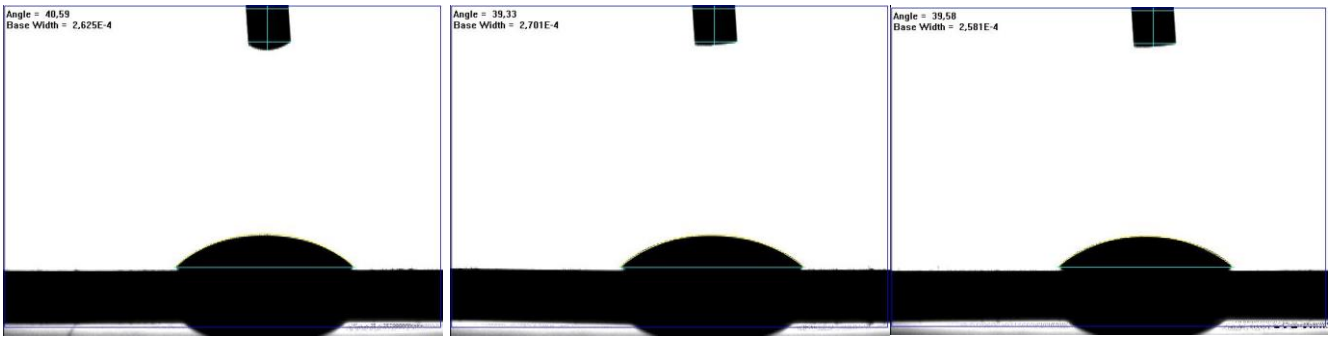

Diiodomethane contact angle diagrams of Sample 3B (Second category of samples)

Appendix AB| Diiodomethane contact angle diagrams of the second category of samples (NTP deposited PO_x thin films)

Water contact angle diagrams of silicon as the reference

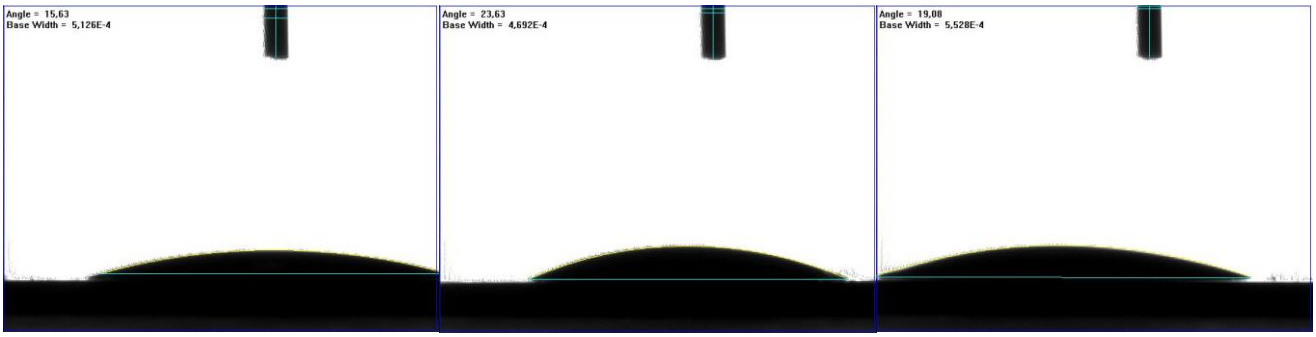

Water contact angle diagrams of sample 1 (first category of samples)

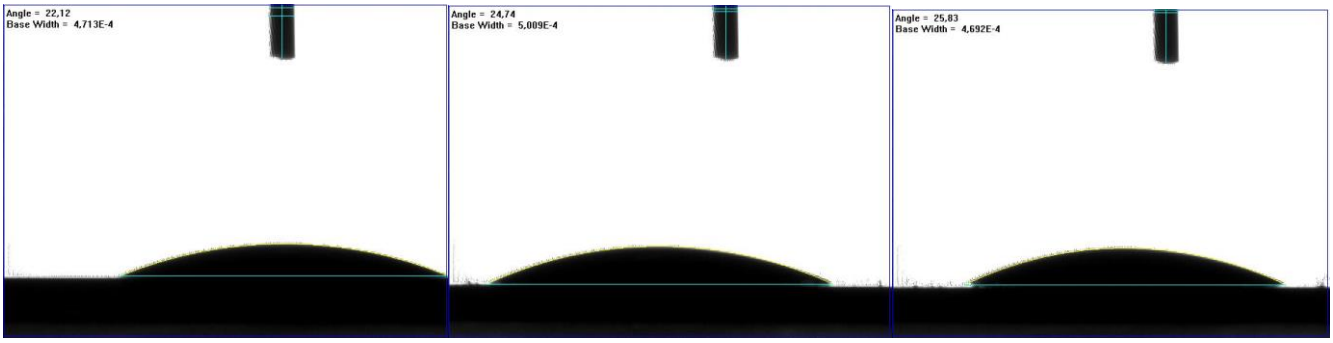

Water contact angle diagrams of sample 2 (first category of samples)

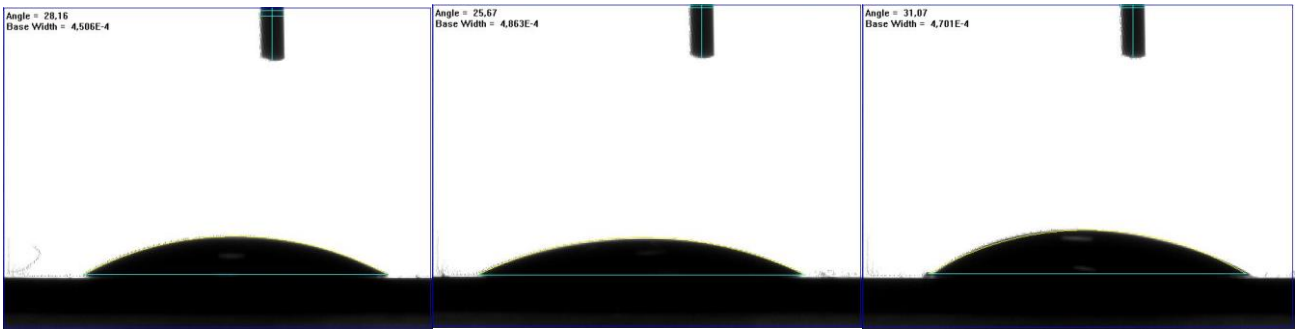

Water contact angle diagrams of sample 3 (first category of samples)

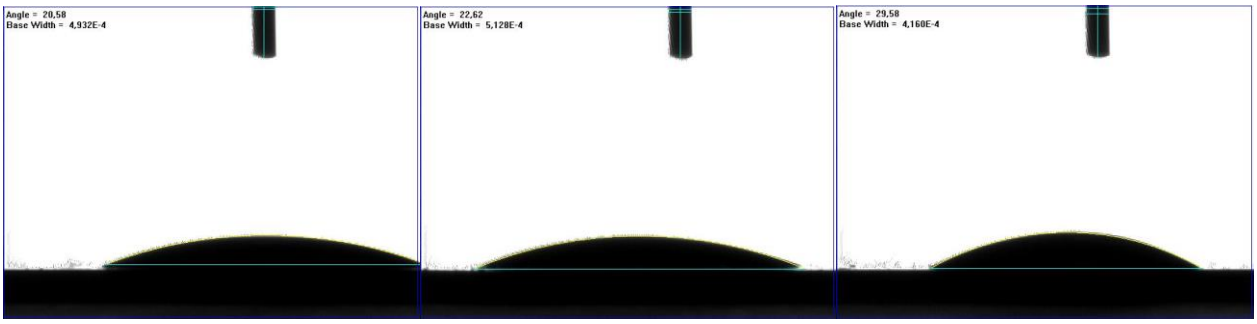

Water contact angle diagrams of sample 4 (first category of samples)

Water contact angle diagrams of sample 5 (first category of samples)

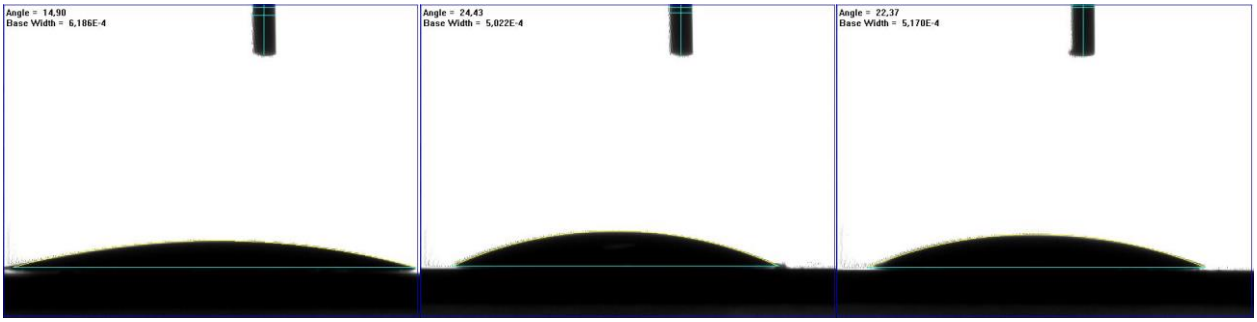

Water contact angle diagrams of sample 6 (first category of samples)

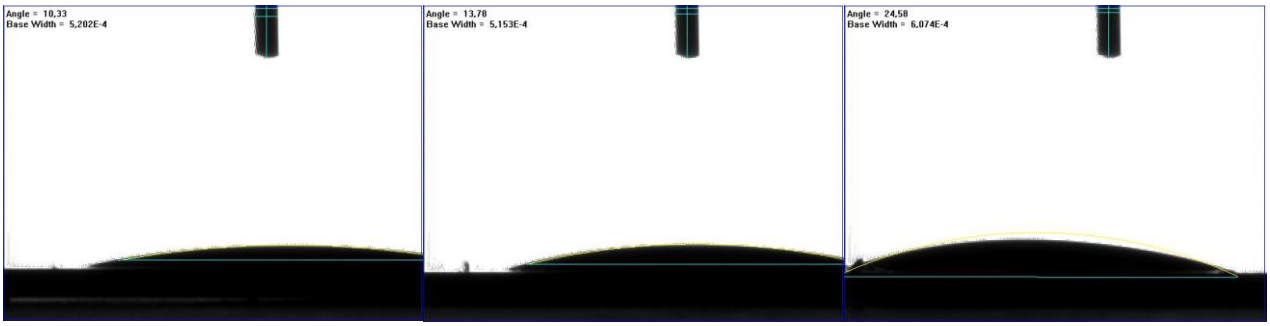

Water contact angle diagrams of sample 7 (second category of samples)

Appendix AC| Water contact angle diagrams of the lone category of samples (NTP deposited Terpinene-4-ol thin film)

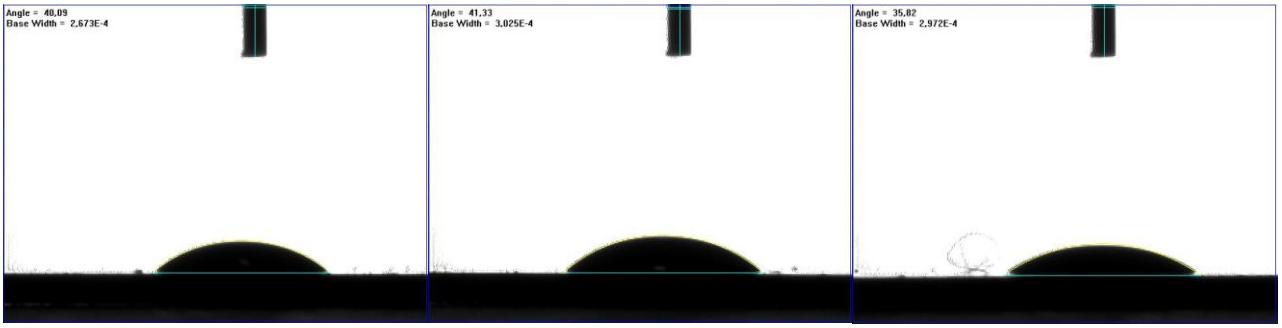

Diiodomethane contact angle diagrams of silicon as the reference

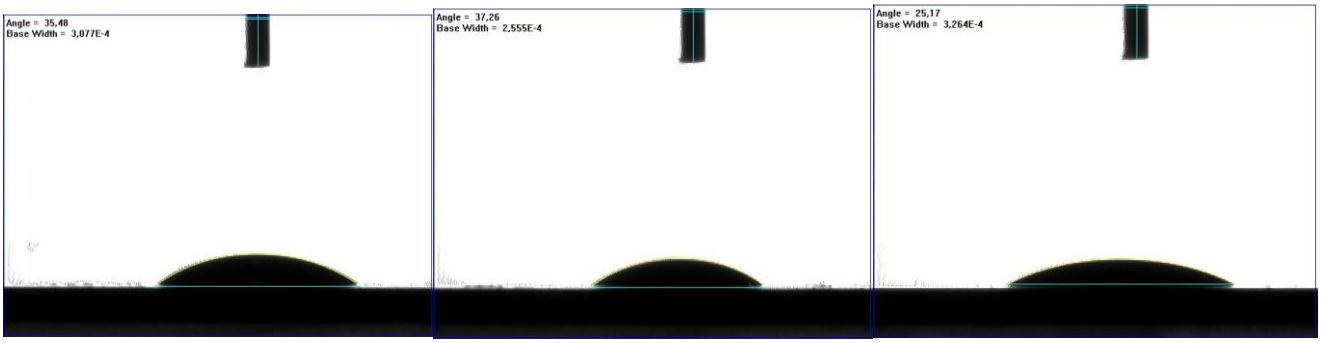

Diiodomethane contact angle diagrams on sample 1 (first category of samples)

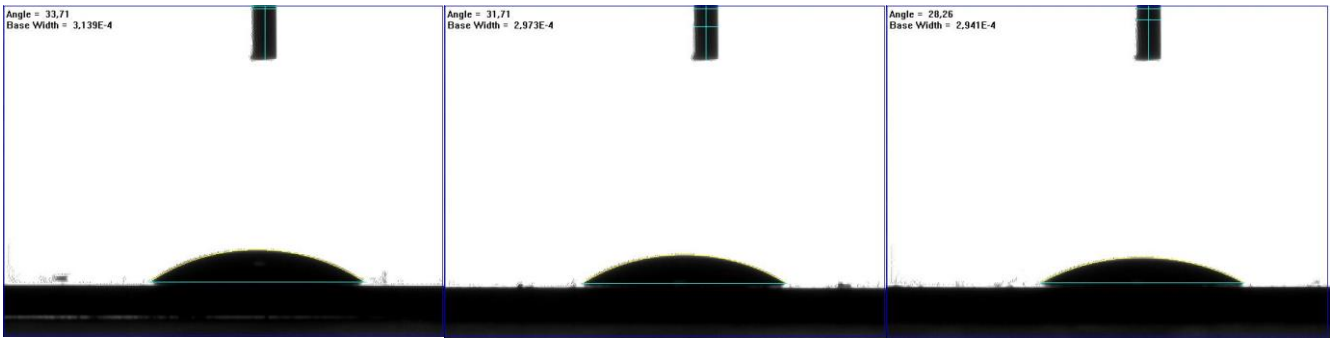

Diiodomethane contact angle diagrams on sample 2 (first category of samples)

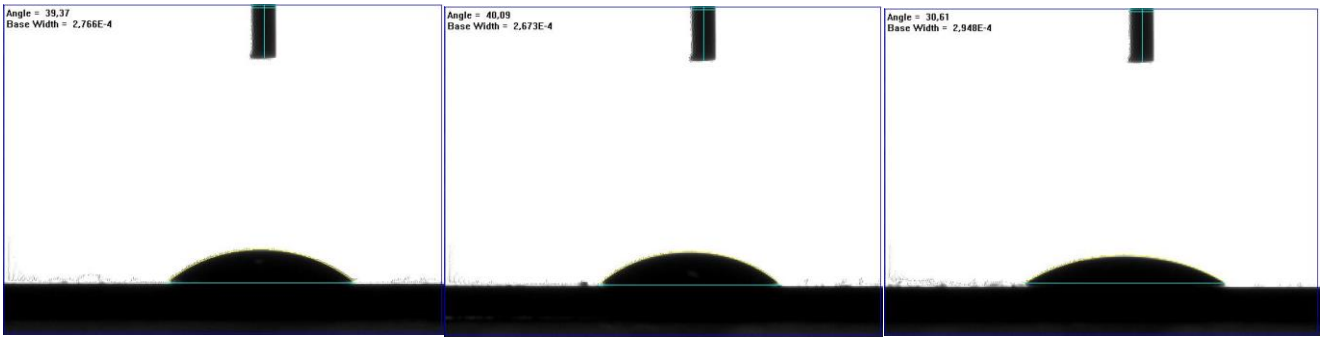

Diiodomethane contact angle diagrams on sample 3 (first category of samples)

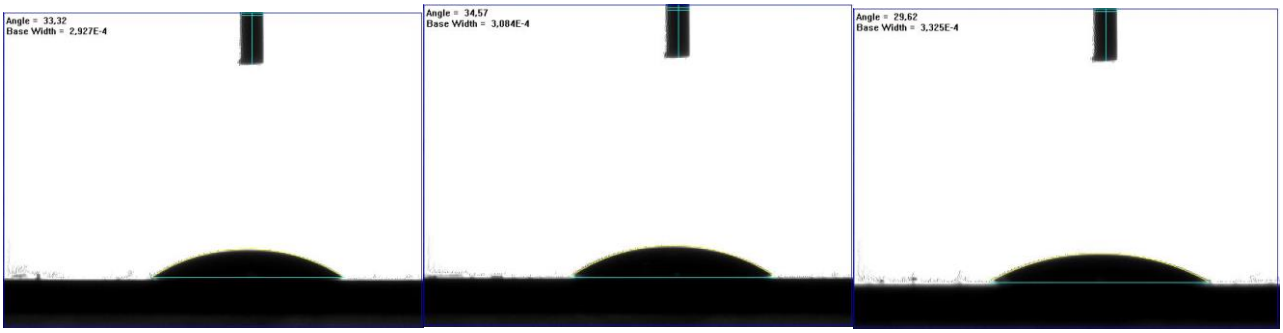

Diiodomethane contact angle diagrams on Sample 4 (first category of samples)

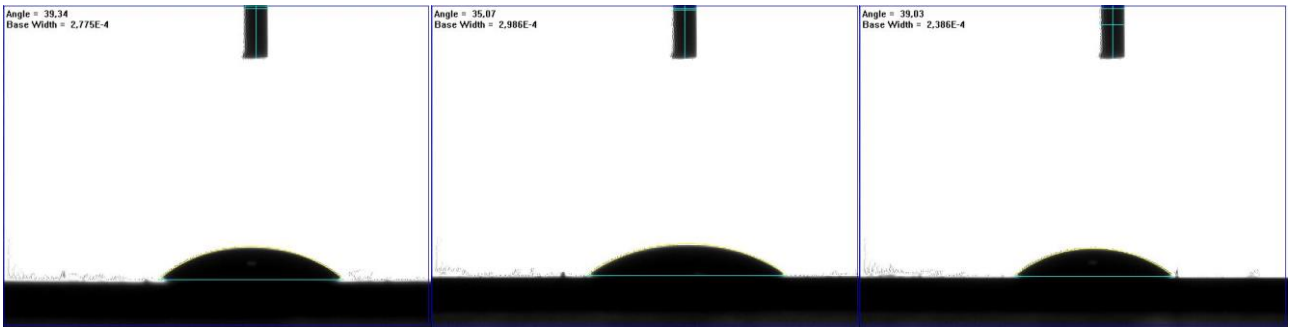

Diiodomethane contact angle on Sample 5 (first category of samples)

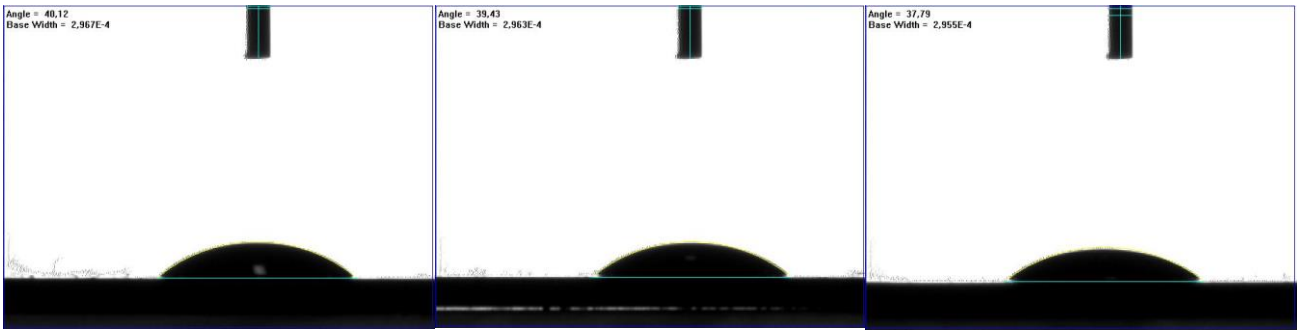

Diiodomethane contact angle on Sample 6 (first category of samples)

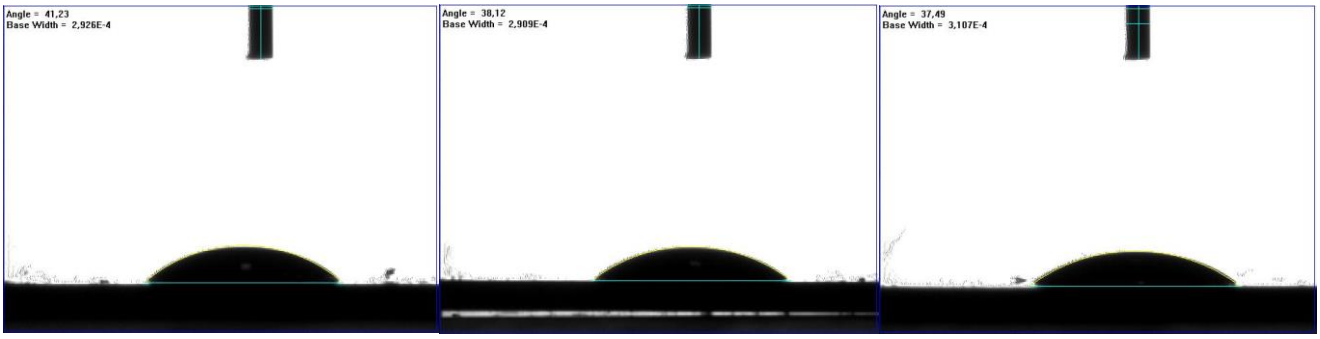

Diiodomethane contact angle on Sample 7 (first category of samples)

Appendix AD| Diiodomethane contact angle diagrams of the lone category of samples (Terpinene-4-ol thin film)

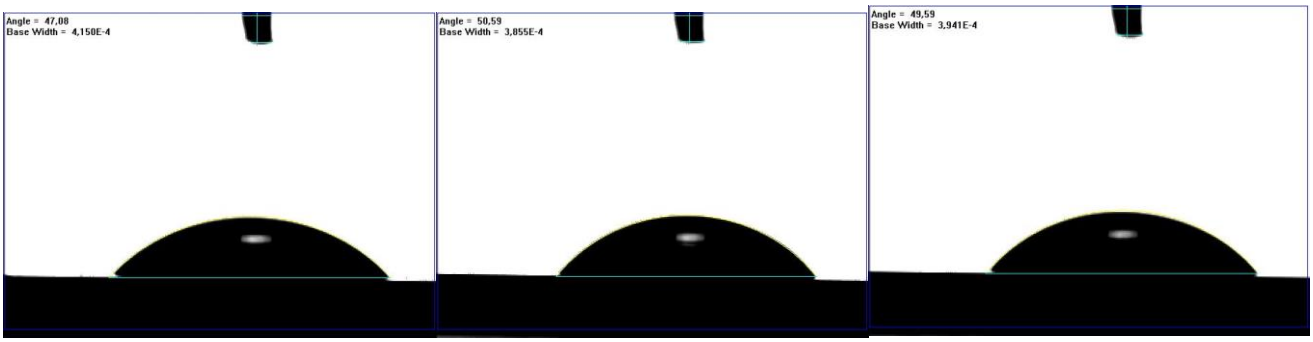

Water contact angle diagrams of silicon as the reference

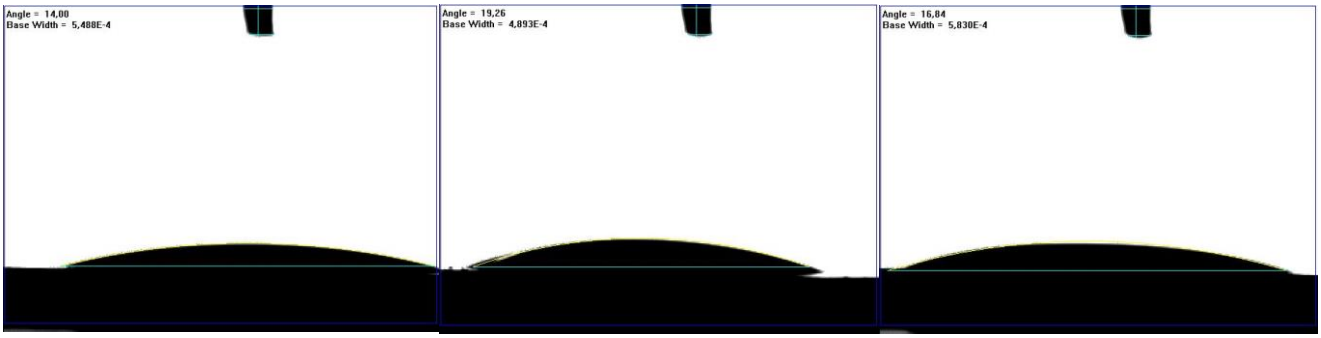

Water contact angle diagrams of sample 1 (lone category of samples)

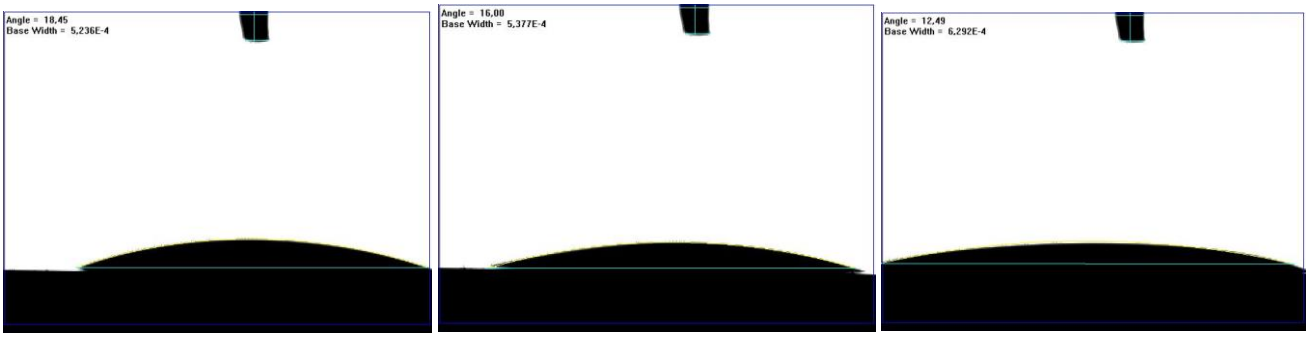

Water contact angle diagrams of sample 2 (lone category of samples)

Appendix AE| Water contact angle diagrams of the lone category of samples (NTP deposited Dimethyl amino) ethyl methacrylate thin film)

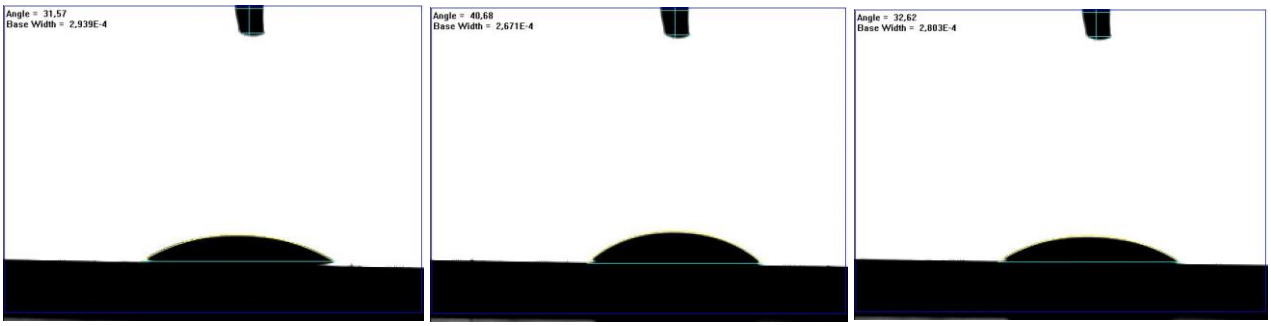

Diiodomethane contact angle diagrams of silicon as the reference (lone category of samples)

Diiodomethane contact angle diagrams of sample 1 (lone category of samples)

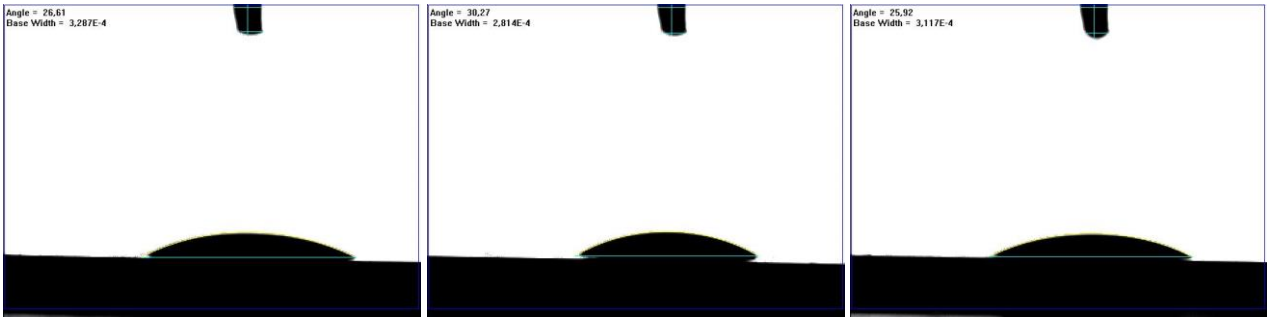

Diiodomethane contact angle diagrams of sample 2 (lone category of samples)

Appendix AF| Diiodomethane contact angle diagrams of the lone category of samples (NTP deposited Dimethylamino) ethyl methacrylate thin film)

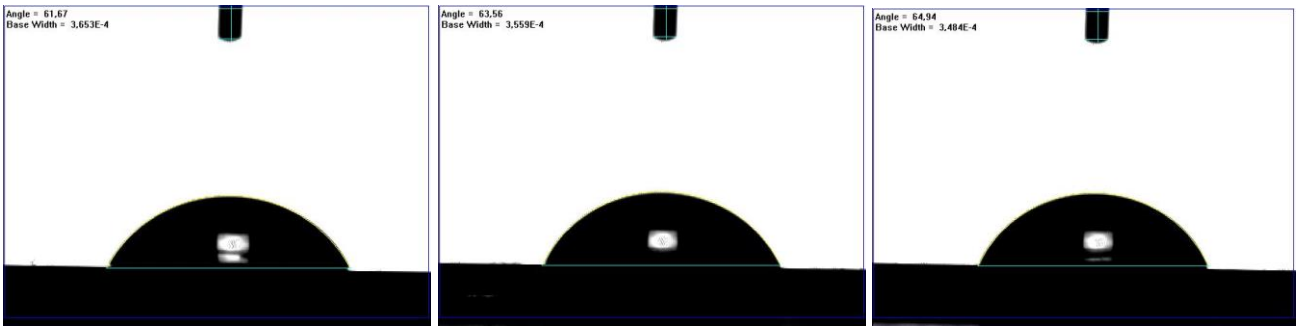

Water contact angle diagrams of silicon as the reference

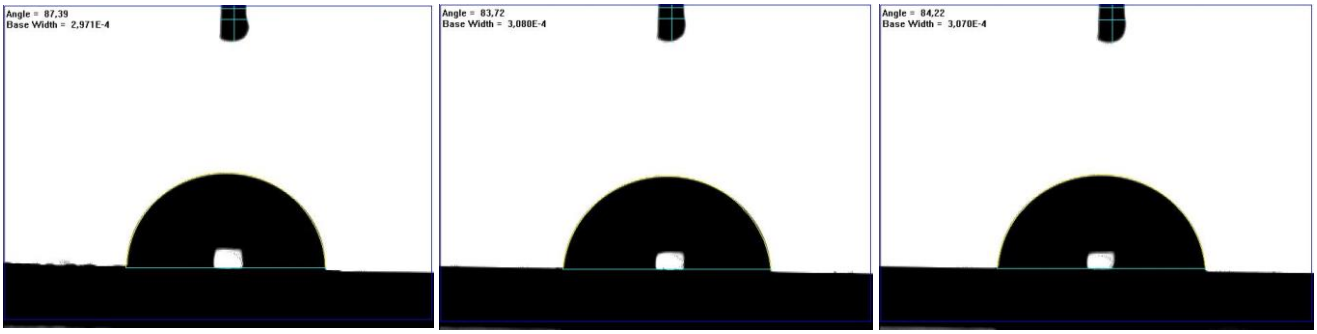

Water contact angle diagrams of the lone sample (Bis(dimethyl amino) dimethyl silane thin film)

Appendix AG| Water contact angle diagrams of the lone category of samples (NTP deposited Bis(dimethylamino) dimethyl silane thin film)

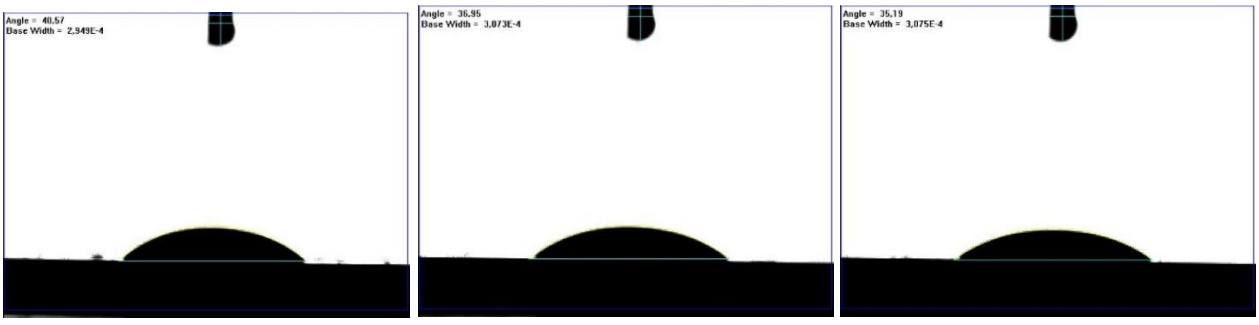

Diiodomethane contact angle diagrams of silicon as the reference

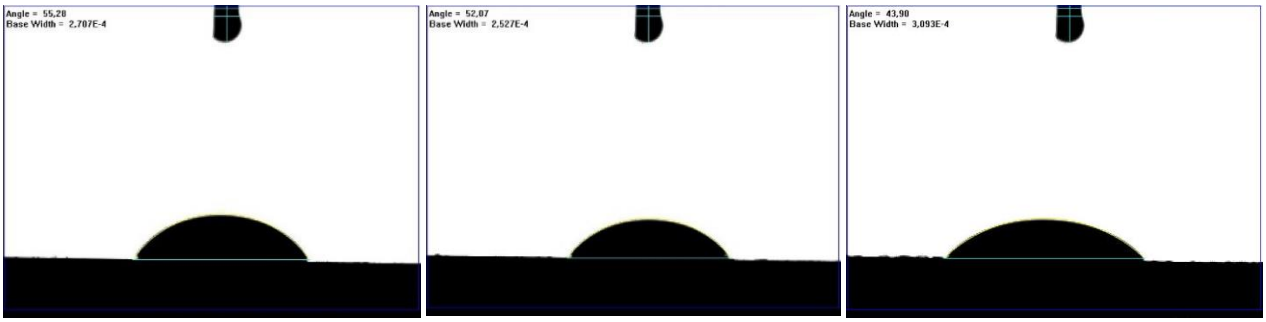

Diiodomethane contact angle diagrams of the lone sample (Bis(dimethyl amino) dimethyl silane thin film)

Appendix AH| Water contact angle diagrams of the lone sample (NTP deposited Bis(dimethyl amino) dimethyl silane thin film)

References

[1] N. Nandkumar, "Plasma—the fourth state of matter," *Int J Sci Technol Res,* vol. 3, no. 9, pp. 49-52, 2014.

[2] S. Choi *et al.*, "Structural and functional analysis of lysozyme after treatment with dielectric barrier discharge plasma and atmospheric pressure plasma jet," *Scientific reports,* vol. 7, no. 1, pp. 1-10, 2017.

[3] S. H. Kim, J. H. Kim, and B.-K. Kang, "Decomposition reaction of organophosphorus nerve agents on solid surfaces with atmospheric radio frequency plasma generated gaseous species," *Langmuir,* vol. 23, no. 15, pp. 8074-8078, 2007.

[4] S. Saboohi, B. R. Coad, H. J. Griesser, A. Michelmore, and R. D. Short, "Synthesis of highly functionalised plasma polymer films from protonated precursor ions via the plasma α–γ transition," *Physical Chemistry Chemical Physics,* vol. 19, no. 7, pp. 5637-5646, 2017.

[5] M. López *et al.*, "A review on non-thermal atmospheric plasma for food preservation: Mode of action, determinants of effectiveness, and applications," *Frontiers in microbiology,* vol. 10, p. 622, 2019.

[6] G. Isbary *et al.*, "Cold atmospheric plasma devices for medical issues," *Expert review of medical devices,* vol. 10, no. 3, pp. 367-377, 2013.

[7] M. Lieberman and A. Lichtenberg, "Electrostatic Probe Diagnostics," *Principles of Plasma Discharges and Materials Processing, 2nd ed., Ch., doi,* vol. 10, no. 0471724254, pp. 185-203.

[8] J. J. Vargo, "Clinical applications of the argon plasma coagulator," *Gastrointestinal endoscopy,* vol. 59, no. 1, pp. 81-88, 2004.

[9] T. Matsumoto, D. Wang, T. Namihira, and H. Akiyama, "Non-thermal plasma technic for air pollution control," *Air pollution-a comprehensive perspective,* 2012.

[10] C. Hoffmann, C. Berganza, and J. Zhang, "Cold Atmospheric Plasma: methods of production and application in dentistry and oncology," *Medical gas research,* vol. 3, no. 1, pp. 1-15, 2013.

[11] H. Uchiyama *et al.*, "EPR-spin trapping and flow cytometric studies of free radicals generated using cold atmospheric argon plasma and X-ray irradiation in aqueous solutions and intracellular milieu," *Plos one,* vol. 10, no. 8, p. e0136956, 2015.

[12] D. Kolacyak, J. Ihde, C. Merten, A. Hartwig, and U. Lommatzsch, "Fast functionalization of multi-walled carbon nanotubes by an atmospheric pressure plasma jet," *Journal of colloid and interface science,* vol. 359, no. 1, pp. 311-317, 2011.

[13] T. none Namihira, "Non-Thermal Plasma Technic for Air Pollution Control," *Chapters,* 2012.

[14] S. Kalghatgi *et al.*, "Effects of non-thermal plasma on mammalian cells," *PloS one,* vol. 6, no. 1, p. e16270, 2011.

[15] S. Yonemori and R. Ono, "Flux of OH and O radicals onto a surface by an atmospheric-pressure helium plasma jet measured by laser-induced fluorescence," *Journal of Physics D: Applied Physics,* vol. 47, no. 12, p. 125401, 2014.

[16] Z. Liu *et al.*, "Production of simplex RNS and ROS by nanosecond pulse N2/O2 plasma jets with homogeneous shielding gas for inducing myeloma cell apoptosis," *Journal of Physics D: Applied Physics,* vol. 50, no. 19, p. 195204, 2017.

[17] Y. Jiao, F. R. Tay, L.-n. Niu, and J.-h. Chen, "Advancing antimicrobial strategies for managing oral biofilm infections," *International journal of oral science,* vol. 11, no. 3, pp. 1-11, 2019.

[18] F. Tan, Y. Fang, L. Zhu, and M. Al-Rubeai, "Controlling stem cell fate using cold atmospheric plasma," *Stem Cell Research & Therapy,* vol. 11, no. 1, pp. 1-10, 2020.

[19] M. Domonkos, P. Tichá, J. Trejbal, and P. Demo, "Applications of Cold Atmospheric Pressure Plasma Technology in Medicine, Agriculture and Food Industry," *Applied Sciences,* vol. 11, no. 11, p. 4809, 2021.

[20] H. D. Stryczewska, "Supply systems of non-thermal plasma reactors. Construction review with examples of applications," *Applied Sciences,* vol. 10, no. 9, p. 3242, 2020.

[21] J. Šimončicová, S. Kryštofová, V. Medvecká, K. Ďurišová, and B. Kaliňáková, "Technical applications of plasma treatments: current state and perspectives," *Applied microbiology and biotechnology,* vol. 103, no. 13, pp. 5117-5129, 2019.

[22] S. K. Pankaj, Z. Wan, and K. M. Keener, "Effects of cold plasma on food quality: A review," *Foods,* vol. 7, no. 1, p. 4, 2018.

[23] G. D. Deepak, N. Joshi, and R. Prakash, "Model analysis and electrical characterization of atmospheric pressure cold plasma jet in pin electrode configuration," *AIP Advances,* vol. 8, no. 5, p. 055321, 2018.

[24] O. Lunov *et al.*, "Cell death induced by ozone and various non-thermal plasmas: therapeutic perspectives and limitations," *Scientific reports,* vol. 4, no. 1, pp. 1-11, 2014.

[25] J. Julák, H. Soušková, V. Scholtz, E. Kvasničková, D. Savická, and V. Kříha, "Comparison of fungicidal properties of non-thermal plasma produced by corona discharge and dielectric barrier discharge," *Folia microbiologica,* vol. 63, no. 1, pp. 63-68, 2018.

[26] S. Tabibian, M. Labbafi, G. Askari, A. Rezaeinezhad, and H. Ghomi, "Effect of gliding arc discharge plasma pretreatment on drying kinetic, energy consumption and physico-chemical properties of saffron (Crocus sativus L.)," *Journal of Food Engineering,* vol. 270, p. 109766, 2020.

[27] L. Gao, X. Shi, and X. Wu, "Applications and challenges of low temperature plasma in pharmaceutical field," *Journal of Pharmaceutical Analysis,* vol. 11, no. 1, pp. 28-36, 2021.

[28] E. Liston, L. Martinu, and M. Wertheimer, "Plasma surface modification of polymers for improved adhesion: a critical review," *Journal of adhesion science and technology,* vol. 7, no. 10, pp. 1091-1127, 1993.

[29] F. Fanelli and F. Fracassi, "Atmospheric pressure non-equilibrium plasma jet technology: general features, specificities and applications in surface processing of materials," *Surface and Coatings*

Technology, vol. 322, pp. 174-201, 2017.

[30] L. V. Shepsis, P. D. Pedrow, R. Mahalingam, and M. A. Osman, "Modeling and experimental comparison of pulsed plasma deposition of aniline," *Thin Solid Films,* vol. 385, no. 1-2, pp. 11-21, 2001.

[31] E. Çıtak *et al.*, "Vapor deposition of quaternary ammonium methacrylate polymers with high antimicrobial activity: Synthetic route, toxicity assessment, and durability analysis," *Journal of vacuum science & technology a: vacuum, surfaces, and films,* vol. 38, no. 4, p. 043203, 2020.

[32] A. Tripathy *et al.*, "Fabrication of low-cost flexible superhydrophobic antibacterial surface with dual-scale roughness," *ACS Biomaterials Science & Engineering,* vol. 4, no. 6, pp. 2213-2223, 2018.

[33] C. Adlhart *et al.*, "Surface modifications for antimicrobial effects in the healthcare setting: A critical overview," *Journal of Hospital Infection,* vol. 99, no. 3, pp. 239-249, 2018.

[34] H. E. Emam *et al.*, "Copper (I) oxide surface modified cellulose fibers—Synthesis, characterization and antimicrobial properties," *Surface and Coatings Technology,* vol. 254, pp. 344-351, 2014.

[35] S. Silver, "Bacterial silver resistance: molecular biology and uses and misuses of silver compounds," *FEMS microbiology reviews,* vol. 27, no. 2-3, pp. 341-353, 2003.

[36] J. A. Lemire, J. J. Harrison, and R. J. Turner, "Antimicrobial activity of metals: mechanisms, molecular targets and applications," *Nature Reviews Microbiology,* vol. 11, no. 6, pp. 371-384, 2013.

[37] A. Singh and A. K. Dubey, "Various biomaterials and techniques for improving antibacterial response," *ACS Applied Bio Materials,* vol. 1, no. 1, pp. 3-20, 2018.

[38] I. Yudovin-Farber, J. Golenser, N. Beyth, E. I. Weiss, and A. J. Domb, "Quaternary ammonium polyethyleneimine: antibacterial activity," *Journal of nanomaterials,* vol. 2010, 2010.

[39] S. Saidin, M. A. Jumat, N. A. A. M. Amin, and A. S. S. Al-Hammadi, "Organic and inorganic antibacterial approaches in combating bacterial infection for biomedical application," *Materials Science and Engineering: C,* vol. 118, p. 111382, 2021.

[40] Y. Chen *et al.*, "Comparative assessment of the stability of nonfouling poly (2-methyl-2-oxazoline) and poly (ethylene glycol) surface films: An in vitro cell culture study," *Biointerphases,* vol. 9, no. 3, p. 031003, 2014.

[41] W.-R. Li *et al.*, "The dynamics and mechanism of the antimicrobial activity of tea tree oil against bacteria and fungi," *Applied microbiology and biotechnology,* vol. 100, no. 20, pp. 8865-8875, 2016.

[42] J. H. Nogueira, E. Gonçalez, S. R. Galleti, R. Facanali, M. O. Marques, and J. D. Felício, "Ageratum conyzoides essential oil as aflatoxin suppressor of Aspergillus flavus," *International Journal of Food Microbiology,* vol. 137, no. 1, pp. 55-60, 2010.

[43] I. JAVED, "International Bureau (43) International Publication Date 12 November 2009 (12.11. 2009)."

[44] D. Davies, "Understanding biofilm resistance to antibacterial agents," *Nature reviews Drug discovery,* vol. 2, no. 2, pp. 114-122, 2003.

[45] A. Tripathy, P. Sen, B. Su, and W. H. Briscoe, "Natural and bioinspired nanostructured bactericidal surfaces," *Advances in colloid and interface science,* vol. 248, pp. 85-104, 2017.

[46] P. Tatar, N. Kiraz, M. Asiltürk, F. Sayılkan, H. Sayılkan, and E. Arpac, "Antibacterial thin films on glass substrate by sol–gel process," *Journal of Inorganic and Organometallic Polymers and Materials,* vol. 17, no. 3, pp. 525-533, 2007.

[47] J. Lombard, "Once upon a time the cell membranes: 175 years of cell boundary research," *Biology direct,* vol. 9, no. 1, pp. 1-35, 2014.

[48] C. Tanford, *The hydrophobic effect: formation of micelles and biological membranes 2d ed*. J. Wiley., 1980.

[49] G. L. Nicolson, "Transmembrane control of the receptors on normal and tumor cells: I. Cytoplasmic influence over cell surface components," *Biochimica et Biophysica Acta (BBA)-Reviews on Biomembranes,* vol. 457, no. 1, pp. 57-108, 1976.

[50] K. Jacobson, E. D. Sheets, and R. Simson, "Revisiting the fluid mosaic model of membranes," *Science,* vol. 268, no. 5216, pp. 1441-1443, 1995.

[51] T. J. Silhavy, D. Kahne, and S. Walker, "The bacterial cell envelope," *Cold Spring Harbor perspectives in biology,* vol. 2, no. 5, p. a000414, 2010.

[52] L. Brown, J. M. Wolf, R. Prados-Rosales, and A. Casadevall, "Through the wall: extracellular vesicles in Gram-positive bacteria, mycobacteria and fungi," *Nature Reviews Microbiology,* vol. 13, no. 10, pp. 620-630, 2015.

[53] D. Mengin-Lecreulx and B. Lemaitre, "Structure and metabolism of peptidoglycan and molecular requirements allowing its detection by the Drosophila innate immune system," *Journal of endotoxin research,* vol. 11, no. 2, pp. 105-111, 2005.

[54] P. R. J. Yulo and H. L. Hendrickson, "The evolution of spherical cell shape; progress and perspective," *Biochemical Society Transactions,* vol. 47, no. 6, pp. 1621-1634, 2019.

[55] D. T. Kysela, A. M. Randich, P. D. Caccamo, and Y. V. Brun, "Diversity takes shape: understanding the mechanistic and adaptive basis of bacterial morphology," *PLoS Biology,* vol. 14, no. 10, p. e1002565, 2016.

[56] A. Kornberg and T. A. Baker, *DNA replication*. Wh Freeman New York, 1992.

[57] M. A. Croxen and B. B. Finlay, "Molecular mechanisms of Escherichia coli pathogenicity," *Nature Reviews Microbiology,* vol. 8, no. 1, pp. 26-38, 2010.

[58] C. Berne, C. K. Ellison, A. Ducret, and Y. V. Brun, "Bacterial adhesion at the single-cell level," *Nature Reviews Microbiology,* vol. 16, no. 10, pp. 616-627, 2018.

[59] M. Breitbart and F. Rohwer, "Here a virus, there a virus, everywhere the same virus?," *Trends in*

microbiology, vol. 13, no. 6, pp. 278-284, 2005.

[60] J. Louten, "Virus structure and classification," *Essential Human Virology,* p. 19, 2016.

[61] M. Charman, C. Herrmann, and M. D. Weitzman, "Viral and cellular interactions during adenovirus DNA replication," *FEBS letters,* vol. 593, no. 24, pp. 3531-3550, 2019.

[62] R. F. Bruinsma, G. J. Wuite, and W. H. Roos, "Physics of viral dynamics," *Nature Reviews Physics,* vol. 3, no. 2, pp. 76-91, 2021.

[63] P. U. Joshi, D. G. Turpeinen, M. Weiss, G. Escalante-Corbin, M. Schroeder, and C. L. Heldt, "Tie line framework to optimize non-enveloped virus recovery in aqueous two-phase systems," *Journal of Chromatography B,* vol. 1126, p. 121744, 2019.

[64] N. Castaño *et al.*, "Fomite transmission and disinfection strategies for SARS-CoV-2 and related viruses," *arXiv preprint arXiv:2005.11443,* 2020.

[65] P. D. Rakowska *et al.*, "Antiviral surfaces and coatings and their mechanisms of action," *Communications Materials,* vol. 2, no. 1, pp. 1-19, 2021.

[66] E. Joonaki, A. Hassanpouryouzband, C. L. Heldt, and O. Areo, "Surface chemistry can unlock drivers of surface stability of SARS-CoV-2 in variety of environmental conditions," *Chem,* 2020.

[67] Y. Sun, Y. Qiu, A. Nie, and X. Wang, "Experimental research on inactivation of bacteria by using dielectric barrier discharge," *IEEE Transactions on Plasma Science,* vol. 35, no. 5, pp. 1496-1500, 2007.

[68] N. Philip, B. Saoudi, M.-C. Crevier, M. Moisan, J. Barbeau, and J. Pelletier, "The respective roles of UV photons and oxygen atoms in plasma sterilization at reduced gas pressure: The case of N/sub 2/-O/sub 2/mixtures," *IEEE Transactions on Plasma Science,* vol. 30, no. 4, pp. 1429-1436, 2002.

[69] N. Mehle, I. Gutierrez-Aguirre, D. Kutnjak, and M. Ravnikar, "Water-mediated transmission of plant, animal, and human viruses," *Advances in virus research,* vol. 101, pp. 85-128, 2018.

[70] H. Ghomi, S. Mohades, N. Navab Safa, and H. Dabiri, "Surface decontamination by dielectric barrier discharge plasma," *Journal of Biomedical Physics and Engineering,* vol. 2, no. 2, 2012.

[71] A. Filipić, I. Gutierrez-Aguirre, G. Primc, M. Mozetič, and D. Dobnik, "Cold plasma, a new hope in the field of virus inactivation," *Trends in Biotechnology,* vol. 38, no. 11, pp. 1278-1291, 2020.

[72] H. J. Lee, H. Jung, W. Choe, J. S. Ham, J. H. Lee, and C. Jo, "Inactivation of Listeria monocytogenes on agar and processed meat surfaces by atmospheric pressure plasma jets," *Food microbiology,* vol. 28, no. 8, pp. 1468-1471, 2011.

[73] T. Calvo, A. Alvarez-Ordóñez, M. Prieto, A. Bernardo, and M. López, "Stress adaptation has a minor impact on the effectivity of Non-Thermal Atmospheric Plasma (NTAP) against Salmonella spp," *Food research international,* vol. 102, pp. 519-525, 2017.

[74] J. Guo, K. Huang, and J. Wang, "Bactericidal effect of various non-thermal plasma agents and the influence of experimental conditions in microbial inactivation: A review," *Food Control,* vol. 50, pp. 482-490, 2015.

[75] X. Liao, F. Forghani, D. Liu, and T. Ding, "Cumulative damage by nonthermal plasma (NTP) exceeds the defense barrier of multiple antibiotic-resistant Staphylococcus aureus: a key to achieve complete inactivation," *Food Quality and Safety,* vol. 5, 2021.

[76] T. Winter *et al.*, "Characterization of the global impact of low temperature gas plasma on vegetative microorganisms," *Proteomics,* vol. 11, no. 17, pp. 3518-3530, 2011.

[77] C. B. Beggs, "A quantitative method for evaluating the photoreactivation of ultraviolet damaged microorganisms," *Photochemical & Photobiological Sciences,* vol. 1, no. 6, pp. 431-437, 2002.

[78] M. Y. Alkawareek, S. P. Gorman, W. G. Graham, and B. F. Gilmore, "Potential cellular targets and antibacterial efficacy of atmospheric pressure non-thermal plasma," *International journal of antimicrobial agents,* vol. 43, no. 2, pp. 154-160, 2014.

[79] D. Dobrynin, G. Fridman, G. Friedman, and A. Fridman, "Physical and biological mechanisms of direct plasma interaction with living tissue," *New Journal of Physics,* vol. 11, no. 11, p. 115020,

2009.

[80] I. Digel, A. T. Artmann, K. Nishikawa, M. Cook, E. Kurulgan, and G. Artmann, "Bactericidal effects of plasma-generated cluster ions," *Medical and Biological Engineering and Computing,* vol. 43, no. 6, pp. 800-807, 2005.

[81] M. Laroussi, "Nonthermal decontamination of biological media by atmospheric-pressure plasmas: review, analysis, and prospects," *IEEE Transactions on plasma science,* vol. 30, no. 4, pp. 1409-1415, 2002.

[82] O. Lunov *et al.*, "Non-thermal plasma mills bacteria: Scanning electron microscopy observations," *Applied Physics Letters,* vol. 106, no. 5, p. 053703, 2015.

[83] U. Zimmermann, G. Pilwat, and F. Riemann, "Dielectric breakdown of cell membranes," *Biophysical journal,* vol. 14, no. 11, pp. 881-899, 1974.

[84] J. Zimmermann, T. Shimizu, H. Schmidt, Y. Li, G. Morfill, and G. Isbary, "Test for bacterial resistance build-up against plasma treatment," *New Journal of Physics,* vol. 14, no. 7, p. 073037, 2012.

[85] A. Patelli *et al.*, "A customised atmospheric pressure plasma jet for conservation requirements," in *IOP Conference Series: Materials Science and Engineering*, 2018, vol. 364, no. 1: IOP Publishing, p. 012079.

[86] R. Tiede, J. Hirschberg, G. Daeschlein, T. von Woedtke, W. Vioel, and S. Emmert, "Plasma applications: a dermatological view," *Contributions to Plasma Physics,* vol. 54, no. 2, pp. 118-130, 2014.

[87] A. Arkhangelskiy, D. Maniglio, A. Bucciarelli, V. K. Yadavalli, and A. Quaranta, "Plasma-Assisted Deposition of Silk Fibroin on Different Surfaces," *Advanced Materials Interfaces,* p. 2100324, 2021.

[88] D. J. Economou, "Pulsed plasma etching for semiconductor manufacturing," *Journal of Physics D: Applied Physics,* vol. 47, no. 30, p. 303001, 2014.

[89] A. Al-Jumaili, K. Bazaka, and M. V. Jacob, "Retention of antibacterial activity in geranium plasma polymer thin films," *Nanomaterials,* vol. 7, no. 9, p. 270, 2017.

[90] A. W. Adamson and A. P. Gast, *Physical chemistry of surfaces*. Interscience publishers New York, 1967.

[91] D. K. Owens and R. Wendt, "Estimation of the surface free energy of polymers," *Journal of applied polymer science,* vol. 13, no. 8, pp. 1741-1747, 1969.

[92] V. Alt *et al.*, "An in vitro assessment of the antibacterial properties and cytotoxicity of nanoparticulate silver bone cement," *Biomaterials,* vol. 25, no. 18, pp. 4383-4391, 2004.

[93] T. Kim *et al.*, "Antimicrobial effects of metal ions (Ag+, Cu2+, Zn2+) in hydroxyapatite," *Journal of materials science: Materials in Medicine,* vol. 9, no. 3, pp. 129-134, 1998.

[94] Y. Sun *et al.*, "Inactivation of Candida biofilms by non-thermal plasma and its enhancement for fungistatic effect of antifungal drugs," *PloS one,* vol. 7, no. 7, p. e40629, 2012.

[95] C. Martins, J. Moreira, and J. Martins, "Corrosion in water supply pipe stainless steel 304 and a supply line of helium in stainless steel 316," *Engineering Failure Analysis,* vol. 39, pp. 65-71, 2014.

[96] A. Morro, F. Catalina, J. Pablos, T. Corrales, I. Marin, and C. Abrusci, "Surface modification of poly (ε-caprolactone) by oxygen plasma for antibacterial applications. Biocompatibility and monitoring of live cells," *European Polymer Journal,* vol. 94, pp. 405-416, 2017.

[97] A. Kumar *et al.*, "Pulse plasma deposition of Terpinen-4-ol: an insight into polymerization mechanism and enhanced antibacterial response of developed thin films," *Plasma Chemistry and Plasma Processing,* vol. 40, no. 1, pp. 339-355, 2020.

[98] N. Zhang, T. Pompe, I. Amin, R. Luxenhofer, C. Werner, and R. Jordan, "Tailored poly (2-oxazoline) polymer brushes to control protein adsorption and cell adhesion," *Macromolecular bioscience,* vol. 12, no. 7, pp. 926-936, 2012.

[99] V. Mazánková *et al.*, "Atmospheric pressure plasma polymerized 2-ethyl-2-oxazoline based thin films for biomedical purposes," *Polymers,* vol. 12, no. 11, p. 2679, 2020.

[100] M. Ramiasa *et al.*, "Plasma polymerised polyoxazoline thin films for biomedical applications," *Chemical Communications,* vol. 51, no. 20, pp. 4279-4282, 2015.

[101] M. Narimisa, F. Krčma, Y. Onyshchenko, Z. Kozáková, R. Morent, and N. De Geyter, "Atmospheric pressure microwave plasma jet for organic thin film deposition," *Polymers,* vol. 12, no. 2, p. 354, 2020.

[102] A. Meshkova, F. Elam, S. Starostin, M. van de Sanden, and H. de Vries, "The role of carrier gas flow in roll-to-roll AP-PECVD synthesized silica moisture barrier films," *Surface and Coatings Technology,* vol. 339, pp. 20-26, 2018.

[103] M. Lapteva *et al.*, "Influence of temperature and plasma parameters on the properties of PEALD HfO 2," *Optical Materials Express,* vol. 11, no. 7, pp. 1918-1942, 2021.

[104] K.-S. Tseng and Y.-L. Lo, "Effect of sputtering parameters on optical and electrical properties of ITO films on PET substrates," *Applied surface science,* vol. 285, pp. 157-166, 2013.

[105] Y. S. Jung, "Spectroscopic ellipsometry studies on the optical constants of indium tin oxide films deposited under various sputtering conditions," *Thin Solid Films,* vol. 467, no. 1-2, pp. 36-42, 2004.

[106] H. Setyawan, M. Shimada, Y. Hayashi, K. Okuyama, and S. Yokoyama, "Particle formation and trapping behavior in a TEOS/O2 plasma and their effects on contamination of a Si wafer," *Aerosol science and technology,* vol. 38, no. 2, pp. 120-127, 2004.

[107] M. Akhtaruzzaman *et al.*, "Impact of Ar Flow Rates on Micro-Structural Properties of WS2 Thin Film by RF Magnetron Sputtering," *Nanomaterials,* vol. 11, no. 7, p. 1635, 2021.

[108] S. N. Ogugua, O. M. Ntwaeaborwa, and H. C. Swart, "Latest development on pulsed laser deposited thin films for advanced luminescence applications," *Coatings,* vol. 10, no. 11, p. 1078, 2020.

[109] D. Stawski and A. Nowak, "Thermal properties of poly (N, N-dimethylaminoethyl methacrylate)," *PloS one,* vol. 14, no. 6, p. e0217441, 2019.

[110] R. Di Mundo, R. d'Agostino, F. Fracassi, and F. Palumbo, "A Novel Organosilicon Source for Low Temperature Plasma Deposition of Silicon Nitride-like Thin Films," *Plasma processes and Polymers,* vol. 2, no. 8, pp. 612-617, 2005.

[111] J. Coates, "Interpretation of infrared spectra, a practical approach," ed: Citeseer, 2000.

[112] C. E. Viana, A. N. da Silva, N. I. Morimoto, and O. Bonnaud, "Analysis of SiO2 thin films deposited by PECVD using an oxygen-TEOS-argon mixture," *Brazilian Journal of Physics,* vol. 31, pp. 299-303, 2001.

[113] S. N. Hazmin, M. H. Mamat, and N. A. Muhamad, "Effect of nozzle-substrate distance on the structural and optical properties of AZO thin films deposited by spray pyrolysis technique," in *AIP Conference Proceedings*, 2021, vol. 2332, no. 1: AIP Publishing LLC, p. 120001.

[114] A. Perraudeau, C. Dublanche-Tixier, P. Tristant, C. Chazelas, S. Vedraine, and B. Ratier, "Low-temperature deposition of TiO2 by atmospheric pressure PECVD towards photoanode elaboration for perovskite and solid-state dye-sensitized solar cells," *EPJ Photovoltaics,* vol. 10, p. 5, 2019.

[115] J. Ryssy *et al.*, "Chemical and physical processes in the retention of functional groups in plasma polymers studied by plasma phase mass spectroscopy," *Physical Chemistry Chemical Physics,* vol. 18, no. 6, pp. 4496-4504, 2016.

[116] R. Radjef, K. L. Jarvis, C. Hall, A. Ang, B. L. Fox, and S. L. McArthur, "Characterising a Custom-Built Radio Frequency PECVD Reactor to Vary the Mechanical Properties of TMDSO Films," *Molecules,* vol. 26, no. 18, p. 5621, 2021.

[117] K. Jarvis and S. McArthur, "Exploiting reactor geometry to manipulate the properties of plasma polymerized acrylic acid films," *Materials,* vol. 12, no. 16, p. 2597, 2019.

[118] J. Wang, C. Liu, X. Lu, and M. Yin, "Co-polypeptides of 3, 4-dihydroxyphenylalanine and L-lysine

to mimic marine adhesive protein," *Biomaterials,* vol. 28, no. 23, pp. 3456-3468, 2007.

[119] Y.-Y. Yu, A.-H. Jiang, and W.-Y. Lee, "Organic/inorganic nano-hybrids with high dielectric constant for organic thin film transistor applications," *Nanoscale research letters,* vol. 11, no. 1, pp. 1-9, 2016.

[120] P. Sťahel *et al.*, "Atmospheric pressure plasma polymerized oxazoline-based thin films—antibacterial properties and cytocompatibility performance," *Polymers,* vol. 11, no. 12, p. 2069, 2019.

[121] A. M. Wrobel and P. Uznanski, "Hard silicon carbonitride thin-film coatings produced by remote hydrogen plasma chemical vapor deposition using aminosilane and silazane precursors. 1: Deposition mechanism, chemical structure, and surface morphology," *Plasma Processes and Polymers,* vol. 18, no. 5, p. 2000240, 2021.

[122] M.-J. Lee, J.-S. Kwon, H. B. Jiang, E. H. Choi, G. Park, and K.-M. Kim, "The antibacterial effect of non-thermal atmospheric pressure plasma treatment of titanium surfaces according to the bacterial wall structure," *Scientific reports,* vol. 9, no. 1, pp. 1-13, 2019.

[123] J. M. Stevenson and Y. Shi, "Theoretical Study of Decomposition Kinetics and Thermochemistry of Bis (dimethylamino) silane—Formation of Methyleneimine and Silanimine Species," *The Journal of Physical Chemistry A,* vol. 125, no. 37, pp. 8175-8186, 2021.

[124] R. Di Mundo, F. Palumbo, F. Fracassi, and R. d'Agostino, "Thin film deposition in capacitively coupled plasmas fed with bis (dimethylamino) dimethylsilane and oxygen: an FTIR study," *Plasma Processes and Polymers,* vol. 6, no. 8, pp. 506-511, 2009.

[125] P. Peng, J. Yang, Q. Wu, M. Wu, J. Liu, and J. Zhang, "Fabrication of N-halamine polyurethane films with excellent antibacterial properties," *e-Polymers,* vol. 21, no. 1, pp. 047-056, 2021.

[126] F. Hizal *et al.*, "Nanoengineered superhydrophobic surfaces of aluminum with extremely low bacterial adhesivity," *ACS applied materials & interfaces,* vol. 9, no. 13, pp. 12118-12129, 2017.

[127] K. M. Reddy, K. Feris, J. Bell, D. G. Wingett, C. Hanley, and A. Punnoose, "Selective toxicity of

zinc oxide nanoparticles to prokaryotic and eukaryotic systems," *Applied physics letters,* vol. 90, no. 21, p. 213902, 2007.

[128] V. Parthasarathi and G. Thilagavathi, "Synthesis and characterization of zinc oxide nanopartilce and its application on fabrics for microbe resistant defence clothing," *International Journal of Pharmacy and Pharmaceutical Sciences,* vol. 3, no. 4, pp. 392-398, 2011.

[129] A. Kumar, A. Al-Jumaili, K. Bazaka, P. Mulvey, J. Warner, and M. V. Jacob, "In-Situ Surface Modification of Terpinen-4-ol Plasma Polymers for Increased Antibacterial Activity," *Materials,* vol. 13, no. 3, p. 586, 2020.

[130] D. Yu, J. Wang, X. Shao, F. Xu, and H. Wang, "Antifungal modes of action of tea tree oil and its two characteristic components against Botrytis cinerea," *Journal of applied microbiology,* vol. 119, no. 5, pp. 1253-1262, 2015.

[131] M. Mousa and M. Khairy, "Synthesis of nano-zinc oxide with different morphologies and its application on fabrics for UV protection and microbe-resistant defense clothing," *Textile Research Journal,* vol. 90, no. 21-22, pp. 2492-2503, 2020.

[132] M. Vaara, "Agents that increase the permeability of the outer membrane," *Microbiological reviews,* vol. 56, no. 3, pp. 395-411, 1992.

[133] P. K. S. Mural, B. Kumar, G. Madras, and S. Bose, "Chitosan immobilized porous polyolefin as sustainable and efficient antibacterial membranes," *ACS Sustainable Chemistry & Engineering,* vol. 4, no. 3, pp. 862-870, 2016.

[134] N. Hilal, V. Kochkodan, L. Al-Khatib, and T. Levadna, "Surface modified polymeric membranes to reduce (bio) fouling: a microbiological study using E. coli," *Desalination,* vol. 167, pp. 293-300, 2004.

[135] U. Daood, J. P. Matinlinna, M. R. Pichika, K.-K. Mak, V. Nagendrababu, and A. S. Fawzy, "A quaternary ammonium silane antimicrobial triggers bacterial membrane and biofilm destruction," *Scientific reports,* vol. 10, no. 1, pp. 1-14, 2020.

[136] S. Al-Saadi, R. S. Raman, and C. Panter, "A Two-Step Silane Coating Incorporated with Quaternary Ammonium Silane for Mitigation of Microbial Corrosion of Mild Steel," *ACS omega,* vol. 6, no. 26, pp. 16913-16923, 2021.

[137] B. Ahlström, R. Thompson, and L. Edebo, "The effect of hydrocarbon chain length, pH, and temperature on the binding and bactericidal effect of amphiphilic betaine esters on Salmonella tvphimurium," *Apmis,* vol. 107, no. 1-6, pp. 318-324, 1999.

[138] A. Isquith, E. Abbott, and P. Walters, "Surface-bonded antimicrobial activity of an organosilicon quaternary ammonium chloride," *Applied microbiology,* vol. 24, no. 6, pp. 859-863, 1972.

[139] Y. Yuan, M. P. Hays, P. R. Hardwidge, and J. Kim, "Surface characteristics influencing bacterial adhesion to polymeric substrates," *RSC advances,* vol. 7, no. 23, pp. 14254-14261, 2017.

[140] S. Jasmee, G. Omar, M. Nordin, N. Masripan, and A. Kamarolzaman, "Hydrophobicity performance of thermoplastic polyurethane coated with TiO2 under thermal aging effect," in *1st Colloquium Paper: ADVANCED MATERIALS AND MECHANICAL ENGINEERING RESEARCH (CAMMER'18)*, 2018, vol. 1: Penerbit Universiti, Universiti Teknikal Malaysia Melaka, p. 65.

[141] P. Sengupta, S. S. Surwase, and B. L. Prasad, "Modification of porous polyethylene scaffolds for cell attachment and proliferation," *International journal of nanomedicine,* vol. 13, no. T-NANO 2014 Abstracts, p. 87, 2018.

[142] B. Li and B. E. Logan, "Bacterial adhesion to glass and metal-oxide surfaces," *Colloids and surfaces B: Biointerfaces,* vol. 36, no. 2, pp. 81-90, 2004.

[143] R. Bott *et al.*, "Brock Biology of Microorganisms," 2014.

[144] J. Van Impe *et al.*, "State of the art of nonthermal and thermal processing for inactivation of micro-organisms," *Journal of Applied Microbiology,* vol. 125, no. 1, pp. 16-35, 2018.

[145] P. Bourke, D. Ziuzina, L. Han, P. Cullen, and B. F. Gilmore, "Microbiological interactions with cold plasma," *Journal of applied microbiology,* vol. 123, no. 2, pp. 308-324, 2017.